DOCTOR OF SCIENCES

Depth profiling of hybrid multilayers using ToF-SIMS from model samples to photonic devices

Noel, Céline

Award date:
2019

Awarding institution:
University of Namur

UNIVERSITÉ DE NAMUR

Depth profiling of hybrid multilayers using ToF-SIMS: from model samples to photonic devices

Keywords: Depth profiling, ToF-SIMS, Low-energy Cesium, Hybrid materials, Perovskite solar cell, OLED

Dissertation présentée par

Céline Noël

en vue de l'obtention du grade de Docteur en Sciences

Avril 2019

Composition du jury

Dr. Laetitia Bernard (EMPA)

Dr. Yan Busby (UNamur)

Dr. Francesca Cecchet (UNamur)

Prof. Arnaud Delcorte (UCLouvain)

Prof. Anouk Galtayries (Chimie Paris Tech)

Prof. Laurent Houssiau (Promoteur, UNamur)

Depth profiling of hybrid multilayers using ToF-SIMS: from model samples to photonic devices

Abstract

In diverse areas such as medicine, energy, aerospace or electronics, the technology around us is constantly growing in sophistication. To improve device performances, advanced materials are combined into thin films multilayers or to form complex 3D architectures.

At the same time, the search for miniaturization pushes the device features to dimensions in the nanometer range, which confers a preponderant role to interfaces in the macroscopic behavior of devices. The understanding of complex phenomena taking place at thin films interfaces is mandatory to identify degradation mechanisms and also to rationally prevent or limit these effects. Therefore, methods for in-depth characterization need to be developed to implement strategies and to guide both the design and the processing conditions of thin film stacks; this would finally allow increasing both the device performance and lifetime.

In this context, time-of-flight secondary ion mass spectrometry (ToF-SIMS) has shown its ability to provide in-depth molecular information, combining an extremely high detection limit and surface sensitivity, high mass and depth resolutions, and convenient lateral resolution to image 3D features.

In this thesis work, ToF-SIMS surface and depth profile analysis is applied to investigate model and applied thin film architectures using different analysis and erosion ion beams conditions. In particular, the fundamental interaction mechanisms between ion beams and materials surfaces are highlighted by varying the nature, energy and size of the ion beam projectile. For hybrid (organic/inorganic) thin films, the sputtering and analysis beams conditions have been optimized to limit the materials modifications induced by the ion beam exposure while maintaining intense and characteristic (high mass fragments) molecular signals and reasonable sputtering yields (i.e. analysis time).

On particularly challenging hybrid device architectures for OLEDs and solar cells applications, the results unambiguously show that low energy cesium ion beam (Cs^+ at ~ 500 eV) and argon clusters ion beams (Ar_n^+) with reduced size (n~500 atoms) at a relatively high energy (~20 keV) are the most suitable conditions to perform depth profile analysis.

Profilage ToF-SIMS de multicouches hybrides : de l'étude d'échantillons modèles aux dispositifs photoniques

Résumé

Dans des domaines aussi divers que la médecine, l'énergie, l'aérospatial ou l'électronique, la technologie qui nous entoure ne cesse de gagner en sophistication. Pour améliorer les performances des dispositifs, des matériaux innovants sont agencés en multicouches ou forment des architectures 3D élaborées.

Parallèlement, la recherche de miniaturisation nous amène à manipuler des structures de l'ordre du nanomètre, ce qui confère aux interfaces un rôle prépondérant dans le comportement macroscopique des dispositifs. La compréhension des phénomènes complexes se produisant aux interfaces des couches minces est indispensable pour identifier les mécanismes de dégradation et également pour prévenir ou limiter de manière rationnelle ces effets. Par conséquent, des méthodes de caractérisation en profondeur doivent être développées pour mettre en œuvre des stratégies et pour guider à la fois la conception et les conditions d'utilisation de ces structures, ce qui permettrait in fine d'augmenter les performances et la durée de vie du dispositif.

Dans ce contexte, la spectrométrie de masse d'ions secondaires par temps de vol (ToF-SIMS) a montré sa capacité à fournir des informations moléculaires en profondeur, combinant une limite de détection et une sensibilité de surface extrêmement élevées, d'excellentes résolutions en masse et en profondeur, ainsi qu'une résolution latérale permettant d'effectuer de l'imagerie 3D.

Dans ce travail, des analyses ToF-SIMS de surface et en profondeur sont appliquées pour étudier des assemblages de films minces modèles ou constituant des dispositifs réels, à l'aide de différentes conditions d'analyse et d'érosion. En particulier, les mécanismes fondamentaux d'interaction des faisceaux avec la surface sont mis en évidence en faisant varier la nature, l'énergie et la taille du projectile du faisceau d'ions. Les meilleurs paramètres d'analyse en vue de pulvériser des couches minces, organiques et hybrides organiques/inorganiques, sont ensuite étudiés. Ces paramètres idéaux permettent de limiter la modification du matériau induite par l'exposition au faisceau d'ions tout en maintenant des signaux moléculaires intenses et caractéristiques (fragments de grande masse) et des rendements de pulvérisation raisonnables (temps d'analyse réduit).

Sur des architectures hybrides particulièrement complexes, telles que des OLED et des cellules solaires, les résultats montrent sans ambiguïté que les faisceaux d'ions césium de basse énergie (Cs^+ à ~ 500 eV) et les clusters d'argon (Ar_n^+) de taille réduite (n ~ 500 atomes) à une énergie élevée (~ 20 keV) sont les conditions les plus appropriées pour effectuer une analyse de profilage en profondeur.

Remerciements

Outre l'enrichissement scientifique, ces six années ont souvent été la source de grandes joies sur le plan personnel et, à l'heure du bilan, je souhaiterais remercier celles et ceux qui ont contribué à l'accomplissement de ce travail de thèse.
Tout d'abord, je tiens à remercier chaleureusement les membres du jury pour leur lecture attentive. Le manuscrit final a grandement bénéficié de leurs commentaires et de leurs conseils avisés.

Plus particulièrement, merci Laurent, pour les nombreuses discussions, scientifiques et moins scientifiques et pour ton encadrement résolument bienveillant. Merci pour la confiance que tu m'as très vite témoignée et la latitude que tu m'as laissée par rapport à mes choix de sujets de recherche. Dans ces conditions, il n'a pas été difficile de trouver ses marques.

Yan et Alex, vous avez été tour à tour mes fabuleux colocataires de bureau, mes co-promoteurs et mes grands frères. Pour les petits conseils, les grands coups de pouce et les fous rires, merci !

Mathieu, Polo, Louis, Adri et Romain, 10 ans déjà se sont écoulés depuis notre première année. Merci d'avoir été égaux à vous-mêmes tout ce temps. Vous m'êtes précieux.

Vous avez à un moment ou un autre été mes collègues, mais vous vous êtes surtout distingués de la mêlée par la qualité des moments passés ensemble, qu'il s'agisse de barbecues improvisés, de festivals de musique, de fêtes nationales, de matches de football ou d'honorables réunions de la BTS. Emile, Bruno, Seb P., Tija, Mika, Nico G., Seb M., Mirko, Xaxou et Steevo, vous vous étiez probablement reconnus, mais dans le doute...

Et en parlant de moments de qualité, la vie au labo, passe aussi par les pauses à la salle café. Merci du fond du cœur à Math, Julie, Jef, Luc, Pauline, Céline, Pierre H., Nico et tous les autres, pour les temps de midi animés, la bonne ambiance et les discussions du vendredi. Et à ce titre, je tiens à remercier plus particulièrement Pierre L., le maître en matière d'animation de débats. Grand enfant, quand il s'agit de nous taquiner, il sait se montrer une oreille attentive lorsque la sagesse du « Papy » est nécessaire.

Je retiens aussi de ma thèse les conférences, et les amis qu'on s'y fait. Ces semaines étaient très denses mais ont eu, grâce à Valentina, Alexis, Stefania, Nunzio, Stéphane et bien d'autres, des petits airs de colonies de vacances.

Finalement, un merci particulier à toutes les personnes qui, bien qu'exerçant un métier parfois très éloigné du domaine scientifique, se sont toujours montrées intéressées par ma recherche et savaient

se montrer disponibles pour me changer les idées. Vous tous, dont le soutien a été apprécié plus que vous ne le pensez, je ne me risquerai pas à vous citer, tant vous êtes nombreux. Merci à mes amis d'enfance, du basket, de l'Université, ou d'ailleurs encore, ma famille, les Poumay, Pounch, Moeder, Ros et Math, merci d'avoir été présents pour reléguer au second plan mes petits tracas occasionnels.

Table of Contents

1 INTRODUCTION

Organic and inorganic materials are combined in a growing number of modern devices applications. New and more complex combinations of materials, based on sophisticated hybrid organic/inorganic heterostructures, have been constantly developed to improve the device performance (**Figure 1**).

Such hybrid heterostructures typically consist either in stacked organic and inorganic thin layers (multilayers) or in a composite layer in which inorganic nanomaterials (nanoparticles, 2D materials, etc.) are embedded in an organic matrix. A large variety of technologies are concerned by the advent of hybrid materials: just to name a few, medicine, communication, cosmetics, aerospace, semiconductor industry and energy production and storage, which constitutes one of the most important challenges of our society. These innovative materials are expected to improve the performance of green technologies including solar cells, fuel cells, batteries to replace conventional energy sources based on oil, gas or nuclear fuels.

In the semiconductors industry, small organic molecules and polymers have attracted intense and growing research in the last twenty years. When charges are injected into organic semiconductors, they show a conductive behavior,[1] and these properties earned Shirakawa, Heeger, and McDiarmid the Nobel Prize in Chemistry in 2000. In modern electronic devices, organic semiconductors are typically combined with inorganic electrode materials (metals and conductive oxides). Since the beginning of this century, the numerous benefits provided by organic electronics, namely low-cost processing and simple deposition processes, malleability, transparency or tunable optical and electrical properties, have promoted their application in a multitude of state-of-the-art devices such as new generation solar cells,[2] organic light-emitting diodes (OLEDs),[3] organic field-effect transistors (OFETs)[4] and batteries.[5]

Among these innovative materials, hybrid organo-lead halide perovskites have received interest from a growing scientific community.[6] The peculiar crystalline structure of such perovskites, combining both metal and organic cations, makes it an ideal intrinsically-hybrid material. In the solar energy field, perovskite solar cells (PSCs) are considered the most promising technology, also because of the spectacular rise of their solar to power conversion efficiency (PCE). With a recent record of 22.6 %PCE[7] (starting from only 3.8 % in 2009[8]) on small area devices, perovskite technology currently competes with silicon-based PV cells. The major limitation that prevents the wide distribution of PSCs on the market are the toxicity of some components such as lead and the poor intrinsic stability of the

perovskite material. The increase of the device performance and stability has brought to a progressive increase of the PSCs formulation complexity: many configurations and materials for hole and electron extraction layers have been combined and the chemical composition of perovskite has been finely engineered with multiple materials. This complexity requires investigating degradation phenomena taking place at the interfaces and within thin layers in order to further optimize the devices.

Figure 1 - Example of structures found in hybrid organic/inorganic devices. Left: Perovskite solar cell [9] ; Right: OLED for display application [Source: https://oled.com/oleds/].

For solar cells and also many other photonics and organic electronics applications, there is an urgent need in further developing advanced characterization tools and protocols to understand more in depth, at the nanometer scale, degradation processes occurring at the interfaces. The development of new technologies opens opportunities and requires in parallel to develop and optimize analysis conditions using advanced characterization techniques.

Time-of-Flight Secondary Ion Mass Spectrometry (ToF-SIMS) and X-Ray Photoelectron Spectroscopy (XPS) coupled to ion beam depth profiling are versatile and complementary techniques to characterize the in-depth chemical and molecular composition of multilayers and to monitor the interfaces. Both techniques offer routine analysis of metal alloys, inorganic compounds, polymers or biological samples if the parameters are adequately chosen. In particular, ToF-SIMS presents an extremely high surface sensitivity and allows the molecular depth profiling of both organic and inorganic layers, with a depth resolution in the nanometer range. In a depth profile, molecular signals are displayed as a function of the ion beam sputtering time. Generally speaking, one expects steep rises and falls of molecular signal intensities at the interfaces. Conversely, blurred transitions are more difficult to interpret, because it can either indicate defects arising during the device processing, or degradation induced by some aging effect or a consequence of the ion beam bombardment during the analysis. To discriminate between these three effects, one should accurately design experiments, be aware of the sample preparation and be able to characterize the ion beam-surface interaction processes. This will greatly help the

differentiation of "real" degradation mechanisms from ion beam induced artifacts. This issue is addressed in **Chapter 2** (Materials and Methods) when discussing practical aspects of ToF-SIMS i.e. the operating principles and a description of the different analysis modes.

Amongst the large variety of analytical techniques, ToF-SIMS offers an excellent combination of surface sensitivity, molecular analysis capability and lateral resolution allowing for imaging. Complementary information is accessible with XPS analysis. A comparison between both techniques is given in this section. Besides the analysis techniques, the deposition process of thin layers affects the interpretation of the depth profiles, since the quality of the samples is an essential prerequisite for high-quality in-depth analyses. This is the reason why we focus on the experimental deposition parameters and motivate the selection of the deposited materials. Finally, a data treatment method based on multivariate analysis (Principal Component Analysis, PCA) is briefly introduced. This last paragraph, although not exhaustive, should provide adequate fundamental aspects for the comprehension of results involving PCA treatment.

Optimizing the depth profiling conditions, of course, requires mastering the parameters that influence the depth resolution and understand how this latter is measured. **Chapter 3** is dedicated to depth profiling, along with a history of the existing ion sputtering sources and the sputtering mechanisms that are involved. A first insight is given to summarize the advantages and drawbacks associated with the different ion sources, for different materials (organic, inorganic), and the parameters which can be adjusted to optimize the sputtering conditions. Challenges regarding the in-depth molecular characterization of hybrid stacks are also discussed in the light of existing studies and analytical methods.

Chapter 4 presents the results divided into four sections, each accounting for a specific publication. The busy reader can skip the introduction and experimental sections of the scientific papers, which contain a certain amount of redundancy with the main text. It is worth noticing that each article is an independent entity, with its own bibliography, while the references associated with the main text are sent back to **Chapter 6**.

Section 4.1 assesses the depth profiling of organic materials using low energy Cs^+. In particular, model samples that were already studied in previous works from our group, and for which the depth profiles, obtained with low-energy Cs^+ and Ga^+ beams were not successful (in a way that will be explained), have been analyzed with different analysis beam conditions and the parameters of the analysis gun are discussed. It appears that, more than the sputter gun parameters, the final depth resolution is strongly impacted by the analysis primary ions nature and fluence, despite the very low fluence when compared to the sputter gun. The results show that the best depth resolution achievable using Cs^+ (less than 4 nm in our best conditions) competes with the ultimate resolution obtained when using Ar_n^+ clusters (4-5 nm)[10,11].

After investigating organic model samples, **Section 4.2** focuses on the study of hybrid model stacks made of metal thin layers (either gold or chromium) and amino acid layers deposited on a silicon substrate. We discuss key parameters such as the recoil depth, degradation rate and changes in erosion rates during the profile, depending on the metal (Au or Cr) and on whether the soft (organic) material is deposited on the top of or below the metallic layer. On such samples, notoriously difficult to depth profile, the Cs^+ beam allows obtaining excellent depth resolutions.

Partnerships with multiple research groups across Europe allowed disposing of state-of-the-art optoelectronic devices. Knowing that Cs^+ constitutes a convenient erosion source for hybrid depth profiling, we applied these ions in **Section 4.3** on complex organic light emitting diodes (OLEDs) multilayers. In parallel, we challenged a PCA-assisted procedure for the unsupervised localization of interfaces and identification of characteristic molecular peaks. This method proves to be fast, user-independent and very efficient in differentiating layers, except when interfaces are excessively degraded. In this case, we proposed that the user has to consider a higher number of Principal Components (PCs). Also, the relatively high fragmentation induced by monatomic ion beam sputtering sometimes hinders discrimination between too similar organic molecules.

In **Section 4.4**, the study of perovskite monolayers and perovskite solar cells brings a higher level of complexity. This intrinsically hybrid material (used in solar cells, LEDs or sensors) was deposited on a glass substrate and depth profiled using Cs, monoatomic Ar and Ar clusters in a wide range of cluster sizes and energies. We compare a variety of different sputtering conditions, in terms of the depth profile quality and propose optimized parameters, in order to keep the perovskite modification as low as possible. This is an essential prerequisite to safely identify degradation features. It appears that the best conditions are obtained with 500 eV Cs^+ and small argon clusters with high energy per atom (Ar_{500}^+ at 20 keV).

Overall, this work discusses the challenges regarding the depth profiling of organic and hybrid samples and compares the performances of different ion sources. In particular, it draws the attention of the operator about the importance of both erosion and analysis beams parameters and guides him/her in the selection of optimized conditions (i.e. limit the damage induced by the beam, provide high sputter rates and maintain high intensities of molecular fragments). By progressively increasing the complexity of the studied systems (starting from simple organic model multilayers to thin metal layers deposited on amino acids, to full optoelectronic devices), we are now in a position to provide recommendations for the extraction of 3D information from complex hybrid systems. The present work also demonstrates that, thanks to their versatility, low-energy Cs and Ar clusters (whose size and energy can be easily tuned) allow investigating buried thin layers and interface effects in organic, inorganic and hybrid multilayers.

2 MATERIALS & METHODS

2.1 TIME OF FLIGHT SECONDARY ION MASS SPECTROMETRY (TOF-SIMS)

2.1.1 Basic operating principles

Time of Flight Secondary Ion Mass Spectrometry (ToF-SIMS) is a powerful surface analysis technique that provides a molecular identification of the first atomic layers of the sample. The surface is bombarded with primary ions that are back-scattered or implanted into the surface. The scattering cross-section, i.e. the probability of interaction between the projectile and the target decreases with the projectile incident energy like $1/E^2$.[12] In SIMS, the relatively low energy ranges (a few keV) compared to nuclear analysis techniques (usually, a few MeV) allows the incident ions to deliver a part of their energy to the target atoms. Following the example of billiard balls, this energy is then dissipated into the material through collision cascades. Eventually, some branches of this collision return to the surface, leading to the ejection of ionized and neutral fragments or molecules that are characteristic of the sample surface. When moving away from the impact point, where only small fragments are ejected, the energy that returns to the surface has dissipated and allows higher mass molecular fragments to be desorbed. Simultaneously, electrons and photons can be emitted from the surface following de-excitation processes (**Figure 2**).[13]

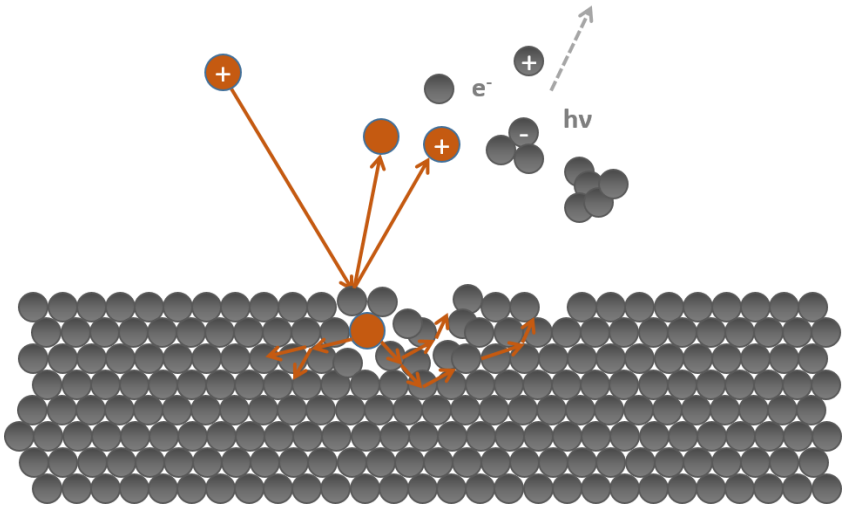

Figure 2 – Primary ion bombardment in SIMS. The primary ions are backscattered or implanted in the surface. In this case, it gives rise to collision cascades and the ejection of neutral and ionized fragments.

A voltage of typically 2 kV, called extraction voltage, is set 1.5 millimeters above the sample (which is usually grounded) and the potential difference generates an electric field that accelerates the ionized fragments towards the analyzer column. These so-called secondary ions, representing only a small proportion of the ejected matter, constitute the only information collected by the technique, while neutral fragments and molecules stay in the chamber and are pumped or redeposited. This means that the signal intensity (output) depends on the ionization, and the ejection probabilities, making ToF-SIMS a semi-quantitative technique. Indeed, for elemental secondary ions, the ionization is due to electron exchange between the ejected atom and the surface. This process can be dramatically affected by the chemical environment of the surface. It is for example well known that oxidation can vary the ionization yields by several orders of magnitude[14]. Molecular fragments are also subject to this matrix effect, despite different ionization mechanisms are involved[15]. Overall, the detected intensity I_M of a species M is governed by this fundamental equation:

$$I_M = \alpha\, Y_M\, I_P\, [M]\, \eta \qquad (1)$$

Where α is the ionization probability, Y_M is the total yield of the species M (the number of sputtered particles M per primary ion), I_P is the number of primary ions per second, [M] is the relative concentration of the fragment M in the sample and η is related to the transmission of the analyzer and the detector efficiency. Obviously, the intensity in the spectrum cannot be directly assimilated to the concentration.

Under the effect of the electric field, secondary ions acquire a fixed kinetic energy (i.e. 2 keV) and travel through a drift region of a known length with a velocity that is characteristic of their mass (**Figure 3**). The Time of Flight (ToF) of each ion from the sample surface to the detector is recorded and a simple conversion allows for the mass calculation of molecular fragments following the relation:

$$\mathrm{z.e.V} = \frac{\mathrm{m.v^2}}{2} = \frac{\mathrm{m.(L/t)^2}}{2} \Leftrightarrow \frac{\mathrm{m}}{\mathrm{z}} = \frac{\mathrm{2.e.V}}{\mathrm{(L/t)^2}} = \mathrm{2.e.V}\frac{\mathrm{t^2}}{\mathrm{L^2}} \qquad (2)$$

where z.e stands for the ionic charge, V is the extraction potential and v denotes the velocity of a specific ion, which can be easily calculated, knowing the distance between the sample surface and the detector L and by measuring the time needed by this ion to reach the detector, t.

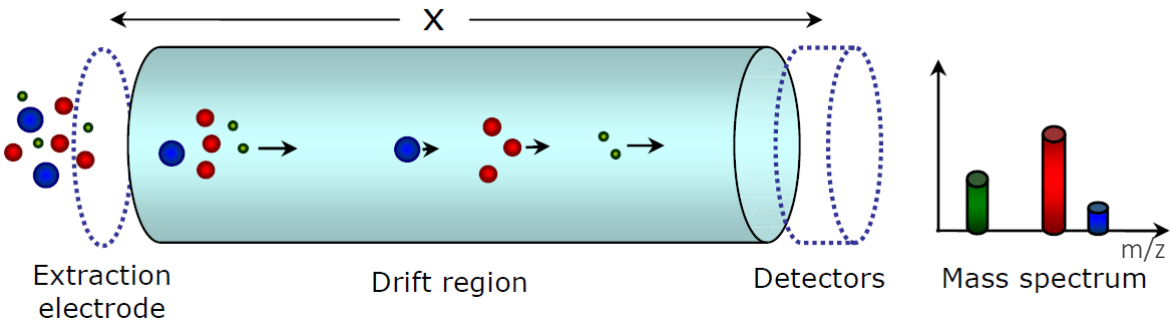

Figure 3 – Working principle of a time of flight detector.[16]

The analysis source used in this work emits simultaneously Bi^+ and small Bi clusters (Bi_3^+, Bi_5^+, Bi_7^+). They all have the same energy, but different masses, resulting in different velocities, which in turn affects the mass resolution. In order to select a single species, one uses a Wien filter[1], a mass selector constituted by an electric field crossed with a magnetic field. The particles are not deflected when the Coulomb's law equals the magnetic force of Lorentz's law, $qE = qvB$, thus $v = E/B$. In other words, by adjusting the values of E and B, it is possible to select a single species of analysis ions. The choice between monoatomic ions and small clusters is motivated by whether one needs to enhance the signal intensity or to preserve high mass intensities by decreasing the average energy per atom, respectively. Measuring times of flight implies that the analysis beam has to be pulsed. This is made possible by the chopper, in which a square signal voltage with a frequency of 5 kHz is applied to two deflection plates. Most of the time, when the voltage is set to V_{max} or $-V_{max}$, the beam is deflected out of the aperture, but every time the signal polarity is reversed (meaning every 100 µs), the beam passes through the aperture for 10 to 100 ns, giving the length of the primary pulse. Reducing the pulse length narrows the dispersion of the measured times of flight for fragments of the same mass and consequently, it increases the mass resolution. Beyond the chopper, the ions enter into the buncher, which is made of two plates that are both grounded when the pulse enters the zone in between them. When the pulse is located exactly between the plates, the rear plate is set to a positive voltage that accelerates the ions, the last ones being more accelerated than the first ones (**Figure 4**). This allows the reduction of the pulse length to a value of 1 ns and improves considerably the mass resolution. However, this broadens the kinetic energy distribution of the ions inside a pulse, implying they are not deflected the same way inside the optical focalization system (chromatic aberration). The diameter of the beam is thus negatively affected, and the lateral resolution is degraded. For this reason, when high lateral accuracy is needed, the buncher cannot be used, implying that the mass resolution is sensibly reduced.

[1] This description refers to the equipment of a ToF-SIMS IV from ION-TOF (Münster, Germany) and differs for more recent tools.

Practically, it is possible to partially workaround and find a trade-off between mass resolution and lateral resolution, as will be briefly explained in the next section.

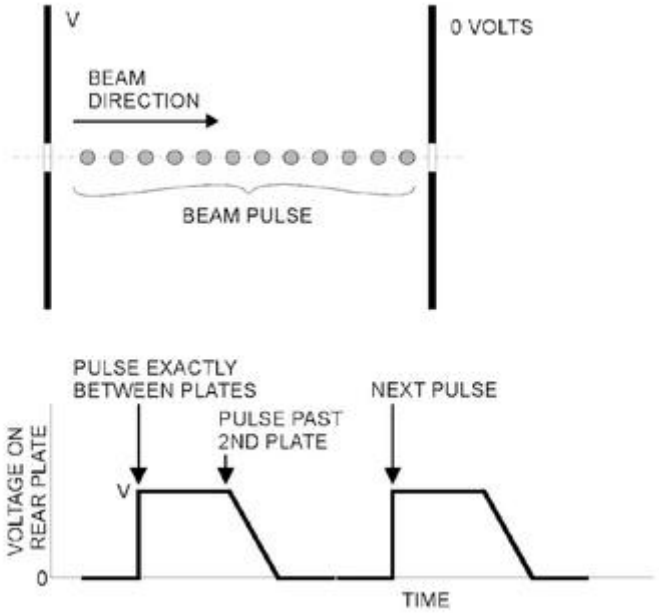

Figure 4 – Schematic of a buncher. [17]

Finally, localized charge effects arising from the intake of positive charge (and the ejection of ionized fragments and electrons) may spread the energy distribution of secondary ions or even deflect the primary beam, due to the buildup of a surface voltage. A flood gun is used to compensate this charge by flooding low-energy electrons over the surface. However, the topography (that affects the electric field and the distance traveled from the sample to the detector) and the initial kinetic energy distribution of the different species sputtered from the surface can also affect the times of flight. The mass resolution is thus badly degraded on uneven surfaces.

In order to lessen the time of flight distribution of the ions with the same mass, a uniform electrical field curves the trajectory of the ions at the top of the analyzer column, in a so-called reflectron electrostatic mirror (**Figure 5)**.

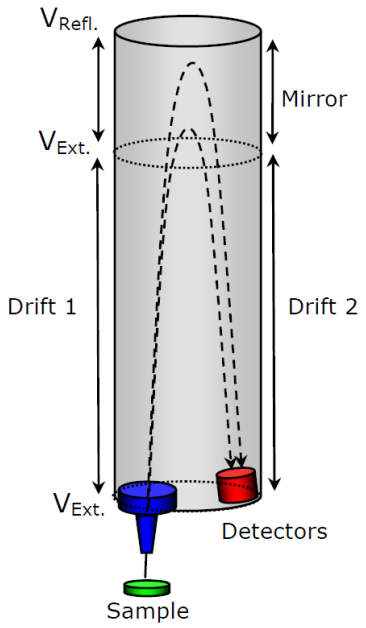

Figure 5 – Sketch of a *reflectron* ion mirror, placed at the top of the analyzer column.[16]

This way, for the same mass, the most energetic ions travel a longer distance and reach the detector simultaneously with the other ions. Indeed, from the equation (2), we know that the time of flight is:

$$t = \mathrm{L}\,.\sqrt{\frac{\mathrm{m}}{2.\mathrm{z.e.V}}} \tag{3}$$

We can also write that $m=2.E.t^2/L^2$, where E is the energy attributed to every ion of charge z.e by the potential ΔV. Then the differential expression of the mass is:

$$\mathrm{dm} = \frac{4\mathrm{Et}}{\mathrm{L}^2}\,\mathrm{dt} + \frac{2\mathrm{t}^2}{\mathrm{L}^2}\,\mathrm{dE} - \frac{4\mathrm{Et}^2}{\mathrm{L}^3}\,\mathrm{dL} = 2\mathrm{m}\,\frac{\mathrm{dt}}{\mathrm{t}} + \mathrm{m}\,\frac{\mathrm{dE}}{\mathrm{E}} - 2\mathrm{m}\,\frac{\mathrm{dL}}{\mathrm{L}} \tag{4}$$

The inverse of the mass resolution can thus be written by:

$$\frac{\Delta\mathrm{m}}{\mathrm{m}} = 2\frac{\Delta\mathrm{t}}{\mathrm{t}} + \frac{\Delta\mathrm{E}}{\mathrm{E}} - 2\frac{\Delta\mathrm{L}}{\mathrm{L}}, \tag{5}$$

meaning that the parameters which are responsible for the mass resolution degradation are Δt and ΔE, the energy distribution of the secondary ions when they are emitted from the surface. The reflectron voltage is set at +- 25 V at the top of the detection column, allowing the most energetic ions to travel a longer distance. This additional ΔL impacts positively the mass resolution, i.e. reduces Δm/m and compensates for the degradation brought by the ΔE.

2.1.2 ToF SIMS analysis modes

As mentioned previously, ToF-SIMS allows molecular characterization of layers through the parallel detection of all the ionized fragments emitted from the surface. Practically, the analyzed surface is divided into pixels. A mass spectrum is acquired at each pixel (one pulse of Bi_n^+ ions) and the primary

beam is rastered along the total area. This analysis mode is called *Static SIMS* (**Figure 6a**) and is considered as non-destructive, as long as the primary ion fluence does not exceed the static limit of 10^{12} ions/cm² since the probability of the same target atom being bombarded twice is extremely low. Indeed, considering the typical atomic concentration of 10^{15} atoms/cm², only 0.1% of the atomic sites should be impacted. In these conditions, the information comes from the first atomic layers.

Since each pixel is associated with a spectrum, we can map the information laterally, but as stated above, the lateral resolution is quite poor if the beam is bunched. Conversely, to achieve a lateral resolution of 100 nm, no bunching is allowed, so the length of the pulse has to be increased, thus sacrificing mass resolution. This so-called *imaging mode* (**Figure 6b**) also provides information that is limited to the topmost atomic layers. Using the "Burst Mode" however, a tradeoff between mass and lateral resolutions is possible: long non-bunched pulses can be chopped into several short pulses, which in the spectrum results in a multiplicity of peaks for each mass.[18] The mass resolution is somewhat preserved, but the spectra get difficult to handle in case mass interferences are present. The other way to fulfill the double requirement of mass and lateral resolutions is to delay the extraction after the primary ions impact.[19–21] In delayed extraction mode, the ejected matter forms a cloud above the surface that expands in the absence of an electric field. Then, when the extractor voltage is set, the ions that are further from the extractor experience a higher potential difference, thus undergoing the effect of the acceleration for a longer time, than ions with a higher velocity that almost reach the analyzer column. In these conditions, the time of flight depends less on the pulse length.

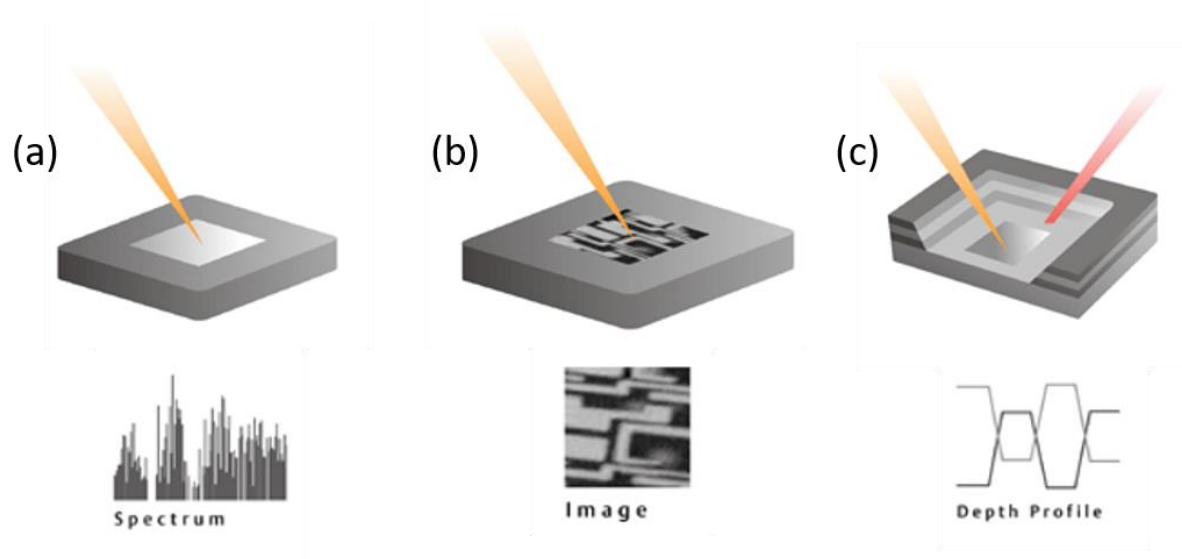

Figure 6 – Analyses modes with ToF-SIMS. (a) Surface spectrometry or static SIMS, (b) surface imaging, (c) depth profiling. [Source: https://www.iontof.com]

For in-depth analysis, an erosion gun is used alternately with the analysis gun. The matter ejected during the sputtering process is not analyzed; during this phase, the previously rastered surface is

removed and a "fresh" surface deeper into the sample is dug up for the next analysis cycle. This last *3D depth-profiling* mode (**Figure 6c**) will be the focus of our attention. Alternating two different guns for the analysis and erosion phases corresponds to the so-called dual beam experiment. This offers some major advantages with respect to a dynamic SIMS experiment:

- The pulsed beam allows the time of flight detection and thus the parallel detection of all fragments and allows the user to reconstruct results retrospectively.
- Despite very low currents involved for the pulsed analysis beam, high sputter yields are ensured by the erosion beam.
- Each beam can raster a different area, which means that one can select a smaller analysis area, avoiding the detection of fragments coming from the borders.
- It offers the possibility to focus the analysis beam while keeping the erosion beam defocused and thus limiting the induced roughness. In addition, high lateral (3D) resolution imaging is possible with highly focused analysis beams.

In dual beam analyses, two different approaches can be used: 1) the *interlaced mode* where both beams are used quasi-simultaneously and 2) the non-interlaced mode that we used for most of the studies of this work. In the *non-interlaced mode*, at least one analysis cycle is completed before the erosion gun is set on. The final spectrum will thus consist in the integration of n mass spectra (where n is equal to the squared number of pixels) built up at each pulse between two sputtering phases. For example, if we chose 128 pixels, 128x128 pulses of 100 µs will hit the raster surface, leading to an analysis cycle time of 1.64 s ($128x128x10^{-4}$). The analysis is followed by the sputtering cycle whose length can be set independently.

The non-interlaced mode is particularly recommended for the study of insulating samples because it allows a longer charge compensation interval since the flood gun is in use during the whole sputtering cycle. It is possible to select any integer number of analysis cycles, which increases the signal intensity. However, even if the analysis beam current is much lower than the erosion beam one, the energy involved is much greater (25 keV vs. 500 eV). We previously demonstrated that the bismuth rastering should be limited to one frame.[22] Similarly, one should favor Bi_3^+ instead of Bi^+, since it improves dramatically the depth profile quality. The influence of the analysis primary ions on depth resolution will be demonstrated hereafter. Moreover, limiting the Bi_n^+ impacts relative to the sputtering ions ones is the main interest of the non-interlaced mode.

2.2 X-RAY PHOTOELECTRON SPECTROSCOPY (XPS)

The aim of this section is not to provide an exhaustive description of the XPS technique, but rather to demonstrate its complementarity with TOF-SIMS and to draw up an inventory of the advantages and drawbacks of each technique.

Photoelectron spectroscopy is a technique that allows the chemical, elemental and quantitative characterization of a material surface. The sample is irradiated with X-Rays that transfer their energy to core electrons, so that characteristic photoelectrons are ejected from the material surface and their kinetic energy denoted E_k below, is measured by an analyzer. Knowing the energy of the initial photon (here, for the X-Ray from Al Kα E_{ph} = 1486.7 eV), the electron binding energy, E_b, is simply deduced by the relation:

$$E_b = E_{ph} - (E_k + \phi_{sp}), \quad (6)$$

where ϕ_{sp} stands for the work function of the spectrometer. The binding energy of an electron from a specific orbital is characteristic of the chemical element and is also affected by the local bonding environment of the atom.

The XPS survey spectrum consists of the number of electron counts detected as a function of the deduced binding energy. The number of electrons detected can be related to the surface atomic composition, through the known atomic sensitivity factors, making XPS a quantitative technique (with ~1% accuracy). However, no detection of hydrogen nor helium is possible, imaging is limited because of the difficulty in focalizing X-rays, and the XPS technique is about 1000 times less sensitive than ToF-SIMS (see detection limit values in Table 1).

The XPS signal is representative of the first 10 nm under the material surface (assumed homogeneous) and can be possibly coupled to an ion beam sputtering for depth profiling. In our lab, the two XPS spectrometers are equipped with an Ar sputtering gun. On the ESCALAB spectrometer, both monoatomic Ar^+ and Ar_n^+ clusters sources can be selected either to clean off the surface contamination or to obtain in-depth information. Like for ToF-SIMS, a flood gun provides the charge compensation of insulating surfaces.

ToF-SIMS	**XPS**
Semi-quantitative	Quantitative
Molecular characterization	Elemental and chemical characterization
Information depth: first atomic layers ~1 nm	Information depth: ~10 nm
lateral resolution: 100 nm	10 µm (3 µm in 2D imaging mode)
Detection limit: 1 ppm	Detection limit: 0.1 at.%

Detection of hydrogen	No detection of hydrogen
Destructive	Nearly non-destructive
Might be tricky for the occasional user	Rather quick to learn
Time-consuming data processing	Fast data treatment

Table 1 - Comparison of the characteristics of ToF-SIMS and XPS analyses.

2.3 DEPOSITION TECHNIQUES

In this work, organic and inorganic materials were deposited using different techniques that are depicted hereafter.

2.3.1 Resistive evaporation of organic thin films

Combinations of tyrosine and phenylalanine were deposited on silicon substrates using resistive evaporation. Both materials were extensively studied in the past by our group and were chosen in the present work to allow a direct comparison with former scientific papers from our lab.[23–25] It is particularly true in Section 4.1 where delta multilayers are studied. These two amino acids present very similar chemical structures (**Figure 7**) so that a molecular analytical technique is required to differentiate them. Thanks to their relatively low mass (181 uma for tyrosine and 165 uma for phenylalanine), entire molecules can be detected despite the fragmentation induced by low energy cesium. It is worth noticing that tyrosine and phenylalanine are reticulating polymers, which makes their depth profiling potentially very challenging, but highlight the free-radical scavenging properties of cesium instead.

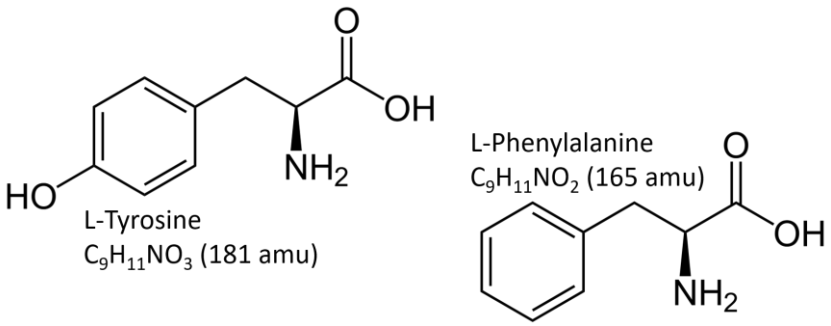

Figure 7 – Chemical structures of tyrosine and phenylalanine.

During resistive evaporation, the material to be deposited is heated in vacuum, which causes its sublimation before it condensates on the substrate about 15 cm above the crucible. The material can either take the form of a resistive wire or be contained in a tungsten crucible that offers a higher amount of material (and allows thicker coatings). In both cases, a large electric current induces heat

by Joule effect. In our case, a crucible was used, since the amino acids that were evaporated take the form of powders. The tool is a Cressington Evaporation Supply LT 1500 308R (Watford, UK).

As will be developed in the next section, the roughness of the film can strongly affect the general course of the depth profiles. In order to maximize the confidence about the flatness of the coating, and ensure its purity and uniformity, operating pressures were as low as 10^{-7} mbar, despite it is already possible to work at a pressure of 10^{-5} mbar. Also, the powders were meticulously compacted inside the crucible, with particular attention for the levelness of the top surface.

For the evaporation of phenylalanine and tyrosine, ideal temperatures of 220-250°C and 330-360°C, respectively, were controlled using a thermocouple on the crucible. Those temperatures are chosen to avoid hopping of the powder, while maintaining convenient deposition rates, in this case between 0.5 and 1 nm/s. Indeed, higher deposition rates reduce the risk of impurities inclusion and therefore ensures a higher quality of the coating. The temperature threshold can vary as a function of the quantity of powder, but also whether the powder is fresh or has already been heated during previous evaporation.

The layer thickness was measured in the chamber by a quartz microbalance, that was calibrated beforehand by measuring the thickness of each material on silicon by ellipsometry (EP-5 ellipsometer from Semilab-Sopra, analyses performed by Dr. Sébastien Mouchet) and by surface profilometry (Dektak). Also, the roughness was measured by AFM, giving values in the range of 1 nanometer (**Figure 8**). The films' thickness of ~100 nm was chosen to minimize the error on the thickness measurement introduced by the quartz microbalance while ensuring a reasonably low depth profile analysis time.

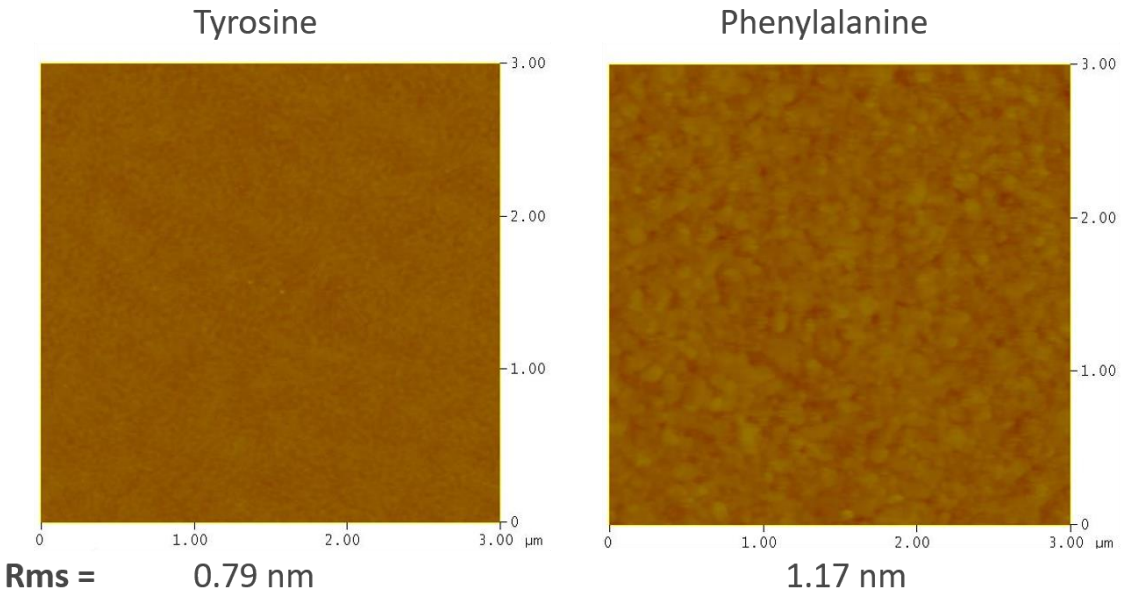

Figure 8 – AFM measurements of the roughness on Tyrosine and Phenylalanine coatings of ~100 nm deposited on silicon.

2.3.2 Physical Vapor Deposition (PVD) of metal layers

In order to prepare hybrid model samples, analyzed in Section 4.2, gold and chromium layers were grown by physical vapor deposition (PVD) and more specifically by magnetron sputtering (schematically explained in **Figure 9**) and were associated with tyrosine in model organic-inorganic multilayers. Chromium was chosen because of its reactivity. We thought it could be interesting to study the interaction between organic layers and these highly reactive atoms. Conversely, gold is an inert metal, that was associated with an organic compound and depth profiled in a reference work from Winograd's group[26], and on which we build our feasibility study.

We first tried to deposit gold by thermal evaporation, but PVD, although being a slower process, resulted in higher homogeneity, since the formation of islands could be avoided. The thickness plays a major role in the homogeneity of the layer since films shallower than 10 nm exhibit uneven coverage of the surface.[27,28] On the other hand, in order to guarantee reasonable analysis times, the metallic layer should not be too thick.

During magnetron sputtering, an inert gas (in our case Ar) is injected in the chamber, with pressures ranging between 5.10^{-3} and 5.10^{-1}mbar. Through the application of a magnetic field, electrons are trapped near the target cathode, where they collide with argon atoms and trigger a cold plasma by ionizing these atoms. The fact that electrons are magnetically confined increases the ionization efficiency, allowing reducing the amount of incorporated gas. In turn, these energetic Ar^+ ions collide with the negatively charged target and cause the ejection of the material to be deposited. The substrate is located about 50 mm under the target.

The tool is a Quorum Q150 T E/S from Quorum Technologies (Laughton, UK) from which sputter targets were also purchased. DC voltage is typically comprised between 100 and 300 V, and currents of 20 and 120 mA were used for Au and Cr, respectively. Once again, the layer thickness was controlled with a Quartz microbalance and calibrated with a profilometer.

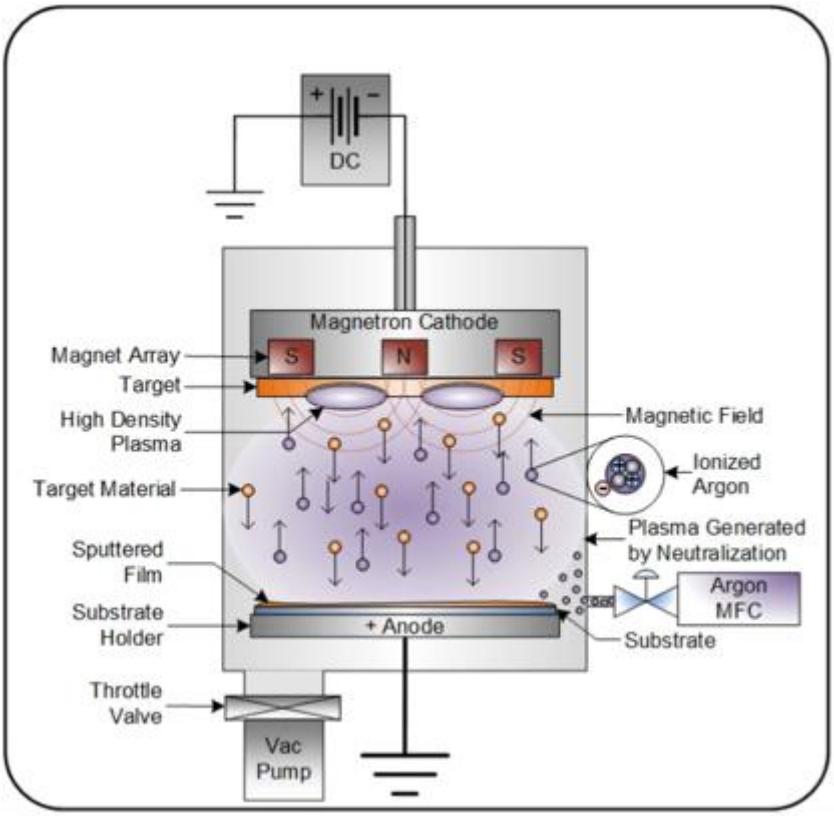

Figure 9 – Schematic representation of magnetron sputtering deposition.[29]

2.4 PRINCIPAL COMPONENT ANALYSIS

The present section is not intended to provide an exhaustive theory about Principal Component Analysis (PCA), but rather to assist the reader in understanding the data treatment performed in **Section 4.3**.

PCA denotes a multivariate analysis that aims at compressing data by mathematically removing redundant dimensions, i.e. by limiting the number of variables. The initial huge amount of correlated variables are transformed through an orthogonal linear transformation into a smaller subset of uncorrelated variables, in a new coordinate system (see **Figure 10**). This allows rapidly highlighting the main differences between a large number of observations, i.e. peaks intensities in the case of ToF-SIMS spectra.

Data are first arranged into a matrix, as follows: rows are samples (here, SIMS spectra) and columns are variables (here peak intensities). Let us call this matrix X and build its covariance matrix, cov(X);

$$cov(X) = \frac{X^T X}{m-1} \tag{7}$$

After application of the eigenvalue equation,

$$cov(X)\, p_i = \lambda_i\, p_i, \tag{8}$$

the eigenvalues of cov(X), λ_i, are determined and sorted by increasing values. The eigenvectors, p_i, are called the loadings and are simply the coefficients of the linear combination connecting the initial variables.

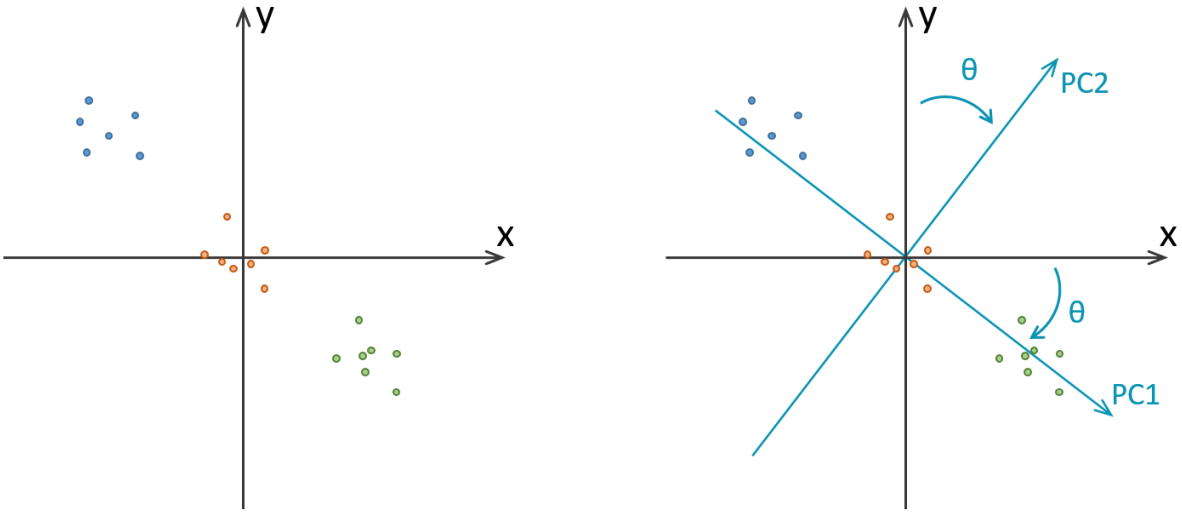

Figure 10 – choice of a new coordinate system, based on the orientation of the largest amount of variance in the dataset.

Let us consider p_1, the eigenvector associated with the highest eigenvalue. Then, X can be decomposed as followed:

$$X = t_1 p_1^T + E \tag{9}$$

$t_1 p_1^T$ is the first principal component (PC1) and accounts for the highest possible variance in the data while the residuals, E, contains the amount of variance that is not captured by the latter. The vector t_1 contains the scores of PC1. Scores can be graphically seen as the projection on the new axis and describe the similarities or differences between samples, while the loadings describe which peaks account for the differences between samples.

This procedure is repeated on the residuals matrix n times, progressively removing the variance of the previous principal components and explaining the maximum proportion of the remaining variance. The number of iterations, n, stands for the number of principal components one needs to consider, with regards to the desired expressed variance.

$$X = t_1 p_1^T + \cdots + t_n p_n^T + E \tag{10}$$

As previously mentioned, the principal components are linear combinations of the original variables weighted by their contribution to explaining the variance in a particular orthogonal dimension. The procedure removes covariance between different dimensions (off-diagonal elements of the covariance

matrix, mathematically forced to be uncorrelated) and strengthens the variances, that are the diagonal elements. Thereby, PCA transformation accounts to diagonalize the covariance matrix.

Preprocessing the data is essential to ensure that the variance in the dataset is not related to external factors, such as the instrument. Data is thus normalized (for example by the total intensity or a selected peak) and mean-centered (by subtracting the mean of each column to the column). In our case, the preprocessing treatment includes a wavelet transformation that allows noise removal thus data compression, as will be explained in Chapter 4.

3 DEPTH PROFILING: STATE OF THE ART

3.1 FUNDAMENTAL ASPECTS OF DEPTH PROFILING

Depth profiling, i.e. the alternation of surface analysis and ion beam sputtering, can provide for the 3D characterization of multilayers, which allows probing interface phenomena, layers composition and eventually the migration of atomic and molecular species. We already stressed the interest for applying depth profile analysis to optoelectronic devices to highlight structure-to-properties correlation or to investigate aging/failure mechanisms and rationally propose solutions to increase the materials stability. In parallel, there is also an increasing demand for developing analytical tools to determine the depth distribution of molecular species in or interacting with biological systems.

In our approach, the first and key step is to prepare reliable model samples, that present a high reproducibility in terms of flatness and homogeneity (see paragraph C in "Materials and Methods"). Achieving such a high control on state-of-the-art photonic devices is not always possible, because most of the samples were made in collaboration with external research institutes, involving long travel distance and time before the analysis was performed. Moreover, ideally sharp interfaces are not always associated with more efficient devices!

The second step is to perform a rigorous and systematic comparison of different depth profile conditions on the same sample (ABA), or of the same settings on different sample architectures (ABA, BAB, etc.), for example organic thin layers deposited on metals and metals on organics, in order to find the best conditions, as "gentle" as possible, while ensuring reasonable sputtering yield.

The fragmentation rate, the variation of sputtering yields, the roughness before and after the analysis or the depth resolution are the main indicators that need to be taken into consideration to directly compare different setup conditions.

For clarity, let us first define three key parameters for depth profiling: the *depth resolution* (and how it is calculated), the *useful yield* and the *sputtering yield*.

The **depth resolution** can be as the broadening of the measured profile with respect to the depth distribution. Practically, it can be defined as the interval between 16% and 84% of the maximum intensity of the rising signal when crossing a planar interface[30]. Delta layers analysis can give a more complete insight into the intrinsic depth resolution. The obtained profile of delta layers is a convolution of the ideal profile (a box function as narrow as possible) with a response function. This response function itself, according to the Mixing-Roughness-Information depth model (or MRI),[31] is a convolution between a growing exponential, accounting for the information depth, a Gaussian,

characteristic of the interface roughness (natural or induced) and a decreasing exponential, taking into account the atomic mixing length. The contribution of the atomic mixing might be substantial for inorganic shallow layers but is assumed negligible in organic materials, given the large size of molecules. The information depth using ToF-SIMS is known to be less than one nanometer[32]. The depth resolution is then mainly governed by the roughness at the interface (which can sometimes be reduced by rotating the sample during the profile[33]).

The **useful yield**, not to be confused with the sputtering yield, is the number of detected ions (parameter I_M in equation (1)) normalized on the number of atoms that are ejected from the sample surface.

The **sputtering yield**, Y, is defined as the number of atoms ejected per primary ion and is therefore expressed in [atoms/ion]. It can be calculated following this expression:

$$Y = (d.A.\rho.N_A .n/M) / (I.t/e) \quad (11)$$

The numerator represents the number of atoms emitted: *d* is the film thickness, *A* is the sputtering beam raster and $\rho.N_A.n/M$ is the number of atoms per unit volume (volumetric mass density of the target ρ, Avogadro number N_A, number of atoms per molecule *n*, divided by the molar mass of the target *M*). The denominator stands for the number of incident ions (erosion beam current *I*, duration of sputtering *t* divided by the electronic charge *e*). The sputtering yield is influenced by the penetration depth into the surface. When the implantation depth, which can be schematically seen as the damaged layer, is reduced, the energy is deposited closer to the surface and the probability of fragments ejection is higher. The parameters that impact the penetration depth are related to the properties of the primary ions (nature, energy, incidence angle) and the properties of the sample itself (density of the surface, binding energy, crystallinity, temperature).

A sufficiently high sputtering yield constitutes a key-parameter for achieving successful depth profiling for three main reasons: (i) it helps to avoid damage accumulation, as the sputtering beam is supposed to remove the volume affected by beam-induced modifications during the previous cycle, generated by both analysis and erosion guns (**Figure 11**). Generally, the sputtered depth (measured easily, or calculated if the sputtering yield is known) must imperatively be more than half of the damaged depth (possibly accessible through simulations). It ensures that a fixed depth is not altered by two consecutive analysis cycles.

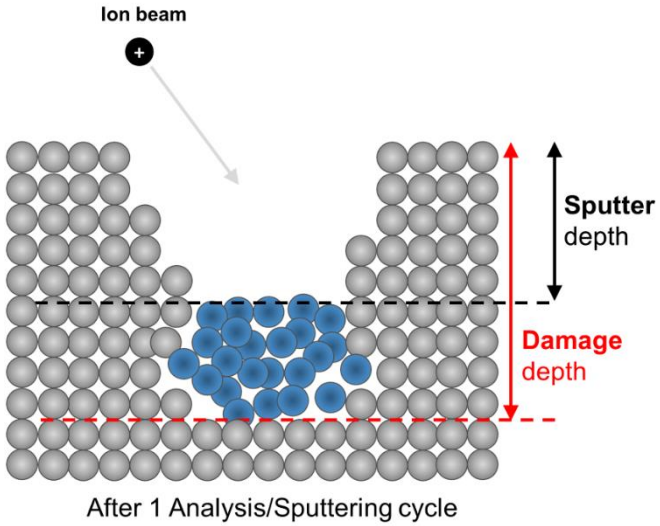

Figure 11 – Comparison of sputtered and damaged depth. To ensure that damages do not accumulate, the erosion beam must remove at least half of the damaged depth.

For the study of inorganic layers, a parameter R was introduced to determine whether the analysis beam-induced damage has to be taken into account. The parameter R is defined as the proportion of atoms that are ejected by the sputtering beam compared to the ones ejected by the analysis beam.[34] It is expressed by the ratio between the sputter rates of the erosion and analysis beams R_{sp} and R_{an}, respectively, that are in turn proportional to I.Y / A, where I stands for the current, Y for the sputtering yield and A for the raster area:

$$R = \frac{\mathrm{I}_{sp} \,.\, \mathrm{Y}_{sp} \,/\mathrm{A}_{sp}}{\mathrm{I}_{an} \,.\, \mathrm{Y}_{an} \,/\mathrm{A}_{an}} \qquad (12)$$

In inorganics, in order to neglect the mixing effect from the analysis beam, R should be at least 100,[34] meaning that only 1% of the ejected atoms are sputtered by the analysis beam. Practically, a ratio in the range of few hundreds guarantees a good profile quality, even if this value may strongly depend on the primary ions and sample characteristics[35]. This implies to find a tradeoff between the count rate and the depth resolution. Similar reasoning has been conducted for organic samples. This will be exposed in the next section. (ii) Besides, a variation of the sputtering yield inside a layer can denote ion beam degradation, typically by cross-linking, carbonization (for organic layers) or by preferential sputtering. (iii) Finally, when profiling hybrid multilayers, the difference between the sputtering yields of organic and inorganic thin layers can induce a certain number of artifacts that will be discussed in **Section 3.3.**

Depth profiling being a destructive and highly perturbing analysis, in order to reveal and differentiate intrinsic thin layers properties from the modifications induced by the analysis (involving the ion beams bombardment), the effects from the profiling process must be investigated and minimized in order to

leave the sample as "undisturbed" as possible. While interactions of the ion beam with the surface cannot be avoided, they can be limited by choosing the energy and nature of the primary ions. This involves an accurate and rational choice of the analysis parameters and conditions, which should be adapted to the sample.

3.2 DEPTH PROFILING OF ORGANIC MATERIALS: INFLUENCE OF THE PRIMARY IONS

Since the ’70s, atomic ion beams have been used for the in-depth characterization of inorganic materials by SIMS. So far, high-energy monoatomic ion species such as Ga^+, Ar^+ or Xe^+ have demonstrated to provide a rapid (convenient sputter yields) and accurate (depth resolution around 1 or 2 nanometers) analysis of embedded inorganic layers.[36] This property is of particular interest for the analysis of electronic devices. However, when considering organic samples, the molecular information is rapidly lost (drop of molecular signals) because the amount of energy carried by primary ions induces the break of covalent bonds, finally altering the chemical structure. This limitation led the scientific community to conclude that ToF-SIMS was not a suitable technique for organic depth profiling. Conventional monatomic sources, such as Ga^+ (70 amu) and Ar^+ (40 amu) are low-mass projectiles, which penetrate deeply into materials and result in a weak ejection probability; consequently, many impacts are needed to sputter a fixed amount of matter. Increasing the primary ion mass allows increasing its stopping power under the material's surface. In other words, this leads to a lower deposition depth of the projectile energy and thereby to higher ejection probability and ion yield. This was the initial motivation when starting to work with gold and bismuth (197 and 209 amu, respectively), and subsequently with small clusters Au_n^+ [37] and Bi_n^+, with n = 3, 5 or 7 atoms, in which the energy is evenly distributed between the constituting atoms. It is worth noticing that the size of Au_3^+ corresponds approximately to the interatomic spacing in the bulk material.

This strategy led to a sensible increase of the secondary ion yield, however for many organic compounds, this was still not sufficient for ejecting high-mass fragments. Detecting entire molecules involves overwhelming many issues related to the difficulty to desorb high-mass molecules, to ionize them or to prevent their fragmentation or other chemical reactions such as cross-linking.

The quest for analyzing biological samples using ToF-SIMS triggered intense research directed to the enhancement of the molecular sensitivity. To that end, the winning strategy was to further enlarge the size of polyatomic primary ions.[2]

[2] This comment concerns the erosion source. Bi_n^+ ions, like Ga^+ are produced using a liquid metal ion gun technology and therefore provide highly focused beams. This justifies their use as analysis primary ions in dual beam experiments, even though they create more damage.

It is only in 1998 that Gillen et al. successfully performed depth profiles for the first time, using the polyatomic ions SF_5^+on various organic materials.[38] This paved the way for what would later be a prolific research field of organic depth profiling with ToF-SIMS, and in particular about the 3D imaging in biological and pharmaceutical research.[18,39–41] Since this first breakthrough, a large variety of cluster sources have been released. In 2003, C_{60}^+ (720 amu) demonstrated its ability to extract information from organic compounds[42] and polymer systems beyond the static limit[43] with secondary ion yields much larger than when using SF_5^+ and Au_3^+.[44,45] Despite the fact that great performances were established on a wide range of samples, including cellulose, biopolymers (that couldn't have been depth profiled hitherto using $SF5^+$)[46] and even metals like gold[47] and Ni-Cr multilayers,[48] some issues remained. In particular, C_{60}^+ was not suitable for cross-linking polymers, such as polystyrene[49] and a high roughness could develop on silicon due to carbon deposition occurring faster than what the sputter rate allows to remove, for energies under 12 keV.[48]

The advantage of cluster sources lays in the fact that, unlike atomic primary ions whose sputtering mechanism can be simplistically explained by a binary collisional model (analogously to billiard balls undergoing elastic collisions), clusters bombardment involves non-linear collective processes, similar to a meteor hitting the ground (**Figure 12**), as stressed by numerous molecular dynamics (MD) simulations.[50–56] MD simulations help to predict experimental data and in turn, experiments bring precious information to refine theoretical model regarding complex ionization and ejection processes. In these models, it was shown that the kinetic energy is equally distributed between the atoms constituting the cluster. As soon as the cluster reaches the surface, its loosely-bound atoms disaggregate and release a high amount of energy to atoms from the first nanometers, ensuring a reduced penetration depth (and interlayer mixing), together with high sputter yields, which is helpful in limiting the ion beam induced damage accumulation through the profile. For example, on a silver substrate[57] and on PMMA,[49] it was shown that bombarding with C_{60}^+ instead of Ga^+ allowed increasing the yields. From Figure 12, one can see that a single C_{60}^+ impact apparently causes more damage than Ga^+. However, during a C_{60}^+ profile, the total surface damage is lower compared to monoatomic ions: since the Ga^+ primary ions exhibit a much lower sputtering yield because of their sensibly higher implantation depth, the high fluence that is thus required with Ga sputtering leads to strong damage accumulation.

In 2002, an argon gas cluster ion beam (Ar_n^+ GCIB) was applied for the first time as primary ion source for ToF-SIMS depth profiling of a Ta film deposited on Si.[50] These large clusters (up to few thousands of atoms, singly ionized) are formed through the adiabatic expansion of high-pressure argon gas into vacuum. Increasing Ar cluster size limits the fragmentation and damage accumulation compared to C_{60}^+, leading to the ejection of heavier molecular fragments. This is a fundamental asset for the analysis of organic samples, as demonstrated by Ninomiya et al., who successfully depth-profiled polymers

(namely, PMMA, PS, and PC) using Ar_{700}^+ at 5.5 keV[58]. Molecular information can be potentially retained over depths up to 15 µm, thanks to the high "cleanup" efficiency demonstrated by clusters[59]. However, the useful yield obtained with Ar_n^+ clusters might not be higher than with C_{60}^+ since, at a given energy, the ionization efficiency was found to decay linearly with the argon cluster size (n).[60]

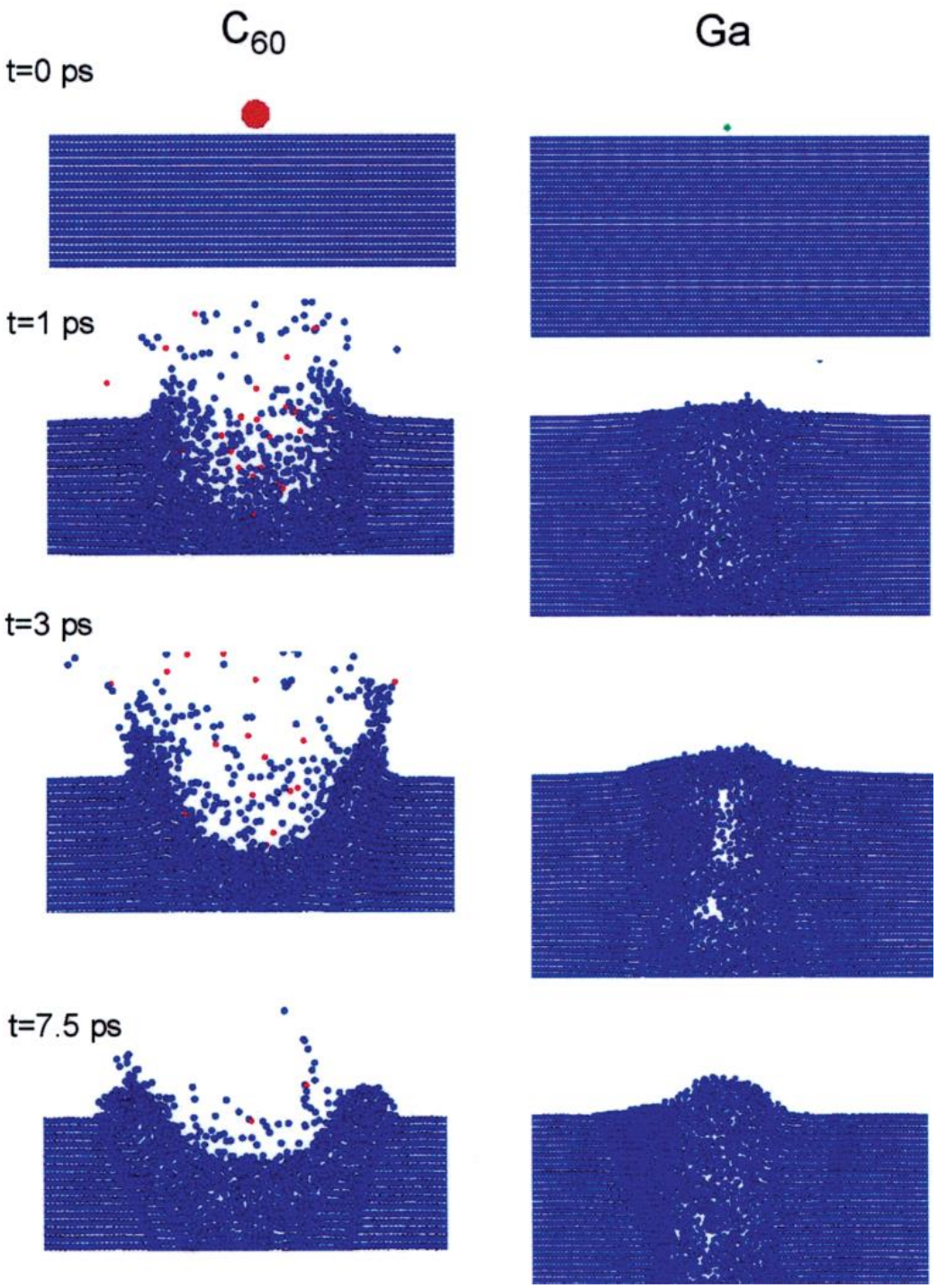

Figure 12 – Direct comparison of the sputtering processes involved under 15 keV C_{60}^+ and Ga^+ bombardment of a silver substrate (cross-sectional view). Taken from reference [57].

Practically, the possibility to vary independently the cluster size and its energy increases the versatility of this beam but also its complexity. Whether it is the total kinetic energy, E, the number of Ar atoms, n or the energy per atom, E/n, all these three parameters affect the fragmentation, the sputter rate, and the damage accumulation.[61,62] Some research papers advocate that low energy and large cluster size should reduce the mixing length, and therefore are supposed to improve the depth resolution.[63] Other works recommend increasing the sputter yield by increasing the energy and/or decreasing the size, in order to limit the induced roughness and the resolution degradation due to the damage accumulation.[64–66] To Cheng et al., successful depth profiles are obtained using a large cluster size, together with high energies.[67] This should provide large sputtering yields and small damaged layer thickness, which is supported by an erosion model relying on three distinct fluxes: (i) F_{supply}, the intact molecules progressively supplied by the bulk from depths greater than the altered layer thickness, as the sample is etched; (ii) $F_{sputter}$, the decrease of the number of those intact molecules after their ejection during the sputtering and (iii) F_{damage}, the loss of intact molecules due to their beam-induced degradation. The variation of the concentration of intact molecules contained in the altered layer, C_s, as a function of the primary ion fluence, f, is expressed as an equilibrium between the three fluxes[67,68]:

$$\frac{\mathrm{d}C_S}{\mathrm{df}} = F_{supply} - F_{sputter} - F_{damage} = \frac{YC_B}{d} - \frac{YC_S}{d} - \sigma_D C_S \quad (13)$$

In this equation, Y is the sputtering yield, C_B stands for the concentration of molecules in the bulk, d is the thickness of the altered layer and σ_D is defined as the damage cross-section.

This equilibrium, the "result of the competition between the creation of primary beam damage and its removal by sputtering", as described by Gillen[69], has been validated experimentally on Irganox delta layers[70], on tetraglyme films[35], or on trehalose using C_{60}^+.[67,71]

Besides the increase of the sputtering yield by increasing the size/mass of the projectile, it can be seen from the equation (1) that the secondary ion intensity of a species M, I_M, can also be enhanced by promoting the ionization probability, α.

An alternative approach to enhance sensitivity is to increase the ionization, instead of increasing the yield. It appears that using low-energy (less than 1000 eV) Cs^+ or O^+ as erosion source fulfills this task.[72,73] Cesium is an alkali metal and sits in the first column of the periodic table. It is the most electropositive non-radioactive chemical element. Unlike Ar^+ or Xe^+, the reactivity of cesium definitely constitutes its main asset. Indeed, low energy cesium ions implanted during the sputtering cycle are rapidly neutralized in the materials, where they can react with free radicals generated by the ionic bombardment. Negatively charged fragments M^- are formed and are then ejected, during the following analysis cycle, as summarized by the reaction equation

$$M + Cs \rightarrow M^- + Cs^+ \quad (14)$$

where M is a molecule or a radical. This equation accounts for the increase of negative ionization probability but explains, in addition, the major role played by Cs as a free radical scavenger.[74] This explains why ionic bombardment with Xe^+, although these ions have a mass similar to cesium, induce chemical bonds breaking, generation of free radicals leading to cross-linking and eventually graphitization on polystyrene (PS), polycarbonate (PC)[74] or phenylalanine.[75] In the event of damage accumulation, both molecular signal intensities and sputter rates are affected. In contrast, constant molecular in-depth intensities and sputter yields were observed with Cs^+, proving its free-radical quenching properties.[75–77]

The major drawback of Cs^+ ions is the relatively high fragmentation rate, either under the effect of ionic bombardment at higher energies (when the energy is increased to more than 500 eV, the molecular signals of PC decrease drastically[74]); or following reaction of oxygen-containing molecules with reactive cesium ions. For this latter reason, Xe^+ demonstrated better results on trehalose, than Cs^+ at the same energy. Depth profiling with Cs^+ is generally performed only in the negative polarity, but MCs_n^+ clusters may also be collected in the positive polarity.[16,77]

Still with the aim of enhancing ionization efficiency, another strategy consists in the injection of a reactive gas in the analysis chamber. For example, ambient oxygen shows an increase of the positive ionization probability as a function of the oxygen partial pressure.[78] Similar results were obtained with nitric oxide gas dosing[79], water vapor injection[80] or deposition of neutral Cs at the surface.[81,82]

Considering the recent developments on etching sources, ToF-SIMS offers an in-depth molecular characterization with a sensitivity and a lateral resolution that is currently unachievable from any other technique[68]. However, it is worth mentioning that other techniques can be efficiently applied for depth-profiling experiments including XPS and radiofrequency pulsed glow discharge - time of flight mass spectrometry (rf-PGD-ToFMS). The latter allowed detecting organic fragments and discriminating various polymers (PMMA, PS, PAMS, and PET)[83]. Derived from GD-OES (that only provides elemental information about organic and polymeric materials), rf-PGD-ToFMS uses a pulsed discharge, which decreases the power transmitted to the surface and preserves small organic fragments. Like ToF-SIMS, a depth resolution in the nanometer range and a limit of detection in the ppm can be achieved. More recently, rf-PGD-ToFMS also offered an interesting study of the elemental distribution inside perovskite layers, contributing to identifying diffusion phenomena.[84]

3.3 DEPTH PROFILING OF HYBRID ORGANIC-INORGANIC SYSTEMS, THE CURRENT CHALLENGE

When profiling inorganic layers, polyatomic ions typically show sputtering yields that are two or three orders of magnitude lower than what it is commonly observed on organic layers.[85]

This sputtering yield difference may lead to considerable artifacts during the depth profiling of hybrid samples. This is commonly observed in optoelectronic devices, in which organic multilayers are usually covered with metallic electrodes. Namely, residual metallic atoms are implanted in the soft organic underlayer, their sputter rate drops, increased fragmentation of organic molecules is observed and the in-depth resolution is progressively degraded.[26,86]

Different strategies have been tested in order to achieve the in-depth characterization of hybrid samples using SIMS.

Cumpson and Portoles measured the sputter rate of variable-size Ar clusters on a wide range of materials. The sputtering yield gap existing between organic and inorganic materials (called the "selectivity") is concluded as an asset to probe buried hybrid interfaces[87]: the drop of the sputter yield at the organic/inorganic interface ensures not digging into the underlying inorganic material and avoiding atomic mixing. Once the organic layer is removed by Ar clusters, one can switch to XPS analysis with angular resolution to explore the harder underlayer. The recommended energy per atom is comprised between 3 and 9 eV/atom since it combines reasonable etching rate in the organic layer while avoiding the removal of inorganic materials. However, no solution is given in case the inorganic layer is deposited on the top of the organic layer.

At LIST, Philipp *et al.* examined hybrid model multilayers, composed of organic compounds capped with a silver overlayer. These samples present a clear interest for optoelectronic devices. If only atomic information is required, dynamic Secondary Ion Mass Spectrometry can be used.[88] Unlike ToF-SIMS, dynamic SIMS uses a continuous, focused primary ion beam, which enhances the sensitivity (parts per million to parts per billion) and makes it ideal for the elemental detection of trace impurities, but impedes the acquisition of molecular information. The primary ions are 250 eV to 1 keV Cs^+. In the same paper, the authors also suggest that peeling off the silver layer before the analysis of the organic layer allows discriminating between the beam-induced diffusion and the diffusion occurring during the deposition process.

A similar approach is investigated at CEA, in Grenoble, where Langer *et al.* studied hybrid profiling with both Cs^+ and Ar cluster ions. They have shown that switching from 2 keV Cs^+ to 5 keV Ar_{5000}^+ clusters during the depth profiling at the interface between inorganic and organic layers is not the optimal solution (unpublished). Indeed, at such energy, cesium ions alter the integrity of the organic underlayer during the depth profiling of the inorganic top layer. They proposed a method based on three steps: (i) the inorganic layer is sputtered using Cs^+; then, (ii) elsewhere on the sample, the inorganic layer is

mechanically removed, exposing the organic material and finally, (iii) a molecular analysis is performed under the removed electrode by using argon clusters.

Another methodology consists of the preliminary bombardment of the surface with high energy, finely focused Ga^+ beam, milling the sample for the fabrication of a cross-section. This processing technique, called Focused Ion Beam (FIB-milling), induces important damage at the surface that needs to be removed by subsequent Ar clusters sputtering. The surface of the cross-section is then ready for static SIMS imaging, providing relevant 3D chemical information[89]. This was applied by Iida et al.[90] on a polycarbonate matrix loaded with glass fibers, after an unsuccessful attempt of depth profiling with Ar_{2500}^+ at 20 keV.

Recently, a 20 keV C_{60}^+ beam was applied successfully on full perovskite solar devices, showing its ability to sputter both organic materials and silver electrodes[91]. They highlighted three mechanisms supposedly responsible for the poor efficiency and stability of the cell: a small degradation of the silver electrode into the HTM, as well as a strong migration of Li^+ ions across the perovskite and ETM, and an inter-diffusion between perovskite and TiO_2. However, it was previously mentioned that C_{60}^+ is not a suitable source for the study of cross-linking polymers and suffers from strong artifacts on silicon. It is claimed that C_{60}^+ profiling is incompatible with a good depth resolution on semiconductors[48] since the high energies required to depth profile them increases the implantation depth.

Most of these strategies to profile hybrid stacks are rather tedious since they involve the combination of several beams, or even several techniques, or delicate sample preparation. Some of these methods require samples with planar interfaces. In the following chapter, we will demonstrate that using low energy Cs^+ ions or small argon clusters with high energy (so, with relatively high energy-per-atom) as erosion source aims at simplifying the depth profiling of hybrid samples, by giving the opportunity to perform the analysis with only one set of parameters. Molecular information can be obtained within reasonable analysis times, with no need to pre-process the sample. The sputter rates are rather similar on organics and inorganics (only a factor of 5.5 between the sputter rates of gold and tyrosine for Cs), which limits the topography development during the analysis. However, it is worth noticing that the relatively high fragmentation rate during Cs sputtering somewhat reduces the useable mass range, and this might hinder the discrimination between very similar organic molecules, as will be seen in the study of OLEDs structures presented hereafter. We will assess the potential of low-energy cesium for the depth profiling of hybrid structures in **Sections 4.2** to **4.4** and of Ar_{500}^+ in **Section 4.4.**

4 RESULTS

4.1 ORGANIC MULTILAYERS DEPTH PROFILING USING LOW ENERGY CESIUM: THE INFLUENCE OF THE ANALYSIS BEAM

Previous studies from our group on phenylalanine/tyrosine multilayers provided only poor depth resolutions using Ga^+ as analysis primary ions and 500 eV Cs^+ as erosion source. In 2012, the gallium source installed on the ToF-SIMS instrument was replaced with a bismuth gun. As mentioned before, the use of Bi instead of Ga, and even more of small clusters Bi_n^+ (n=3, 5, 7), enhances the sputtering yield, since Bi ions are three times heavier than Ga ions. This restrains the damaged depth and extends the useable mass range.

Before starting the analysis of more complex samples, one has to validate that high depth resolutions can be obtained on organic materials using Cs^+ sputtering ions. To that end, similar amino acids multilayers were depth profiled using low energy cesium and bismuth primary ions, with two different fluences of bismuth, and compared to results previously obtained with gallium. We compared two sets of parameters as a function of the fluence/cycle (expressed in ions/cm²), instead of the parameter R discussed in the previous chapter. Actually, the methodology is similar (since the fluence is contained in the expression of Y), but better suited for the analysis of organic layers, in accordance with Brison et al.[35] Indeed, on organics, determining experimentally the sputtering yield of the analysis beam is very challenging because the surface is rapidly damaged and the yields drop under the effect of graphitization and cross-linking.

While, the initial aim of this work is to investigate the depth resolution reachable using Cs, I am fully aware that a more systematic study would greatly strengthen the message about the influence of the analysis beam fluence, nature (Bi_5^+ and Bi_7^+) and energy, which is argued as a key parameter to explain the dramatic effect of the analysis beam.

The paper below shows that:

- Low energy Cs has the capability to achieve high depth resolutions on organic delta layers;
- The analysis beam parameters have to be selected carefully since they affect significantly the depth profile quality;
- In the conditions tested, halving the analysis fluence improved the depth resolution by ~1nm.

ToF-SIMS depth profiling of organic delta layers with low-energy cesium ions: depth resolution assessment

Céline Noël, Yan Busby, Nicolas Mine, Laurent Houssiau*

Laboratoire Interdisciplinaire de Spectroscopie Electronique (LISE), Namur Institute of Structured Matter (NISM), University of Namur, rue de Bruxelles 61, 5000 Namur, Belgium

*Corresponding author: laurent.houssiau@unamur.be

Keywords: ToF-SIMS, depth profiling, depth resolution, low-energy cesium

Abstract

The advent of cluster ion beams has paved the way to the routine 3D analysis of organic heterojunctions. Alternatively, organic thin layers have also been successfully depth profiled with a low-energy cesium ion beam (Cs^+), to exploit the high chemical reactivity of cesium atoms, acting as free-radical scavengers. Despite of this, little is known about the depth resolution associated with low-energy Cs^+ sputtering on organic multilayers. In this work, amino acids multilayers, consisting of phenylalanine delta layers alternated with tyrosine spacers were used as model systems to assess the depth resolution associated with 500 eV Cs^+ depth profiles. High yields were obtained for quasi-molecular ions from both amino acids and no significant chemical alteration was noticed under the monoatomic bombardment. A depth resolution as low as 4 nm is demonstrated without sensible degradation on a rather long profile depth (300 nm). Limited depth-resolution (> 10 nm) along with high molecular degradation was previously reported on similar systems by combining low-energy Cs^+ with Ga^+ analysis beam. The use of the Bi_3^+ analysis beam results in a dramatic improvement of both the characteristic molecular signals intensities and the depth resolution. Even though the analysis beam fluence is very low compared to the sputtering beam fluence, data suggest that further reducing the analysis Bi_3^+fluence could improve the depth resolution by ~1 nm.

1. Introduction

ToF-SIMS molecular depth-profiling of organic materials has become a major topic in surface science. This success is due to the possibility of achieving 3D molecular imaging on complex organic stacks. Remarkable progress was made possible by the advent of polyatomic sputtering ion beams, that were first applied for molecular depth-profiling of organic materials back in 1998 by Gillen and Roberson,[1] using SF_5^+ primary ions. Later, depth-profiles obtained with large argon gas clusters ions beams (Ar_n^+ GCIBs) sputtering, with clusters composed of few thousand Ar atoms and a few keV energy demonstrated the high potential in ensuring stable and intense signals from large molecular ions. The advantage of large cluster primary ions relies on their high sputtering yields, short implantation depth and low energy-per-atom values (few eV). These features allow limiting the ion beam induced in-depth modifications since high erosion rates ensure that the induced damages are completely removed during the next sputtering cycle so that modifications do not accumulate during the profile, allowing for molecular information to be preserved.[2]

An alternative approach to improve the molecular useful yield, i.e. the number of molecular ions which are detected divided by the number of molecules that are removed from the surface, is to improve the ionization yield. This can be done by sputtering with Cs^+ primary ions. Low-energy (below 1 keV) Cs^+ beam has already demonstrated its efficiency for depth profiling cross-linking polymer layers and organic biomolecules.[3–5] The assumed ionization mechanism to generate molecular ions at the sample surface involves the chemical interaction of cesium with the organic molecules, improving the secondary ion useful yield.[6] More details about the advantageous radical scavenging effect allowing to avoid organic molecules crosslinking were already provided elsewhere.[7, 8] This mechanism can be schematized as a charge exchange from implanted cesium atoms to the organic molecule, following the generic reaction:

$$M + Cs \rightarrow M^- + Cs^+$$

where M is a molecule or a radical. In a dual beam profile, the analysis primary ions hit the cesiated surface and lead to preferential ejection of negative molecular fragments (M^-) formed during the previous sputtering cycle.

More recently, low-energy Cs^+ source was successfully applied to profile optoelectronic devices made of hybrid (organic-inorganic) multilayers;[9–13] for these samples, compared to conventional Ar GCIBs sources, Cs^+ has a relevant advantage of providing similar sputter rates on soft (organic) and hard (inorganic) materials.[14] However, Cs^+ sputtering is of little interest if it

does not ensure a high depth profile quality, i.e. high molecular signals intensities and high in-depth resolution. The aim of the present work is thus to assess the depth resolution using low-energy Cs^+, keeping in mind that the best resolution achieved with Ar_n^+ GCIBs is ~4-5 nm.[15]
In order to assess the depth resolution, we profiled model organic heterojunctions made of cross-linking amino-acids delta layers of phenylalanine (Phe) sandwiched between tyrosine (Tyr) spacers. The device was fully processed by thermal evaporation under UHV.[5, 16] This sample structure was chosen based on previous results showing that alternative sputtering primary ion beams, such as xenon, oxygen or fullerenes could not succeed in-depth profiling these materials.[5, 16] For the sample made of three Phe delta layers inserted between Tyr spacers, high-quality molecular depth-profiles were achieved with argon GCIBs sputtering and Bi_3^+ analysis,[17] while the combination of 500 eV Cs^+ with Ga^+ analysis beam failed to resolve comparatively well the Phe delta layers. To get more insights into the depth profile resolution limiting factors, in this work we assess the depth resolution and molecular ions intensities associated with low-energy Cs^+ sputtering as a function of the nature (Bi_3^+ or Ga^+) and the fluence of the analysis primary ion beam.

2. Material and Methods

2.1 Samples preparation

Organic Phe/Tyr amino acids stacks were deposited by UHV thermal evaporation. The layers' thickness was monitored *in-situ* by a quartz crystal microbalance (QCM), which was previously calibrated to ensure a reliable and reproducible thickness control on each material and to take into account the different locations of the QCM and the substrates in the reactor. More in details, the layer thickness was calibrated by measuring the thickness of each material on silicon by ellipsometry (EP-5 ellipsometer from Semilab-Sopra) and by surface profilometry (Dektak). For example, for tyrosine, a thickness of 100 nm indicated by the QCM corresponded to 138 nm as measured by ellipsometry and 135 nm by profilometry. The last measure could possibly be influenced by the deformation of the soft surface by the tip. The calibration resulted in empirical thickness correction factors n_{tyr}=1.38 for the *Tyr* and n_{Phe}=1.34 for the *Phe*. From these coefficients, the multilayered structure deposition was directly monitored from the QCM output. For *Tyr/Phe* bilayers, we start by depositing a 24 nm thick *Phe* layer on Si, followed by 77 nm thick *Tyr* layer. *Tyr/Phe* multilayers consist of three *Phe* delta layers (6 nm thick) separated by 95 nm thick *Tyr* spacers, forming a total of 7 organic layers.

2.2 ToF-SIMS analysis

Model organic stacks are depth profiled using a ToF-SIMS IV instrument from IONTOF (Münster, Germany) in dual beam non-interlaced mode (one analysis frame and 1 s pause for each cycle), in negative polarity and with analysis and sputtering ion beams oriented at 45° with respect to the sample surface. In order to estimate the impact of Bi_3^+ fluence, two depth profiles were acquired at a constant Cs^+ fluence (5.5×10^{14} ions/cm² per cycle), while varying the Bi_3^+ fluence by a factor of 1.8. Specifically, in the *high fluence* condition, the Cs^+ sputtering beam (500 eV, 16 nA, 5 s/cycle) rasters a 300×300 µm² area and the Bi_3^+ analysis beam (25 keV, 0.30 pA) rasters a 100×100 µm² area corresponding to a fluence of 3.0×10^{10} ions/cm². In the *low fluence* condition, the sputtering raster area is 600×600 µm² and the analysis is 135×135 µm²; the Cs^+ current (31.5 nA) and sputter time (10 s/cycle) were both doubled in order to keep the same Cs^+ fluence in the two experiments. In this way, the Cs^+ fluence (and so the erosion speed) required to reach the organic/inorganic interface (amino acid/SiO_2) is still 5.5×10^{14} ions/cm² per cycle, while the Bi_3^+ fluence is reduced by a factor of 1.8 (1.7×10^{10} ions/cm² per cycle). The sample surface was flooded using a defocused low-energy electron beam in order to ensure fast surface charge compensation.

3. Results

3.1. Determination of the sputtering yield of Phe and Tyr

As the main aim of this work is to relate the in-depth resolution of the low-energy Cs^+ profile, a precise measurement of the two amino acids sputtering yields in our specific dual beam conditions (erosion and analysis) is a prerequisite to convert the sputtering time into a layer thickness. To do so, we started by profiling pure *Phe* and *Tyr* layers evaporated on Si wafers and then we analyzed Phe/Tyr and Tyr/Phe structures. In the heterojunction, we define the interface position as the time at which the underlying layer characteristic signal reaches 50 % of its plateau intensity. The sputtering yields derived from *Tyr* and *Phe* layers are 0.30 nm³/ion (32 atoms/ion) and 0.24 nm³/ion (24 atoms/ion), respectively. These values correspond, with the Cs^+ beam conditions given in the Experimental section, to erosion rate of 0.50 nm/s for the *Phe* layer, and a slightly higher rate for the *Tyr* layer (0.59 nm/s). These rates are rather high for such a low energy and monatomic source.

3.2. ToF-SIMS profile of Phe delta layers

The depth profile obtained with 500 eV Cs^+ and 25 keV Bi_3^+ analysis beam on the three Phe delta layers sample is shown in **Figure 1**. The depth profile displays the molecular signals from the deprotonated tyrosine ion ($C_9H_{10}NO_3^-$, [Tyr-H]$^-$) the deprotonated phenylalanine ions ($C_9H_{10}NO_2^-$, [Phe-H]$^-$) and the silicon substrate (SiO_2^-) as a function of the Cs^+ fluence. Remarkably, the three *Phe* delta layers are very well resolved together with a sharp drop of the [Tyr-H]$^-$ signal even in the third delta layer. Interestingly, the fluences needed to sputter the second and third *Tyr* and *Phe* layers are the same, meaning that the sputter rate remains rigorously constant throughout the whole depth profile. The constant sputtering yield implies that no damage, accumulation or crosslinking effects occur during the profile. Because of the strong similarity between *Phe* and *Tyr* molecules, the [Phe-H]$^-$ ion can also be generated from the fragmentation of the *Tyr* molecule by losing a hydroxyl group ([*Tyr-OH*]$^-$). This explains why the [Phe-H]$^-$ signal remains intense even when sputtering the *Tyr* layer.

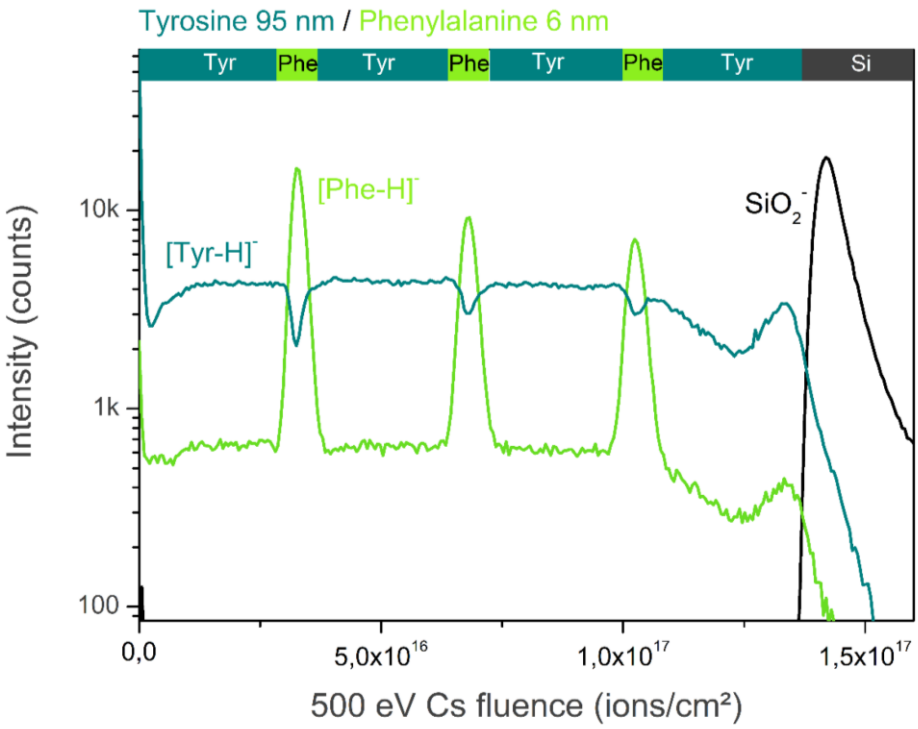

Figure 1 – ToF-SIMS depth profile of three 6 nm thick *Phe* delta layers separated by 95 nm thick *Tyr* spacer layers. The profile is obtained with 500 eV Cs^+ sputtering and 25 keV Bi_3^+ analysis beams.

Similar Tyr/Phe multilayers have been previously depth profiled by combining 500 eV Cs^+ sputtering and 15 keV Ga^+ analysis or by combining 20 keV C_{60}^+ or 2.5 keV Ar_{1700}^+ sputtering and 25 keV Bi_3^+ analysis.[17] This work showed that the best depth resolution (~6 nm) was achieved with 2.5 keV Ar_{1700}^+ sputtering and 25 keV Bi_3^+ analysis resulting in well-defined 10 nm thick Phe delta layers, while the quality of the profile obtained with low-energy Cs^+ was very poor (Figure 2). The main artefacts are (i) the low depth resolution, as testified by the enlargement of Phe delta layers, (ii) the accumulation of molecular fragmentation during the profile, as testified by the difficulty in identifying the third delta layer and(iii) the fact that only the $C_8H_8NO^-$ fragment could be monitored to identify the Tyr layer because the [Tyr-H]- intensity was too weak. From the comparison between Figure 1 and 2, we clearly see how the nature of the analysis beam (Bi_3^+ or Ga^+) affects the depth profile quality and the depth resolution. This is in agreement with a previous report from Cramer *et al.* on low-energy Cs^+ profiles on polycarbonate films.[4]

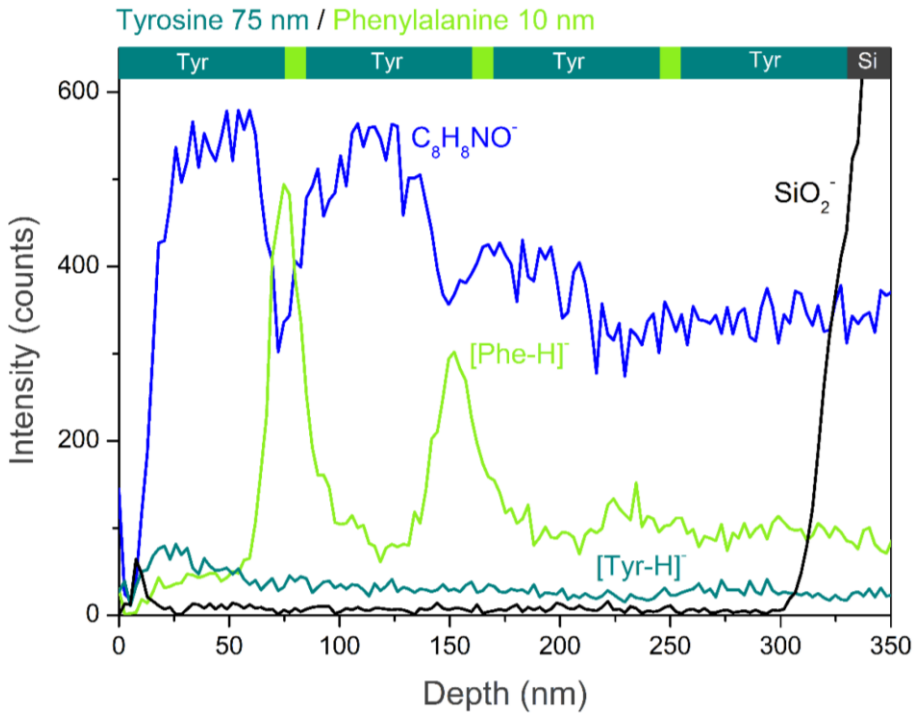

Figure 2. ToF-SIMS profile of three Phe delta layers (10 nm) sandwiched between Tyr spacers (75 nm) obtained with 500 eV Cs^+ sputtering and 15 keV Ga^+ analysis beams (adapted from Wehbe et al.[17]).

3.3. Evaluation of the depth resolution on Tyr/Phe profiles

A zoom on the rise of the $[Phe\text{-}H]^-$ signal at the Tyr/Phe interface in a bilayer sample is shown in **Figure 3**. The depth resolution is estimated based on the 16% - 84% criterion, calculated from the maximum $[Phe\text{-}H]^-$ intensity. For simplicity, we assume a constant sputter rate in the interface region, equal to the *Phe* one. This might cause a slight overestimation of the actual depth resolution (i.e. a few percent lower value). The 16%-84% depth resolution measured on this interface is 4.2 nm, which gives an estimate of the depth resolution obtained in this "high fluence" condition. Further details will be given in the next section from the analysis of *Phe* delta layers.

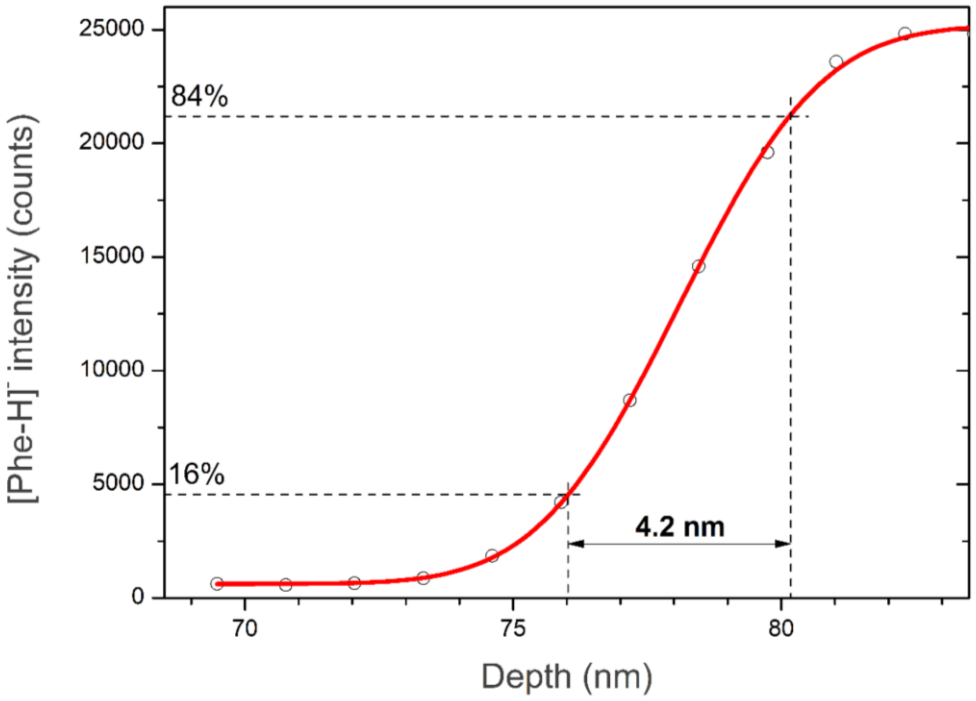

Figure 3. Zoom of the *Tyr/Phe* interface in the bilayer depth profile with 500 eV Cs^+ and 25 keV Bi_3^+ showing the rise of the $[Phe\text{-}H]^-$ molecular signal. Open circles are experimental points and the curve corresponds to the fit with *Eq. 1*.

4. Discussion

4.1. Depth resolution assessment

The profile analysis is performed by fitting the data with an error function, obtained by convoluting the ideal concentration profile with a Gaussian curve. This is correct if we assume that only the interface roughness (initial and induced) contributes to the depth resolution and that no molecular diffusion occurs. The escape depth of molecular ions is also neglected by this approach. For bilayers, the measured profile is thus modeled as the convolution of a step function with a Gaussian of variance σ. In this case, the function modeling the measured profile is:

$$f(x) = \frac{a}{2}\left[1+erf\left(\frac{x-x_0}{\sigma\sqrt{2}}\right)\right]+b \qquad \text{(Eq. 1)}$$

where a is the bottom layer signal maximal intensity, b is an offset, x_0 defines the interface location and x is the depth. The 16-84% distance previously defined is by definition given by the value 2σ, expressing the depth resolution associated with the profile conditions. For example, the rise of the $[Phe\text{-}H]^-$ molecular signal in the *Tyr/Phe* bilayer interface shown in Figure 3 is fitted with Eq. 1 with a variance σ=2.1 nm, thus indicating that the 16-84% depth resolution is 4.2 nm. The R^2=0.99961 value shows that the model is appropriate to describe the sputtering process.

An ideal delta layer can be schematically modeled as a boxcar function between the depths x_1 and x_2. The delta layer thickness is, therefore (x_2-x_1). The experimental depth profile over a delta layer can thus be modeled by the convolution of this box function with a Gaussian function of variance σ:

$$f(x) = \frac{a}{2}\left[erf\left(\frac{x-x_1}{\sigma\sqrt{2}}\right)-erf\left(\frac{x-x_2}{\sigma\sqrt{2}}\right)\right]+b \qquad \textit{(Eq. 2)}$$

where a and b have the same meaning as in *Eq. 1*. This function was applied to fit the profile of the first *Phe* delta layer in Figure 1. The fluence scale was converted into a depth scale by assuming a constant sputtering yield of the *Phe* of 0.24 nm^3/ion. Knowing that the delta layer width (x_2-x_1) is 6 nm, the fit of the experimental data with *Eq. 2*, gives the value σ=2.45 nm, corresponding to a depth resolution of 4.9 nm (Figure 4a). The R^2 coefficient (0.99557) is slightly lower in comparison to the bilayer sample, however, it still indicates a reasonably good match. As shown in Figure 4a, the fit follows much better the rising edge (top *Tyr/Phe* interface) with respect to the trailing edge (Phe/Tyr interface), suggesting that the top interface is sharper possibly because of the lower interface roughness or mixing. In order to take into account the beam induced roughening, the

model is refined by introducing two variances, σ_1 and σ_2 corresponding to the top and bottom interface roughness:

$$f(x) = \frac{a}{2}\left[erf\left(\frac{x-x_1}{\sigma_1\sqrt{2}}\right) - erf\left(\frac{x-x_2}{\sigma_2\sqrt{2}}\right)\right] + b \qquad \text{(Eq. 3).}$$

The fit of the first *Phe* delta layer by *Eq. 3* (Figure 4b) gives σ_1=2.05 nm and σ_2=2.9 nm, corresponding to a depth resolution on the rising edge of about 4.1 nm, agreeing well with the one measured on the bilayer system, and 5.8 nm on the trailing edge. The profile fitting with two Gaussian curves results in a fit accuracy of R^2=0.99877. We can thus safely assess that the intrinsic depth resolution obtained with 500 eV Cs^+ is ~4-5 nm, which is a remarkably low value for an organic depth profile.

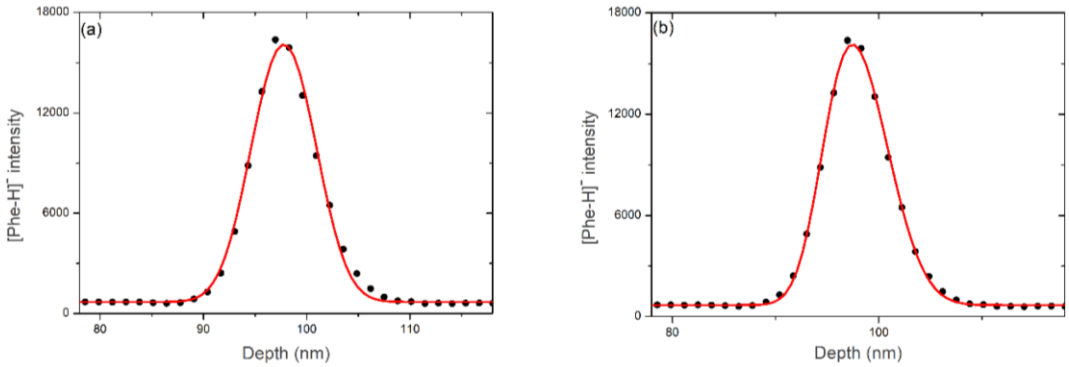

Figure 4. Zoom on the $[Phe\text{-}H]^-$ signal from the first 6-nm-thick *Phe* delta layer sputtered with 500 eV Cs^+ and analyzed with 25 keV Bi_3^+ beams. Open circles are experimental data and the curve fits are derived from *Eq. 2* (a) and *Eq. 3* (b).

4.2. Possible effect of the analysis beam fluence on the depth resolution

The striking difference between dual beam depth profiles combining 500 eV Cs^+ with Ga^+ or Cs^+ reveals the strong impact of the analysis beam nature on the organic profile depth resolution. This is particularly remarkable if we consider that in dual beam depth profiling, within one sputtering/analysis cycle, the sputtering beam fluence is typically five orders of magnitude higher than the analysis one. For example, the profiles in Figure 1 and 4 are obtained with a Bi/Cs fluence ratio of 5.5×10^{-5}, meaning that 18000 Cs^+ ions strike the surface for each Bi_3^+ cluster. We have also investigated the effect of the Bi_3^+ fluence on the depth resolution on *Tyr/Phe* multilayers with 6 nm *Phe* delta layers. The Bi_3^+ fluence was simply lowered by increasing the analysis area. The $[Phe\text{-}H]^-$ profiles obtained on the first *Phe* delta layer with the Bi/Cs fluence ratio of $R_H=5.5\times10^{-5}$

(high fluence) and $R_L=3.1\times10^{-5}$ (low fluence) are shown in **Figure 5**. While the sputtering yield ratio has been frequently taken as a good parameter to characterize and compare different ion beam conditions on inorganic samples, here we use the fluence ratio because the rapid degradation of organic layers induced by the analysis beam bombardment may result in a significant variation of the sputtering yield with the analysis time and this would limit our accuracy in calibrating the sputtering yields. The decrease of the analysis beam fluence seems to improve the depth resolution, as shown by the delta layer FWHM decrease from δ_H=7.1 nm to δ_L=6.5 nm. By using *Eq. 1*, this corresponds to a reduction of 2σ from $2\sigma_H$=4.9 nm to $2\sigma_L$=3.7 nm. If we apply the two-variances model (*Eq. 3*), the low fluence condition gives an average depth resolution of about 3.8 nm (σ_{1L}=1.6 nm and σ_{2L}=2.2). The reduction of the Bi_3^+ fluence could therefore slightly improve the depth resolution to a value below 4 nm. However, such a small difference of ~1 nm might not be significant as it could be due to the sample structure itself (i.e. local roughness) or even to fluctuations in the analysis area centering with respect to the sputter crater.

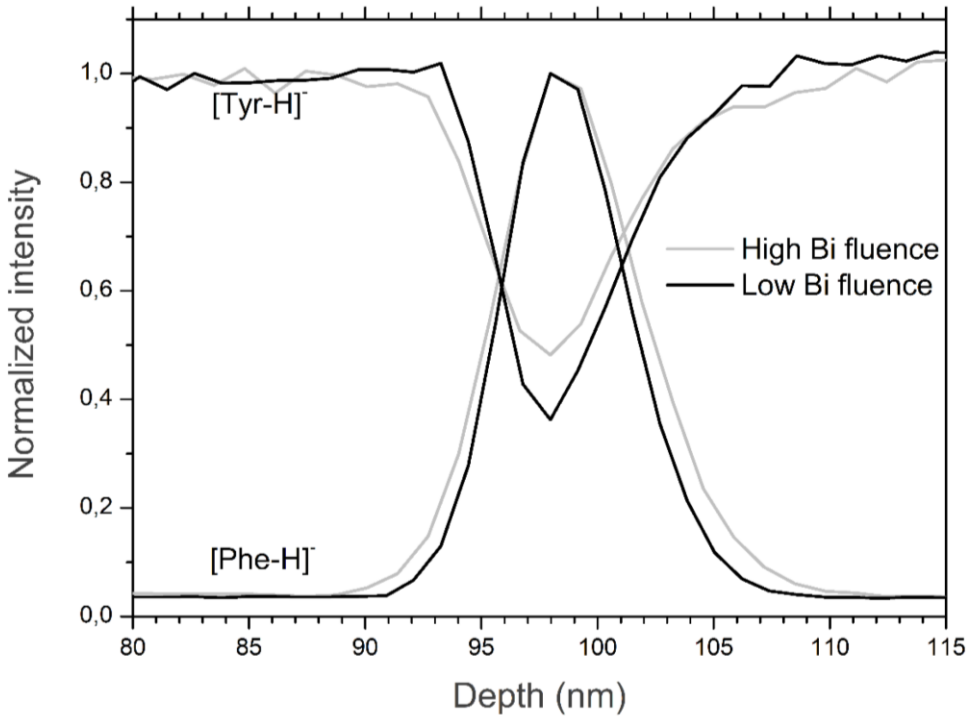

Figure 5. Effect of the 25 keV Bi_3^+ as analysis beam fluence (high fluence in black, low fluence in grey) on the profile of the first 6 nm *Phe* delta layer. The sputtering beam is 500 eV Cs^+.

The fluence of the analysis beam also affects the [Tyr-H]$^-$ signal drop in the *Phe* layer (Figure 5). Namely, a sharper drop of the [Tyr-H]$^-$ signal is observed in low-fluence condition; the normalized intensity minima at the middle of the *Phe* layer are m_H=0.48 for the high Bi_3^+ fluence and m_L=0.35 for the low Bi_3^+ fluence. If we fit the [Tyr-H]$^-$ profile in the *Phe* delta layer with a simple convolution with a Gaussian function:

$$g(x) = 1 - \frac{1}{2}\left[erf\left(\frac{x-x_1}{\sigma\sqrt{2}}\right) - erf\left(\frac{x-x_2}{\sigma\sqrt{2}}\right)\right],$$

where $\delta = x_2 - x_1$ corresponds to the *Phe* thickness of 6 nm. The minimum value, at the center of the delta, is:

$$g(x_1 + \delta/2) = 1 - \frac{1}{2}\left[erf\left(\frac{\delta}{2\sigma\sqrt{2}}\right) - erf\left(\frac{-\delta}{2\sigma\sqrt{2}}\right)\right]$$

From the above relation and based on the σ values, the expected (normalized) minima would be m_H=0.22 (σ_H=2.45) and m_L=0.11 (σ_L=1.85). The difference between the experimental and the fit minima is ascribed to the fact that the information depth is neglected in the pure Gaussian model. Practically, when the profile reaches the apex of the [Phe-H]$^-$ signal, because of both the surface roughness and the information depth, a small [Tyr-H]$^-$ signal is already detected from the underlying tyrosine layer. Again, although the drop in *Tyr* intensity hints at an improved depth resolution, one cannot rule out slight variations in the Phe delta layer thickness in the order of ~1 nm that would also affect the *Tyr* intensity in the middle of the layer.

4.3. Evolution of the depth resolution with the sputtering time

For ideal *Tyr/Phe* multilayer profiles, in which interface effects can be neglected, by knowing the individual sputter rates on each pure material, the *Phe* delta layers centroids in Figure 1 would be centered at z_1=98, z_2=196 and z_3=294 nm. The evolution of the delta layer thicknesses (δ_i, with i=1,2,3) can be used to estimate the decrease of the depth resolution as a function of the sputtering time (or the depth) for the two Bi_3^+ fluence regimes.

The depth resolution at high and low Bi_3^+ fluence ($2\sigma_i$) estimated from the Gaussian fit (*Eq. 1*) are respectively 4.9 and 3.7 nm for $2\sigma_1$, 5.9 and 3.7 nm for $2\sigma_2$, and 6.9 and 5.1 nm for $2\sigma_3$, indicating that, over a depth of 400 nm, the depth resolution lowers by approximately 1 nm every 100 nm of sputtering (see **Figure 6**). These results suggest that the analysis beam fluence has a non-negligible impact on the decrease of the depth resolution and it should be definitely limited in long profiles of organic materials.

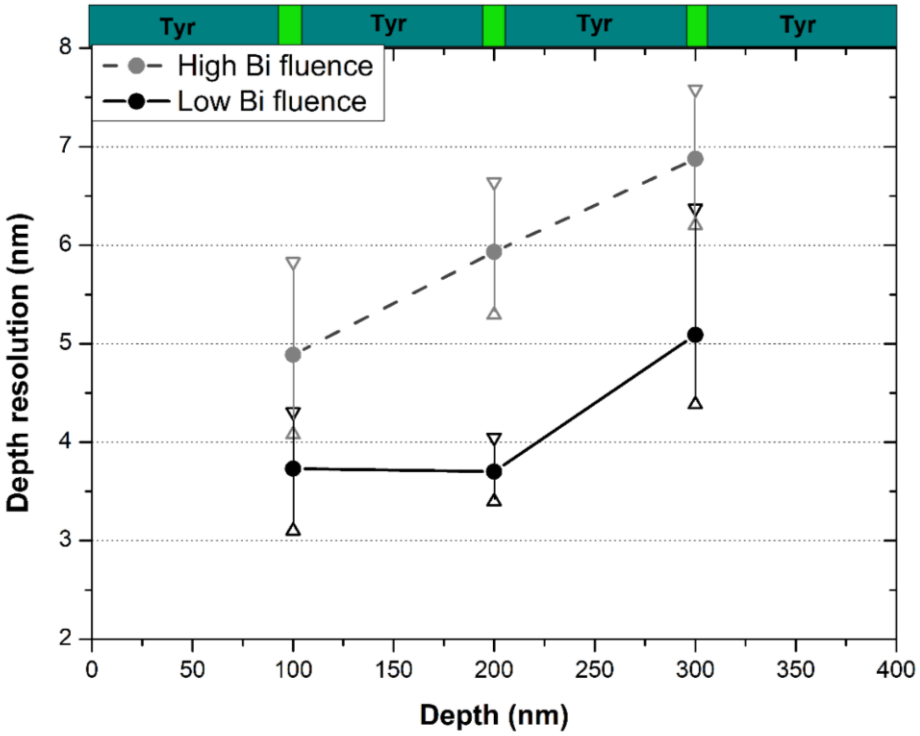

Figure 6 - Depth resolution vs. depth measured on the three *Phe* delta layers. The sputter beam is 500 eV Cs^+ and the analysis beam is 25 keV Bi_3^+ with a high fluence (grey curve) and a low fluence (black curve). The errors bars represent the depth resolutions obtained with the asymmetric response function, the lower bound standing for the resolution on the rising edge and the higher bound for the trailing edge.

5. Conclusions

In this work, we have produced model samples with organic delta layer in order to assess the depth resolution in organic depth profiles with low-energy Cs^+. First of all, even if the sputtering is performed with monoatomic ions, intense and stable quasi-molecular ions profiles from *Phe* and *Tyr* were obtained testifying the ability of Cs^+ in enhancing negative ionization yields and preventing the accumulation of molecular damage, until the substrate was reached. Results show that, in the best conditions, corresponding to the lower analysis beam fluence, few nm thick *Phe* delta layers embedded into Tyr barriers are successfully profiled with a depth resolution around 4 nm at the first *Phe* layer and degradation of about 1 nm every 100 nm of sputtering. This constitutes

a major improvement from previously published data on similar samples, obtained with Ga^+ as analysis beam. The degradation of the depth resolution appears therefore severely affected by the roughening and mixing induced by the analysis beam, even though its fluence is about 10^5 times smaller than the one from the sputtering beam. The depth resolution measured on the first delta layer seems to be further improved by halving the Bi_3^+ fluence, but the magnitude of this effect (~1 nm) could be comparable to local variations in the sample roughness and/or to the curvature of the crater bottom. Low-energy Cs^+ sputtering results in a depth resolution of 4 nm, which is even higher than what was previously reported in similar *Tyr/Phe* organic stacks and analysis beam conditions, by using Ar_{1700}^+ clusters profiles sputtering (~6 nm). This fact is relevant because, with respect to Ar clusters, low-energy Cs^+ provides for much lower sputter yield gap between organic and inorganic materials (metals and oxides), thus allowing to profile hybrid stacks. Overall, *Phe/Tyr* stacks appear as very useful samples to optimize the depth profile conditions and follow the depth resolution degradation as a function of the sputtering depth.

Incoming measurements will assess this topic within a more systematic study. Namely, further reducing the bismuth fluence should give an insight about the ultimate depth resolution that can be reached with cesium sputtering gun. Moreover, exploring a larger range of energies and sizes of Bi_n^+ clusters (n = 1, 3, 5, 7) should illustrate the compromise existing between signal intensity and degradation, and this way advocate optimal conditions for the depth profiling of organics.

Acknowledgments

This research used resources of the "Synthesis, Irradiation and Analysis of Materials" (SIAM) platform of the University of Namur. The authors would like to thank Dr. Alexandre Felten for his helpful comments.

References

1. Gillen, G., Roberson, S.: Preliminary evaluation of an SF5+ polyatomic primary ion beam for analysis of organic thin films by secondary ion mass spectrometry. Rapid Commun. Mass Spectrom. 12, 1303–1312 (1998)
2. Ninomiya, S., Ichiki, K., Yamada, H., Nakata, Y., Seki, T., Aoki, T., Matsuo, J.: Molecular depth profiling of multilayer structures of organic semiconductor materials by secondary ion mass spectrometry with large argon cluster ion beams. Rapid Commun. Mass Spectrom. 23, 3264–3268 (2009)
3. Mine, N., Douhard, B., Brison, J., Houssiau, L.: Molecular depth-profiling of polycarbonate with low-energy Cs+ ions. Rapid Commun. Mass Spectrom. 21, 2680–2684 (2007)
4. Cramer, H.-G., Grehl, T., Kollmer, F., Moellers, R., Niehuis, E., Rading, D.: Depth profiling of organic materials using improved ion beam conditions. Appl. Surf. Sci. 255, 966–969 (2008)
5. Brison, J., Mine, N., Wehbe, N., Gillon, X., Tabarrant, T., Sporken, R., Houssiau, L.: Molecular depth profiling of model biological films using low energy monoatomic ions. Int. J. Mass Spectrom. 321–322, 1–7 (2012)
6. Wehbe, N., Pireaux, J.-J., Houssiau, L.: XPS Evidence for Negative Ion Formation in SIMS Depth Profiling of Organic Material with Cesium. J. Phys. Chem. C. 118, 26613–26620 (2014)
7. Houssiau, L., Mine, N.: Molecular depth profiling of polymers with very low energy reactive ions. Surf. Interface Anal. 42, 1402–1408 (2010)
8. Houssiau, L., Mine, N.: Molecular depth profiling with reactive ions, or why chemistry matters in sputtering. Surf. Interface Anal. 43, 146–150 (2011)
9. Busby, Y., Agresti, A., Pescetelli, S., Di Carlo, A., Noel, C., Pireaux, J.-J., Houssiau, L.: Aging effects in Interface-engineered perovskite solar cells with 2D nanomaterials: A depth profile analysis. Mater. Today Energy. 9, 1–10 (2018)
10. Matteocci, F., Busby, Y., Pireaux, J.-J., Divitini, G., Cacovich, S., Ducati, C., Di Carlo, A.: Interface and Composition Analysis on Perovskite Solar Cells. ACS Appl. Mater. Interfaces. 7, 26176–26183 (2015)
11. Busby, Y., Nau, S., Sax, S., List-Kratochvil, E.J.W., Novak, J., Banerjee, R., Schreiber, F., Pireaux, J.-J.: Direct observation of conductive filament formation in Alq3 based organic resistive memories. J. Appl. Phys. 118, 075501 (2015)
12. Noël, C., Houssiau, L.: Hybrid Organic/Inorganic Materials Depth Profiling Using Low Energy Cesium Ions. J. Am. Soc. Mass Spectrom. 27, 908–916 (2016)
13. Tortora, L., Urbini, M., Fabbri, A., Branchini, P., Mariucci, L., Rapisarda, M., Barra, M., Chiarella, F., Cassinese, A., Di Capua, F., Aloisio, A.: Three-dimensional characterization of OTFT on modified hydrophobic flexible polymeric substrate by low energy Cs + ion sputtering. Appl. Surf. Sci. 448, 628–635 (2018)
14. Shen, K., Mao, D., Garrison, B.J., Wucher, A., Winograd, N.: Depth Profiling of Metal Overlayers on Organic Substrates with Cluster SIMS. Anal. Chem. 85, 10565–10572 (2013)
15. Niehuis, E., Möllers, R., Rading, D., Cramer, H.-G., Kersting, R.: Analysis of organic multilayers and 3D structures using Ar cluster ions. Surf. Interface Anal. 45, 158–162 (2013)
16. Wehbe, N., Houssiau, L.: Comparative Study of the Usefulness of Low Energy Cs^+, Xe^+, and O_2^+ Ions for Depth Profiling Amino-Acid and Sugar Films. Anal. Chem. 82, 10052–10059 (2010)
17. Wehbe, N., Tabarrant, T., Brison, J., Mouhib, T., Delcorte, A., Bertrand, P., Moellers, R., Niehuis, E., Houssiau, L.: TOF-SIMS depth profiling of multilayer amino-acid films using large Argon cluster Ar_n^+, C_{60}^+ and Cs^+ sputtering ions: A comparative study: ToF-SIMS depth profiling of multilayer amino-acid films. Surf. Interface Anal. 45, 178–180 (2013)

4.2 HYBRID MODEL SAMPLES DEPTH PROFILING WITH LOW ENERGY CS – FEASIBILITY STUDY

The previous paragraph validated the capacity of low-energy Cs to efficiently depth-profile organics, displaying high molecular fragments intensities and excellent depth resolution. The goal of the next paper is to go further and to determine if Cs source could be suitable for providing in-depth molecular information about hybrid samples, in an easy, fast and reliable way. We synthesized model samples made of gold or chromium and tyrosine and analyzed them in order to understand the sputtering mechanisms involved, such as recoil depth, modification of the etching rate or fragmentation. We show that hybrid multilayers can be depth-profiled with moderate degradation using cesium ions.

The favorable effect of Cs sputtering was also observed by Edwards et al. on polymer loaded with inorganic nanoparticles.[92] They compare the performances of 500 eV Cs^+, 10 keV Ar_{3000}^+ and 20 keV Ar_{1000}^+ for the depth profiling of polycarbonate (PC), and PC combined with different types of inorganic nanocomposites. In particular, on PC with inclusions of graphene oxide decorated by Fe_3O_4 nanoparticles, they noticed an alteration of the polymer under Ar clusters bombardment. Conversely, low energy Cs^+ allowed maintaining constant molecular intensities, indicating that no damage accumulation occurred in these conditions. However, a higher topography developed in the polymer reference sample under Cs^+ bombardment, which confirms the superiority of large Ar clusters for the depth profiling of polymers.

The following scientific paper assesses the feasibility of depth profiling a hybrid sample comprising a metallic overlayer and constitutes, to our knowledge, the first successful attempt of this type using ToF-SIMS. While this feasibility study does not aim at providing a detailed discussion on the chemical interaction processes between amino acids and metals, we feel that some interesting features should be pinpointed.

(i) In the profiles below, the fluctuations of the signal intensities near the interfaces is attributed to a variation of the Cs concentration, due to abrupt changes in sputtering yield, leading to Cs pileup at the interface The matrix effect related to the change in the surface composition (i.e. enhanced negative ionization) could explain this phenomenon. Also, gold was proved to impact the positive ionization probability[27,28] and it is conceivable that the negative ionization probability could be affected as well, even if this is not reported in the literature.

(ii) On the chromium/tyrosine systems, a strong signal of chromium oxide appears in response to a strong reactivity of the metal with ambient oxygen and oxygen contained in the tyrosine layer. More surprisingly, a high signal of Cr_2^- is observed in the middle of the layer,

despite the small thickness of the chromium layer (10 nm). We suspect different oxidation states of the Cr atoms directly in contact with the organic layer or with the atmosphere, than the ones inside the metal layer. XPS measurement might shed light on this issue.

(iii) The signal of SiO_2^- is monitored to localize the interface with the substrate. Interestingly, the intensity of this signal increases at the extreme surface of the samples, and at the interfaces, except in the case of the gold layer deposited on tyrosine. Diffusion of the silicon substrate through the layer is highly improbable, but we cannot completely reject the possibility of uneven coverage of the substrate. However, we assume that the intensity should present a plateau in that case. We suspect contamination with polydimethylsiloxane (PDMS) while transferring the sample for the PVD chamber, to the evaporation facility. The possibility of a mass interference is a priori excluded.

Hybrid organic/inorganic materials depth profiling using low energy cesium ions.

*Céline Noël, Laurent Houssiau**

University of Namur, Research Centre in Physics of Matter and Radiation, Namur, Belgium.

*Corresponding author: Laurent.houssiau@unamur.be

ABSTRACT

The structures developed in organic electronics, such as OLEDs (organic light emitting diodes) or OPVs (organic photovoltaics) devices always involve hybrid interfaces, joining metal or oxide layers with organic layers. No satisfactory method to probe these hybrid interfaces physical chemistry currently exists. One promising way to analyze such interfaces is to use *in situ* ion beam etching, but this requires ion beams able to depth profile both inorganic and organic layers. Mono- or diatomic ion beams commonly used to depth profile inorganic materials usually perform badly on organics, while cluster ion beams perform excellently on organics, but yield poor results when organics and inorganics are mixed. On the contrary, low energy Cs^+ beams (< 500 eV) allow organic and inorganic materials depth profiling with comparable erosion rates. This paper shows a successful depth profiling of a model hybrid system made of metallic (Au, Cr) and organic (tyrosine) layers, sputtered with 500 eV Cs^+ ions. Tyrosine layers capped with metallic overlayers are depth profiled easily, with high intensities for the characteristic molecular ions and other specific fragments. Metallic Au or Cr atoms are recoiled into the organic layer where they cause some damage

near the hybrid interface as well as changes in the erosion rate. However, these recoil implanted metallic atoms do not appear to severely degrade the depth profile overall quality. This first successful hybrid depth profiling report opens new possibilities for the study of OLEDs, organic solar cells or other hybrid devices.

KEYWORDS: Organic electronics, OLEDs, OPVs, hybrid materials, SIMS, cesium

INTRODUCTION

Time-of-Flight Secondary Ion Mass Spectrometry (ToF-SIMS) has been repeatedly used to depth profile inorganic and, more recently, organic samples. An increasing amount of literature demonstrates that polyatomic primary ions such as SF_5^+, C_{60}^+ and Ar_n^+ are suitable for this purpose[1,2,3,4,5,6]. The total energy is shared by each atom in the cluster, limiting the penetration depth and thereby the extent of the chemically damaged layer under the surface. Due to their high sputtering yield, these ions show a high cleaning efficiency and thus avoid damage accumulation on materials removed layer-by-layer[7,8,9].

Recently, hybrid samples (organic *and* inorganic multilayers) have played an important role in a broad range of fields, especially in microelectronics with the development of OLEDs and organic solar cells. Other application fields include catalyst devices for air or water purification[10] and assemblies containing hybrid metal/polymer interfaces used in the automotive and aviation industry. Presently, the challenge is to further improve their performances (lifetime, stability, etc.) by understanding the phenomena which occur at the interfaces inside their multilayer structure (interlayer diffusion or degradation mechanisms depending on illumination, temperature variations and atmospheric conditions[11,12]). Despite their excellent performance on organic samples, cluster ions are rather inefficient to depth

profile inorganic samples[13], so that it remains a challenge to use them efficiently on hybrid samples[14]. The main issue for this type of analysis is the extreme sputter rate difference between organics and inorganics[15]. The literature reports three different ways to obtain depth profiles on hybrid systems. The first approach consists on removing the inorganic layers from the device, then to subsequently analyze the remaining organic parts with cluster ion beams. This has been performed for instance on OLED systems, in which the metallic cathode is removed mechanically before the organic layers analysis[16]. Another approach consists on switching ion sources while crossing hybrid interfaces, e.g. using a monoatomic Ar source on inorganic layers, then switching to Argon cluster ion beams in the organic layers[17]. Finally, hybrid depth profiling with only one source has been attempted on 1.4 to 3.5 nm gold layer embedded in cholesterol deposits[14], sputtered with C_{60}^+ ion source. On these model systems, the organic layer shows an important molecular ion signal decrease after the gold is removed. Regardless the metal layer thickness, fragmentation enhancement is observed, as well as a decrease of both the sputtering yield and cleanup efficiency, compared to the upper cholesterol layer.

In this context, we managed to assess the impact of low energy Cs^+ as a sputter source for hybrid organic/inorganic samples depth profiling. Cs high reactivity ensures a negative ion signal enhancement, along with free radicals scavenging[18]. This source already proved its efficiency on both inorganics[19,20,21,22] and organics[23,24,25]. In this paper, we analyze model systems made of different metals (gold or chromium) and tyrosine multilayer systems deposited on silicon substrates. We show how it is possible not only to reach the silicon substrate with a single set of parameters, but also to keep a high intensity for the deprotonated tyrosine molecular ion even after sputtering through 10 nm gold or chromium.

EXPERIMENTAL SECTION

Sample description

Hybrid multilayer samples consist of gold or chromium layers grown by physical vapor deposition (PVD) and evaporated tyrosine (denoted "Tyr" below) on silicon substrates.

Silicon substrates <100> were purchased from Si-Mat (Kaufering, Germany). Prior to analysis, they were cut into 1 cm dices and cleaned by sonicating them in an isopropanol bath for 15 minutes. Then they were immediately dried under a nitrogen flow.

L-Tyrosine ($C_9H_{11}NO_3$, Sigma-Aldrich ≥ 97%) was deposited by thermal evaporation in a Cressington evaporation supply LT 1500 308R (Watford, UK). The chamber was first brought to a 10^{-7} mbar pressure. The crucible containing the tyrosine powder was then heated up to 330-350°C. The pressure during evaporation never exceeded 10^{-6} mbar and the deposited thickness was controlled by a Quartz microbalance, which was calibrated with ellipsometry and profilometry in turns.

Gold and chromium layers were grown by PVD with a Quorum Q150 T E/S device from Quorum Technologies (Laughton, UK), from which sputter targets were also purchased. 20 and 120 mA currents were used for Au and Cr, respectively. The distance between the target and the sample was 50 mm. The layer thickness was once again measured with a Quartz microbalance and calibrated with a profilometer.

Using these disposition approaches, the following metal/organic systems were prepared:

- A one-layer sample for sputtering yields measurements (Tyr/Si), (Cr/Si) and (Au/Si),
- Two-layer samples (10 nm Cr/94 nm Tyr/Si), (92 nm Tyr/10 nm Cr/Si), (10 nm Au/92 nm Tyr/Si) and (92 nm Tyr/10 nm Au /Si),

- Three-layer samples (92 nm Tyr/10 nm Au/92 nm Tyr/Si),(92 nm Tyr/10 nm Cr/94 nm Tyr/Si).

ToF-SIMS measurements

ToF-SIMS depth profiles were acquired in dual beam mode[26] using a ToF-SIMS IV (Ion-Tof GmbH, Münster, Germany). The analysis beam (Bi_3^+ at 25 keV; current: ~25 pA, pulse width: 20 ns; pulse width after bunching: 0.75 ns; repetition rate: 10 kHz), rastered over a 300 X 300 µm² area and the erosion beam (Cs^+ at 500 eV, current: 37-41 nA), rastered over a 500 X 500 µm² area were operated in non-interlaced mode with 1 analysis frame (1.6384 s), 10 s erosion and 1 s pause per cycle, both with a 45° incidence angle to the sample surface. A low energy flood gun ensured charge compensation. The secondary ions were extracted at a 2 kV acceleration voltage. The spectra were calibrated with C_5^-, $C_8H_7O^-$ and $C_9H_{10}NO_3^-$ peaks and were acquired from 0 to 880 m/z. The mass resolution (m/Δm) at the $C_9H_{10}NO_3^-$ (m/z 180) and Si^- (m/z 28) peaks were typically above 8500 and 10500 in negative ion polarity. Ion intensities in depth profiles are expressed in ions/cycle units (simply denoted by "counts" in the graphs), which is the number of ions of a given species detected per analysis cycle, lasting 128 x 128 x 10^{-4} s, or 1.6384 s.

Sputtering yields. The sputtering yields of single layers deposited on Si were determined by using the following relation:

$$Y = \frac{eAd}{It} \qquad \text{Eq. 2.}$$

where e stands for the electron charge (1.6 X 10^{-19} C/ion), A is the sputtered area in nm², d is the layer thickness in nm, determined by profilometry, I indicates the sputtering current and t

is the time necessary to reach 50% of the steady state intensity of the following layer characteristic signal.

RESULTS AND DISCUSSION

a) organics on metals

The depth profile results for the Tyr/Au/Si system are shown in Fig. 1a. and the results for the Tyr/Cr/Si system are shown in Fig. 1b. As expected, both the tyrosine[27] and inorganic films are easily depth profiled with 500 eV Cs^+, with a very sharp interface. The Tyr layer is readily identified with a $C_9H_{10}NO_3^-$ molecular ion or $[Tyr\text{-}H]^-$, at m/z 180. Other characteristic fragments are also monitored: $C_8H_8NO^-$ at m/z 134, $C_8H_7O^-$ at m/z 119 (not shown) and $C_6H_5O^-$ at m/z 93 (not show). The molecular ion $[Tyr\text{-}H]^-$ signal drops rapidly at the beginning of the depth profiles, then it rises to reach a steady state value. Intensity oscillations are also noticed at the organic/metal interface. This behavior is common with low energy Cs^+ depth profiling as was shown in previous works[18,24]. The initial drop is caused by rapid fragmentation of the Tyr molecules caused by the Cs^+ ions, leading to the formation of free radicals. When the sputtered depth reaches that of the implanted Cs atoms, reactions between Cs atoms and the free radicals quench the chemical damage processes, such as crosslinking or hydrogen abstraction. Closer to the hybrid interface, Cs concentration variations occur, leading to transients in the molecular signal, probably related to changes in the negative ionization probability.

The Au signal plotted in figure 1a is represented by the gold dimer Au_2^-, as opposed to the monomer Au^-, because the Au^- ions saturate the detector. The Cr signal in figure 1b is also represented by the dimerized Cr_2^- signal. The ion $^{50}CrO_2^-$ at m/z 82, plotted in fig. 1b, is a marker for native chromium oxide layers. In both cases, no metal (Cr, Au) is detected in the

Tyr layer, meaning that no significant diffusion of metal occurs into the organic layer. The second interface (metal/Si) is identified with a SiO_2^- ion (native oxide).

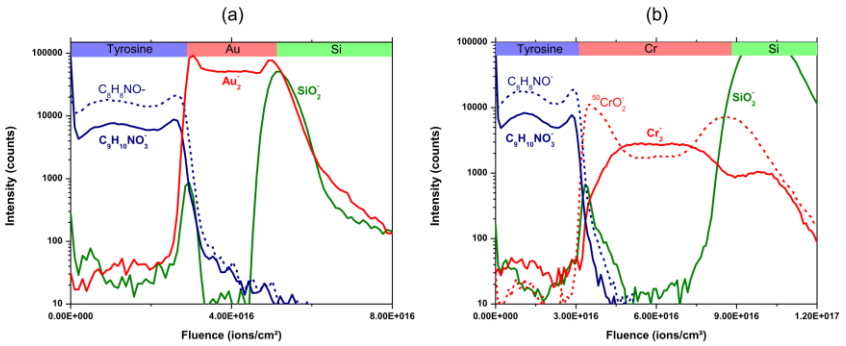

Fig. 1. 500 eV Cs^+ depth profiling of 92 nm Tyr/ 10 nm Au/Si multilayers (a) and 92 nm Tyr/10 nm Cr/Si multilayers (b).

b) Metal on organics

Metal on organic films are much more challenging hybrid systems to characterize with ToF-SIMS compared to the converse situation (organic on metal films). This is because the energetic metal atoms in the collision cascade are injected into the softer and less dense underlying Tyr layer, where they produce extensive molecular damage. Fig. 2a. shows the depth profile obtained with 500 eV Cs^+ on the Au/Tyr/Si system. The first remarkable observation is the sharp rise of the $[Tyr-H]^-$ signal at the Au/Tyr interface, followed by a high and slightly fluctuating intensity of the molecular ion within the Tyr layer. The Au_2^- intensity remains constant within the Au overlayer, then drops exponentially in the Tyr layer, indicating a broad ion beam induced diffusion of metal into the organic layer. This diffusion is not observed in the reverse layer (Tyr/Au) and is therefore due to collisions between the incident Cs^+ ions and Au atoms, pushing these atoms deeper into the Tyr underlayer. This

experiment demonstrates that Tyr molecules withstand the collisions with Au atoms with relatively low damage. The initial Tyr intensity drop beyond the Au/Tyr interface could be due to Tyr molecules fragmentation. However, the signal tends to increase deeper in the Tyr layer, where the Au concentration is lower, which strongly limits the collisions between Au atoms and Tyr molecules. The intensity drop measured at the Au/Tyr interface for all secondary ions is attributed to a temporary charging effect arising when crossing the interface from the highly conductive gold layer to the insulating Tyr layer. This leads to a brief loss of total secondary ion emission and also to sudden peak shifts, which are taken into account in the plotted peak areas.

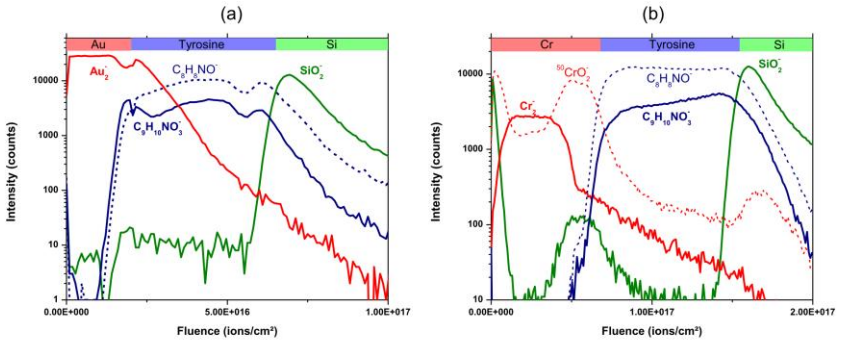

Fig. 2. 500 eV Cs^+ depth profiling of 10 nm Au/ 92 nm Tyr/Si multilayers (a) and 10 nm Cr/94 nm Tyr/Si multilayers (b).

Fig. 2b. shows the depth profile obtained with 500 eV Cs^+ in the Cr/Tyr/Si system. Once again, the Tyr signal, monitored by the $[Tyr\text{-}H]^-$ ion, as well as the $C_8H_8NO^-$ fragment, rises rapidly at the Cr/Tyr interface, up to a steady-state, proving that the molecular depth profiling remains efficient beyond the metallic overlayer. The Cr layer is identified by means of Cr_2^- ions at m/z 52 and $^{50}CrO_2^-$ ions at m/z 82. The Cr_2^- profile is flat in the Cr layer. Then it decreases slowly in the Tyr layer, suggesting again an intensive ion beam induced diffusion

of Cr atoms into the Tyr layer. Like in the previous case (Au/Tyr), this diffusion is produced by recoiling the Cr atoms with incident Cs^+ ions deeper through the organic layer. The chromium layer oxidation is measured by means of $^{50}CrO_2^-$ ions. Chromium appears to be oxidized at its surface (native oxide layer) and at the Cr/Tyr interface.

c) organic/metal/organic/Si multilayers

Trilayer systems offer two hybrid interfaces (organic/inorganic and inorganic/organic), therefore allowing a direct comparison of molecular signals before crossing the metal film (top Tyr layer) and after crossing the metal film (buried Tyr layer). The depth profile obtained with 500 eV Cs^+ on the Tyr/Au/Tyr/Si system is shown in fig. 3a. Once again, the hybrid depth profiling is successful when looking at the $[Tyr-H]^-$ peak and all the Tyr related fragments (only the $C_8H_8NO^-$ fragment at m/z 134 is shown in fig. 3a). The $[Tyr-H]^-$ steady-state intensity reaches about 6000 ions/cycle in the first layer, then drops sharply, as expected, at the Tyr/Au interface. Furthermore, the signal rises again sharply at the Au/Tyr interface, then reaches a maximum intensity ca. 4000 ions/cycle. Naturally, the signal decreases again when reaching the Si substrate. Similar conclusions can be drawn for the large fragment at m/z 134, with a maximum intensity still exceeding 10000 ions/cycles in the second Tyr layer. The Au_2^- signal also helps to identify the Au layer and to estimate the Au ion beam induced diffusion through the Tyr layer. The signal rise at the first interface is extremely sharp, but its decay is slow beyond the second interface, as noticed in fig.2a. The high amount of Au atoms injected in the Tyr layer evidently increases molecular damage, but the molecular signal loss beyond the 10 nm thick Au layer remains quite limited. Compared to the bilayer shown in Fig. 2a., a residual Tyr signal is still detected within the Au layer. The

reason might be that Au layers evaporated on a Tyr substrate exhibit some defects, such as pinholes, compared to Au layers evaporated on Si.

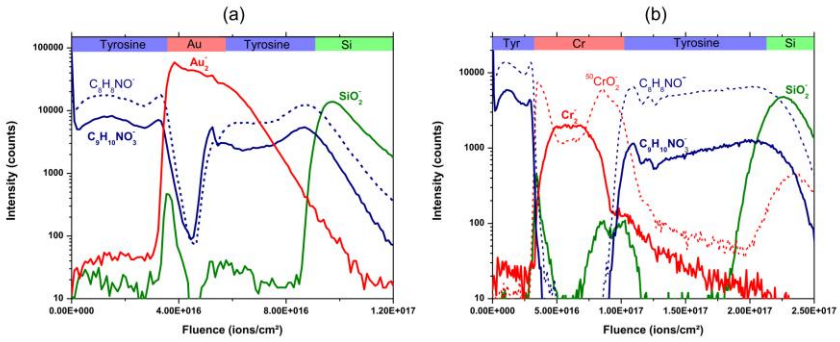

Fig. 3. 500 eV Cs^+ depth profiling of 92 nm Tyr/10 nm Au/92 nm Tyr/Si multilayers (a) and 92 nm Tyr/10 nm Cr/94 nm Tyr/Si multilayers.

The depth profile obtained with 500 eV Cs^+ in a Tyr/Cr/Tyr/Si system is shown in Fig. 3b. The general features are similar to the previous profile (fig. 3a.), with a high $[Tyr\text{-}H]^-$ ion intensity in the first layer (~6000 counts/cycle), a sharp drop at the first interface, followed by another sharp rise at the second interface and an immediate molecular signal recovery. Some oscillations are observed, until the signal reaches a maximum around 1300 counts/cycle, which is lower than in the Tyr/Au/Tyr case, but still remains adequate for molecular depth profiling. Again, an extensive Cr ion beam induced diffusion (followed by Cr_2^- and $^{50}CrO_2^-$ ions) is observed. In order to understand the origin of the Tyr signal intensity oscillations, 3D imaging data (not shown) was reconstructed in the second interface region. It turns out that the intensity loss is related to dark spots observed on all secondary ion images, i.e. areas where the secondary ion intensity is depressed. This is most likely due to differential charging effects at the metal/insulator interface, which are temporarily not fully compensated by electron flooding.

d) Discussion

Metal injection in the organic layer

The key issue in metal/organics depth profiling is the injection of metal atoms into organic layers[28]. In the systems analyzed here, Cr and Au atoms are recoiled from the metallic overlayer through the Tyr layer. As shown in figs 2 and 3, the Cr and Au ion beam induced diffusion is evident on the depth profiles, with a long exponential tail observed for all Cr and Au containing ions. Fig. 4 compares the intensity decay of Au^- and Cr^- ions into the Tyr layer for bilayers (Au or Cr/Tyr). The horizontal scale is now a depth scale calibrated such as the Tyr layer thickness is 92 nm for Au and 94 nm for Cr. The Au^- ions saturate the detector at high concentration (dashed line in Fig. 4). Then the signal follows an exponential decay deeper in the Tyr layer. Assuming that the Au or Cr decay obeys the law:

$$I(x)=I_0 \exp(-x/d_{Au \text{ or } Cr}), \qquad \text{Eq. 1.}$$

where $I(x)$ is the secondary ion intensity, I_0 is a constant, x is the depth and $d_{Au\ or\ Cr}$ is the decay length, which can be measured from depth profiles. From the experiments shown in Fig. 4., the decay length for Au atoms d_{Au} = 12 nm, whereas for Cr d_{Cr} = 33 nm. Therefore, Cr atoms appear to be knocked in much more extensively than Au atoms upon the Cs^+ impact. The energetic metal atoms penetrating the Tyr layer are atoms in motion in the deepest part of the collision cascade initiated in the metal layer upon the Cs^+ impact. We therefore performed SRIM[29] simulations to roughly estimate if a metal is more injected than the other. Two layers are considered in the model: a thin metal (Cr or Au) layer on top of a stoichiometric $C_9H_{11}NO_3$ layer. Fig. 5 shows the recoil distribution of Cr and Au for a 1 nm metal overlayer, expressed as an atomic concentration per fluence unit: (atoms/cm³)/(Cs^+ ions/cm²). It appears that significantly more Cr atoms are recoiled just below the interface than Au atoms. It is also the case for 0.5 nm and 1.5 nm simulated metallic layers (not

shown). For metallic layers thicker than 2 nm, no Cr or Au atoms are recoiled beyond the interface, since the layer thickness exceeds that of the collision cascade. Moreover, the fluence needed to sputter a given depth of Cr is about 3 times larger than for a Au layer, so that the atomic Cr concentration below the hybrid interface must be about one order of magnitude higher than the Au concentration. Differences in the depth profiles between Cr and Au are therefore interpreted by assuming that the Tyr layer is much more affected by beam injected Cr atoms than by Au atoms.

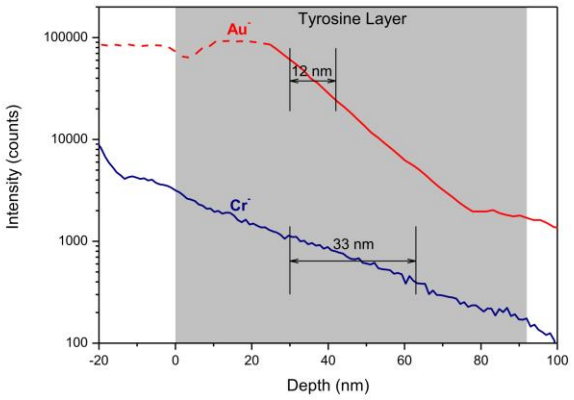

Fig. 4. Measurement of the decay length of metallic ions in the tyrosine layer, for bilayers Au or Cr/Tyr sputtered with 500 eV Cs^+ ions

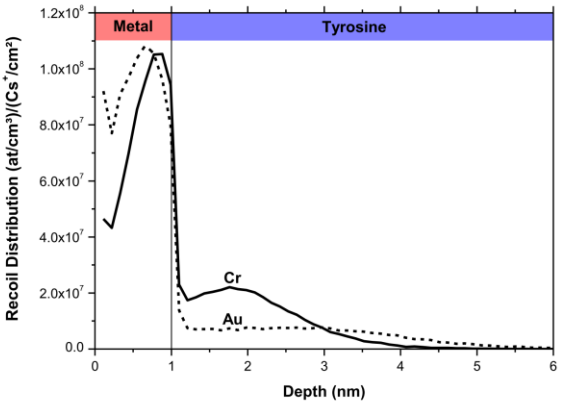

Fig. 5. SRIM simulation of the recoil distribution of Cr and Au for a 1 nm metal overlayer on tyrosine.

Sputtering yields.

Table 1 shows the differences in sputtering yields observed between Tyr and metals, depending on whether they are part of the one-layer, two-layer or the three-layer samples.

Sample	**Tyr S.Y (nm³/ion)**	**Au S.Y. (nm³/ion)**	**Cr S.Y (nm³/ion)**
Single layers	0.28	5.0×10^{-2}	1.6×10^{-2}
Bilayer Tyr/Au	0.31		
Bilayer Tyr/Cr	0.29		
Bilayer Au/Tyr	0.22		
Bilayer Cr/Tyr	0.089		
Trilayer Tyr/Au/Tyr 1st layer	0.25		
Trilayer Tyr/Au/Tyr 2nd layer	0.25		
Trilayer Tyr/Cr/Tyr 1st layer	0.27		
Trilayer Tyr/Cr/Tyr 2nd layer	0.082		

Table 1. Tyrosine, gold and chromium sputtering yields under a 500 eV Cs^+ sputtering.

4.3 DEPTH PROFILING OF HYBRID OLED STACKS – VALIDATION OF W-PCA AUTOMATED DATA TREATMENT

Organic materials, which are usually considered as insulators, can behave like semiconductors, or even like conductors if charges are injected, either by doping with selected ions (I, Br or Cl for example) or by application of an electrical potential difference across the material. The organic materials can consist of small organic molecules or intrinsically conductive polymers, such as phthalocyanine (p-type material) or perylene (n-type).[93] These polymers present delocalized electrons in conjugated π-orbitals that can have high mobility when the material is doped. The lowest unoccupied molecular orbital (LUMO) is equivalent to the conduction band in inorganic semiconductors, and the valence band is replaced by the highest occupied molecular orbital (HOMO). The many benefits provided by these so-called organic semiconductors i.e. reduced manufacturing costs, flexibility or tunable electrical properties (depending on the doping level and the voltage value), draw attention from scientists and industrials.

In most modern devices, these organic semiconductors are combined with inorganic oxides or metallic electrodes to form multilayers in the nanometer or micrometer range. Given the small dimensions, the behavior of the devices is governed by interface phenomena. Highlighting them is therefore critical to develop a clear understanding of how the devices can be improved.

The ability of low energy cesium to maintain a molecular signal with depth, with convenient sputter rates on both organics and inorganics, and therefore to depth profile efficiently model hybrid samples promotes the use of ToF-SIMS to study state-of-the-art optoelectronic devices, in order to understand the degradation mechanisms at the interfaces and improve their performances. A few successful analyses of applied samples were performed using low energy Cs: for example, degradation mechanisms were counteracted in perovskite solar cell [94–97] or surface modifications were detected and located in organic thin film transistors (OTFT)[98] and memory devices[99].

Light Emitting Devices (LEDs) have currently replaced most of the incandescent bulbs but they are also found in cell phone displays and for signal transmission through optical fibers. A LED is a p-n junction biased with an electrical potential (**Figure 13**). The electric field drives the charge carriers to the junction, where an electron can recombine with a hole, and release energy radiatively by the emission of a photon. Electrical energy is converted into light.

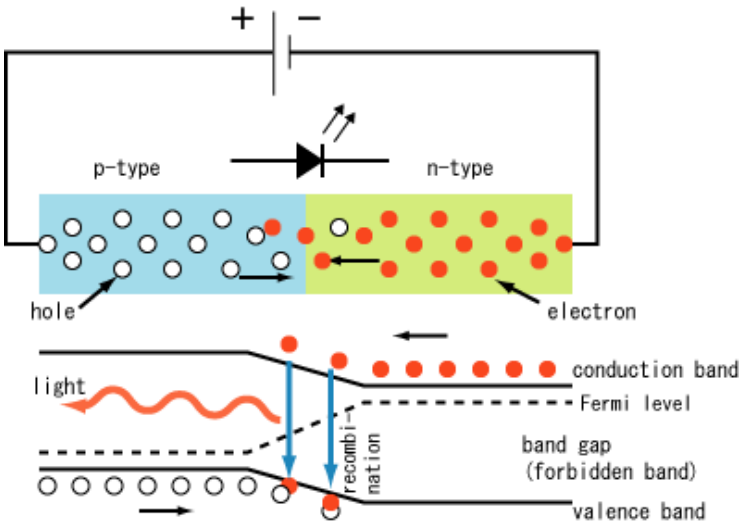

Figure 13 - Working principle of a LED. An electrical bias injects electrons in the conduction band of the n-type material while withdrawing them (thus injecting holes) from the valence band of the p-type material. A photon is emitted when charge carriers recombine at the junction.

[Source: https://en.wikipedia.org/wiki/Light-emitting_diode]

In organic-LEDs (OLEDs, **Figure 14**), the inorganic emissive layer is replaced by an organic semiconductor and is usually combined to a conductive layer in order to favor the charge injection and avoid charge recombination at the opposite electrode. These two layers are surrounded by the anode, (usually ITO, that is transparent and conductive), where electrons are withdrawn from the HOMO of the organic layer, and the cathode (in general aluminum or calcium), where electrons are injected into the LUMO.[100]

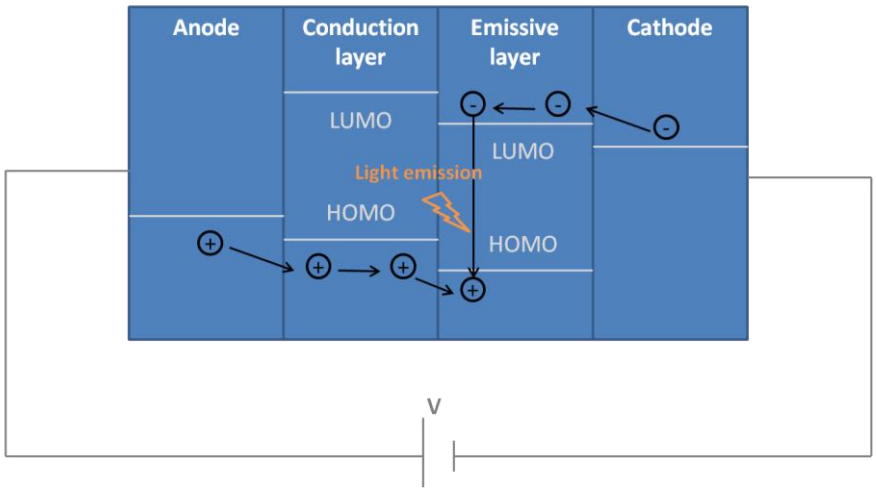

Figure 14 – Working principle of an OLED. Electrical power is converted into light through the recombination of hole-electron pairs in the emissive organic layer.

The paper below presents the study of rather complex OLED structures, as a first attempt to characterize applied full devices using ToF-SIMS. Therefore, we initiated a collaboration with Dr. Manuel Auer-Berger and Prof. Emil List-Kratochvil, who provided us with these samples. OLED stacks are composed of successive polymer layers (up to four layers) deposited on ITO and capped with an aluminum electrode. Molecular in-depth information can be obtained for each layer, either organic or inorganic. In addition, it appeared that those challenging OLED multilayers also presented an interest for our colleagues from the University of Catania (Italy), Prof. Nunzio Tuccitto and Prof. Antonino Licciardelllo, who developed a PCA-automated procedure to identify the interfaces depths and provide the characteristic peaks of each layer. More than validating the analysis feasibility, we evaluated the ability of this unsupervised procedure to provide a reliable characterization of hybrid multilayers. More details about PCA can be found above, in Section 2.4.

Assisted analysis of OLED hybrid stacks by ToF-SIMS depth profiling coupled with Wavelet-PCA

Céline Noël[1], Nunzio Tuccitto[2], Yan Busby[1*], Manuel Auer-Berger[3], Antonino Licciardello[2], Emil J. W. List-Kratochvil[4], and Laurent Houssiau[1]

(1) Laboratoire Interdisciplinaire de Spectroscopie Electronique, Namur Institute of Structured Matter, University of Namur, 61 Rue de Bruxelles, 5000 Namur, Belgium

(2) Department of Chemical Sciences and CSGI, University of Catania, Viale A. Doria 6, 95125, Catania, Italy

(3) Joanneum Research Materials, Institut für Oberflächentechnologien und Photonik, Franz-Pichler-Straße 30, Weiz 8160, Austria.

(4) Institut für Physik, Institut für Chemie & IRIS Adlershof, Humboldt-Universität zu Berlin, Brook-Taylor-Straße 6, 12489 Berlin, Germany

* Corresponding Author: yan.busby@unamur.be

Keywords: ToF-SIMS; Wavelet transform; PCA; Low-energy Cesium; interface analysis; OLEDs

Abstract

The investigation of interface effects in hybrid organic/inorganic electronic and photonic devices is a key step for improving their performance and operation stability. Depth profile analysis by time-of-flight secondary ion mass spectrometry (ToF-SIMS) is a consolidated tool for the molecular analysis and imaging of thin layers, however, the ion beam conditions need to be finely tuned in order to analyze hybrid stacks. In this work, low-energy (500 eV) Cs^+ ions beam is applied to depth profile two full (i.e. including electrodes) organic light-emitting diodes (OLED) stacks. Results show that characteristic molecular fragments are preserved in these conditions, however, the non-negligible molecular fragmentation results in the sensible increase of the mass spectra complexity. In order to simplify the dataset analysis, we have investigated the application of the wavelet principal component analysis (w-PCA) for data reduction and for assisting at least the first screening of such complex depth profiles.

1. Introduction

The advent of organic and hybrid electronics, ensuring for practical and cost-efficient processing on large scale, malleability, transparency, and tunable optical/electrical properties, has affected a growing number of applications. For light-emitting devices[1] (LEDs) and organic solar cells,[2] the integration of organic materials is mainly limited by their long-term stability and interface effects.

Organic light-emitting devices (OLEDs) are within the most complex stacks and can combine above 20 molecular layers for band engineering and improving the injection and radiative recombination of charge carriers.

The simplest OLED stack is comprised of the transparent anode, conventionally ITO, a low work function metal cathode, a hole injecting/transporting organic layer, an emission layer and an electron injecting/transporting layer, which are typically processed by vapor deposition, spin-coating or printing methods. During the device processing and operation, thin organic semiconducting layers can degrade and interface modifications may lead to device failure.[3]

In this framework, it is urgent to understand the degradation mechanisms to find effective strategies allowing increasing the device lifetime based on the rational design of improved materials combinations and device architectures.

Time-of-flight secondary ion mass spectrometry (ToF-SIMS) depth profiling is a powerful tool to characterize the in-depth molecular composition of interfaced materials stacks and it has been

already applied to OLED structures[4,5] to monitor interdiffusion, phase segregation and chemical reactions at the nanoscale. The main advantage of dual-beam ToF-SIMS depth profiling relies on its 3D molecular imaging capability, detection limit in the part-per-million range, mass resolution up to m/Δm~10000, extreme surface sensitivity (~1 nm sampling depth) and lateral resolution down to few hundred nanometers.

Alternated soft/hard materials, as for organic/inorganic stacks are particularly difficult to profile because of the different ion beam sputtering rates. Specifically, large argon clusters (Ar_n^+, with n>1000 atoms) are very efficient for profiling organic materials, but can hardly sputter metals and metal oxides unless the cluster energy is increased above 10-20 keV.[6,7] In these conditions, the fragmentation of large organic molecules can no longer be avoided.[8]

Recently, high energy C_{60} sputtering was applied to profile hybrid perovskite solar cells.[9]

Alternatively, nitric oxide-assisted C_{60} sputtering[10] or low-energy (200-1000 eV) cesium ion beam has been shown as a viable solution when looking for a versatile erosion beam, suitable for profiling organic[11], inorganic and hybrid materials stacks.[12–15] When using Cs^+ ion beam to profile hybrid stacks, a certain degree of fragmentation of large organic molecules cannot be avoided.[16,17]

For this reason, to safely separate ion beam induced modifications from intrinsic effects, one needs to design experiments based on comparative analyses.

Besides this, the increasing complexity of mass spectra due to fragmentation, chemical modifications, variable sputtering/ionization yields, matrix effects or mass overlaps, can sensibly increase the data analysis time required to identify characteristic molecular fragments from each layer. Practically, even when the nominal composition and thickness of the different layers are known, the operator still has to struggle to unambiguously identify the most relevant characteristic molecular fragments amongst the hundreds or thousands of peaks when acquiring high mass-resolution ToF-SIMS.[18]

For this reason, developing data reduction/treatment methods is highly desirable to open the way to "routine" analyses on complex hybrid stacks. In the literature, data manipulation methods such as gentle-SIMS (G-SIMS) have been proposed for simplifying mass spectra.[19,20]

Recently, a new automated data treatment procedure was proposed for features extraction from ToF-SIMS depth profiles called wavelet-PCA (w-PCA).[21–23]

This method is based on the application of the wavelet transform to the depth profile raw data for compression and noise removal. Data are then examined by a standard PCA multivariate analysis. The w-PCA output provides reconstructed depth-profiles (henceforth *pseudoprofiles*)

from the scores values of the most significant principal components (having the highest explained variance) and reconstructed *pseudospectra* by computing the inverse-wavelet transform of the loadings values. In such a way, reliable discrimination of the most statistically relevant peaks is obtained, based on the study of PCA loadings without any initial user-dependent interpretation of the original data. A steadfast identification of the different layers can be obtained by simply analyzing the scores plot.[21–23] It is worth noticing that the original mass resolution of the ToF-SIMS spectrum is preserved after the application of the w-PCA; this is usually not the case for the direct PCA data treatment method, for which the peak selection, mass data binning and integration processes would considerably reduce the mass resolution.

In this work, two full OLED structures are profiled using low-energy Cs^+ sputtering beam; the identification of characteristic peaks to be displayed in the final depth-profile is firstly derived "manually" and then by applying w-PCA assisted analysis for the fast identification of the number of layers, their composition, and some interface effects. The results show an excellent agreement between the manually selected high-intensity characteristic peaks and the most statistically relevant molecular fragments, of relatively high-mass (m/z>100 amu), highlighted from the w-PCA pseudospectra using only the first four principal components.

Overall, the w-PCA analysis is shown as a practical tool to guide the selection of molecular fragments and the identification of layers and the main interface degradation mechanisms, however, because of the intrinsic nature of the w-PCA approach, it has some limitations in highlighting more subtle interface effects or in presence of highly degraded layers for which a higher number of principal components must be considered.

2. Experimental

2.1 Processing of OLED structures

The two OLED structures considered in this work are displayed in **Figure 1**. The OLED B device was fabricated using the standard assembly: ITO/PEDOT:PSS/Poly-TPD:alpha-NPB (1:1)/BCPO:FIrpic (6 wt%)/TAZ (50 nm)/Ca/Al. ITO-covered glass substrates were first cleaned mechanically by acetone and isopropanol, afterward, the substrates were sonicated in toluene and isopropanol followed by a dry-cleaning step by oxygen plasma. The PEDOT:PSS layer was spin-coated on the ITO in ambient conditions and dried under dynamic vacuum according to the specifications, yielding to a 40 nm film. The hole transport layer (HTL) was prepared by spin coating Poly-TPD (Poly[N,N'-bis(4-butylphenyl)-N,N'-bisphenylbenzidine):alpha-NPB (N,N′-Di(1-naphthyl)-N,N′-diphenyl-(1,1′-biphenyl)-4,4′-

diamine) (1:1) from DCM at a concentration of 3 g/L. After spin-coating, the substrates were baked at 180 °C under high vacuum for 30 min to crosslink the polymer layer and prevent it from being washed off in the subsequent spin coating process of the emissive material layer (EML). The EML was made from a solution of BCPO (bis-4-(N-carbazolyl)phenyl)phenylphosphine oxide) acting as host molecules and 6 wt% Bis(3,5-difluoro-2-(2-pyridyl)phenyl-(2-carboxypyridyl)iridium(III) (FIrpic) acting as a blue-emitting dopant. Spin-coating parameters were chosen to yield a 50 nm thick layer from a 6 g/L DCM solution. After spin-coating, the substrates were baked at 110 °C under high vacuum for 30 min before they were transferred to an evaporation chamber, where 50 nm of (3-(Biphenyl-4-yl)-5-(4-tert-butylphenyl)-4-phenyl-4H-1,2,4-triazole) TAZ was deposited at a base pressure of 10^{-6} mbar. Ca (10 nm) and Al (100 nm) were deposited as cathode materials in an evaporation chamber under high vacuum (p $<10^{-6}$ mbar) through a shadow mask; thus defining multiple devices with a device area of 9 mm^2 on a single substrate. The OLED A device is a simplified version of OLED B, where the TAZ and Poly-TPD:alpha-NPB (1:1) layers are absent.

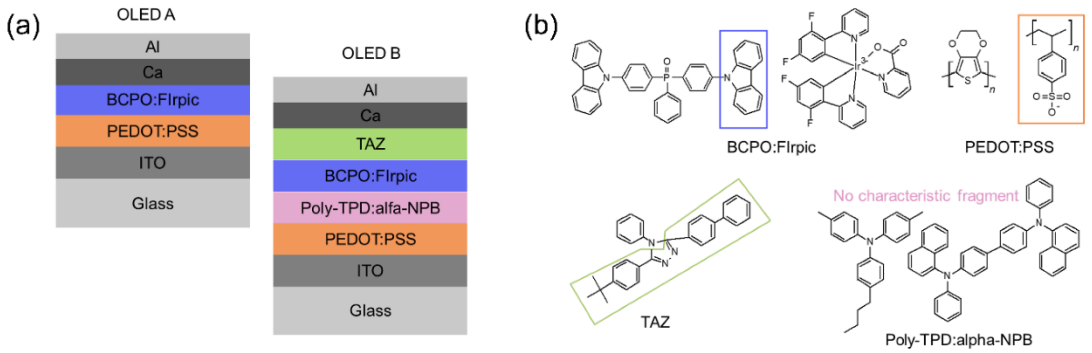

Figure 1. (a) Schematic view of the two OLEDs stacks. (b) Chemical structure of the respective organic molecules. The colored boxes indicate the characteristic molecular fragments that have been selected in the ToF-SIMS depth profile. No characteristic fragment could be identified from the poly-TPD-alpha-NPB layer.

2.2 ToF-SIMS analysis

ToF-SIMS depth profiles were acquired using a ToF-SIMS IV spectrometer from ION-TOF GmbH (Münster, Germany) in non-interlaced mode, alternating 1-frame analysis with Bi_3^+ (energy 25 keV at the ion current of ~0.3 pA, analysis area of 200×200 μm^2 and 10 s of sputtering with 500 eV Cs^+ at an ion current of ~30 nA, raster area of 500×500 μm^2) with a 1 s

pause between the cycles. When the erosion gun was on, the sample surface was flooded using a defocused low-energy electron beam in order to ensure fast surface charge compensation.

2.3 Wavelet-PCA data treatment

In a dual-beam ToF-SIMS profile, the full mass spectrum from the sputtered crater surface is obtained at each analytical scan. The ION-TOF instrument used in this work collects the mass spectrum by splitting the time-of-flight into 50 ps intervals (channels) and storing the counts per channel in a raw data file with a proprietary format that can be exported to a readable format file. The procedure is implemented by a script programmed in Python (a registered trademark of the Python Software Foundation). We applied the PyWavelet library to perform the wavelet transformation (www.pybytes.com/pywavelets) and Scikit-learn, a machine learning Python-based library (http://scikit- learn.org) for the PCA of the ToF- SIMS spectra. The dataset matrix was created by compressing the whole spectrum at each scan. The wavelet transform analysis uses a mother wavelet function with variable scale. Sharp wavelets are used to approximate the narrow features, whereas wider wavelets are used for fitting the larger trends of the signal. The mother wavelet is moved along the signal direction, and it is stretched or compressed until the best depiction of the signal is found. Numerous wavelet mother functions and several compression levels were previously investigated for the proper compression of ToF-SIMS spectra using several parameters to estimate the filtering quality.[23] In this study, we selected the *Coiflets 5* mother function and compression *level 4* to ensure the most accurate filtering quality based on the root mean square error (RMSE), signal-to-noise ratio (S/N) and the peak area change. More details about the procedure are reported elsewhere.[22] The compressed spectra, acquired at each analytical scan, represent the objects of the matrix, while the variables are the wavelet compression coefficients. Before the multivariate analysis, the compressed dataset was mean centered to ensure that the differences in the scores were due to variation around the mean value and not to the variance of the mean values. Afterward, the score values of the most important principal components (PC) are reported in plots (pseudoprofiles) as a function of the sputtering cycle (i.e. of the depth). In these pseudoprofiles, interfaces can simply be identified at the depths where at least one of the PC scores inverts its sign. In this way, each layer can be practically identified by its unique "vector" given by the ordered sequence of signs of the PC scores (PC1, PC2, etc). In the present work, the selection of 4 PCs, explaining 70% of the variance, proved to be sufficient for grasping, even in an unsupervised way, the main features of the investigated hybrid structure, while finer features require a higher value of explained variance. The pseudospectrum from each layer is then computed by applying the inverse

wavelet transform on the loadings values of each PC. For the sake of simplicity, in this paper, we present only the cumulative pseudospectrum for each layer, which has been computed by summing up the absolute values of the loadings from the four characteristic spectra associated to each layer.

3. Results and discussion

3.1 Manual identification of the OLED depth profile characteristic peaks.

The two OLED stacks shown in Figure 1 are profiled in a few hours with low-energy (500 eV) Cs^+ sputtering beam without any sample preparation. This represents a simplification with respect to previous works on hybrid stacks, where the metallic electrode had to be removed mechanically prior to the depth-profile analysis with cluster ion beams,[24] or where FIB and ToF-SIMS were combined,[25]or where the co-sputtering with Ar^+ and C_{60}^+ was necessary to ensure convenient erosion rates.[26] Indeed, with low-energy Cs^+, the interplay between chemical and mechanical sputtering ensures convenient sputtering rates on both soft and hard materials. Interestingly, layer and interfaces are successfully characterized by at least one characteristic fragment ion (at relatively high-mass) and the layers degradation could be identified and discussed. Synthetically, Figure 2 shows that both OLED structures are profiled and that well-defined interfaces are obtained, with two exceptions. The first involves the degradation of about half of the PEDOT:PSS layer by indium-related species diffusing from the underlying ITO electrode. The strong mobility of indium ions across organic and inorganic interfaces (reaching ~1 atomic % at the device surface) was previously evidenced by ToF-SIMS and XPS depth profiles on resistive switching devices.[27] Here, 2D reconstructions show a diffuse and homogeneous In diffusion through the PEDOT:PSS layer.

The second is the absence of a distinguishable interface between the poly-TPD:α-NPB polymer and the BCPO:FIrpic layer. This effect is explained by the possible intermixing of thin layers or by the induced degradation due to the sputtering ion beam. Indeed, no characteristic fragment could be pinpointed from the Poly-TPD:alphaNPB layer. While the relative intensities of aromatic-based molecular signals slightly change (possibly relying on the addition of signals from large C_n^- clusters), however, the similarities between Poly-TPD:alpha-NPB and BCPO hinder their discrimination by ToF-SIMS when using low-energy Cs^+ sputtering.

Besides, in OLED A, the resulting CaO^- signal is weak and diffuses into the neighboring layers, suggesting that the calcium layer was degraded in this device. We ascribe this to the rather long

atmosphere and humidity exposure (months) of the sample which may have led to partial degradation of the layer and the diffusion of Ca species.

A well-known difficulty in analyzing ToF-SIMS depth profiles is to deal with mass overlaps and matrix effects, which can sensibly influence molecular ionization yields.

For example, the increase of Al-related fragments signals (Al_2^- and $Al_2O_3^-$) is observed at the interface with the high oxygen-containing ITO matrix (and similarly for $In_3O_3^-$). The $C_8H_7SO_3^-$ signals in the B-doped SiO_2 and silica-related signals (see the $Si_3O_7^-$ profile in Figure 2), interfere with strong organic fragments from the PEDOT:PSS, due to an insufficient mass resolution.

In OLED A, the Al electrode seems thinner than in OLED B (despite the same nominal thickness); this is mainly ascribed to the lower Cs^+ current during the profile, however, it may also result from defects in the underlying Ca layer which resulted in a lower sticking coefficient of Al during the electrode deposition. In OLED B, the persisting Al signal (homogeneous on the analysis area) is ascribed to the diffusion of small Al particles in the underlying Ca layer whose signal may persist because of the lower erosion rate as compared to the underlying organic layers.

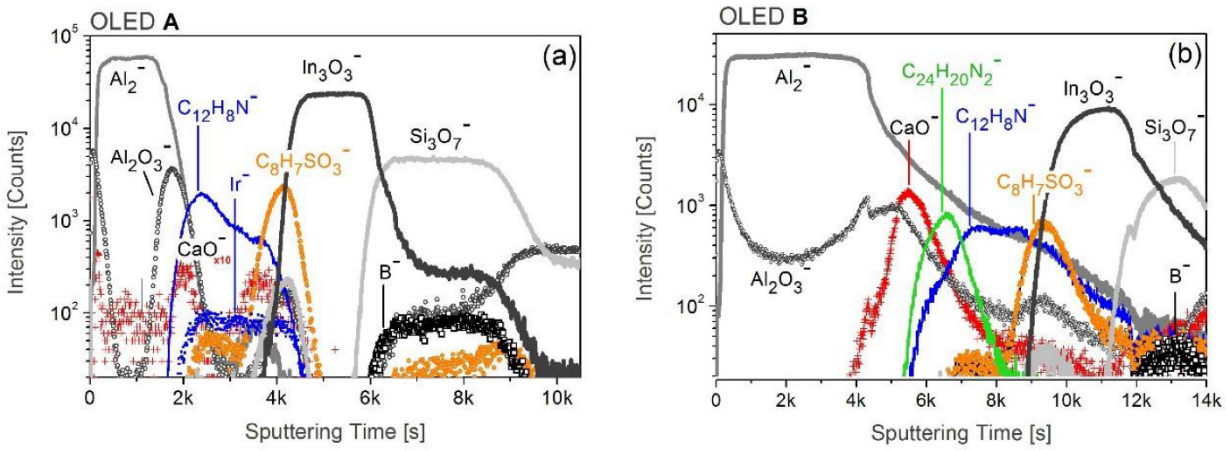

Figure 2. Selected molecular depth profiles obtained on OLED A (a) and OLED B (b). The characteristic molecular ions are schematically shown in Figure 1.

3.2 w-PCA assisted data treatment of depth profiles

OLED A

Subsequently, the same raw data files are examined with the w-PCA in order to compare this automated treatment with the previous manual procedure. The w-PCA data treatment allows obtaining a reliable identification of the most statistically-relevant mass peaks from each layer, without any mass data binning, peak finding and integration or any operator-dependent interpretation of the original dataset.

Each selected peak should fulfill the following guidelines: (i) it should appear in the corresponding pseudospectrum with a high loading; (ii) it must have a convenient intensity in the original spectrum (i.e. it should be intense enough for allowing the reconstruction of clear cross-sections or z-integrated XY images, but must not be affected by detector saturation as for the most intense signals); (iii) it should have no substantial mass overlap.

The application of the above criteria has led to the selection of identical characteristic mass fragments than the profiles displayed in Figure 2.

The scores plot obtained for the OLED A depth profile, showing the four first PC scores values (PC1-4) as a function of the number of sputtering cycles (10 s erosion with 500 eV Cs^+), is reported in **Figure 3**. This procedure allows identifying five out of the six layers that were expected in OLED A and the "splitting" of layer 3 due to indium contamination.

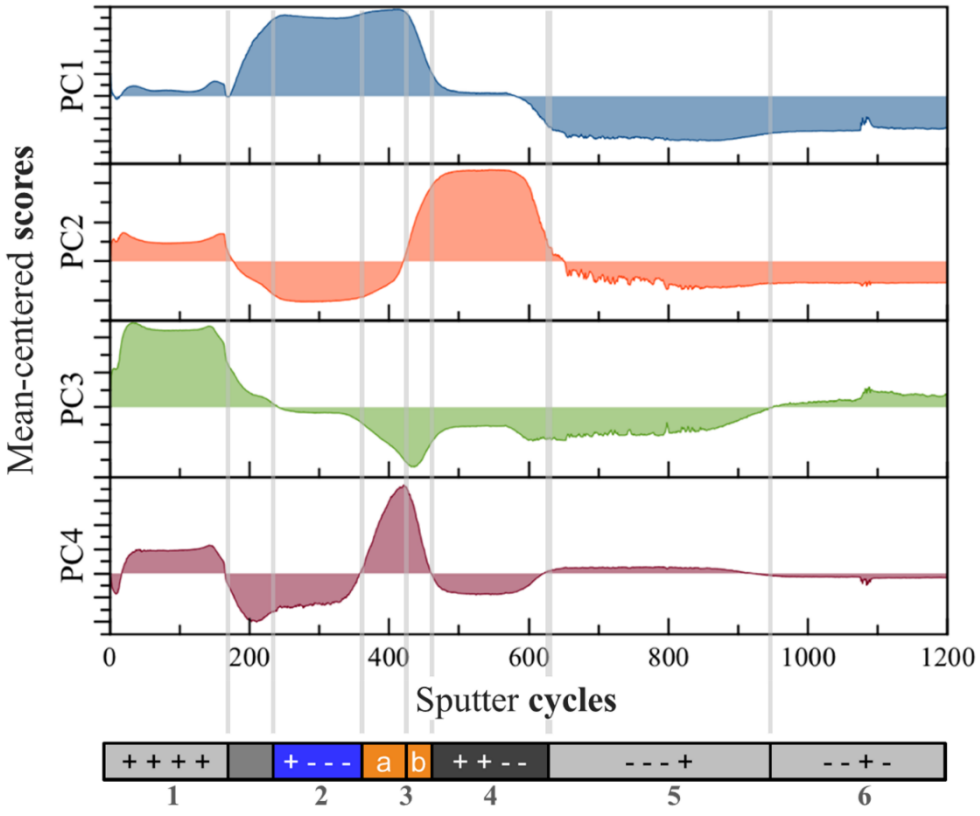

Figure 3. w-PCA pseudoprofile from OLED A. The scores plots derived from PC1-4 allow distinguishing five (out of six) layers and their pseudospectra can be successively generated. The vertical dashed lines indicate the location of interfaces as marked by the score sign inversion in at least one PC.

The mean-centered scores dataset allows discriminating the different layers, namely, the change in the score sign marks the transition between layers with different compositions. From the loadings plot, one can then directly reconstruct the most probable mass pattern from the specific portion of the depth profile. In particular, the uppermost layer (layer 1) is characterized by all positive PC scores signs ([PC1, PC2, PC3, PC4] = [+,+,+,+]). As described in section 2, the pseudospectrum associated to the first layer is generated from the loading values of each PC by selecting all variables (m/z) having positive loadings in all first 4 PCs. As shown in **Figure 4**, the procedure unambiguously indicates that layer 1 corresponds to the aluminum electrode, as indicated by the sequence of Al_n^- clusters and the weaker AlO_x-related peaks. The generated pseudospectra cannot be directly compared to the experimental spectrum from the layer (reconstructed by integrating over the specific sputtering time interval) because the peak intensities are affected by the probability of a peak to belong to this specific layer.
Similarly, layer 2 is identified by the scores vector [+,-,-,-] associated with the pseudospectrum shown in **Figure 5.** Layer 2 is clearly an organic layer; in particular, by looking at high-mass peaks, peaks at m/z=166 m/z=193 were selected and ascribed to the characteristic fragments $C_{12}H_8N^-$ and Ir^-, which identify the BCPO and FIrpic molecules.

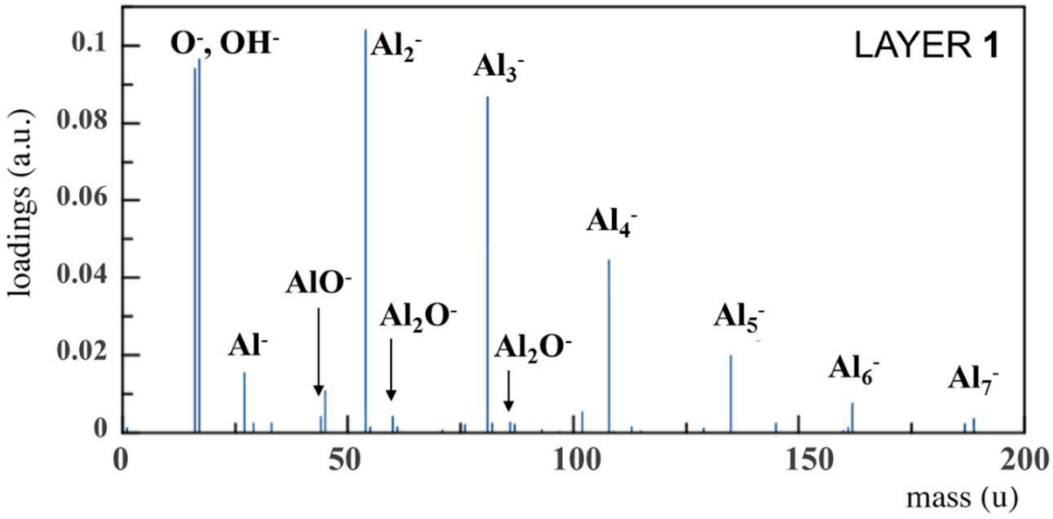

Figure 4. Pseudospectrum of layer 1 generated from [+,+,+,+] PC scores.

It is worth noticing that matrix effects, interface roughness and interdiffusion may result in a complex (non-linear) variation of the ToF-SIMS peaks intensities at the interfaces; since the PCA is based on the linear combination of the PC scores, so, without an implementation of the analysis, this intrinsically limits the accuracy in identifying the exact interface position.

Based on the stack structure, below the aluminum layer we would expect the calcium one; however due to the previously discussed degradation and therefore, the lack of well-defined interfaces, the number of PCs has to be increased up to PC8 to identify this diffused layer straddling between the aluminum and BCPO:FIrpic layers (see Supporting Information **Figure S11**).

The pseudospectrum of layer 3a (PEDOT:PSS, **Figure 5**) is identified by the scores vector [+,-,-,+] showing high-intensity peaks at m/z=183 (characteristic from PSS, $C_8H_7SO_3^-$) and at m/z=80 (characteristic from PEDOT, C_4S^-). Here, the indium contamination of the layer is evidenced by the different scores values of the layer 3a ([+,-,-,+]) and 3b ([+,+,-,+]). Following to layer 4 (ITO layer, **Figure S1a** in Supporting Information), the generated pseudospectrum features the high-intensity and high-mass signal at m/z=393 ascribed to $In_3O_3^-$ fragment.

Layer 5 (scores vector [-,-,-,+]) corresponds to the boron-implanted SiO_x overlayer and was identified by the signal at m/z=11 ascribed to $^{11}B^-$ (**Figure S1b**).

Finally, the glass substrate (layer 6) was identified by the mass peak at m/z=196 ascribed to the $Si_3O_7^-$ fragment (see **Figure S1c** in Supporting Information).

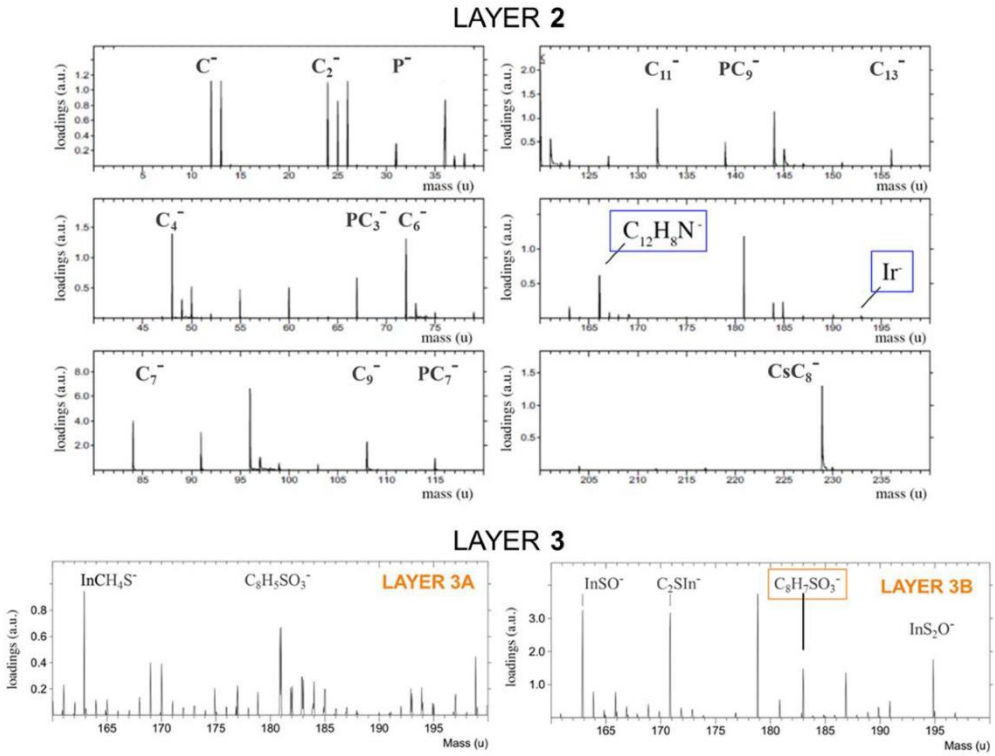

Figure 5. Pseudospectra of layer 2 (BCPO:FIrpic) from m/z 0 to 235 u, layer 3A (PEDOT:PSS) from m/z 160 to 200 u and layer 3B corresponding to the indium contaminated PEDOT:PSS interface.

Concerning the procedure, it is worth noticing that the discrimination between adjacent peaks characterized by a marked tail overlap can be considerably simplified using pseudospectra. For example, the Ir^- signal at m/z 193 could be distinguished from the background signal and correctly assigned to layer 2 despite its very low intensity (the depth-integrated peak intensity is only ~1000 counts) and the overlap with the tail of the SiO_2Cs^- peak appearing when the profile reaches the glass substrate. This allows evidencing the presence of the photoactive Iridium complex in the BCPO layer.

OLED B

The identical procedure was applied to the OLED B profile. The w-PCA scores plot, showing the mean-centered four first PC values along the depth profile, is shown in **Figure 6**. Interestingly, thanks to the presence of well-defined interfaces the linear combinations of the four first scores signs are sufficient to identify all the different layers in this complex stack,

except for Poly-TPD, for which no fragment could be identified even using a higher number of PCs. The inversion of the score sign of PC5 at ~7700 s sputtering time (**Figure S9**) suggests the presence of an interface, however, nor the analysis of the loadings in the wavelet-PCA nor the profile of the weak Ir- signal could unambiguously help identify the Poly-TPD:alphaNPB layer.

As for OLED A, we generate the characteristic mass pseudospectra from each identified layer (**Figure S2-S8** in Supporting Information). Remarkably, high-mass and high-loading characteristic molecular fragments could be identified in the pseudospectra from each layer. For layer 1A and 1B, corresponding to the Al electrode with an oxidation layer on the top, we selected the peak at m/z=54, corresponding to the Al_2^- peak.

In the OLED B profile, the calcium layer is clearly identified by the peak at m/z=56, corresponding to the CaO^- fragment. For layer 3 ([-,-,-,+], TAZ) the high mass peak at m/z=336 is selected and associated with the $C_{24}H_{20}N_2^-$ fragment.

For layer 4 ([+,-,-,-], BCPO:FIrpic) the peak at m/z=166, corresponding to the $C_{12}H_8N^-$ fragment is selected (the Ir- signal could not be selected because of a strong mass overlap).

For layer 5 ([+,+,+,+], PEDOT:PSS) the peak at m/z=183, corresponding to the $C_8H_7SO_3^-$ fragment and finally for layer 6 (ITO) and layer 7 (glass substrate) we have selected the same fragments as for OLED A.

Interestingly, the PEDOT:PSS layer does not result in a sharp interface in the score plots from neither OLED A (layer 3 in Figure 3) nor OLED B (layer 5 in Figure 6). The PC scores of the PEDOT:PSS layer feature a relatively smooth rise and fall profile which could be explained either by high interface roughness, defects (i.e. holes) or by the presence of a composition gradient made by the diffusion of indium species. Recently, depth profile analysis has shown that the diffusion of indium oxide species from the ITO could degrade the PEDOT:PSS layer.[28–30] Based on the low roughness of the ITO, as evidenced by the abrupt profile of the $In_3O_3^-$ fragment along the YZ cross section reconstruction (see **Figure S10)**, we ascribe the broad PEDOT:PSS profile to its partial degradation by indium species rather than ion beam induced roughening or other profile-related artifacts.

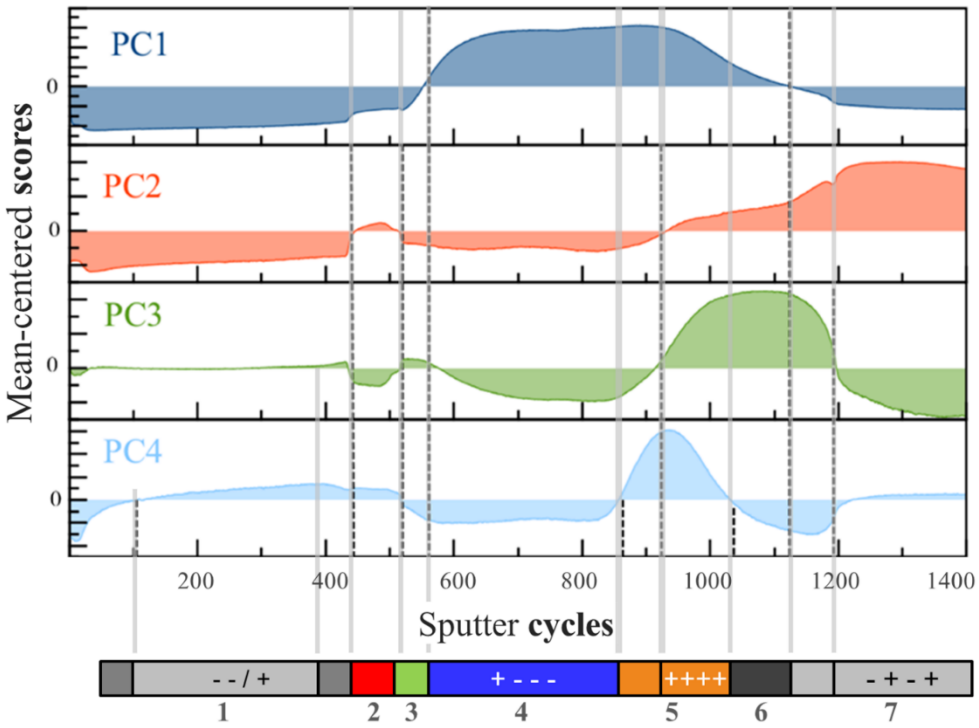

Figure 6. Scores plot from the four first principal components (PC1-4) values obtained for the OLED B (Al/ Ca/ TAZ/ BCPO:Firpic/ PEDOT:PSS/ Boron implanted SiO_2/SiO_2) profile. The vertical dashed lines indicate the approximate location of the interfaces resulting from the criterion of score sign inversion in at least one of the PCs.

4. Summary

In conclusion, two OLEDs stacks have been profiled using low-energy (500 eV) Cs^+ sputtering beam and the depth profiles datasets are analyzed manually and by the w-PCA assisted procedure. The capability of low-energy monatomic Cs^+ to preserve characteristic molecular signals is demonstrated, with the advantage of having convenient (and similar) erosion rates on soft (organic) and hard (inorganic) materials. Despite this, a certain complexity is associated with the manual identification of the most relevant ions to characterize layers and interface or degradation effects because of the presence of ion beam induced fragmentation of organic molecules, matrix effects, and mass overlaps. To mitigate this complexity and assist and speed up the analysis process, we applied w-PCA data treatment. This processing is useful to extract key information to save time and avoid missing characteristic fragments or interface effects

during the complex data analysis of such OLED structures.

The w-PCA has shown real potential in the prescreening of such a complex dataset and for guiding the selection of the most representative and meaningful characteristic peaks, including those "hidden" behind mass overlaps, useful for the reconstruction of the "standard" depth profiles or 3D images. Compared to the bare PCA, the w-PCA approach allows avoiding some preliminary time-consuming tasks such as peak finding, integration, and mass binning. Moreover, results show that a few PC scores (4 in our examples) have to be considered to identify the main layers in such challenging profiles. The demonstrated approach is successful in evidencing interface effects such as layers degradation, diffusion of species and intermixing, which could be of critical interest for guiding the rational selection of improved materials or processing conditions for achieving long-term stability.

On the other hand, it is nonetheless important to precise that the operator has to carefully look to higher PCs scores to identify shallow layers (resulting from degradation or intermixing effects). The totally unsupervised analysis of unknown samples is not realistic in these conditions, making the benefit brought by the automated procedure less distinct.

Despite this active role of the operator, the coupling of ToF-SIMS depth profiling with low-energy Cs^+ and w-PCA data treatment results in a practical methodology to investigate complex hybrid organic/inorganic electronic and photonic devices.

Acknowledgments

This research used resources of the "Synthesis, Irradiation and Analysis of Materials" (SIAM) platform of the University of Namur. NT and AL wish to acknowledge the support from the University of Catania through the "Piano della Ricerca di Ateneo 2016-2018". The authors declare no competing financial interest.

References

(1) Thejokalyani, N.; Dhoble, S. J. Novel Approaches for Energy Efficient Solid State Lighting by RGB Organic Light Emitting Diodes – A Review. *Renew. Sustain. Energy Rev.* **2014**, *32*, 448–467. https://doi.org/10.1016/j.rser.2014.01.013.

(2) Hou, J.; Inganäs, O.; Friend, R. H.; Gao, F. Organic Solar Cells Based on Non-Fullerene Acceptors. *Nat. Mater.* **2018**, *17* (2), 119–128. https://doi.org/10.1038/nmat5063.

(3) Scholz, S.; Kondakov, D.; Lüssem, B.; Leo, K. Degradation Mechanisms and Reactions in Organic Light-Emitting Devices. *Chem. Rev.* **2015**, *115* (16), 8449–8503. https://doi.org/10.1021/cr400704v.

(4) Yu, B.-Y.; Lin, W.-C.; Wang, W.-B.; Iida, S.; Chen, S.-Z.; Liu, C.-Y.; Kuo, C.-H.; Lee, S.-H.; Kao, W.-L.; Yen, G.-J.; et al. Effect of Fabrication Parameters on Three-Dimensional Nanostructures of Bulk Heterojunctions Imaged by High-Resolution Scanning ToF-SIMS. *ACS Nano* **2010**, *4* (2), 833–840. https://doi.org/10.1021/nn9014449.

(5) Höfle, S.; Bernhard, C.; Bruns, M.; Kübel, C.; Scherer, T.; Lemmer, U.; Colsmann, A. Charge Generation Layers for Solution-Processed Tandem Organic Light Emitting Diodes with Regular Device Architecture. *ACS Appl. Mater. Interfaces* **2015**, *7* (15), 8132–8137. https://doi.org/10.1021/acsami.5b00883.

(6) Yang, L.; Seah, M. P.; Gilmore, I. S. Sputtering Yields for Gold Using Argon Gas Cluster Ion Beams. *J. Phys. Chem. C* **2012**, *116* (44), 23735–23741. https://doi.org/10.1021/jp307203f.

(7) Noël, C.; Pescetelli, S.; Agresti, A.; Franquet, A.; Spampinato, V.; Felten, A.; di Carlo, A.; Houssiau, L.; Busby, Y. Hybrid Perovskites Depth Profiling with Variable-Size Argon Clusters and Monatomic Ions Beams. *Materials* **2019**, *12* (5), 726. https://doi.org/10.3390/ma12050726.

(8) Moritani, K.; Mukai, G.; Hashinokuchi, M.; Mochiji, K. Energy-Dependent Fragmentation of Polystyrene Molecule Using Size-Selected Ar Gas Cluster Ion Beam Projectile. *Surf. Interface Anal.* **2011**, *43* (1–2), 241–244. https://doi.org/10.1002/sia.3551.

(9) Lin, W. C.; Kovalsky, A.; Wang, Y. C.; Wang, L. L.; Goldberg, S.; Kao, W. L.; Wu, C. Y.; Chang, H. Y.; Shyue, J. J.; Burda, C. Interpenetration of CH3NH3PbI3 and TiO2 Improves Perovskite Solar Cells While TiO2 Expansion Leads to Degradation. *Phys. Chem. Chem. Phys.* **2017**, *19*, 21407–21413. https://doi.org/10.1039/c7cp03116e.

(10) Havelund, R.; Licciardello, A.; Bailey, J.; Tuccitto, N.; Sapuppo, D.; Gilmore, I. S.; Sharp, J. S.; Lee, J. L. S.; Mouhib, T.; Delcorte, A. Improving Secondary Ion Mass Spectrometry C_{60}^{n+} Sputter Depth Profiling of Challenging Polymers with Nitric Oxide Gas Dosing. *Anal. Chem.* **2013**, *85* (10), 5064–5070. https://doi.org/10.1021/ac4003535.

(11) Brison, J.; Mine, N.; Wehbe, N.; Gillon, X.; Tabarrant, T.; Sporken, R.; Houssiau, L. Molecular Depth Profiling of Model Biological Films Using Low Energy Monoatomic Ions. *Int. J. Mass Spectrom.* **2012**, *321–322*, 1–7. https://doi.org/10.1016/j.ijms.2012.04.001.

(12) Matteocci, F.; Busby, Y.; Pireaux, J.-J.; Divitini, G.; Cacovich, S.; Ducati, C.; Di Carlo, A. Interface and Composition Analysis on Perovskite Solar Cells. *ACS Appl. Mater. Interfaces* **2015**, *7* (47), 26176–26183. https://doi.org/10.1021/acsami.5b08038.

(13) Palma, A. L.; Cinà, L.; Busby, Y.; Marsella, A.; Agresti, A.; Pescetelli, S.; Pireaux, J.-J.; Di Carlo, A. Mesoscopic Perovskite Light-Emitting Diodes. *ACS Appl. Mater. Interfaces* **2016**, *8* (40), 26989–26997. https://doi.org/10.1021/acsami.6b07750.

(14) Noël, C.; Houssiau, L. Hybrid Organic/Inorganic Materials Depth Profiling Using Low Energy Cesium Ions. *J. Am. Soc. Mass Spectrom.* **2016**, *27* (5), 908–916. https://doi.org/10.1007/s13361-016-1353-9.

(15) Tortora, L.; Urbini, M.; Fabbri, A.; Branchini, P.; Mariucci, L.; Rapisarda, M.; Barra, M.; Chiarella, F.; Cassinese, A.; Di Capua, F.; et al. Three-Dimensional Characterization of OTFT on Modified Hydrophobic Flexible Polymeric Substrate by Low Energy Cs + Ion Sputtering. *Appl. Surf. Sci.* **2018**, *448*, 628–635. https://doi.org/10.1016/j.apsusc.2018.04.097.

(16) Houssiau, L.; Mine, N. Molecular Depth Profiling with Reactive Ions, or Why Chemistry Matters in Sputtering. *Surf. Interface Anal.* **2011**, *43* (1–2), 146–150. https://doi.org/10.1002/sia.3528.

(17) Terlier, T.; Zappalà, G.; Marie, C.; Leonard, D.; Barnes, J.-P.; Licciardello, A. ToF-SIMS Depth Profiling of PS- *b* -PMMA Block Copolymers Using Ar_n^+, C_{60}^{++}, and Cs^+ Sputtering Ions. *Anal. Chem.* **2017**, *89* (13), 6984–6991. https://doi.org/10.1021/acs.analchem.7b00279.

(18) Passarelli, M. K.; Pirkl, A.; Moellers, R.; Grinfeld, D.; Kollmer, F.; Havelund, R.; Newman, C. F.; Marshall, P. S.; Arlinghaus, H.; Alexander, M. R.; et al. The 3D OrbiSIMS—Label-Free Metabolic Imaging with Subcellular Lateral Resolution and High Mass-Resolving Power. *Nat. Methods* **2017**, *14* (12), 1175–1183. https://doi.org/10.1038/nmeth.4504.

(19) Gilmore, I. S.; Seah, M. G-SIMS of Crystallisable Organics. *Appl. Surf. Sci.* **2003**, *203–204*, 551–555. https://doi.org/10.1016/S0169-4332(02)00757-2.

(20) Gilmore, I. S.; Seah, M. . Static SIMS: Towards Unfragmented Mass Spectra — the G-SIMS Procedure. *Appl. Surf. Sci.* **2000**, *161* (3–4), 465–480. https://doi.org/10.1016/S0169-4332(00)00317-2.

(21) Tuccitto, N. Automated Data Mining of Secondary Ion Mass Spectrometry Spectra: W-PCA of ToF-SIMS Spectra. *J. Chemom.* **2017**, e2968. https://doi.org/10.1002/cem.2968.
(22) Tuccitto, N.; Zappalà, G.; Vitale, S.; Torrisi, A.; Licciardello, A. A Wavelet-PCA Method Saves High Mass Resolution Information in Data Treatment of SIMS Molecular Depth Profiles: Wavelet-PCA Data Treatment of Molecular Depth Profiles. *Surf. Interface Anal.* **2016**, *48* (6), 317–327. https://doi.org/10.1002/sia.5943.
(23) Cristaudo, V.; Collette, S.; Tuccitto, N.; Poleunis, C.; Melchiorre, L. C.; Licciardello, A.; Reniers, F.; Delcorte, A. Molecular Surface Analysis and Depth-Profiling of Polyethylene Modified by an Atmospheric Ar-D_2O Post-Discharge. *Plasma Process. Polym.* **2016**, *13* (11), 1106–1119. https://doi.org/10.1002/ppap.201600061.
(24) Niehuis, E. Depth Profiling in Organic Electronics. In *ToF-SIMS: Materials Analysis by Mass Spectrometry*; IM Publications, 2013; pp 637–660.
(25) Iida, S.; Carr, D. M.; Fisher, G. L.; Miyayama, T. Accurate and Reproducible In-Depth Observation of Organic-Inorganic Hybrid Materials Using FIB-TOF-SIMS. *J. Vac. Sci. Technol. B Nanotechnol. Microelectron. Mater. Process. Meas. Phenom.* **2018**, *36* (3), 03F107. https://doi.org/10.1116/1.5013670.
(26) Yu, B.-Y.; Chen, Y.-Y.; Wang, W.-B.; Hsu, M.-F.; Tsai, S.-P.; Lin, W.-C.; Lin, Y.-C.; Jou, J.-H.; Chu, C.-W.; Shyue, J.-J. Depth Profiling of Organic Films with X-Ray Photoelectron Spectroscopy Using C_{60}^+ and Ar^+ Co-Sputtering. *Anal. Chem.* **2008**, *80* (9), 3412–3415. https://doi.org/10.1021/ac702626n.
(27) Busby, Y.; Nau, S.; Sax, S.; List-Kratochvil, E. J. W.; Novak, J.; Banerjee, R.; Schreiber, F.; Pireaux, J.-J. Direct Observation of Conductive Filament Formation in Alq3 Based Organic Resistive Memories. *J. Appl. Phys.* **2015**, *118* (7), 075501. https://doi.org/10.1063/1.4928622.
(28) Wong, K. W.; Yip, H. L.; Luo, Y.; Wong, K. Y.; Lau, W. M.; Low, K. H.; Chow, H. F.; Gao, Z. Q.; Yeung, W. L.; Chang, C. C. Blocking Reactions between Indium-Tin-Oxide and Poly (3,4-Ethylene Dioxythiophene):Poly(Styrene Sulphonate) with a Self-Assembly Monolayer. *Appl. Phys. Lett.* **2002**, *80* (15), 2788–2790. https://doi.org/10.1063/1.1469220.
(29) de Jong, M. P.; van IJzendoorn, L. J.; de Voigt, M. J. A. Stability of the Interface between Indium-Tin-Oxide and Poly(3,4-Ethylenedioxythiophene)/Poly(Styrenesulfonate) in Polymer Light-Emitting Diodes. *Appl. Phys. Lett.* **2000**, *77* (14), 2255–2257. https://doi.org/10.1063/1.1315344.
(30) Mouhib, T.; Poleunis, C.; Wehbe, N.; Michels, J. J.; Galagan, Y.; Houssiau, L.; Bertrand, P.; Delcorte, A. Molecular Depth Profiling of Organic Photovoltaic Heterojunction Layers by ToF-SIMS: Comparative Evaluation of Three Sputtering Beams. *Analyst* **2013**, *138* (22), 6801–6810.

SUPPORTING INFORMATION

Assisted Analysis of OLED Hybrid Stacks by ToF-SIMS Depth Profiling Coupled with Wavelet-PCA

Céline Noël[1], Nunzio Tuccitto[2], Yan Busby[1*], Manuel Auer[3], Antonino Licciardello[2], Emil J. W. List-Kratochvil[4] and Laurent Houssiau[1]

(1) Laboratoire Interdisciplinaire de Spectroscopie Electronique, Namur Institute of Structured Matter, University of Namur, 61 Rue de Bruxelles, 5000 Namur, Belgium

(2) Department of Chemical Sciences and CSGI, University of Catania, viale A. Doria 6, 95125, Catania, Italy

(3) Joanneum Research Materials, Institut für Oberflächentechnologien und Photonik, Franz-Pichler-Straße 30, Weiz 8160, Austria.

(4) Institut für Physik, Institut für Chemie & IRIS Adlershof, Humboldt-Universität zu Berlin, Brook-Taylor-Straße 6, 12489 Berlin, Germany

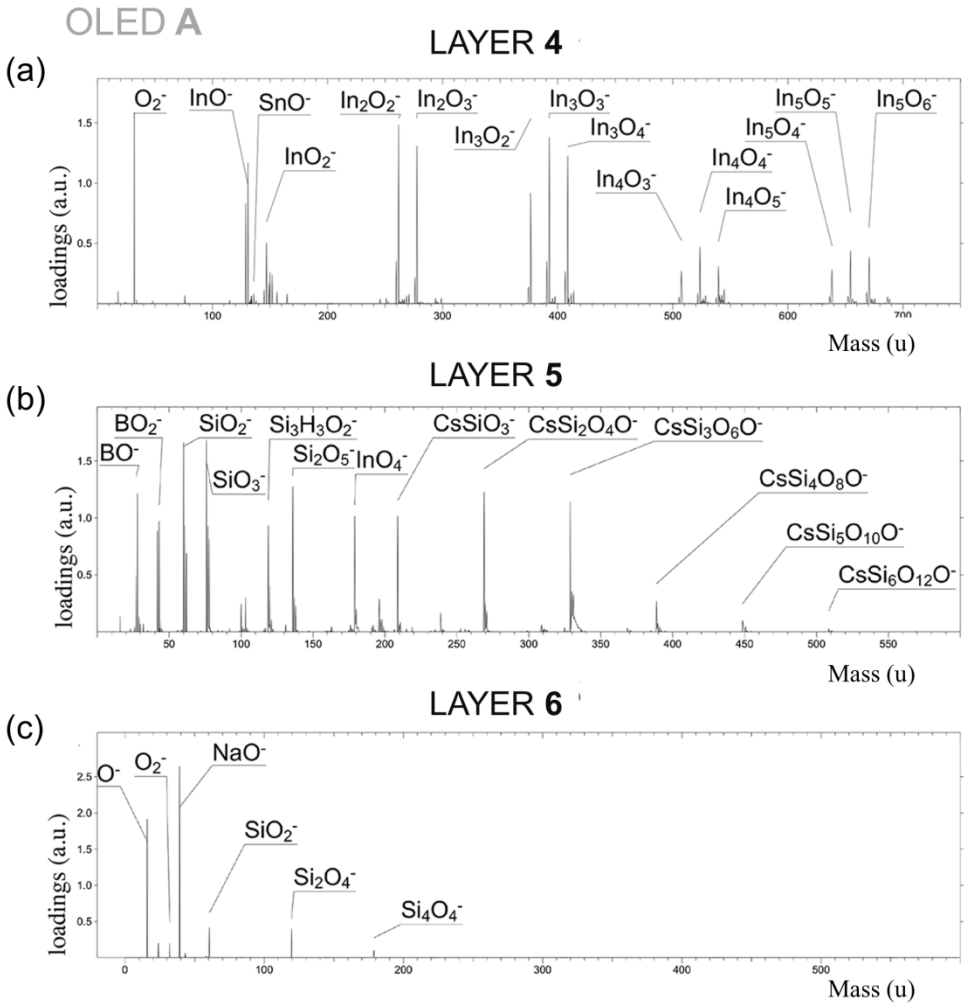

Figure S1. Pseudospectrum reconstruction of the ToF-SIMS profile on OLED A: (a) layer 4 (ITO) from m/z 0 to 750 u; (b) layer 5 (boron-implanted glass) from m/z 0 to 600 u; (c) layer 6 (glass substrate) from m/z 0 to 600 u.

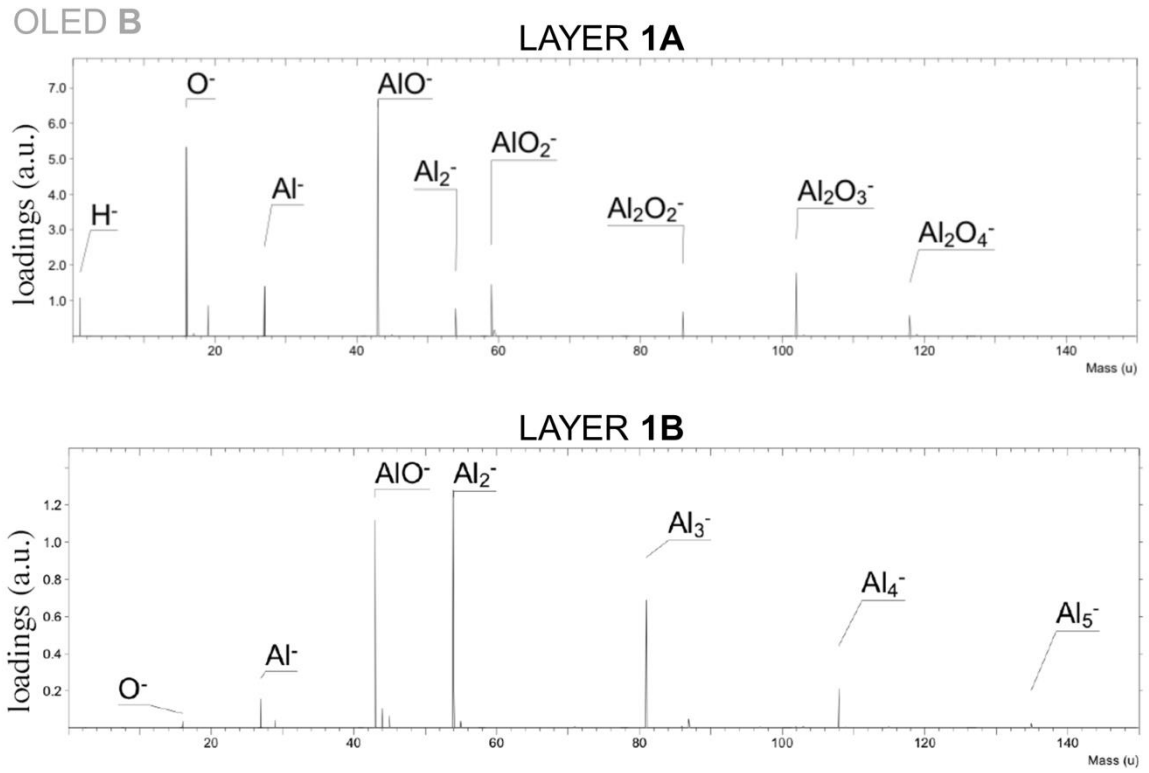

Figure S2. Pseudospectrum reconstruction from layer 1 (Al cathode) from OLED B.

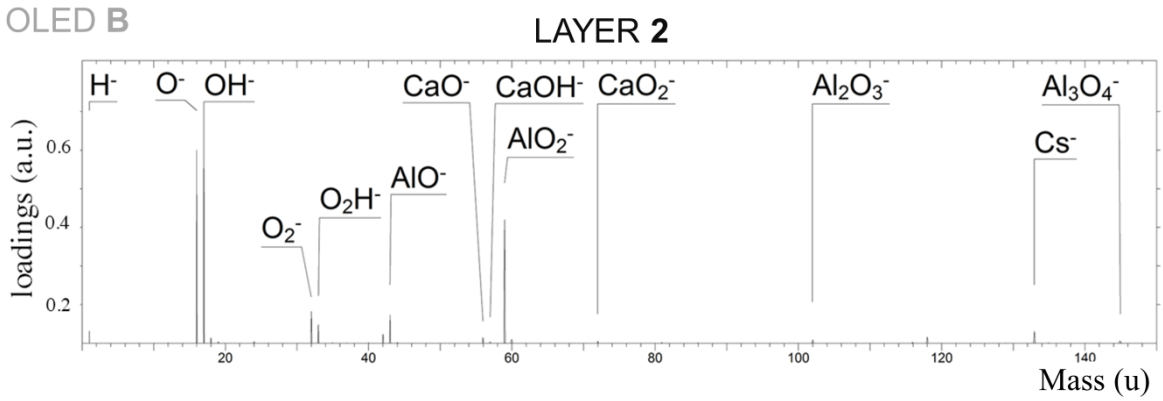

Figure S3. Pseudospectrum reconstruction of layer 2 (Ca) from OLED B.

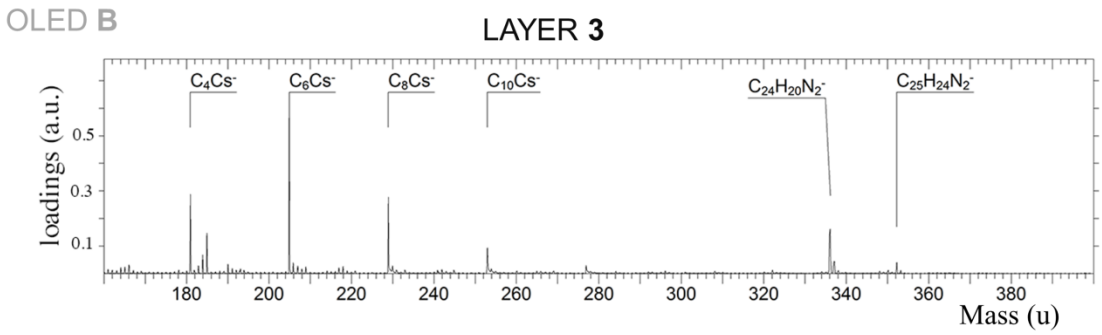

Figure S4. Pseudospectrum reconstruction of layer 3 (TAZ) from OLED B.

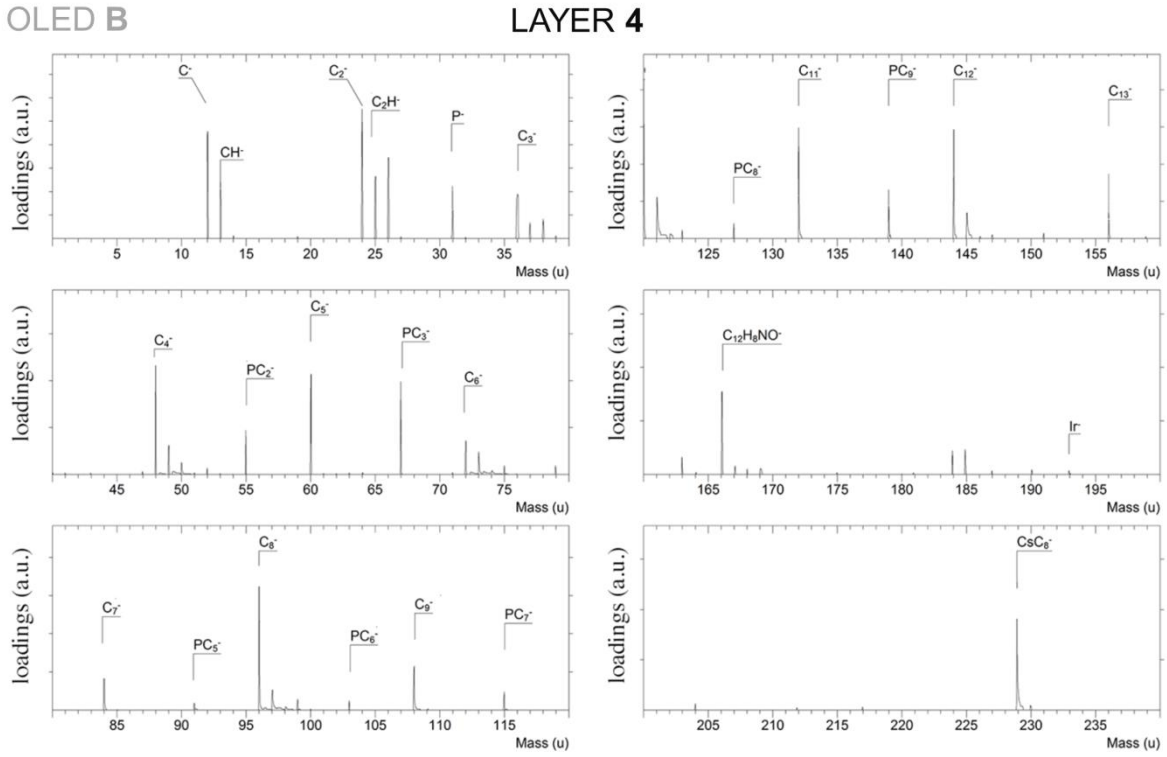

Figure S5. Pseudospectrum reconstruction of layer 4 (BCPO:FIrpic) from OLED B.

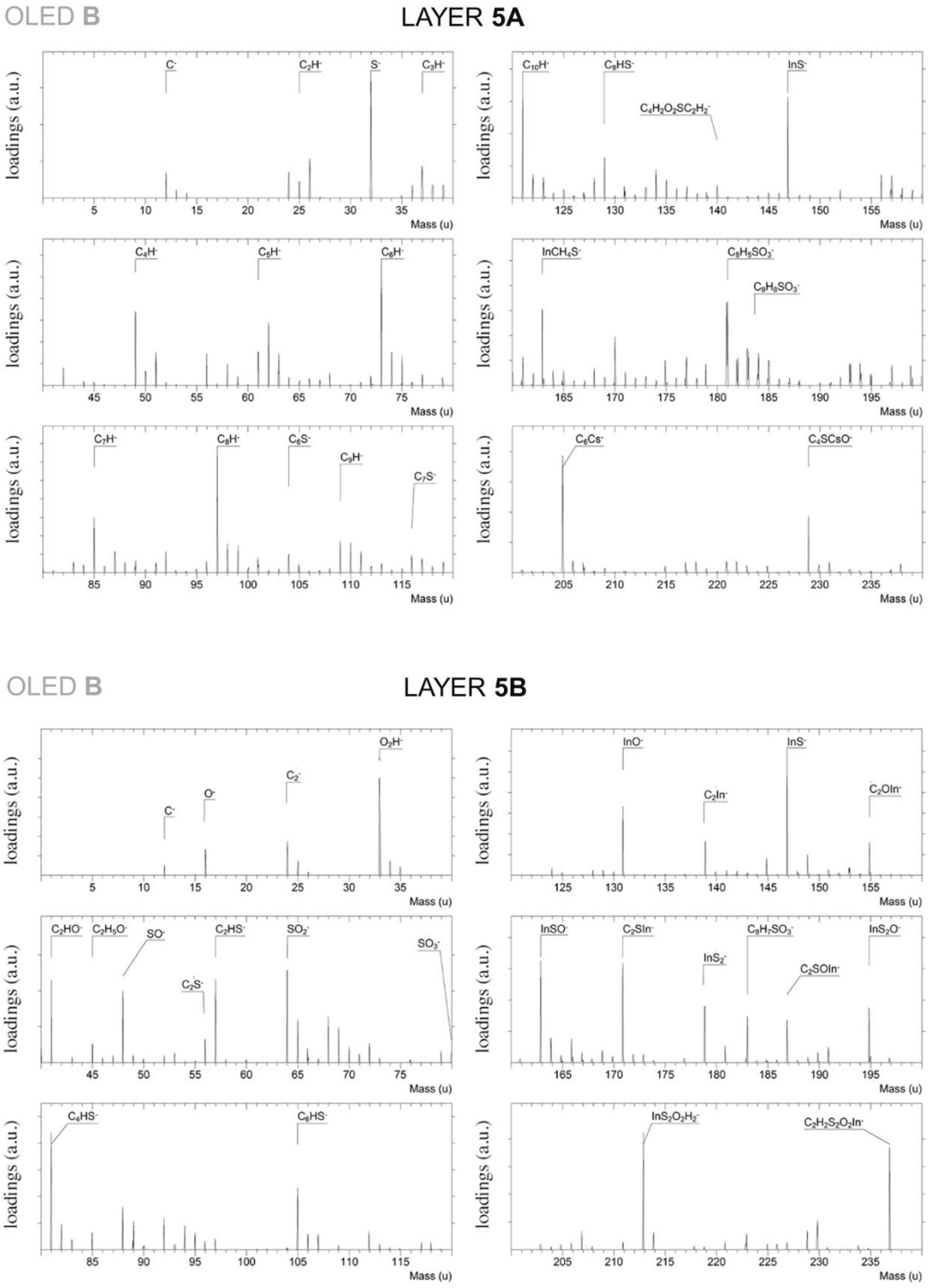

Figure S6. Pseudospectra from layer 5 (PEDOT:PSS) from OLED B. The layer 5B corresponds to the indium degraded interface.

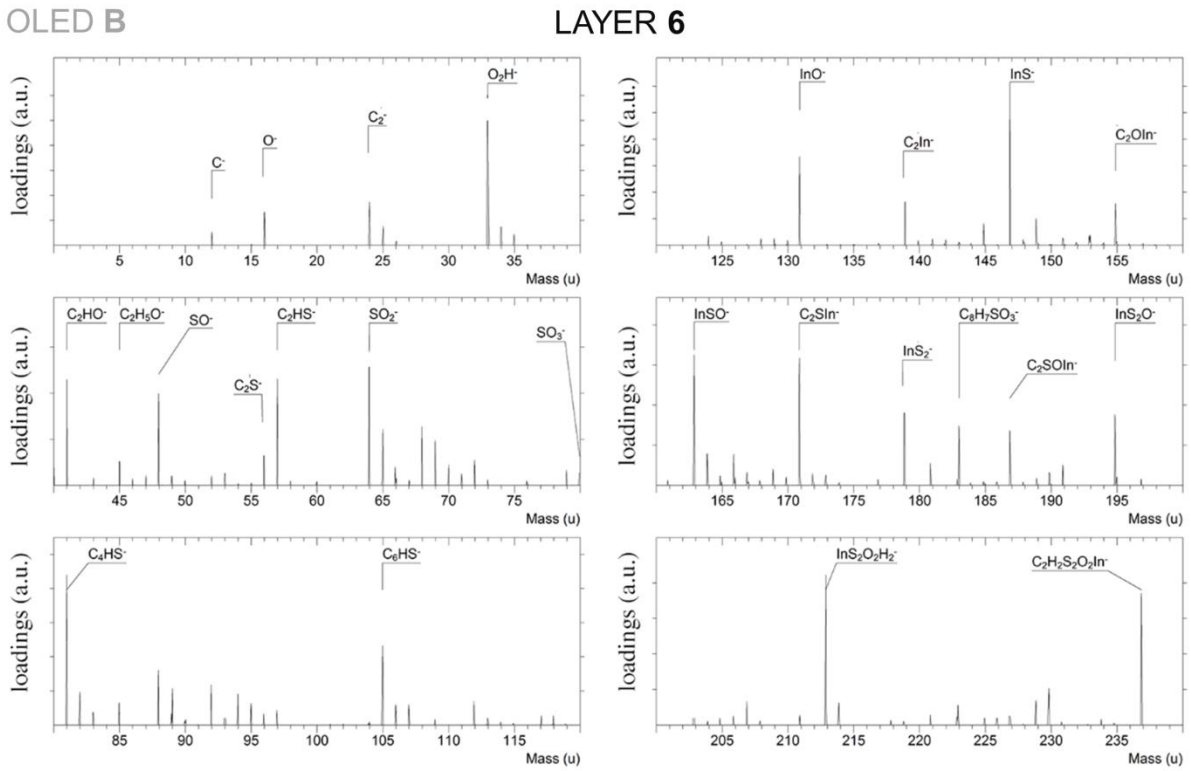

Figure S7. Pseudospectrum of layer 6 (ITO) from OLED B.

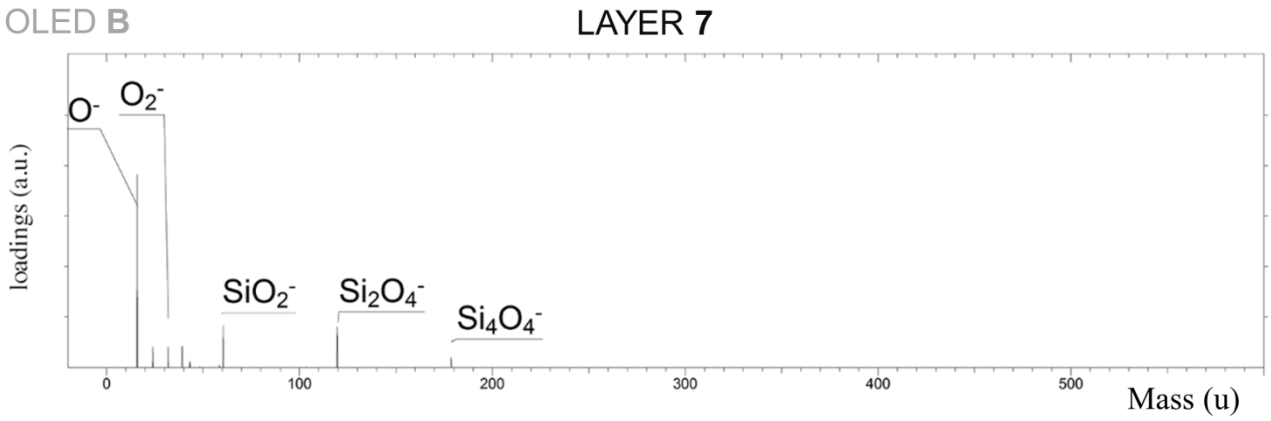

Figure S8. Pseudospectrum of layer 7 (Glass substrate) from OLED B.

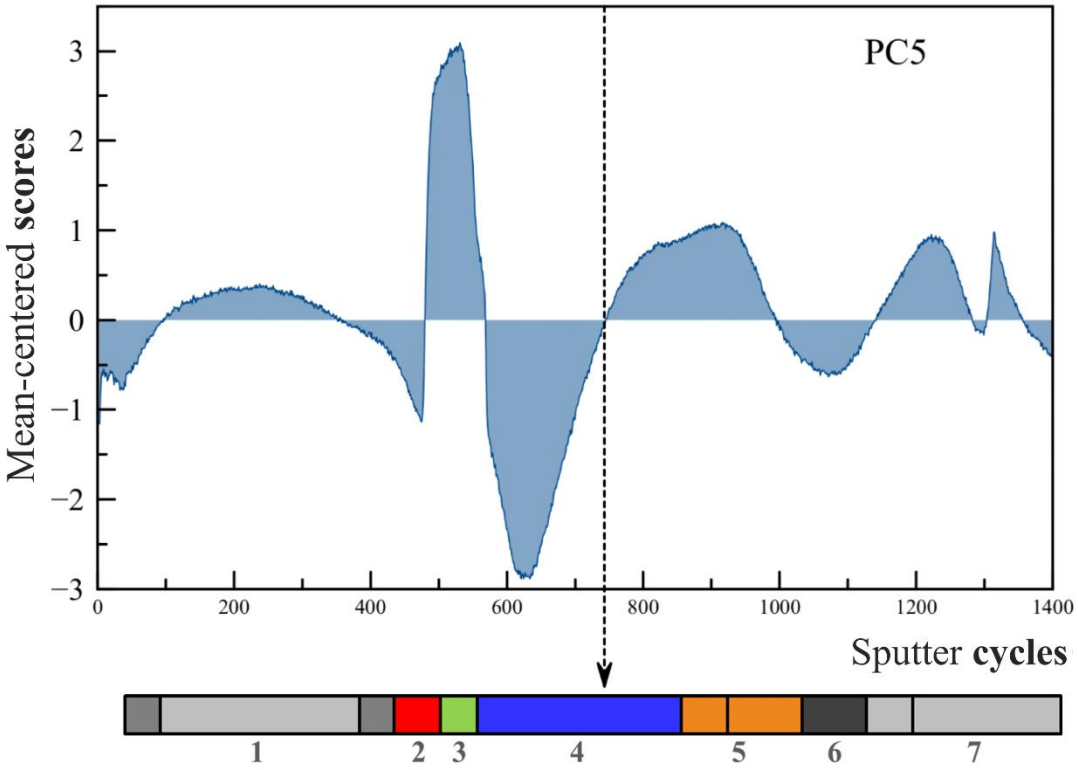

Figure S9. Scores plot from the fifth principal component (PC5) values obtained for the OLED B. It highlights the presence of an interface at about 770 sputter cycles (7700 s).

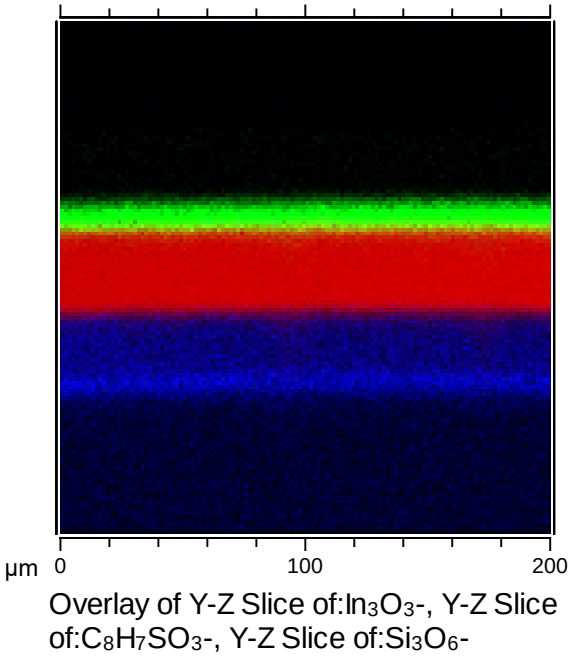

Figure S10. ToF-SIMS YZ cross-section reconstruction, showing a flat interface between ITO and PEDOT:PSS. The green layer stands for PEDOT:PSS ($C_8H_7SO_3^-$), the red layer for ITO ($In_3O_3^-$) and the blue layer for glass substrate ($Si_3O_6^-$)

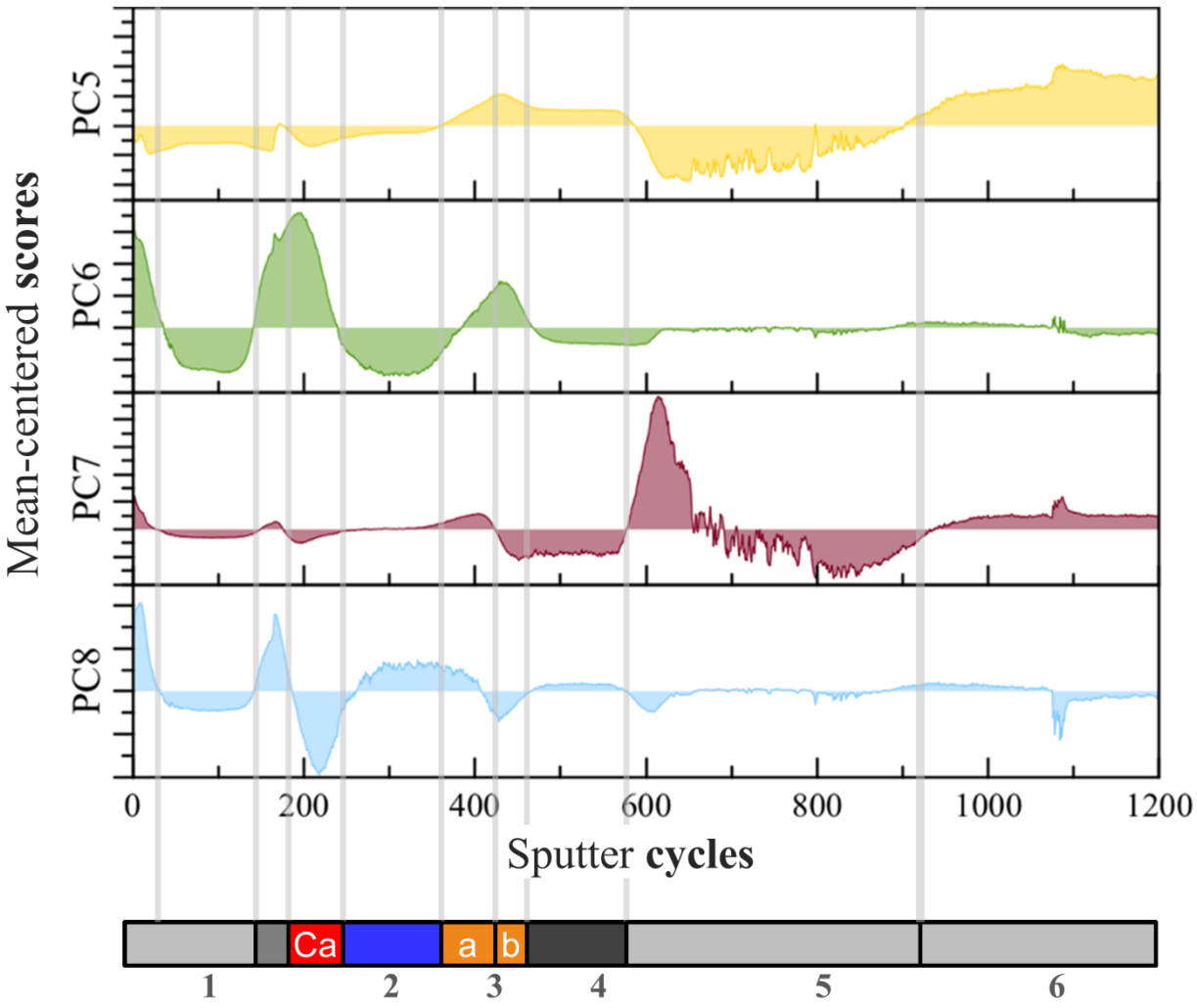

Figure S11. Scores plot from the eight first principal components obtained for the OLED A. It highlights the presence of the diffusing Ca layer (third segment from the left).

4.4 DEPTH PROFILING OF HYBRID PEROVSKITE LAYERS AND SOLAR CELLS – CONDITIONS OPTIMIZATION

After conclusive results about the ability of cesium to extract molecular information from hybrid applied samples, we wanted to extend our expertise to state-of-the-art devices, in order to answer issues at the forefront of technological development. This has been made possible through a collaboration with the group of Prof. Aldo di Carlo, at the C.H.O.S.E. Laboratory in Rome. In particular, they provided us with new-generation perovskites solar cells, on which Cs^+ bombardment could unambiguously highlight degradation features and refine their processing design[101]. We compared the performances of reference solar cells and engineered ones, in which graphene nanoflakes and 2H-MoS_2 layer were added at the interfaces. Gold and iodine diffusions could be avoided in the engineered device, leading to better preservation of the perovskite layer and therefore better retention of the Power Conversion Efficiency (PCE). More details can be found in the scientific paper added in the **Annex II**.

However, despite excellent results on hybrid optoelectronic devices, a grey area remains regarding the influence of cesium ions on the final depth profile, yet an essential aspect to discriminate between "real" degradation pathways and irradiation-induced damage. Following discussions in conferences and scientific meetings, we had the intuition that using small clusters at high energy could combine convenient sputtering yields in inorganic layers while maintaining a sufficiently low fragmentation rate on organics. On organic photovoltaic heterojunctions, Mouhib et al. already demonstrated the superiority of 10 keV Ar_{1700}^+ over 500 eV Cs^+. In our case, however, the presence of a metallic electrode in the full device portends the necessity to increase the energy per atom, either by increasing the total energy or decreasing the size, whereas Mouhib advised against increasing the energy per atom over 6 eV/at.

The ideal conditions to achieve high-quality depth profiles were assessed on a state-of-the-art perovskite layer and a full solar cell (i.e. including the metallic electrode) using Cs^+, monoatomic Ar^+, and Ar_n^+ cluster ions, for different energies and cluster sizes. Depth-profiles obtained with Ar-GCIB were acquired on an SPM-SIMS combined tool at IMEC (Leuven), with the collaboration of Dr. Valentina Spampinato and Dr. Alexis Franquet. The best results were obtained with 500 eV Cs^+ and 20 keV Ar_{500}^+. When using argon clusters, high energies per atom are required in order to avoid preferential sputtering of organic fragments and damage accumulation, as exposed in the article below. But first, let us briefly recall the working principle of a solar cell and contextualize the enthusiasm surrounding perovskites.

As opposed to LEDs, in solar cells, a light-harvesting active layer absorbs light from the sun to generate hole-electron pairs. The carriers are then separated and transported to the electrodes, where a voltage is generated, delivering enough power to supply electrical devices (**Figure 15**). Generally, a solar cell is composed of a light absorber, in which charge recombination should be avoided. This layer is surrounded by charge carrier transport layers, which ensure the injection of the holes to the cathode (usually metallic) and the electrons to the anode (usually a transparent oxide), respectively. The role of these two electrodes is to maintain a good carrier extraction.

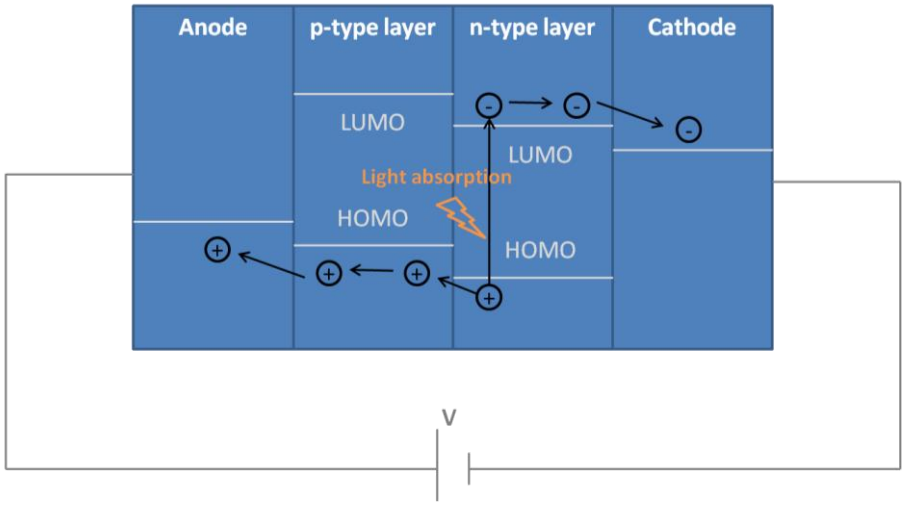

Figure 15 – Schematic representation of an organic solar cell. In contrast to LEDs, the absorption of a photon can generate an electron-hole pair in the optically active layer. Charges are then transported to the cathode and anode, where they take part in the current.

The light-harvesting layer traditionally consists in an inorganic semiconductor, in general silicon. However, like for OLEDs, this material can be replaced by an inexpensive organic layer. More recently, hybrid perovskites absorber crystals have emerged. With their high absorption coefficient enabling ultrathin films of around 500 nm to absorb the complete visible solar spectrum and diffusion lengths for both holes and electrons of over one micrometer.[102],[103] they open the perspective of foldable, lightweight solar panels, with low-cost deposition techniques.

Perovskites are intrinsically hybrid crystals with a structure ABX_3 (see **Figure 16**), where A stands for cations (cesium, methylammonium denoted MA, formamidinium denoted FA and/or rubidium), B stands for metals in a 2+ valence state (lead and/or tin) and X is for negatively charged halides (chlorine, iodine and/or bromine).[104] Mixing A, B and X constituents allows the band gap to be tuned from 1.15 eV to 3.06 eV, leading to the high complexity of the materials.

It is worth noticing that the complexity brings high efficiency but impedes the stability, and vice-versa. For example, single-cation perovskites present high yields but are also highly unstable under temperature or humidity conditions. The advent of triple cations structures enables reproducible films

deposition that is less sensitive to the processing parameters. A stabilized efficiency exceeding 22% was reached under these conditions.[105]

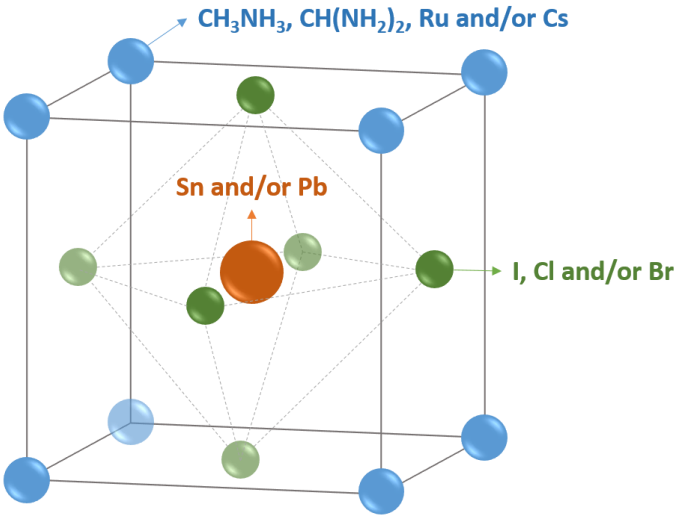

Figure 16 – Structure of a triple cations perovskite.

Recently, efforts have been made to increase efficiency while improving stability. Some quadruple cations perovskites showed an efficiency of 21.6% during 500 hours[106]. This requires a rationally designed architecture, the selection of stable materials, along with an optimized deposition process. Again, this is made possible by the in-depth detection of the aging effects since the performances were shown to strongly depend on the interfaces.[94]

materials

MDPI

Article

Hybrid Perovskites Depth Profiling with Variable-Size Argon Clusters and Monatomic Ions Beams

Céline Noël [1], Sara Pescetelli [2], Antonio Agresti [2], Alexis Franquet [3], Valentina Spampinato [3], Alexandre Felten [4], Aldo di Carlo [2], Laurent Houssiau [1] and Yan Busby [1,*]

1 Laboratoire Interdisciplinaire de Spectroscopie Electronique, Namur Institute of Structured Matter, University of Namur, 5000 Namur, Belgium; celine.noel@unamur.be (C.N.); laurent.houssiau@unamur.be (L.H.)
2 C.H.O.S.E.—Centre for Hybrid and Organic Solar Energy, Department of Electronic Engineering, University of Rome Tor Vergata, 00133 Rome, Italy; pescetel@uniroma2.it (S.P.); antonio.agresti@uniroma2.it (A.A.); aldo.dicarlo@uniroma2.it (A.d.C.)
3 IMEC, 3000 Leuven, Belgium; Alexis.Franquet@imec.be (A.F.); Valentina.Spampinato@imec.be (V.S.)
4 SIAM platform, University of Namur, 5000 Namur, Belgium; alexandre.felten@unamur.be
* Correspondence: busbyan@gmail.com

Received: 26 January 2019; Accepted: 27 February 2019; Published: 2 March 2019

Abstract: Ion beam depth profiling is increasingly used to investigate layers and interfaces in complex multilayered devices, including solar cells. This approach is particularly challenging on hybrid perovskite layers and perovskite solar cells because of the presence of organic/inorganic interfaces requiring the fine optimization of the sputtering beam conditions. The ion beam sputtering must ensure a viable sputtering rate on hard inorganic materials while limiting the chemical (fragmentation), compositional (preferential sputtering) or topographical (roughening and intermixing) modifications on soft organic layers. In this work, model ($Cs_x(MA_{0.17}FA_{0.83})_{100-x}Pb(I_{0.83}Br_{0.17})_3$/c$TiO_2$/Glass) samples and full mesoscopic perovskite solar cells are profiled using low-energy (500 and 1000 eV) monatomic beams (Ar^+ and Cs^+) and variable-size argon clusters (Ar_n^+, 75 < n < 4000) with energy up to 20 keV. The ion beam conditions are optimized by systematically comparing the sputtering rates and the surface modifications associated with each sputtering beam. X-ray photoelectron spectroscopy, time-of-flight secondary ion mass spectrometry, and in-situ scanning probe microscopy are combined to characterize the interfaces and evidence sputtering-related artifacts. Within monatomic beams, 500 eV Cs^+ results in the most intense and stable ToF-SIMS molecular profiles, almost material-independent sputtering rates and sharp interfaces. Large argon clusters (n > 500) with insufficient energy (E < 10 keV) result in the preferential sputtering of organic molecules and are highly ineffective to sputter small metal clusters (Pb and Au), which tend to artificially accumulate during the depth profile. This is not the case for the optimized cluster ions having a few hundred argon atoms ($300 < n < 500$) and an energy-per-atom value of at least 20 eV. In these conditions, we obtain (*i*) the low fragmentation of organic molecules, (*ii*) convenient erosion rates on soft and hard layers (but still different), and (*iii*) constant molecular profiles in the perovskite layer, i.e., no accumulation of damages.

Keywords: depth profiling; Perovskite solar cells; Argon GCIB; XPS; ToF-SIMS; Low-energy Cesium; hybrid materials

1. Introduction

Most modern electronic and photonic devices are made of complex hybrid (organic, inorganic) thin film stacks in which ion migrations and interface effects are known to play a dominant role on the device performance and stability. This is particularly true for hybrid perovskite solar cells (PSCs) which are characterized by increasingly sophisticated chemical composition. The chemical engineering of hybrid perovskites has brought complex formulations involving multiple cations (formamidinium, methylammonium, cesium, [1] rubidium [2] and potassium [3]) and mixed anions (iodine and bromine) which have contributed to the spectacular rise of PSCs power conversion efficiency (PCE), which now exceeds 23.5% [3–5]. Moreover, state-of-the-art PSCs have demonstrated a considerably improved stability as compared to perovskites based on $CH_3NH_3PbI_3$ formula. In particular, hybrid perovskite absorbers with formula $(FA_xCs_{1-x}PbI_3)_{0.85}(MAPbBr_3)_{0.15}$ have reached an efficiency exceeding 22% (PCE) [5] and prolonged stability thanks to the presence of inorganic atomic cations (Cs^+) which are believed to promote the uniform growth of large monolithic perovskite grains showing a considerably lower dependence from the processing conditions [1].

Despite the undeniable progress in the device stability (above 10000 h with 2D/3D perovskites [6] or with CuSCN/rGO/Au counter electrode [7]), the intrinsic and extrinsic aging mechanisms in hybrid perovskites are still insufficiently understood, and structure-to-performance studies in operated solar cells are rare. Recently, depth profile analyses combining X-Ray photoelectron spectroscopy (XPS) and time of flight secondary ion mass spectrometry (ToF-SIMS) have been successfully applied to investigate aging and failure mechanisms in organic solar cells [8], PSCs [9], and perovskite-based mesoscopic Light-Emitting Diodes (LEDs) [10]. Aging effects in solar cells were investigated by comparing pristine and operated cells after prolonged exposure to light, humidity or oxygen [9,11]. While XPS provides a quantitative chemical surface analysis with moderate sensitivity (accuracy of 1 atomic% and a detection limit of typically 0.1 at%), the ToF-SIMS analysis provides for a semi-quantitative 3D molecular analysis with higher lateral resolution (1 μm vs. a few hundred μm in XPS) and a more accurate depth resolution (1 nm) and detection limit (~ppm).

For hybrid perovskites, depth profile analysis was applied to investigate the diffusion of atomic and molecular species, the thin layers composition vs. depth, and the perovskite back-conversion into lead iodide or other chemical modifications of layers and interfaces. The objectives of these studies are to rationally optimize the processing conditions and methodology and to investigate interface engineering or aging mechanisms [12,13]. The main limitation of depth profile analysis is related to the ion beam sputtering process, during which energetic impinging ions can introduce artifacts such as the diffusion of small ions by surface charging, [14] intermixing, reduction of metal oxides by preferential sputtering and fragmentation of organic molecules or surface roughening. While ion beam induced modifications cannot be fully avoided, the nature of the sputtering (and analysis) ions and their energy and fluence should be limited to prevent artifacts coming from the accumulation of damages during the profile [15–17].

Gas cluster ion beams (GCIBs) and in particular Ar_n^+ clusters, with size (n) typically ranging from few hundred to few thousand atoms, are the preferred choice to achieve high erosion rates and preserve the molecular composition of soft materials [18]. The advantage of GCIBs sputtering relies on the possible combination of high-energy clusters (E up to 40 keV) and low energy-per-atom values (E/n ~ few eV). The cluster collision is followed by its disaggregation and the release of its energy to the material surface. Molecular dynamics simulations on cluster collisions have shown that, despite the high sputtering rates, the impact of large argon clusters (n > 1000) on organic layers is associated with a weak penetration of Ar atoms, i.e., a restrained in-depth damaging of the material [19,20].

Meanwhile, GCIBs are well-known to be inefficient in sputtering inorganic layers, at least for energies below 20 keV. This feature has considerably limited their applicability in profiling hybrid stacks. Argon GCIBs resulted in ripples formation on silicon [21,22] and gold [23] surfaces and in the reduction of InAs [24], as shown by XPS analysis. A possible strategy to profile inorganic materials with GCIBs is to increase the E/n value by reducing the cluster size, however, this has been relatively

poorly investigated until now, and guidelines are still controversial [22,25,26]. On the one hand, by lowering the cluster energy (*E* or *E/n*), one would expect to reduce the ion beam induced mixing and thus improve the depth resolution. On the other hand, lowering the cluster energy would result in the lowering of the sputtering rate (profile duration), possibly resulting in the roughening and/or in the accumulation of damages during the profile (induced by both the analysis and the sputtering beam) [27–30]. For model hybrid samples (*Irganox*) and biological samples, increasing the cluster energy up to 40 keV was shown as beneficial to improve the molecular signals intensities and the lateral resolution [31].

Alternatively, hybrid materials can be sputtered using low-energy (<1 keV) monatomic ion beams (Ar^+, Cs^+, O_2^+, etc.). In particular, a low-energy Cs^+ beam has been widely applied in ToF-SIMS profiles of hybrid stacks thanks to (*i*) its ability to sputter organic and inorganic materials at similar rates by the combined chemical-mechanical sputtering, (*ii*) the ability of implanted Cs atoms to increase the negative ionization yield of molecular species, and (*iii*) the ability of Cs atoms to react with radicals formed during the sputtering and limit chemical modifications or crosslinking effects [32]. In this context, for intrinsically hybrid perovskite layers, or for PSCs stacks, combining inorganic (metal and conductive oxides contacts), intrinsically hybrid, and organic layers (as charge carriers extraction layers), it is particularly complicated to predict the best depth profile conditions. Furthermore, systematic studies comparing the surface modifications induced by GCIBs and low-energy monatomic beams are rare.

In this work, we profile hybrid samples based on state-of-the-art triple cation perovskites with nominal composition $(FA_xCs_{1-x}PbI_3)_{0.85}(MAPbBr_3)_{0.15}$ deposited on (flat, compact) c-TiO_2 (referred as model samples) and full mesoscopic solar cells with the stack composition shown in Figure 1. The ion sputtering conditions are varied from low-energy monatomic beams (Ar^+ and Cs^+) to variable-size Ar_n^+ clusters ($100 < n < 4000$) ions in the wide energy-per-atom range (from a few eV–100 eV). The methodology consists of combining ToF-SIMS and XPS depth profiles to identify the ion beam induced modifications on the model hybrid samples, and successively, the best conditions are applied to profile the mesoscopic PSCs. Results show that low-energy Cs^+ sputtering allows the user to quickly profile hybrid materials without inducing the accumulation of modifications, while for argon clusters, the most efficient sputtering conditions correspond to a few hundred atoms clusters with energy-per-atom values above 20 eV. Below this energy, the direct comparison between the depth profiles shows that argon GCIBs are inefficient to sputter metal aggregates (Au, Pb), which leads to their artificial accumulation during the profile.

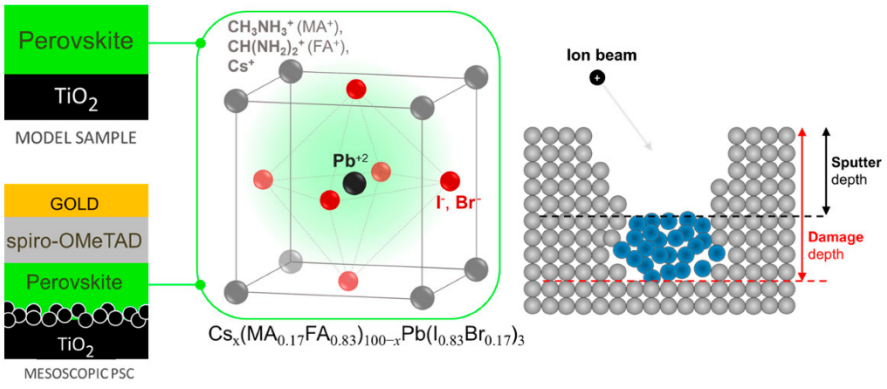

Figure 1. Hybrid perovskite sample schemes and stack composition. The strategy is to identify the best sputtering beam conditions on a model sample and then apply them to profile mesoscopic perovskite solar cells. The basic requirement to avoid the accumulation of damage is that, for each sputtering/analysis cycle, the sputtered depth, as defined in the right scheme, must exceed half of the damage depth induced by the sputtering and the analysis beams.

2. Materials and Methods

2.1. The Fabrication of Model Perovskite/TiO2 Samples

Patterned fluorine-doped tin oxide (FTO) coated glasses were cleaned in an ultrasonic bath with acetone and 2-propanol, then a compact TiO_2 ($cTiO_2$) blocking layer was deposited by spray pyrolysis from a solution of acetylacetone (2 mL), titanium diisopropoxide (3 mL), and ethanol (45 mL) at 460 °C. The triple cation perovskite layer $Cs_x(MA_{0.17}FA_{0.83})_{100-x}Pb(I_{0.83}Br_{0.17})_3$ was deposited on c-TiO_2 following the one-step antisolvent deposition method in a nitrogen-filled glovebox. Organic cations were purchased from Dyesol, lead compounds were purchased from TCI Chemicals, and CsI from abcr GmbH (Karlsruhe, Germany). The precursor perovskite solution was prepared by dissolving, with the molar ratio suggested in Reference [1], the mixture of lead iodide (PbI_2), lead bromide ($PbBr_2$), methylammonium bromide (MABr), formamidinium iodide (FAI) and cesium iodide (CsI) in a solvent mixture of anhydrous N,N-dimethylformamide (DMF) and dimethylsulfoxide (DMSO) in a 3:1 volume ratio. The perovskite precursor solution was spin-coated on the TiO_2 substrate in a two-step program at 1000 and 5000 rpm for 10 and 30 s, respectively. During the second step, 200 µL of chlorobenzene was poured on the spinning substrate 7 s prior to the end of the program. Immediately after spin coating the substrates were annealed at 100 °C for 1 h in a nitrogen-filled glovebox. Glass-sealed samples were sent for the analysis.

2.2. Fabrication of Mesoscopic Perovskite Solar Cells

Glass substrates coated with the patterned FTO and the compact TiO_2 layer were coated with a thin mesoporous TiO_2 ($mTiO_2$) film (~150 nm) by spin coating a TiO_2 paste (Dyesol 30 NR-D paste diluted in ethanol 1:5 in wt.) at 3000 rpm for 20 s, followed by sintering at 460 °C for 30 min in air. The perovskite layer was then deposited on the mesoscopic TiO_2 as described in the model samples. Then, the spiro-OMeTAD (73.5 $g{\cdot}L^{-1}$ in chlorobenzene solution doped with TBP (26.7 $\mu L{\cdot}mL^{-1}$)), LiTFSI (16.6 $\mu L{\cdot}mL^{-1}$), and a Cobalt(III) FK209 complex (7.2 $\mu L{\cdot}mL^{-1}$) were sequentially deposited by spin coating at 2000 rpm for 20 s in a glovebox system. Finally, the ~100 nm thick gold counter electrode was deposited by the high-vacuum thermal evaporation through a shadow mask defining an active area of 0.1 cm^2. The solar cells were encapsulated with a glass lid before being sent for analysis.

2.3. XPS Depth Profile Analysis

The XPS depth profile analysis was performed on an ESCALAB 250Xi spectrometer by Thermo Scientific equipped with monatomic Ar^+ and $Ar_n{}^+$ GCIB source (MAGCIS) allowing to select the cluster size from $n = 75$ to $n = 2000$ and the cluster energy up to 8 keV. Because of the rapid sputtering rate decay, the cluster energy was not lowered below 6 keV. In particular, the systematic study presented in this work refers to the maximum available energy of 8 keV. Typically, the monatomic beam intensity is the few µA range while for clusters it is ~10 nA. Solar cells were stored in dark conditions under vacuum before the analysis and were analyzed by alternating ion sputtering and XPS analysis performed in the scan mode. Both survey and high-resolution scans were acquired at each profile step, especially to monitor Pb 4f and I 3d spectra. The XPS spectrometer is equipped with a monochromatic Al Kα X-ray beam with a spot size set at 200 µm and the sputtering beam raster area was set to 1 mm to ensure that the analysis was safely performed at the center of the crater. A dual beam flood gun was used for charge compensation. The surface atomic percentages (at.%) were evaluated from survey scans acquired at each profile step and chemical analysis was performed on high-resolution spectra fitted with a Shirley-type background using Avantage© software.

2.4. ToF-SIMS Depth Profile Analysis

ToF-SIMS depth profiles were acquired in non-interlaced mode with the analysis area of 100×100 μm^2 and the raster area of 250×250 μm^2. The profiles with monatomic beams were performed on a ToF-SIMS IV instrument, equipped with a 25 keV $Bi_3{}^+$ analysis beam, while profiles with $Ar_n{}^+$ clusters

were collected on a ToF-SIMS V instrument equipped with a 30 keV Bi_3^+ analysis beam and combined with in-situ AFM (IONTOF GmbH Münster, Germany). The ToF-SIMS sputtering beam conditions are reported in Table 1. Because of the relatively wide cluster size distribution (as shown in Figure 2), we avoided selecting cluster sizes below 500 atoms. Specifically, the cluster size and energy were varied in the range $500 < n < 4000$ and $5 < E < 20$ keV, corresponding to the energy-per-atom range $2.5\ eV < E/n < 40$ eV (see Table 1). A flood gun was used for surface charge compensation and most of the profiles were acquired in both positive and negative polarities. However, only results obtained in negative polarity mode have been exploited because of the higher intensity of characteristic molecular ions signals.

Table 1. Ion beam sputtering conditions: Cluster size, energy, energy-per-atom, and typical current values in ToF-SIMS depth profiles.

Sputtering Beam	E (keV)	E/*n* (eV)	Ion Current (nA)
Ar_{4000}^+	10	2.5	1
Ar_{1000}^+	10, 20	10, 20	0.5
Ar_{500}^+	5, 10, 20	10, 20, 40	0.5
Ar^+	0.5, 1	/	~100
Cs^+	0.5, 1	/	35, 75

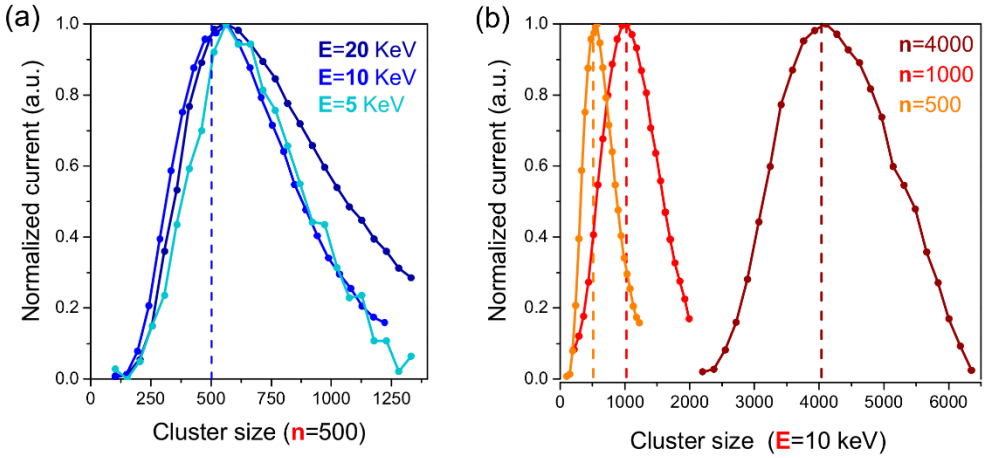

Figure 2. Size distribution (*n*) of Ar_n^+ clusters on the IONTOF V ToF-SIMS spectrometer at (**a**) constant nominal size ($n = 500$ as indicated by the vertical line) and variable cluster energy ($5 < E < 20$ keV), and (**b**) fixed energy (E = 10 keV) and variable nominal cluster size ($500 < n < 4000$).

3. Results and Discussion

3.1. Depth Profiles on Model Perovskite/TiO_2 Samples

Ion beam induced modifications are first checked on model triple cation perovskite thin films with nominal composition $Cs_x(MA_{0.17}FA_{0.83})_{100-x}Pb(I_{0.83}Br_{0.17})_3/cTiO_2/Glass$. The most representative XPS depth profiles showing the peak area variation of I 3d, Pb 4f, O 1s, and Cs 3d spectra as a function of the sputtering time are displayed in Figure 3.

A previously reported, XPS depth profile analysis of $CH_3NH_3PbI_3$ perovskite solar cells with monatomic beams evidenced the presence of two chemical components in the Pb 4f spectrum. One was ascribed to metallic lead (Pb^0, with Pb $4f_{7/2}$ component at ~137 eV binding energy) and the other to lead in the perovskite (Pb^{+2}, with Pb $4f_{7/2}$ component at ~139 eV) [9]. While the origin of such non-negligible Pb^0 content is still controversial, profiles in Figure 3d–f show that the Pb^0 content increases with the sputtering time (depth) and it is clearly affected by the ion beam conditions. Namely,

when sputtering with Ar_n^+ clusters, the Pb^0 component quickly exceeds 50% of the total Pb 4f peak area, while it represents less than 30% of the total Pb 4f area when sputtering with 1 keV Ar^+ beam. The lead reduction may possibly occur (*i*) because of the segregation of Pb excess during the perovskite crystallization, leading to the formation of nanoscale Pb^0 particles, or (*ii*) it may form following the exposure to the X-Rays and/or the ion beam during the depth profile. In both cases, if the Pb^0 was entirely formed during the depth profile, one would expect a progressive modification of the perovskite surface composition, and possibly, an increase of the I/Pb^{+2} ratio (because of the reduction of Pb^{+2} to Pb^0). This is not observed, as for almost each ion beam condition, the Pb^0 increase is associated with a stable or slowly decreasing I/Pb^{+2} ratio (see Figure 3d–f). We conclude that the Pb^0 is already present in the perovskite layer, however, its content is artificially enhanced by the argon GCIB sputtering because of the slower sputtering of Pb^0, which tends to accumulate at the sample surface during the profile.

This explains why the I/Pb ratio (where $Pb=Pb^0+Pb^{+2}$) decreases faster when profiling with argon clusters with respect to monatomic beams. The Ar_{500}^+ beam results in the most stable I/Pb^{+2} ratio (~2.3, Figure 3f), with a value close to the expected value (the nominal value being I/Pb = 2.5); we conclude that this condition ensures the lowest modification of the perovskite surface composition and the non-accumulation of damages during the profile.

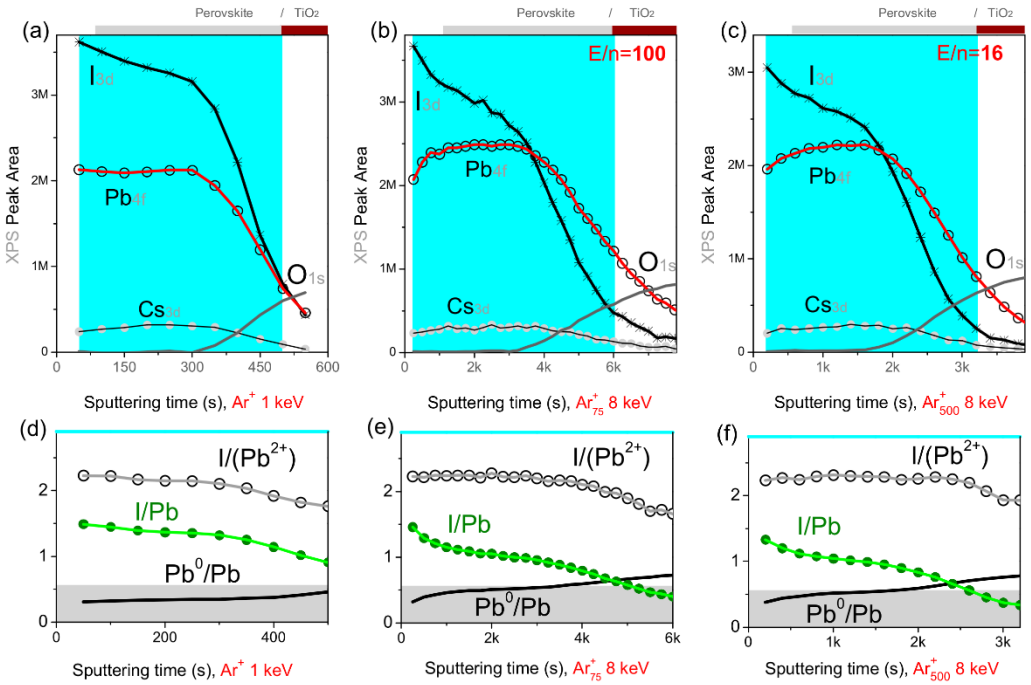

Figure 3. XPS depth profiles acquired on Perovskite/cTiO2 model samples obtained with (**a**,**d**) monoatomic Ar^+ at 1 keV; (**b**,**e**) Ar_{75}^+ clusters at 8 keV; and (**c**,**f**) Ar_{500}^+ clusters at 8 keV. Bottom panels show atomic percent ratios between iodide and lead which are present in two different chemical states (Pb^0 and Pb^{+2} from the perovskite). Bottom panels refer to the perovskite layer highlighted in the top panels for which the upper limit corresponds to the O 1s signal (from $cTiO_2$) reaching 70% of its plateau value.

Additional information on the effect of the ion beam sputtering on intrinsically-hybrid perovskites is derived from ToF-SIMS profiles on model samples. The perovskite composition is monitored from the profiles of intense and characteristic molecular ion fragments, including PbI_3^-, $CH_3NH_3I_3^-$ (MAI_3^-), $CH_5N_2I_2^-$ (FAI_2^-), CN^- and I_2^-. The molecular profiles obtained with low-energy monatomic

sputtering beams (Ar^+ and Cs^+) are displayed in Figure 4. Compared to Ar^+, (Figure 4a,d and Figure S1), Cs^+ profiles (Figure 4b–f) result in clearly less-variable and more intense molecular signals. The signal enhancement is related to the surface implantation of Cs atoms which increase the ionization yield of the negatively-charged sputtered ions [33,34]. To evaluate and compare the ion beam induced modifications between the different sputtering conditions, we have selected two ratio indicators for the fragmentation of organic molecules (CN^-/FAI_2^-) and the preferential sputtering of inorganic species with respect to organic ones (PbI_3^-/CN^-).

Generally, flat molecular profiles (signals or ratios) would indicate that the ion beam induced modifications do not accumulate during the profile. The 500 eV Cs^+ sputtering results in the least-variable indicator profiles and ensures the high sputtering rate (~2.5 nm/s) in the perovskite layer. Monatomic Ar^+ results in highest sputtering rate but also in more variable intensity ratios as compared to Cs^+ (Figure 4d). Moreover, with respect to Ar^+, the fragmentation indicator value is roughly halved with Cs^+ sputtering, possibly because of the increase of the ionization yield of the FAI_2^- fragment.

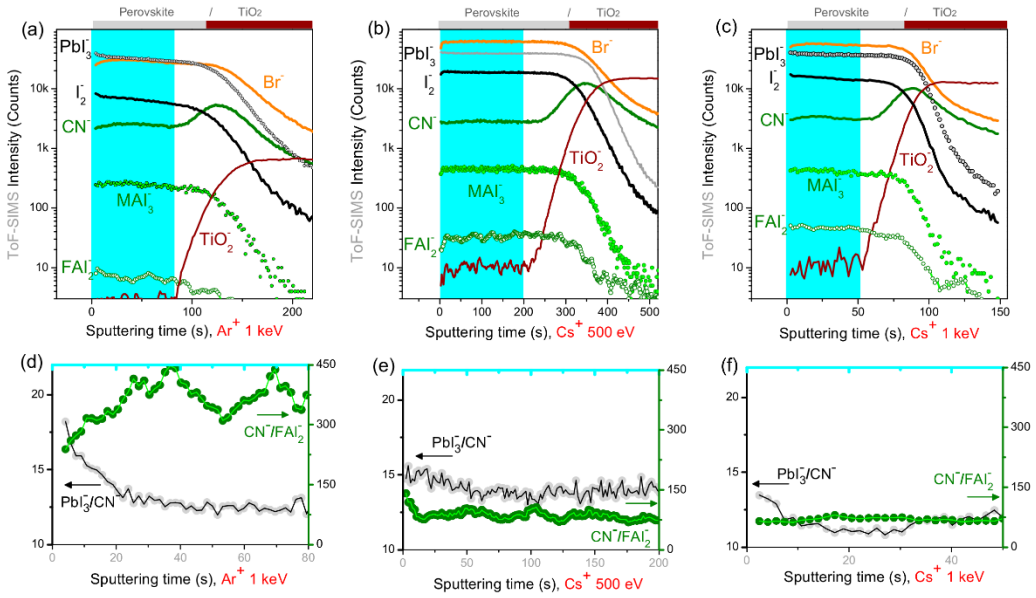

Figure 4. ToF-SIMS depth profiles acquired on Perovskite/$cTiO_2$ model samples obtained with monoatomic beams. (**a**,**d**): Ar^+ at 1 keV; (**b**,**e**): Cs^+ at 500 eV; (**c**,**f**): Cs^+ at 1 keV. Bottom panels show a selected indicator for the preferential sputtering of inorganic/organic species (PbI_3^-/CN^-) and an indicator for molecular fragmentation (CN^-/FAI_2^-) in the highlighted perovskite region, i.e., before the rise of $cTiO_2^-$ signal. Constant profiles indicate the non-accumulation of damages.

ToF-SIMS depth profiles on model hybrid samples have been carried with variable-size argon clusters (Ar_n^+) with energy from 5 to 20 keV. At a constant energy of E = 10 keV, the cluster size sensibly impacts the sputtering rate; in particular, the sputtering rate obtained on the hybrid perovskite layer is ~1 nm/s with Ar_{500}^+ (Figure 5), ~0.3 nm/s with Ar_{1000}^+, and ~0.15 nm/s with Ar_{4000}^+ (Figure S2). At energies above 10 keV, the argon cluster size has a modest impact on the fragmentation indicator (see Figure S2c,d, and Figure 5e), while the preferential sputtering of organic molecules increases dramatically when increasing the cluster size above n = 1000 (Figure S2c,d).

Based on these results, the optimum argon cluster size is found to be a few hundred atoms (n = 500). For this size (Ar_{500}^+), we systematically investigated the effect of the cluster energy (Figure 5). At 5 keV (E/n = 10 eV), the Ar_{500}^+ sputter rate is only ~0.12 nm/s, the perovskite/$cTiO_2$ interface is broad, and molecular signals tend to decrease during the profile. In these conditions, the positive surface charging generated by the ion sputtering could possibly promote the migration of negatively charged

ion species to the crater surface. This phenomenon can explain the progressive iodine decrease during the profile (Figure 5a,b), however, it does not apply to Br^- signal, which rather tends to accumulate toward the bottom interface during long profiles. We conclude that the charging-related ion migration is ruled by the specific ion mobility into the perovskite [35].

With the 20 keV Ar_{500}^+ beam, the $cTiO_2$ interface is reached after only 100 s, corresponding to a sputtering rate of the perovskite material of ~5 nm/s, as confirmed by the AFM profile of the crater region acquired in-situ, showing a 200 nm depth after 40 s sputtering (see Figure S3 in Supporting Information). The 20 keV Ar_{500}^+ profile features constant molecular ions (and indicators) profiles in the whole perovskite layer depth (Figure 5f), indicating that ion beam induced damages do not accumulate during the profile and no preferential sputtering occurs on the different perovskite constituents. Moreover, the fragmentation indicator value is halved with respect to monatomic Ar^+ (Figure 4d), and the Br^- signal does not increase at the perovskite/$cTiO_2$ interface.

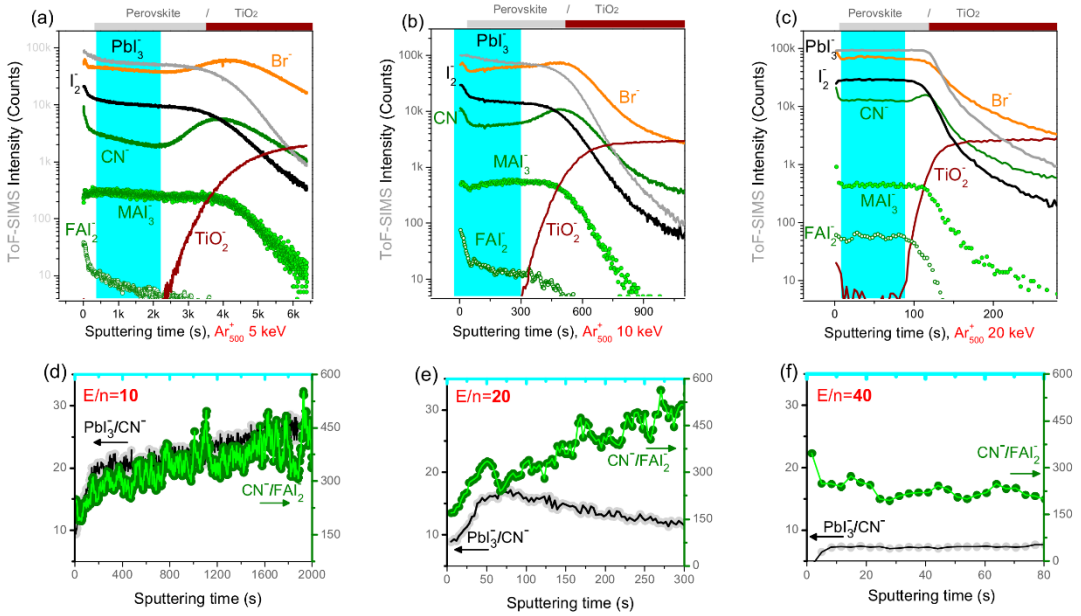

Figure 5. ToF-SIMS depth profiles acquired on Perovskite/$cTiO_2$ model samples with constant argon cluster size (n = 500) and variable energy. Constant profiles indicate the non-accumulation of damages during the profile. (**a**,**d**): E = 5 keV (E/n = 10 eV); (**b**,**e**): E = 10 keV (E/n = 20 eV); (**c**,**f**): E = 20 keV (E/n = 40 eV). Bottom panels show that (*i*) a higher preferential sputtering of organic molecules occurs at low cluster energy (PbI_3^-/CN^- ratios) and (*ii*) a lower fragmentation of organic molecules occurs with 20 keV Ar_{500}^+ beam (CN^-/FAI_2^-).

The effect of the sputtering beam on the hybrid perovskite surface was further investigated by acquiring in-situ AFM topography images inside the crater region during the profile (Figure 6). The initial topography of the perovskite layer features µm-sized monolithic perovskite grains (Figure S4 in Supporting Information). Clearly, the sputtering affects the surface topography; specifically, while argon clusters with n = 1000 and E/n = 10 eV (see Figure 6a and the corresponding profile in Figure S2) tend to preserve the initial morphology and grains are still recognizable in Figure 6a, argon clusters with smaller size (n = 500) or higher energy (E/n = 40 eV) progressively deform the surface topography (Figure 6b,c). The progressive amorphization of the crater surface is confirmed by the lowering of the surface roughness and the disappearance of the grain edges for the crater obtained with Ar_{500}^+ at E/n = 40 eV (Figure 6c).

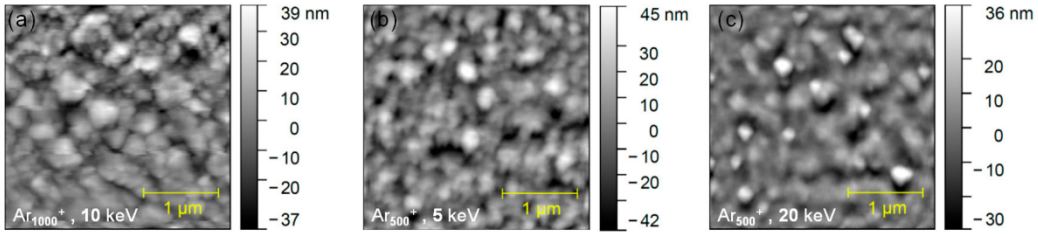

Figure 6. In-situ AFM images acquired in the sputtered crater after 250 s (~210 nm depth) of Ar_{1000}^+ sputtering at 10 keV (**a**), 750 s (~160 nm depth) of Ar_{500}^+ sputtering at 5 keV (**b**), and 40 s (~220 nm depth) of Ar_{500}^+ sputtering at 20 keV (**c**). Monolithic perovskite grains are still visible in (**a**) and progressively disappear in (**c**).

In a simplified view, we can sum up that for argon clusters sizes above n = 1000 or cluster energies below 10 keV (or E/n < 20 eV), the sputtering rate drops and the molecular signals profiles (and their intensity ratios) tend to artificially evolve with the sputtering time. This result agrees with XPS depth profiles showing that large clusters do not efficiently sputter metallic lead. Overall, ToF-SIMS profiles on model samples indicate that the most efficient sources to profile hybrid perovskite are low-energy Cs^+ or argon clusters of a few hundred atoms with energy above 10 keV. These conditions ensure high sputtering rates (few nm/s) and rather constant molecular profiles. In these conditions, the defects induced by both the analysis and the sputtering beams are efficiently removed during the subsequent erosion cycle.

3.2. Depth Profiles on Full Perovskite Solar Cells

The optimum depth profile conditions resulting from the analysis of model samples have been applied to mesoscopic PSCs with structure Au/spiro-OMeTAD/$(FA_xCs_{1-x}PbI_3)_{0.85}(MAPbBr_3)_{0.15}$/m-$TiO_2$/c$TiO_2$/FTO/Glass (Figure 1). Since the maximum cluster energy available on our XPS spectrometer is 8 keV and in order to reduce the profile duration, the top Au electrode and part of the spiro-OMeTAD layer were previously sputtered with the 1 keV Ar^+ beam, and after that, the ion source was switched to the cluster mode (at 8 keV). XPS profiles obtained with Ar^+ (1 keV), Ar_{75}^+ and Ar_{500}^+ are shown in Figure 7. For Ar_{75}^+, despite the high energy-per-atom value (E/n~100 eV), the sputtering rate is only ~0.1 nm/s, and the I/Pb ratio decreases similarly to the Ar_{500}^+ profile. This suggests that the sputtering of Pb^0 particles is also rather ineffective with small clusters, as confirmed by the rather slow decay of the residual Au signal (Figure 7b).

In the explored energy range, argon clusters result in the Pb^0/Pb ratio quickly exceeding 50%; this explains the fast decay of I/Pb. However, the constant I/Pb^{+2} ratio observed for the cluster profiles indicate that surface modifications of the perovskite stoichiometry do not accumulate during the profile. The I/Pb^{+2} value in the perovskite layer is closer to the nominal value 2.5 with Ar_{500}^+ sputtering, while a lower iodine content (I/Pb^{+2}~2) is measured at the perovskite surface is with Ar^+ and Ar_{75}^+ (the XPS analysis refers to the first 10 nm depth).

ToF-SIMS depth profiles obtained on full mesoscopic PSCs are shown in Figure 8. For 1 keV Ar^+ sputtering (Figure 8a), the Au and spiro-OMeTAD layers are efficiently profiled in only ~500 s. The monatomic argon profile results in well-defined interfaces, suggesting a rather low intermixing or roughening at hybrid interfaces. However, signals from organic molecular fragments are rather weak (FAI_2^-), suggesting a high degree of fragmentation in the top surface.

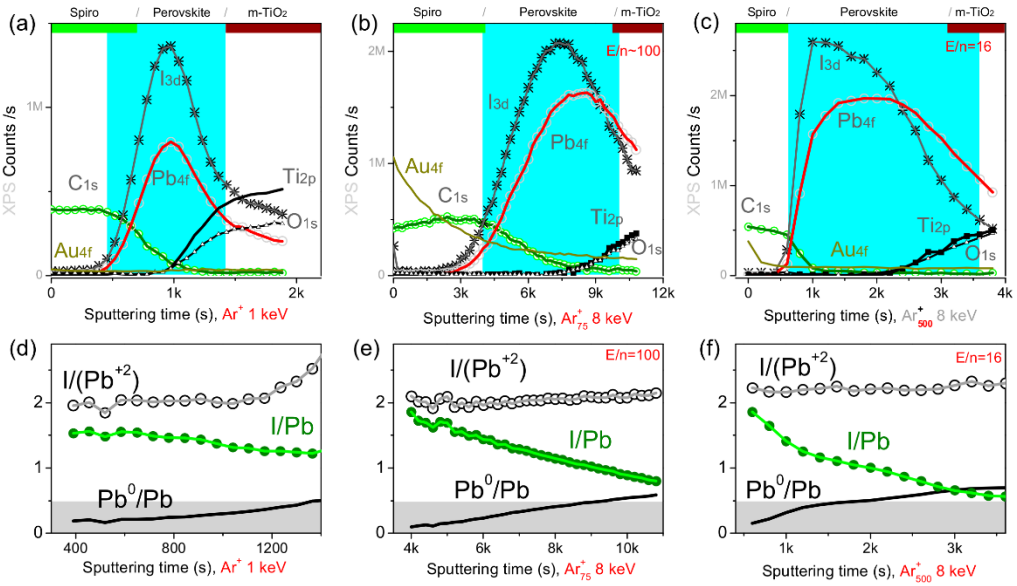

Figure 7. XPS depth profiles acquired on PSCs obtained with (**a**,**d**) monoatomic Ar^+ at 1 keV, (**b**,**e**) Ar_{75}^+ clusters at 8 keV, and (**c**,**f**) Ar_{500}^+ clusters at 8 keV. Bottom panels show atomic percent rations between iodide and lead which are present in two different chemical states (metallic Pb^0 and Pb^{+2} from the perovskite) in the perovskite area. The perovskite layer limits are roughly identified by the rise of the iodine and oxygen signals.

For 500 eV Cs^+ sputtering (Figure 8b), the PSC profile shows sharp interfaces and more intense organic and inorganic molecular signals thanks to the enhanced negative ionization promoted by Cs atoms implantation. Finally, for 20 keV Ar_{500}^+ (Figure 8c), on the one hand, the sputtering time to profile the top Au electrode is about ten times higher (~2000 s) with respect to 1 keV Ar^+. On the other hand, the sputtering of the perovskite layer and the m-TiO_2 are much more efficient, resulting in sharp interfaces. The rather slow drop of the Au_3^- signal at the Au/spiro-OMeTAD interface confirms the inefficient sputtering of small metal particles; this fact is of interest when investigating the gold diffusion in aged devices.

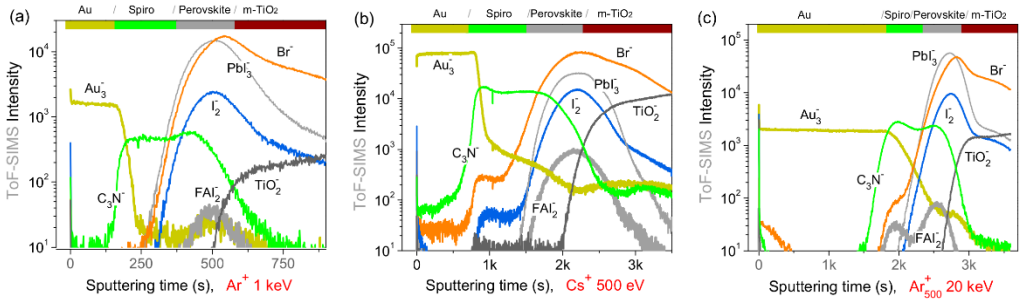

Figure 8. ToF-SIMS depth profiles of PSCs with (**a**) 1 keV Ar^+, (**b**) 500 eV Cs^+, and (**c**) 20 keV Ar_{500}^+.

4. Conclusions

Model triple-cation perovskite thin layers and mesoscopic PSCs are depth profiled with different sputtering ion beam conditions including low-energy monatomic ion beams (Ar^+ and Cs^+) to argon GCIBs at different sizes (n) and energies (E, E/n). For each condition, the main ion beam induced modifications are assessed by evaluating the fragmentation, preferential sputtering, chemical modifications, and the interface sharpness (roughness). Overall, sufficiently high erosion rates (nm/s)

are found to be beneficial in preventing the accumulation of damages and in limiting the total ion dose during the profile (from the analysis and sputtering beams in ToF-SIMS).

Compared to low-energy Ar^+, $Ar_{500}{}^+$ clusters allow us to sensibly reduce the fragmentation of organic molecules thanks to the lower energy-per-atom and the lower implantation depth. However, non-optimized cluster beams result in the preferential sputtering of organic molecules and are inefficient on metals, in particular for the sputtering of small metal clusters (Au, Pb^0). This limitation can be attenuated by choosing few-hundred-atoms clusters and by increasing the energy above 10 keV. In the explored range, the best conditions to profile hybrid perovskites are with 500 eV Cs^+ and $Ar_{500}{}^+$ at 20 keV. In these conditions, we obtain extremely stable ToF-SIMS molecular profiles, stable ratio indicators, and high sputtering rates (few nm/s). In ToF-SIMS profiles, low-energy Cs^+ sputtering sensibly increases the negative ionization yields.

While Ar^+ provides for highest sputtering rate, XPS depth profiles have shown that the surface stoichiometry of the perovskite (I/Pb^{+2}) is slightly altered by the Ar^+ beam, which also strongly reduces the Ti atoms from TiO_2 by the preferential sputtering of oxygen. The best conditions have been successfully applied to depth profile PSCs, resulting in well-defined interfaces and intense molecular signals. These results are believed to be helpful in guiding the choice of the sputtering beam conditions in a wider range of hybrid materials.

Supplementary Materials: The following are available online at http://www.mdpi.com/1996-1944/12/5/726/s1, Figure S1: ToF-SIMS depth profiles acquired on Perovskite/cTiO2 model samples obtained with 500 eV Ar^+ beam. The bottom panel (b) refers to the perovskite region and indicate (i) a preferential sputtering of inorganic species ($PbI3^-/CN^-$ ratio) and (ii) a slowly increasing fragmentation of organic molecules ($CN^-/FAI2^-$ curve), Figure S2: ToF-SIMS depth profiles acquired on Perovskite/cTiO2 model samples obtained with large cluster beams. Constant profiles indicate the non-accumulation of damages. (a, c) $Ar4000^+$ at 10 keV (E/n = 2.5 eV). (b, d) $Ar1000^+$ at 10 keV (E/n = 10 eV). Bottom panels refer to the perovskite region and indicate (i) a higher preferential sputtering of organic species with n = 4000 clusters ($PbI3^-/CN^-$ ratios) and (ii) a similar fragmentation of organic molecules ($CN^-/FAI2^-$ curves), Figure S3: AFM profile of the crater region (grey region) after 40 s of sputtering with $Ar500^+$ beam at 20 keV. The crater depth is ~200 nm which corresponds to the sputtering yield of ~5 nm/s, Figure S4: AFM image of the pristine perovskite layer before the sputtering.

Author Contributions: Conceptualization and methodology, C.N., A.F., and Y.B.; depth profile analysis, C.N., V.S., A.F., and Y.B.; samples, S.P., A.A. and A.d.C.; original draft preparation, C.N.; writing—review and editing, all authors; supervision, Y.B.

Funding: The access to the TOF-SIMS/AFM instrument was financially supported by the HERCULES foundation. Part of this project has received funding from the European Union's Horizon 2020 research and innovation program under both Grant Agreement No.688225 and Grant agreement No 785219—GrapheneCore2.

Conflicts of Interest: The authors declare no conflict of interest.

References

1. Saliba, M.; Matsui, T.; Seo, J.-Y.; Domanski, K.; Correa-Baena, J.-P.; Nazeeruddin, M.K.; Zakeeruddin, S.M.; Tress, W.; Abate, A.; Hagfeldt, A.; et al. Cesium-Containing Triple Cation Perovskite Solar Cells: Improved Stability, Reproducibility and High Efficiency. *Energy Environ. Sci.* **2016**, *9*, 1989–1997. [CrossRef] [PubMed]
2. Saliba, M.; Matsui, T.; Domanski, K.; Seo, J.-Y.; Ummadisingu, A.; Zakeeruddin, S.M.; Correa-Baena, J.-P.; Tress, W.R.; Abate, A.; Hagfeldt, A.; et al. Incorporation of Rubidium Cations into Perovskite Solar Cells Improves Photovoltaic Performance. *Science* **2016**, *354*, 206–209. [CrossRef] [PubMed]
3. Abdi-Jalebi, M.; Andaji-Garmaroudi, Z.; Cacovich, S.; Stavrakas, C.; Philippe, B.; Richter, J.M.; Alsari, M.; Booker, E.P.; Hutter, E.M.; Pearson, A.J.; et al. Maximizing and Stabilizing Luminescence from Halide Perovskites with Potassium Passivation. *Nature* **2018**, *555*, 497–501. [CrossRef] [PubMed]
4. Singh, T.; Miyasaka, T. Stabilizing the Efficiency Beyond 20% with a Mixed Cation Perovskite Solar Cell Fabricated in Ambient Air under Controlled Humidity. *Adv. Energy Mater.* **2018**, *8*, 1700677. [CrossRef]
5. Yang, W.S.; Park, B.-W.; Jung, E.H.; Jeon, N.J.; Kim, Y.C.; Lee, D.U.; Shin, S.S.; Seo, J.; Kim, E.K.; Noh, J.H.; et al. Iodide Management in Formamidinium-Lead-Halide–Based Perovskite Layers for Efficient Solar Cells. *Science* **2017**, *356*, 1376–1379. [CrossRef] [PubMed]
6. Lira-Cantú, M. Perovskite Solar Cells: Stability Lies at Interfaces. *Nat. Energy* **2017**, *2*, 17115. [CrossRef]

7. Arora, N.; Dar, M.I.; Hinderhofer, A.; Pellet, N.; Schreiber, F.; Zakeeruddin, S.M.; Grätzel, M. Perovskite Solar Cells with CuSCN Hole Extraction Layers Yield Stabilized Efficiencies Greater than 20%. *Science* **2017**, *358*, 768–771. [CrossRef] [PubMed]
8. Agresti, A.; Pescetelli, S.; Busby, Y.; Aernouts, T. Thermally Induced Fullerene Domain Coarsening Process in Organic Solar Cells. *IEEE Trans. Electron Devices* **2019**, *66*, 678–688. [CrossRef]
9. Busby, Y.; Agresti, A.; Pescetelli, S.; Di Carlo, A.; Noel, C.; Pireaux, J.-J.; Houssiau, L. Aging Effects in Interface-Engineered Perovskite Solar Cells with 2D Nanomaterials: A Depth Profile Analysis. *Mater. Today Energy* **2018**, *9*, 1–10. [CrossRef]
10. Palma, A.L.; Cinà, L.; Busby, Y.; Marsella, A.; Agresti, A.; Pescetelli, S.; Pireaux, J.-J.; Di Carlo, A. Mesoscopic Perovskite Light-Emitting Diodes. *ACS Appl. Mater. Interfaces* **2016**, *8*, 26989–26997. [CrossRef] [PubMed]
11. Christians, J.A.; Schulz, P.; Tinkham, J.S.; Schloemer, T.H.; Harvey, S.P.; Tremolet de Villers, B.J.; Sellinger, A.; Berry, J.J.; Luther, J.M. Tailored Interfaces of Unencapsulated Perovskite Solar Cells for >1,000 Hour Operational Stability. *Nat. Energy* **2018**, *3*, 68–74. [CrossRef]
12. Ralaiarisoa, M.; Busby, Y.; Frisch, J.; Salzmann, I.; Pireaux, J.-J.; Koch, N. Correlation of Annealing Time with Crystal Structure, Composition, and Electronic Properties of $CH_3NH_3PbI_{3-x}Cl_x$ Mixed-Halide Perovskite Films. *Phys. Chem. Chem. Phys.* **2017**, *19*, 23–25. [CrossRef] [PubMed]
13. Matteocci, F.; Busby, Y.; Pireaux, J.-J.; Divitini, G.; Cacovich, S.; Ducati, C.; Di Carlo, A. Interface and Composition Analysis on Perovskite Solar Cells. *ACS Appl. Mater. Interfaces* **2015**, *7*, 26176–26183. [CrossRef] [PubMed]
14. Wang, Z.; Liu, B.; Zhao, E.W.; Jin, K.; Du, Y.; Neeway, J.J.; Ryan, J.V.; Hu, D.; Zhang, K.H.L.; Hong, M.; et al. Argon Cluster Sputtering Source for ToF-SIMS Depth Profiling of Insulating Materials: High Sputter Rate and Accurate Interfacial Information. *J. Am. Soc. Mass Spectrom.* **2015**, *26*, 1283–1290. [CrossRef] [PubMed]
15. Rabbani, S.; Barber, A.M.; Fletcher, J.S.; Lockyer, N.P.; Vickerman, J.C. TOF-SIMS with Argon Gas Cluster Ion Beams: A Comparison with C_{60}^+. *Anal. Chem.* **2011**, *83*, 3793–3800. [CrossRef] [PubMed]
16. Ninomiya, S.; Ichiki, K.; Yamada, H.; Nakata, Y.; Seki, T.; Aoki, T.; Matsuo, J. Molecular Depth Profiling of Multilayer Structures of Organic Semiconductor Materials by Secondary Ion Mass Spectrometry with Large Argon Cluster Ion Beams. *Rapid Commun. Mass Spectrom.* **2009**, *23*, 3264–3268. [CrossRef] [PubMed]
17. Brison, J.; Muramoto, S.; Castner, D.G. ToF-SIMS Depth Profiling of Organic Films: A Comparison between Single-Beam and Dual-Beam Analysis. *J. Phys. Chem. C* **2010**, *114*, 5565–5573. [CrossRef] [PubMed]
18. Postawa, Z. Sputtering Simulations of Organic Overlayers on Metal Substrates by Monoatomic and Clusters Projectiles. *Appl. Surf. Sci.* **2004**, *231–232*, 22–28. [CrossRef]
19. Aoki, T. Molecular Dynamics Simulations of Cluster Impacts on Solid Targets: Implantation, Surface Modification, and Sputtering. *J. Comput. Electron.* **2014**, *13*, 108–121. [CrossRef]
20. Delcorte, A.; Moshkunov, K.; Debongnie, M. Relationships between Crater and Sputtered Material Characteristics in Large Gas Cluster Sputtering of Polymers: Results from Molecular Dynamics Simulations. *J. Vac. Sci. Technol. B Nanotechnol. Microelectron. Mater. Process. Meas. Phenom.* **2018**, *36*, 03F109. [CrossRef]
21. Lozano, O.; Chen, Q.Y.; Tilakaratne, B.P.; Seo, H.W.; Wang, X.M.; Wadekar, P.V.; Chinta, P.V.; Tu, L.W.; Ho, N.J.; Wijesundera, D.; et al. Evolution of Nanoripples on Silicon by Gas Cluster-Ion Irradiation. *AIP Adv.* **2013**, *3*, 062107. [CrossRef]
22. Conard, T.; Fleischmann, C.; Havelund, R.; Franquet, A.; Poleunis, C.; Delcorte, A.; Vandervorst, W. Inorganic Material Profiling Using Ar n + Cluster: Can We Achieve High Quality Profiles? *Appl. Surf. Sci.* **2018**, *444*, 633–641. [CrossRef]
23. Tilakaratne, B.; Chen, Q.; Chu, W.-K. Self-Assembled Gold Nano-Ripple Formation by Gas Cluster Ion Beam Bombardment. *Materials* **2017**, *10*, 1056. [CrossRef] [PubMed]
24. Barlow, A.J.; Portoles, J.F.; Cumpson, P.J. Observed Damage during Argon Gas Cluster Depth Profiles of Compound Semiconductors. *J. Appl. Phys.* **2014**, *116*, 054908. [CrossRef]
25. Fleischmann, C.; Conard, T.; Havelund, R.; Franquet, A.; Poleunis, C.; Voroshazi, E.; Delcorte, A.; Vandervorst, W. Fundamental Aspects of Ar n + SIMS Profiling of Common Organic Semiconductors: Organic Depth Profiling. *Surf. Interface Anal.* **2014**, *46*, 54–57. [CrossRef]
26. Czerwinski, B.; Delcorte, A. Molecular Dynamics Study of Fullerite Cross-Linking under KeV C 60 and Arn Cluster Bombardment. *J. Phys. Chem. C* **2013**, *117*, 3595–3604. [CrossRef]

27. Tuccitto, N.; Bombace, A.; Torrisi, A.; Licciardello, A. Effect of Sputtering Yield Changes on the Depth Resolution in Cluster Beam Depth-Profiling of Polymers. *J. Vac. Sci. Technol. B Nanotechnol. Microelectron. Mater. Process. Meas. Phenom.* **2018**, *36*, 03F124. [CrossRef]
28. Smith, E.F.; Counsell, J.D.P.; Bailey, J.; Sharp, J.S.; Alexander, M.R.; Shard, A.G.; Scurr, D.J. Sample Rotation Improves Gas Cluster Sputter Depth Profiling of Polymers. *Surf. Interface Anal.* **2017**, *49*, 953–959. [CrossRef]
29. Ellsworth, A.A.; Young, C.N.; Stickle, W.F.; Walker, A.V. New Horizons in Sputter Depth Profiling Inorganics with Giant Gas Cluster Sources: Niobium Oxide Thin Films. *Surf. Interface Anal.* **2017**, *49*, 991–999. [CrossRef]
30. Niehuis, E.; Möllers, R.; Rading, D.; Cramer, H.-G.; Kersting, R. Analysis of Organic Multilayers and 3D Structures Using Ar Cluster Ions. *Surf. Interface Anal.* **2013**, *45*, 158–162. [CrossRef]
31. Angerer, T.B.; Blenkinsopp, P.; Fletcher, J.S. High Energy Gas Cluster Ions for Organic and Biological Analysis by Time-of-Flight Secondary Ion Mass Spectrometry. *Int. J. Mass Spectrom.* **2015**, *377*, 591–598. [CrossRef]
32. Houssiau, L.; Mine, N. Molecular Depth Profiling with Reactive Ions, or Why Chemistry Matters in Sputtering. *Surf. Interface Anal.* **2011**, *43*, 146–150. [CrossRef]
33. Wehbe, N.; Pireaux, J.-J.; Houssiau, L. XPS Evidence for Negative Ion Formation in SIMS Depth Profiling of Organic Material with Cesium. *J. Phys. Chem. C* **2014**, *118*, 26613–26620. [CrossRef]
34. Noel, C.; Houssiau, L. Hybrid Organic/Inorganic Materials Depth Profiling Using Low Energy Cesium Ions. *J. Am. Soc. Mass Spectrom.* **2016**, *27*, 908–916. [CrossRef] [PubMed]
35. Eames, C.; Frost, J.M.; Barnes, P.R.F.; O'Regan, B.C.; Walsh, A.; Islam, M.S. Ionic Transport in Hybrid Lead Iodide Perovskite Solar Cells. *Nat. Commun.* **2015**, *6*, 7497. [CrossRef] [PubMed]

Supporting Information

Hybrid perovskites depth profiling with variable-size argon clusters and monatomic ions beams

Céline Noël [1], Sara Pescetelli [2], Antonio Agresti [2], Alexis Franquet [3], Valentina Spampinato [3], Alexandre Felten [4], Aldo di Carlo [2], Laurent Houssiau [1] and Yan Busby [1,*]

[1] Laboratoire Interdisciplinaire de Spectroscopie Electronique, Namur Institute of Structured Matter, University of Namur, 5000 Namur, Belgium; celine.noel@unamur.be (C.N.); laurent.houssiau@unamur.be (L.H.)
[2] C.H.O.S.E. - Centre for Hybrid and Organic Solar Energy, Department of Electronic Engineering, University of Rome Tor Vergata, 00133 Rome, Italy; pescetel@uniroma2.it (S.P.); antonio.agresti@uniroma2.it (A.A.); aldo.dicarlo@uniroma2.it (A.C.)
[3] IMEC, 3000 Leuven, Belgium; Alexis.Franquet@imec.be (A.F.); Valentina.Spampinato@imec.be (V.S.)
[4] SIAM platform, University of Namur, 5000 Namur, Belgium; alexandre.felten@unamur.be (A.F.)
* Correspondence: busbyan@gmail.com

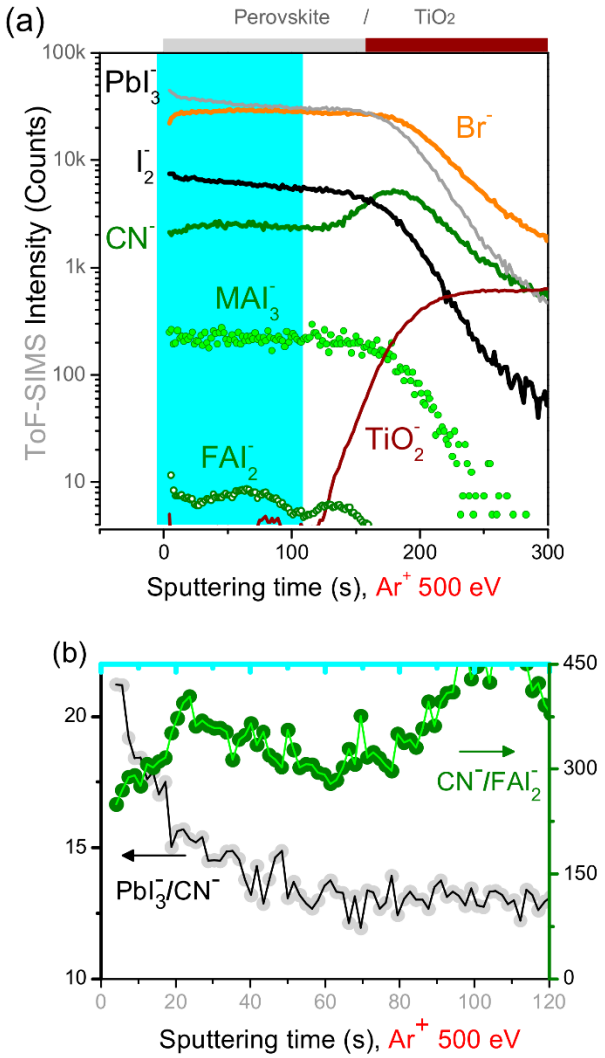

Figure S1. ToF-SIMS depth profiles acquired on Perovskite/cTiO$_2$ model samples obtained with 500 eV Ar$^+$ beam. The bottom panel (**b**) refers to the perovskite region and indicate (i) a preferential sputtering of inorganic species (PbI_3^-/CN^- ratio) and (ii) a slowly increasing fragmentation of organic molecules (CN^-/FAI_2^- curve).

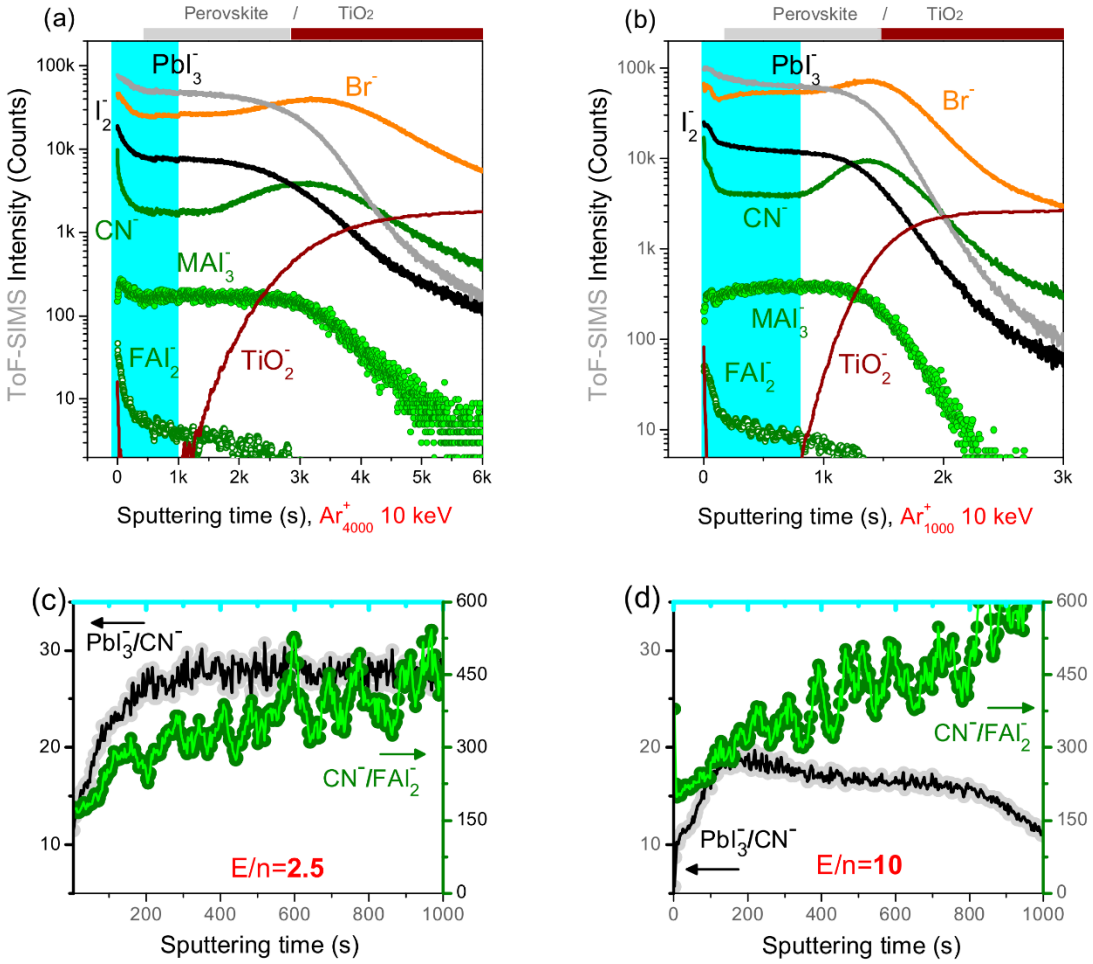

Figure S2. ToF-SIMS depth profiles acquired on Perovskite/cTiO2 model samples obtained with large cluster beams. Constant profiles indicate the non-accumulation of damages. (**a**, **c**) Ar4000+ at 10 keV (E/n=2.5 eV). (**b**, **d**) Ar1000+ at 10 keV (E/n=10 eV). Bottom panels refer to the perovskite region and indicate (i) a higher preferential sputtering of organic species with n=4000 clusters (PbI3-/CN- ratios) and (ii) a similar fragmentation of organic molecules (CN-/FAI2- curves).

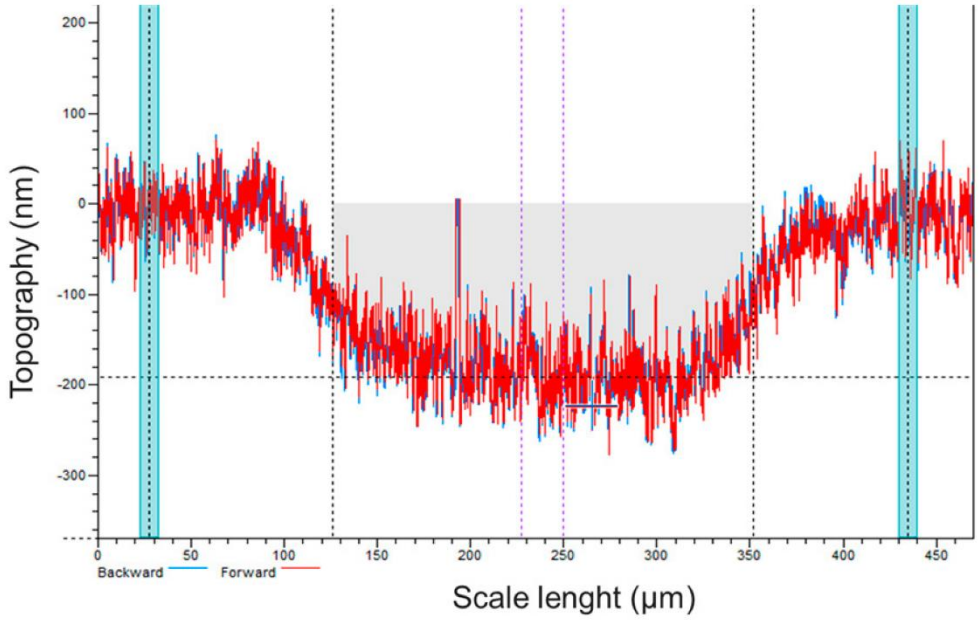

Figure S3. AFM profile of the crater region (grey region) after 40 s of sputtering with Ar_{500}^{+} beam at 20 keV. The crater depth is ~200 nm which corresponds to the sputtering yield of ~5 nm/s.

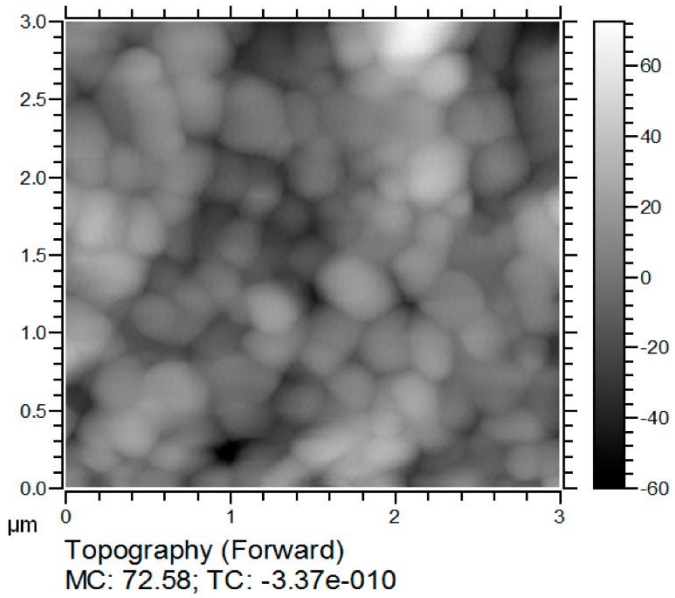

Figure S4. AFM image of the pristine perovskite layer before the sputtering.

5 CONCLUSION AND PERSPECTIVES

The development of modern optoelectronic devices such as solar cells and OLEDs requires to fabricate more and more complex hybrid organic/inorganic multilayers. Their macroscopic device behavior is governed by nanoscale phenomena taking place in layers and interfaces, which are increasingly more complex and numerous. In order to improve the device performance, there is an urgent need for better identifying in-depth degradation mechanisms to propose rational solutions.

For this purpose, ToF-SIMS is a suitable analysis technique, providing the 3D molecular distribution of both organic and inorganic materials, with unprecedented depth and lateral resolutions. Nonetheless, while primary ions based on large clusters, and in particular Ar GCIBs, have shown their ability to preserve intense and fairly intact molecular signals, and to provide high sputtering yields on organic materials, the erosion rate can be unfortunately reduced up to three orders of magnitude for inorganic thin layers. Such a high differential sputtering effect leads to the generation of artifacts during the study of hybrid samples: practically, it can lead to induced roughness, inorganic atoms injection inside the soft material, increasing fragmentation of organic semiconductors, preferential sputtering of the organic fragments, etc.

In order to ensure a more reliable identification of the intrinsic materials alterations affecting the devices performances and stability, one should carefully select the experimental parameters in order to limit the beam-induced modifications during depth profile analysis.

The dual beam operation mode, allowing for individually optimizing the erosion beam and analysis beam conditions is advisable to obtain good profiles since both guns can significantly influence the final depth profile accuracy. From the obtained results we can identify best-practice recommendations for both ion beams.

(i) Choice of the erosion beam conditions

Large Ar_n^+ clusters (n>1000 atoms) are identified as the best choice for organic thin layers. As it was previously demonstrated in many studies, they provide high rates, while preserving the chemical structure of fragile organic (and possibly biological) materials. The possibility of varying both the energy (few keV to tens of keV) and size (from ~100 to 2000 atoms) of Ar-GCIB makes it a very versatile source; however, the results will critically depend on this complex energy/size selection. Namely, to profile inorganic materials, the cluster size should be kept below ~300 atoms and the energy above 10 keV.

Alternately, to Ar GCIBs, we explore the ability of low-energy cesium sputter source to depth profile hybrid multilayers. Cs allows avoiding difficult sample pre-treatments (such as electrode

removal) and changing the ion beam parameter during the full stack analysis. In model Tyr/gold/Tyr hybrid multilayers, the amino acid layer sputtering yield is found to be unchanged before and after crossing the metal layer; furthermore, the ratio between the two sputtering yields is moderate (5.5). This ratio sensibly increases (17) when gold is replaced by chromium. When profiling the Tyr/Cr/Tyr structure, the Tyr sputtering yield is reduced by a factor of three after crossing the inorganic layer. Moreover, in both organic and hybrid model samples, a depth resolution as high as 4 nm is measured.

The fragmentation by Cs beam sometimes hinders the differentiation between too similar organic molecules, as it was shown for Poly-TPD and BCPO:FIrpic. In order to limit that effect, I would recommend not increasing the Cs ion beam energy above 1 keV when profiling organic layers. This is in agreement with previous (unsuccessful) attempts to depth profile conductive polymers using 2 keV Cs^+ (J.-P. Barnes group at CEA).[107] The Cs beam ensures high-intensity molecular signals thanks to the increase of the negative ionization probability. This allowed using cesium sputtering to profile a broad range of applied materials, to identify defects in next-generation perovskite solar cells.

ToF-SIMS depth profiling with low-energy Cs was applied to investigate, in a comparative way, solar aged Interface-engineered PSCs. For the study of such complex hybrid materials, 20 keV Ar_{500}^+ clusters resulted also as suitable sputtering conditions. The relatively high energy-per-atom value in small-size energetic Ar clusters allows to have similar erosion rates on hard and soft materials and to prevent damage accumulation during the profile. These properties are also achieved with monatomic Cs beam thanks to its peculiar chemical reactivity.

(ii) Choice of the analysis beam conditions

In parallel to the erosion beam, the analysis beam also influences dramatically the quality of the depth profile. This was attributed to its high energy (25-30 keV) compared to the erosion beam (~1 keV), despite the fact that the involved currents are much lower. Therefore, if an accurate identification of molecular signals is required, the relative fluence should be kept as low as possible by reducing the number of frames, reducing the Bi current, increasing the analysis raster size and increasing the sputtering time per cycle.

On amino acids delta layers, the depth resolution increased by ~20 % (~1 nm) when halving the bismuth fluence. In addition, the results were significantly improved when replacing Ga^+ primary ion with Bi^+, and even more with Bi_3^+, testifying the importance of the primary ion species. The vast majority of modern instruments exploit Bi analysis source since these ions proved their superiority over the previously used Ga sources. The size of the small cluster Bi_n^+ should be selected considering the trade-off between the current (increasing the count rate)

and the penetration depth (damage rate). For example, compared to Bi^+, Bi_3^+ ions provide higher molecular intensities on organic layers, however, the signal from elemental traces in inorganic bulks is lower because of the lower current.

On the perspectives, for amino acid delta layers, or on model hybrid multilayers, I would carry a systematic study of the influence of the energy, size or raster size associated with the analysis beam. This would give an insight on the ultimate depth resolution that can be achieved using cesium sputtering ions when the fluence of the analysis gun is kept to a minimum.

It would also be important to further challenge the capacities of ToF-SIMS by considering an even higher level of device complexity; for example, polymers could be replaced by biological films, that are more sensitive to fragmentation and for which high-mass ions identification is usually required. This might possibly tilt the balance in favor of Ar clusters. The imaging capability of different ion sources, and in particular the final lateral resolution should be also investigated more in-depth by realizing model samples with controlled buried 3D features.

To our knowledge, no systematic comparison of Cs, Ar clusters and C_{60} were performed on state-of-the-art solar cells so far. This would allow refining the recommendations regarding the best conditions for the accurate in-depth characterization of those devices. Such experiments are being conducted in collaboration with IMEC.

6 BIBLIOGRAPHY

(1) Shirakawa, H.; Louis, E. J.; MacDiarmid, A. G.; Chiang, C. K.; Heeger, A. J. Synthesis of Electrically Conducting Organic Polymers: Halogen Derivatives of Polyacetylene, (CH) x. *Journal of the Chemical Society, Chemical Communications* **1977**, 578. https://doi.org/10.1039/c39770000578.

(2) Nelson, J. Organic Photovoltaic Films. *Current Opinion in Solid State and Materials Science* **2002**, *6* (1), 87–95. https://doi.org/10.1016/S1359-0286(02)00006-2.

(3) Burroughes, J. H.; Bradley, D. D. C.; Brown, A. R.; Marks, R. N.; Mackay, K.; Friend, R. H.; Burns, P. L.; Holmes, A. B. Light-Emitting Diodes Based on Conjugated Polymers. *Nature* **1990**, *347* (6293), 539–541. https://doi.org/10.1038/347539a0.

(4) Koezuka, H.; Tsumura, A.; Ando, T. Field-Effect Transistor with Polythiophene Thin Film. *Synthetic Metals* **1987**, *18* (1), 699–704. https://doi.org/10.1016/0379-6779(87)90964-7.

(5) Novák, P.; Müller, K.; Santhanam, K. S. V.; Haas, O. Electrochemically Active Polymers for Rechargeable Batteries. *Chem. Rev.* **1997**, *97* (1), 207–282. https://doi.org/10.1021/cr941181o.

(6) Correa-Baena, J.-P.; Saliba, M.; Buonassisi, T.; Grätzel, M.; Abate, A.; Tress, W.; Hagfeldt, A. Promises and Challenges of Perovskite Solar Cells. *Science* **2017**, *358* (6364), 739–744. https://doi.org/10.1126/science.aam6323.

(7) Jeon, N. J.; Na, H.; Jung, E. H.; Yang, T.-Y.; Lee, Y. G.; Kim, G.; Shin, H.-W.; Il Seok, S.; Lee, J.; Seo, J. A Fluorene-Terminated Hole-Transporting Material for Highly Efficient and Stable Perovskite Solar Cells. *Nature Energy* **2018**, *3* (8), 682–689. https://doi.org/10.1038/s41560-018-0200-6.

(8) Kojima, A.; Teshima, K.; Shirai, Y.; Miyasaka, T. Organometal Halide Perovskites as Visible-Light Sensitizers for Photovoltaic Cells. *Journal of the American Chemical Society* **2009**, *131* (17), 6050–6051. https://doi.org/10.1021/ja809598r.

(9) Docampo, P.; Ball, J. M.; Darwich, M.; Eperon, G. E.; Snaith, H. J. Efficient Organometal Trihalide Perovskite Planar-Heterojunction Solar Cells on Flexible Polymer Substrates. *Nature Communications* **2013**, *4*, 2761. https://doi.org/10.1038/ncomms3761.

(10) Mouhib, T.; Poleunis, C.; Wehbe, N.; Michels, J. J.; Galagan, Y.; Houssiau, L.; Bertrand, P.; Delcorte, A. Molecular Depth Profiling of Organic Photovoltaic Heterojunction Layers by ToF-SIMS: Comparative Evaluation of Three Sputtering Beams. *Analyst* **2013**, *138* (22), 6801–6810.

(11) Niehuis, E.; Möllers, R.; Rading, D.; Cramer, H.-G.; Kersting, R. Analysis of Organic Multilayers and 3D Structures Using Ar Cluster Ions. *Surface and Interface Analysis* **2013**, *45* (1), 158–162. https://doi.org/10.1002/sia.5079.

(12) Taglauer, E. Low-Energy Ion Scattering and Rutherford Backscattering. In *Surface Analysis – The Principal Techniques*; John Wiley & Sons, Ltd, 2009; pp 269–331. https://doi.org/10.1002/9780470721582.ch6.

(13) Andersen, H. H. *Sputtering by Particle Bombardment*; Springer-Verlag, 1981.

(14) Maul, J.; Wittmaack, K. Secondary Ion Emission from Silicon and Silicon Oxide. *Surface Science* **1975**, *47* (1), 358–369. https://doi.org/10.1016/0039-6028(75)90300-3.

(15) Shard, A. G.; Spencer, S. J.; Smith, S. A.; Havelund, R.; Gilmore, I. S. The Matrix Effect in Organic Secondary Ion Mass Spectrometry. *International Journal of Mass Spectrometry* **2015**, *377*, 599–609. https://doi.org/10.1016/j.ijms.2014.06.027.

(16) Brison, J. On the Understanding of Ionization and Cluster Formation Processes during ToF-SIMS Depth Profiling by Co- Sputtering Cesium and Xenon.

(17) Vickerman, J. C.; Briggs, D. *ToF-SIMS: Materials Analysis by Mass Spectrometry*; IM Publications, 2013.

(18) Brison, J.; Robinson, M. A.; Benoit, D. S. W.; Muramoto, S.; Stayton, P. S.; Castner, D. G. TOF-SIMS 3D Imaging of Native and Non-Native Species within HeLa Cells. *Analytical Chemistry* **2013**, *85* (22), 10869–10877. https://doi.org/10.1021/ac402288d.

(19) Wiley, W. C.; McLaren, I. H. Time-of-Flight Mass Spectrometer with Improved Resolution. *Review of Scientific Instruments* **1955**, *26* (12), 1150–1157. https://doi.org/10.1063/1.1715212.
(20) Haney, L. L.; Riederer, D. E. Delayed Extraction for Improved Resolution of Ion/Surface Collision Products by Time-of-Flight Mass Spectrometry. *Analytica Chimica Acta* **1999**, *397* (1–3), 225–233. https://doi.org/10.1016/S0003-2670(99)00407-9.
(21) Vanbellingen, Q. P.; Elie, N.; Eller, M. J.; Della-Negra, S.; Touboul, D.; Brunelle, A. Time-of-Flight Secondary Ion Mass Spectrometry Imaging of Biological Samples with Delayed Extraction for High Mass and High Spatial Resolutions. *Rapid Communications in Mass Spectrometry* **2015**, *29* (13), 1187–1195. https://doi.org/10.1002/rcm.7210.
(22) Noel, C. Profilage à l'aide d'ions Primaires Césium de Basse Énergie d'acides Aminés En ToF-SIMS: Optimisation de La Résolution En Profondeur Avec Une Source d'ions Primaires d'analyse Au Bismuth. 2013.
(23) Brison, J.; Mine, N.; Wehbe, N.; Gillon, X.; Tabarrant, T.; Sporken, R.; Houssiau, L. Molecular Depth Profiling of Model Biological Films Using Low Energy Monoatomic Ions. *International Journal of Mass Spectrometry* **2012**, *321–322*, 1–7. https://doi.org/10.1016/j.ijms.2012.04.001.
(24) Wehbe, N.; Tabarrant, T.; Brison, J.; Mouhib, T.; Delcorte, A.; Bertrand, P.; Moellers, R.; Niehuis, E.; Houssiau, L. TOF-SIMS Depth Profiling of Multilayer Amino-Acid Films Using Large Argon Cluster Ar_n^+, C_{60}^+ and Cs^+ Sputtering Ions: A Comparative Study: ToF-SIMS Depth Profiling of Multilayer Amino-Acid Films. *Surface and Interface Analysis* **2013**, *45* (1), 178–180. https://doi.org/10.1002/sia.5121.
(25) Houssiau, L.; Noël, C.; Mine, N.; Jung, K. W.; Min, W. J.; Moon, D. W. Investigation of Cs Surface Layer Formation in Cs-SIMS with TOF-MEIS and SIMS: Cs Surface Measurement with ToF-MEIS. *Surface and Interface Analysis* **2014**, *46* (S1), 22–24. https://doi.org/10.1002/sia.5614.
(26) Shen, K.; Mao, D.; Garrison, B. J.; Wucher, A.; Winograd, N. Depth Profiling of Metal Overlayers on Organic Substrates with Cluster SIMS. *Analytical Chemistry* **2013**, *85* (21), 10565–10572. https://doi.org/10.1021/ac402658r.
(27) Prabhakaran, A.; Yunus, S.; Wehbe, N.; Bertrand, P.; Delcorte, A. Secondary Ion Yield Enhancement in Organic Samples Due to Au/Pt Nanoparticle Condensation and Their Substrate Effects. *Surface and Interface Analysis* **2011**, *43* (1–2), 74–77. https://doi.org/10.1002/sia.3477.
(28) Prabhakaran, A.; Yin, J.; Nysten, B.; Degand, H.; Morsomme, P.; Mouhib, T.; Yunus, S.; Bertrand, P.; Delcorte, A. Metal Condensates for Low-Molecular-Weight Matrix-Free Laser Desorption/Ionization. *International Journal of Mass Spectrometry* **2012**, *315*, 22–30. https://doi.org/10.1016/j.ijms.2012.02.009.
(29) What Is Sputtering? Magnetron Sputtering? http://www.semicore.com/what-is-sputtering (accessed Mar 20, 2019).
(30) Hofmann, S. From Depth Resolution to Depth Resolution Function: Refinement of the Concept for Delta Layers, Single Layers and Multilayers. *Surface and Interface Analysis* **1999**, *27* (9), 825–834. https://doi.org/10.1002/(SICI)1096-9918(199909)27:9<825::AID-SIA638>3.0.CO;2-D.
(31) Hofmann, S. Ultimate Depth Resolution and Profile Reconstruction in Sputter Profiling with AES and SIMS. *Surface and Interface Analysis* **2000**, *30* (1), 228–236. https://doi.org/10.1002/1096-9918(200008)30:1<228::AID-SIA821>3.0.CO;2-E.
(32) Delcorte, A.; Bertrand, P.; Arys, X.; Jonas, A.; Wischerhoff, E.; Mayer, B.; Laschewsky, A. ToF-SIMS Study of Alternate Polyelectrolyte Thin Films: Chemical Surface Characterization and Molecular Secondary Ions Sampling Depth. *Surface Science* **1996**, *366* (1), 149–165. https://doi.org/10.1016/0039-6028(96)00779-0.
(33) Zalar, A. Improved Depth Resolution by Sample Rotation during Auger Electron Spectroscopy Depth Profiling. *Thin Solid Films* **1985**, *124* (3), 223–230. https://doi.org/10.1016/0040-6090(85)90269-X.

(34) Grehl, T.; Moellers, R.; Niehuis, E. Low Energy Dual Beam Depth Profiling: Influence of Sputter and Analysis Beam Parameters on Profile Performance Using TOF-SIMS. *Applied surface science* **2003**, *203*, 277–280.
(35) Brison, J.; Muramoto, S.; Castner, D. G. ToF-SIMS Depth Profiling of Organic Films: A Comparison between Single-Beam and Dual-Beam Analysis †. *The Journal of Physical Chemistry C* **2010**, *114* (12), 5565–5573. https://doi.org/10.1021/jp9066179.
(36) Dowsett, M. G. Depth Profiling Using Ultra-Low-Energy Secondary Ion Mass Spectrometry. *Applied Surface Science* **2003**, *203–204*, 5–12. https://doi.org/10.1016/S0169-4332(02)00630-X.
(37) Benguerba, M.; Brunelle, A.; Della-Negra, S.; Depauw, J.; Joret, H.; Le Beyec, Y.; Blain, M. G.; Schweikert, E. A.; Assayag, G. B.; Sudraud, P. Impact of Slow Gold Clusters on Various Solids: Nonlinear Effects in Secondary Ion Emission. *Nuclear Instruments and Methods in Physics Research Section B: Beam Interactions with Materials and Atoms* **1991**, *62* (1), 8–22. https://doi.org/10.1016/0168-583X(91)95922-Z.
(38) Gillen, G.; Roberson, S. Preliminary Evaluation of an SF5+ Polyatomic Primary Ion Beam for Analysis of Organic Thin Films by Secondary Ion Mass Spectrometry. *Rapid Communications in Mass Spectrometry* **1998**, *12* (19), 1303–1312. https://doi.org/10.1002/(SICI)1097-0231(19981015)12:19<1303::AID-RCM330>3.0.CO;2-7.
(39) Tian, H.; Wucher, A.; Winograd, N. Molecular Imaging of Biological Tissue Using Gas Cluster Ions. *Surface and Interface Analysis* **2014**, *46* (S1), 115–117. https://doi.org/10.1002/sia.5509.
(40) Fletcher, J. S.; Lockyer, N. P.; Vaidyanathan, S.; Vickerman, J. C. TOF-SIMS 3D Biomolecular Imaging of *Xenopus Laevis* Oocytes Using Buckminsterfullerene (C_{60}) Primary Ions. *Analytical Chemistry* **2007**, *79* (6), 2199–2206. https://doi.org/10.1021/ac061370u.
(41) Fletcher, J. S.; Rabbani, S.; Barber, A. M.; Lockyer, N. P.; Vickerman, J. C. Comparison of C60 and GCIB Primary Ion Beams for the Analysis of Cancer Cells and Tumour Sections. *Surface and Interface Analysis* **2013**, *45* (1), 273–276. https://doi.org/10.1002/sia.4874.
(42) Shard, A. G.; Ray, S.; Seah, M. P.; Yang, L. VAMAS Interlaboratory Study on Organic Depth Profiling. *Surface and Interface Analysis* **2011**, *43* (9), 1240–1250. https://doi.org/10.1002/sia.3705.
(43) Weibel, D.; Wong, S.; Lockyer, N.; Blenkinsopp, P.; Hill, R.; Vickerman, J. C. A C60 Primary Ion Beam System for Time of Flight Secondary Ion Mass Spectrometry: Its Development and Secondary Ion Yield Characteristics. *Anal. Chem.* **2003**, *75* (7), 1754–1764. https://doi.org/10.1021/ac026338o.
(44) Kollmer, F. Cluster Primary Ion Bombardment of Organic Materials. *Applied Surface Science* **2004**, *231–232*, 153–158. https://doi.org/10.1016/j.apsusc.2004.03.101.
(45) Wucher, A. Molecular Secondary Ion Formation under Cluster Bombardment: A Fundamental Review. *Applied Surface Science* **2006**, *252* (19), 6482–6489. https://doi.org/10.1016/j.apsusc.2006.02.070.
(46) Fletcher, J. S.; Conlan, X. A.; Lockyer, N. P.; Vickerman, J. C. Molecular Depth Profiling of Organic and Biological Materials. *Applied Surface Science* **2006**, *252* (19), 6513–6516. https://doi.org/10.1016/j.apsusc.2006.02.213.
(47) Goacher, R. E.; Gardella, J. A. Analysis of C60+ and Cs+ Sputtering Ions for Depth Profiling Gold/Silicon and GaAs Multilayer Samples by Time of Flight Secondary Ion Mass Spectrometry. *Applied Surface Science* **2010**, *256* (7), 2044–2051. https://doi.org/10.1016/j.apsusc.2009.09.045.
(48) Fahey, A. J.; Gillen, G.; Chi, P.; Mahoney, C. M. Performance of a C60+ Ion Source on a Dynamic SIMS Instrument. *Applied Surface Science* **2006**, *252* (19), 7312–7314. https://doi.org/10.1016/j.apsusc.2006.02.263.
(49) Nieuwjaer, N.; Poleunis, C.; Delcorte, A.; Bertrand, P. Depth Profiling of Polymer Samples Using Ga+ and C60+ Ion Beams. *Surface and Interface Analysis* **2009**, *41* (1), 6–10. https://doi.org/10.1002/sia.2931.

(50) Toyoda, N.; Matsuo, J.; Aoki, T.; Yamada, I.; Fenner, D. B. Secondary Ion Mass Spectrometry with Gas Cluster Ion Beams. **2002**, 5.
(51) Postawa, Z. Sputtering Simulations of Organic Overlayers on Metal Substrates by Monoatomic and Clusters Projectiles. *Applied Surface Science* **2004**, *231–232*, 22–28. https://doi.org/10.1016/j.apsusc.2004.03.019.
(52) Czerwinski, B.; Postawa, Z.; Garrison, B. J.; Delcorte, A. Molecular Dynamics Study of Polystyrene Bond-Breaking and Crosslinking under C60 and Arn Cluster Bombardment. *Nuclear Instruments and Methods in Physics Research Section B: Beam Interactions with Materials and Atoms* **2013**, *303*, 23–27. https://doi.org/10.1016/j.nimb.2012.11.030.
(53) Maciazek, D.; Paruch, R. J.; Postawa, Z.; Garrison, B. J. Micro- and Macroscopic Modeling of Sputter Depth Profiling. *The Journal of Physical Chemistry C* **2016**, *120* (44), 25473–25480. https://doi.org/10.1021/acs.jpcc.6b09228.
(54) Restrepo, O. A.; Gonze, X.; Bertrand, P.; Delcorte, A. Computer Simulations of Cluster Impacts: Effects of the Atomic Masses of the Projectile and Target. *Phys. Chem. Chem. Phys.* **2013**, *15* (20), 7621–7627. https://doi.org/10.1039/C3CP50346A.
(55) Russo, M. F.; Postawa, Z.; Garrison, B. J. A Computational Investigation of C_{60} Depth Profiling of Ag: Molecular Dynamics of Multiple Impact Events. *The Journal of Physical Chemistry C* **2009**, *113* (8), 3270–3276. https://doi.org/10.1021/jp808706y.
(56) Russo, M. F.; Wojciechowski, I. A.; Garrison, B. J. Sputtering of Amorphous Ice Induced by C60 and Au3 Clusters. *Applied Surface Science* **2006**, *252* (19), 6423–6425. https://doi.org/10.1016/j.apsusc.2006.02.243.
(57) Postawa, Z.; Czerwinski, B.; Szewczyk, M.; Smiley, E. J.; Winograd, N.; Garrison, B. J. Enhancement of Sputtering Yields Due to C_{60} versus Ga Bombardment of Ag{111} As Explored by Molecular Dynamics Simulations. *Analytical Chemistry* **2003**, *75* (17), 4402–4407. https://doi.org/10.1021/ac034387a.
(58) Ninomiya, S.; Ichiki, K.; Yamada, H.; Nakata, Y.; Seki, T.; Aoki, T.; Matsuo, J. Molecular Depth Profiling of Multilayer Structures of Organic Semiconductor Materials by Secondary Ion Mass Spectrometry with Large Argon Cluster Ion Beams. *Rapid Communications in Mass Spectrometry* **2009**, *23* (20), 3264–3268. https://doi.org/10.1002/rcm.4250.
(59) Bailey, J.; Havelund, R.; Shard, A. G.; Gilmore, I. S.; Alexander, M. R.; Sharp, J. S.; Scurr, D. J. 3D ToF-SIMS Imaging of Polymer Multilayer Films Using Argon Cluster Sputter Depth Profiling. *ACS Applied Materials & Interfaces* **2015**, *7* (4), 2654–2659. https://doi.org/10.1021/am507663v.
(60) Rabbani, S.; Barber, A. M.; Fletcher, J. S.; Lockyer, N. P.; Vickerman, J. C. TOF-SIMS with Argon Gas Cluster Ion Beams: A Comparison with C_{60}^{+}. *Analytical Chemistry* **2011**, *83* (10), 3793–3800. https://doi.org/10.1021/ac200288v.
(61) Fleischmann, C.; Conard, T.; Havelund, R.; Franquet, A.; Poleunis, C.; Voroshazi, E.; Delcorte, A.; Vandervorst, W. Fundamental Aspects of Ar_n^{+} SIMS Profiling of Common Organic Semiconductors: Organic Depth Profiling. *Surface and Interface Analysis* **2014**, *46* (S1), 54–57. https://doi.org/10.1002/sia.5621.
(62) Czerwinski, B.; Delcorte, A. Molecular Dynamics Study of Fullerite Cross-Linking under KeV C_{60} and Ar_n Cluster Bombardment. *The Journal of Physical Chemistry C* **2013**, *117* (7), 3595–3604. https://doi.org/10.1021/jp310635g.
(63) Conard, T.; Fleischmann, C.; Havelund, R.; Franquet, A.; Poleunis, C.; Delcorte, A.; Vandervorst, W. Inorganic Material Profiling Using Ar n + Cluster: Can We Achieve High Quality Profiles? *Applied Surface Science* **2018**, *444*, 633–641. https://doi.org/10.1016/j.apsusc.2018.02.159.
(64) Ellsworth, A. A.; Young, C. N.; Stickle, W. F.; Walker, A. V. New Horizons in Sputter Depth Profiling Inorganics with Giant Gas Cluster Sources: Niobium Oxide Thin Films. *Surface and Interface Analysis 49* (10), 991–999. https://doi.org/10.1002/sia.6259.
(65) Tuccitto, N.; Bombace, A.; Torrisi, A.; Licciardello, A. Effect of Sputtering Yield Changes on the Depth Resolution in Cluster Beam Depth-Profiling of Polymers. *Journal of Vacuum Science &*

Technology B, Nanotechnology and Microelectronics: Materials, Processing, Measurement, and Phenomena **2018**, *36* (3), 03F124. https://doi.org/10.1116/1.5019698.
(66) Smith, E. F.; Counsell, J. D. P.; Bailey, J.; Sharp, J. S.; Alexander, M. R.; Shard, A. G.; Scurr, D. J. Sample Rotation Improves Gas Cluster Sputter Depth Profiling of Polymers. *Surface and Interface Analysis* **2017**, *49* (10), 953–959. https://doi.org/10.1002/sia.6250.
(67) Cheng, J.; Wucher, A.; Winograd, N. Molecular Depth Profiling with Cluster Ion Beams. *The Journal of Physical Chemistry B* **2006**, *110* (16), 8329–8336. https://doi.org/10.1021/jp0573341.
(68) Niehuis, E. Depth Profiling in Organic Electronics. In *ToF-SIMS: Materials Analysis by Mass Spectrometry*; IM Publications, 2013; pp 637–660.
(69) Gillen, G.; Simons, D. S.; Williams, P. Molecular Ion Imaging and Dynamic Secondary-Ion Mass Spectrometry of Organic Compounds. *Analytical Chemistry* **1990**, *62* (19), 2122–2130. https://doi.org/10.1021/ac00218a014.
(70) Shard, A. G.; Green, F. M.; Brewer, P. J.; Seah, M. P.; Gilmore, I. S. Quantitative Molecular Depth Profiling of Organic Delta-Layers by C_{60} Ion Sputtering and SIMS †. *The Journal of Physical Chemistry B* **2008**, *112* (9), 2596–2605. https://doi.org/10.1021/jp077325n.
(71) Muramoto, S.; Brison, J.; Castner, D. G. ToF-SIMS Depth Profiling of Trehalose: The Effect of Analysis Beam Dose on the Quality of Depth Profiles. *Surface and Interface Analysis* **2011**, *43* (1–2), 58–61. https://doi.org/10.1002/sia.3479.
(72) Lewis, R. K.; Morabito, J. M.; Tsai, J. C. C. Primary Oxygen Ion Implantation Effects on Depth Profiles by Secondary Ion Emission Mass Spectrometry. *Applied Physics Letters* **1973**, *23* (5), 260–262. https://doi.org/10.1063/1.1654881.
(73) Wittmaack, K. Secondary Ion Yield Variations Due to Cesium Implantation in Silicon. *Surface Science* **1983**, *126* (1), 573–580. https://doi.org/10.1016/0039-6028(83)90760-4.
(74) Houssiau, L.; Mine, N. Molecular Depth Profiling with Reactive Ions, or Why Chemistry Matters in Sputtering. *Surface and Interface Analysis* **2011**, *43* (1–2), 146–150. https://doi.org/10.1002/sia.3528.
(75) Wehbe, N.; Houssiau, L. Comparative Study of the Usefulness of Low Energy Cs^+, Xe^+, and O_2^+ Ions for Depth Profiling Amino-Acid and Sugar Films. *Analytical Chemistry* **2010**, *82* (24), 10052–10059. https://doi.org/10.1021/ac101696c.
(76) Houssiau, L.; Mine, N. Molecular Depth Profiling of Polymers with Very Low Energy Reactive Ions. *Surface and Interface Analysis* **2010**, *42* (8), 1402–1408. https://doi.org/10.1002/sia.3159.
(77) Mine, N.; Douhard, B.; Brison, J.; Houssiau, L. Molecular Depth-Profiling of Polycarbonate with Low-Energy Cs+ Ions. *Rapid Communications in Mass Spectrometry* **2007**, *21* (16), 2680–2684. https://doi.org/10.1002/rcm.3135.
(78) Sakamoto, T.; Tomiyasu, B.; Owari, M.; Nihei, Y. Ambient Oxygen Effect in Ga+ FIB-SIMS. *Surface and Interface Analysis* **1994**, *22* (1-12), 106–110. https://doi.org/10.1002/sia.740220126.
(79) Havelund, R.; Licciardello, A.; Bailey, J.; Tuccitto, N.; Sapuppo, D.; Gilmore, I. S.; Sharp, J. S.; Lee, J. L. S.; Mouhib, T.; Delcorte, A. Improving Secondary Ion Mass Spectrometry C_{60}^{n+} Sputter Depth Profiling of Challenging Polymers with Nitric Oxide Gas Dosing. *Analytical Chemistry* **2013**, *85* (10), 5064–5070. https://doi.org/10.1021/ac4003535.
(80) Mouhib, T.; Delcorte, A.; Poleunis, C.; Bertrand, P. Organic Secondary Ion Mass Spectrometry: Signal Enhancement by Water Vapor Injection. *Journal of the American Society for Mass Spectrometry* **2010**, *21* (12), 2005–2010. https://doi.org/10.1016/j.jasms.2010.08.013.
(81) Wirtz, T.; Migeon, H.-N. Development of a Column Delivering a Collimated Stream of Cs0 for SIMS Purposes. *Applied Surface Science* **2004**, *231–232*, 940–944. https://doi.org/10.1016/j.apsusc.2004.03.180.
(82) Priebe, A.; Michler, J. Application of a Novel Compact Cs Evaporator Prototype for Enhancing Negative Ion Yields during FIB-TOF-SIMS Analysis in High Vacuum. *Ultramicroscopy* **2019**, *196*, 10–17. https://doi.org/10.1016/j.ultramic.2018.09.008.

(83) Tuccitto, N.; Lobo, L.; Tempez, A.; Delfanti, I.; Chapon, P.; Canulescu, S.; Bordel, N.; Michler, J.; Licciardello, A. Pulsed Radiofrequency Glow Discharge Time-of-Flight Mass Spectrometry for Molecular Depth Profiling of Polymer-Based Films. *Rapid Communications in Mass Spectrometry* **2009**, *23* (5), 549–556. https://doi.org/10.1002/rcm.3906.
(84) Fernandez, B.; Lobo, L.; Tyagi, P.; Stoichkov, V.; Kettle, J.; Pereiro, R. Rapid Evaluation of Different Perovskite Absorber Layers through the Application of Depth Profile Analysis Using Glow Discharge – Time of Flight Mass Spectrometry. *Talanta* **2019**, *192*, 317–324. https://doi.org/10.1016/j.talanta.2018.09.059.
(85) Seah, M. P. Universal Equation for Argon Gas Cluster Sputtering Yields. *The Journal of Physical Chemistry C* **2013**, *117* (24), 12622–12632. https://doi.org/10.1021/jp402684c.
(86) Kennedy, P. E.; Postawa, Z.; Garrison, B. J. Dynamics Displayed by Energetic C_{60} Bombardment of Metal Overlayers on an Organic Substrate. *Analytical Chemistry* **2013**, *85* (4), 2348–2355. https://doi.org/10.1021/ac303348y.
(87) Cumpson, P. J.; Portoles, J. F.; Barlow, A. J.; Sano, N.; Birch, M. Depth Profiling Organic/Inorganic Interfaces by Argon Gas Cluster Ion Beams: Sputter Yield Data for Biomaterials, *in-Vitro* Diagnostic and Implant Applications: Organic/Inorganic Interfaces by GCIB. *Surface and Interface Analysis* **2013**, *45* (13), 1859–1868. https://doi.org/10.1002/sia.5333.
(88) Philipp, P.; Ngo, K. Q.; Kieffer, J.; Wirtz, T. Silver Diffusion in Organic Optoelectronic Devices: Deposition-Related Processes versus Secondary Ion Mass Spectrometry Analysis Artifacts. *The Journal of Physical Chemistry C* **2015**, *119* (41), 23334–23341. https://doi.org/10.1021/acs.jpcc.5b06860.
(89) Tiddia, M.; Mihara, I.; Seah, M. P.; Trindade, G. F.; Kollmer, F.; Roberts, C. J.; Hague, R.; Mula, G.; Gilmore, I. S.; Havelund, R. Chemical Imaging of Buried Interfaces in Organic–Inorganic Devices Using Focused Ion Beam-Time-of-Flight-Secondary-Ion Mass Spectrometry. *ACS Applied Materials & Interfaces* **2019**, *11* (4), 4500–4506. https://doi.org/10.1021/acsami.8b15091.
(90) Iida, S.; Carr, D. M.; Fisher, G. L.; Miyayama, T. Accurate and Reproducible In-Depth Observation of Organic–Inorganic Hybrid Materials Using FIB-TOF-SIMS. *Journal of Vacuum Science & Technology B, Nanotechnology and Microelectronics: Materials, Processing, Measurement, and Phenomena* **2018**, *36* (3), 03F107. https://doi.org/10.1116/1.5013670.
(91) Lin, W. C.; Kovalsky, A.; Wang, Y. C.; Wang, L. L.; Goldberg, S.; Kao, W. L.; Wu, C. Y.; Chang, H. Y.; Shyue, J. J.; Burda, C. Interpenetration of CH3NH3PbI3 and TiO2 Improves Perovskite Solar Cells While TiO2 Expansion Leads to Degradation. *Physical Chemistry Chemical Physics* **2017**, *19*, 21407–21413. https://doi.org/10.1039/c7cp03116e.
(92) Edwards, R.; Mesfin, H. M.; Pospisilova, E.; Poleunis, C.; Bailly, C.; Delcorte, A. Polymer-Matrix Nanocomposites Bombarded by Large Ar Clusters and Low Energy Cs Ions: Sputtering and Topography Development. *Journal of Vacuum Science & Technology B, Nanotechnology and Microelectronics: Materials, Processing, Measurement, and Phenomena* **2018**, *36* (3), 03F118. https://doi.org/10.1116/1.5015989.
(93) Günes, S.; Neugebauer, H.; Sariciftci, N. S. Conjugated Polymer-Based Organic Solar Cells. *Chemical Reviews* **2007**, *107* (4), 1324–1338. https://doi.org/10.1021/cr050149z.
(94) Matteocci, F.; Busby, Y.; Pireaux, J.-J.; Divitini, G.; Cacovich, S.; Ducati, C.; Di Carlo, A. Interface and Composition Analysis on Perovskite Solar Cells. *ACS Applied Materials & Interfaces* **2015**, *7* (47), 26176–26183. https://doi.org/10.1021/acsami.5b08038.
(95) Domanski, K.; Correa-Baena, J.-P.; Mine, N.; Nazeeruddin, M. K.; Abate, A.; Saliba, M.; Tress, W.; Hagfeldt, A.; Grätzel, M. Not All That Glitters Is Gold: Metal-Migration-Induced Degradation in Perovskite Solar Cells. *ACS Nano* **2016**, *10* (6), 6306–6314. https://doi.org/10.1021/acsnano.6b02613.
(96) Christians, J. A.; Schulz, P.; Tinkham, J. S.; Schloemer, T. H.; Harvey, S. P.; Tremolet de Villers, B. J.; Sellinger, A.; Berry, J. J.; Luther, J. M. Tailored Interfaces of Unencapsulated Perovskite

Solar Cells for >1,000 Hour Operational Stability. *Nature Energy* **2018**, *3* (1), 68–74. https://doi.org/10.1038/s41560-017-0067-y.
(97) Harvey, S. P.; Li, Z.; Christians, J. A.; Zhu, K.; Luther, J. M.; Berry, J. J. Probing Perovskite Inhomogeneity beyond the Surface: TOF-SIMS Analysis of Halide Perovskite Photovoltaic Devices. *ACS Applied Materials & Interfaces* **2018**, *10* (34), 28541–28552. https://doi.org/10.1021/acsami.8b07937.
(98) Tortora, L.; Urbini, M.; Fabbri, A.; Branchini, P.; Mariucci, L.; Rapisarda, M.; Barra, M.; Chiarella, F.; Cassinese, A.; Di Capua, F.; et al. Three-Dimensional Characterization of OTFT on Modified Hydrophobic Flexible Polymeric Substrate by Low Energy Cs + Ion Sputtering. *Applied Surface Science* **2018**, *448*, 628–635. https://doi.org/10.1016/j.apsusc.2018.04.097.
(99) Casula, G.; Busby, Y.; Franquet, A.; Spampinato, V.; Houssiau, L.; Bonfiglio, A.; Cosseddu, P. A Flexible Organic Memory Device with a Clearly Disclosed Resistive Switching Mechanism. *Organic Electronics* **2019**, *64*, 209–215. https://doi.org/10.1016/j.orgel.2018.10.018.
(100) Friend, R. H.; Gymer, R. W.; Holmes, A. B.; Burroughes, J. H.; Marks, R. N.; Taliani, C.; Bradley, D. D. C.; Santos, D. A. D.; Brédas, J. L.; Lögdlund, M.; et al. Electroluminescence in Conjugated Polymers. *Nature* **1999**, *397* (6715), 121–128. https://doi.org/10.1038/16393.
(101) Busby, Y.; Agresti, A.; Pescetelli, S.; Di Carlo, A.; Noel, C.; Pireaux, J.-J.; Houssiau, L. Aging Effects in Interface-Engineered Perovskite Solar Cells with 2D Nanomaterials: A Depth Profile Analysis. *Materials Today Energy* **2018**, *9*, 1–10. https://doi.org/10.1016/j.mtener.2018.04.005.
(102) Stranks, S. D.; Eperon, G. E.; Grancini, G.; Menelaou, C.; Alcocer, M. J. P.; Leijtens, T.; Herz, L. M.; Petrozza, A.; Snaith, H. J. Electron-Hole Diffusion Lengths Exceeding 1 Micrometer in an Organometal Trihalide Perovskite Absorber. *Science* **2013**, *342* (6156), 341–344. https://doi.org/10.1126/science.1243982.
(103) Yin, W.-J.; Shi, T.; Yan, Y. Unique Properties of Halide Perovskites as Possible Origins of the Superior Solar Cell Performance. *Advanced Materials* **2014**, *26* (27), 4653–4658. https://doi.org/10.1002/adma.201306281.
(104) Saliba, M.; Correa-Baena, J.-P.; Grätzel, M.; Hagfeldt, A.; Abate, A. Perovskite Solar Cells: From the Atomic Level to Film Quality and Device Performance. *Angewandte Chemie International Edition* **2018**, *57* (10), 2554–2569. https://doi.org/10.1002/anie.201703226.
(105) Yang, W. S.; Park, B.-W.; Jung, E. H.; Jeon, N. J.; Kim, Y. C.; Lee, D. U.; Shin, S. S.; Seo, J.; Kim, E. K.; Noh, J. H.; et al. Iodide Management in Formamidinium-Lead-Halide–Based Perovskite Layers for Efficient Solar Cells. *Science* **2017**, *356* (6345), 1376–1379. https://doi.org/10.1126/science.aan2301.
(106) Saliba, M.; Matsui, T.; Domanski, K.; Seo, J.-Y.; Ummadisingu, A.; Zakeeruddin, S. M.; Correa-Baena, J.-P.; Tress, W. R.; Abate, A.; Hagfeldt, A.; et al. Incorporation of Rubidium Cations into Perovskite Solar Cells Improves Photovoltaic Performance. *Science* **2016**, *354* (6309), 206–209. https://doi.org/10.1126/science.aah5557.
(107) Langer, E. Advanced Chemical Characterization of Organic Electronic Materials and Devices, 2019.

ANNEX I: LIST OF PUBLISHED AND ACCEPTED PAPERS

Houssiau, L.; Noël, C.; Mine, N.; Jung, K. W.; Min, W. J. ; Moon, D. W. Investigation of Cs Surface Layer Formation in Cs-SIMS with TOF-MEIS and SIMS: Cs Surface Measurement with ToF-MEIS. *Surface and Interface Analysis* **2014***,* 46 (S1), 22-24. https://doi.org/10.1002/sia.5614.

Noël, C.; Houssiau, L. Hybrid Organic/Inorganic Materials Depth Profiling Using Low Energy Cesium Ions. *Journal of The American Society for Mass Spectrometry* **2016***,* 27 (5), 908-916. https://doi.org/10.1007/s13361-016-1353-9.

Montaño-Machado, V.; Noël, C.; Chevallier, P.; Turgeon, S.; Houssiau, L.; Pauthe, E.; Pireaux, J.-J. ; Mantovani, D. Interaction of Phosphorylcholine with Fibronectin Coatings: Surface Characterization and Biological Performances. *Applied Surface Science* **2017**, 396, 1613-1622. https://doi.org/10.1016/j.apsusc.2016.11.224.

Busby, Y.; Noël, C.; Pireaux, J.-J.; Agresti, A.; Pescetelli, S.; Di Carlo, A.; Houssiau, L. XPS Depth Profiles of Organo Lead Halide Layers and Full Perovskite Solar Cells by Variable-Size Argon Clusters. *Proceedings of SPIE – The International Society for Optical Engineering* **2018**, 10724, 1072408. https://doi.org/10.1117/12.2320488.

Busby, Y.; Agresti, A.; Pescetelli, S.; Di Carlo, A.; Noel, C.; Pireaux, J.-J.; Houssiau, L. Aging Effects in Interface-Engineered Perovskite Solar Cells with 2D Nanomaterials: A Depth Profile Analysis. *Materials Today Energy* **2018**, 9, 1-10. https://doi.org/10.1016/j.mtener.2018.04.005.

Diaz-Rodriguez, S; Chevallier, P.; Paternoster, C.; Montaño-Machado, V.; Noël, C.; Houssiau, L.; Mantovani, D. Surface Modification and Direct Plasma Amination of L605 CoCr Alloys: On the Optimization of the Oxide Layer for Application in Cardiovascular Implants. *RSC Advances* **2019**, 9 (4), 2292-2301. https://doi.org/10.1039/C8RA08541B.

Noël, C.; Pescetelli, S.; Agresti, A.; Franquet, A.; Spampinato, V.; Felten, A.; di Carlo, A.; Houssiau, L.; Busby, Y. Hybrid Perovskites Depth Profiling with Variable-Size Argon Clusters and Monatomic Ions Beams. *Materials* **2019**, 12 (5), 726. https://doi.org/10.3390/ma12050726.

Noël, C.; Busby, Y.; Mine, N.; Houssiau, L. ToF-SIMS depth profiling of organic delta layers with low-energy cesium ions: depth resolution assessment. Submitted in Journal of The American Society for Mass Spectrometry

Noël, C.; Tuccitto, N.; Busby, Y.; Auer-Berger, M.; Licciardello, A.; List-Kratochvil, E. J. W.; Houssiau, L. Assisted analysis of OLED hybrid stacks by ToF-SIMS depth profiling coupled with Wavelet-PCA. Submitted in ACS Applied Polymer Materials

Investigation of Cs surface layer formation in Cs-SIMS with TOF-MEIS and SIMS

L. Houssiau*(1), C. Noël(1), N. Mine(1), K.W. Jung(2), W.J. Min(3), D.W. Moon*(2)

(1) Research Centre in Physics of Matter and Radiation, University of Namur, 61 rue de Bruxelles, B 5000 Namur, Belgium

(2)Department of New Biology, DGIST, Sang-Ri 50-1, Dalseong, Daegu, 711-873, Rep. of Korea.

(3)K-MAC, Yongsan-Dong 554, Yuseong-Gu, Daejeon 305-500, Rep. of Korea,

In this report, cesium surface layers formed by Cs^+ ion bombardment on Silicon and Phenylalanine (Phe) samples were analyzed by TOF-MEIS and ToF-SIMS. Si wafers were bombarded with 500 eV Cs^+ ions, then were subsequently bombarded with 5 different Cs^+ fluences corresponding to the transient and equilibrium regimes. The Phe layers were evaporated on Si wafers, up to 100 nm thickness. The samples were subsequently bombarded at 4 different fluences. For Phe, TOF-MEIS shows the formation of a sharp Cs surface layer of ~0.5 nm thickness, on which the peak height increases with Cs^+ ion bombardment and a long Cs tail builds up, penetrating deep into the subsurface. For Si, a similar Cs surface peak forms but it saturates quickly compared to Phe.

*corresponding authors

Keywords: ToF-MEIS, MEIS, ToF-SIMS, SIMS, Cesium, depth profiling, silicon, phenylalanine

1. Introduction

Low energy cesium has been applied in SIMS for decades to depth profile inorganics [1], such as semiconductors, mainly owing to the strong negative ionization enhancement produced by the surface or implanted Cs atoms. More recently, very low energy (<500 eV) Cs^+ has been applied successfully on a ToF-SIMS instrument on organic samples (polymers and organic solids) [2,3], on which molecular information is largely preserved, along with a high negative ion yield. In both cases, the amount of Cs that is actually left at the surface and its depth distribution, or internal depth profile, are key parameters to better understand SIMS depth profiles. The fast change in Cs surface concentration in the very beginning of depth profiles is also useful to assess ion signal changes in the transient regime.

Several groups have attempted to measure the Cs surface concentration on Silicon surfaces, by means of XPS [4,5], AES [6], RBS [4] and MEIS [7], *in situ* or *ex situ*. There is however a large scattering in the published data, probably due to differing experimental conditions (energy, incidence, polarity, extraction field), so that it is hard to draw a general conclusion out of published data. In this study, we have used ToF-MEIS to probe the internal Cs depth profile in Si at the steady state, but also in the transient phase, which has not been published before. The internal profile was also measured, for the first time, on an organic layer (Phenylalanine).

2. Experimental

Two types of materials were loaded with cesium: one naturally oxidized SiO_2/Si(100) surface and a 100 nm layer of Phenylalanine (Phe) evaporated onto a (100) silicon wafer. The Si samples were then sputtered at the University of Namur with 500 eV Cs^+ ions at a 45° incidence in a ToF-SIMS IV instrument from ION-TOF GmbH (Münster, Germany), with a 28.9 nA beam current within a (500 x 500) µm² raster size, for 5 different sputtering times (2, 4, 6, 10 and 20 s) corresponding to ion fluences ranging from $1.5x10^{14}$ ions.cm^{-2} to $1.5x10^{15}$ ions.cm^{-2}. The Phe samples were sputtered with a 28.2 nA, 500 eV Cs^+ beam, within a (500 x 500) µm² raster size, for 6, 20, 60 and 400 s, corresponding to ion fluences ranging from $4.2x10^{14}$ ions.cm^{-2} to $2.8x10^{16}$ ions.cm^{-2}. No extraction field was applied during the sputtering phase to limit Cs redeposition [8]. The Cs loaded samples were subsequently transferred *ex-situ* to the DGIST institute, were they were analyzed by ToF-MEIS with 80 keV (Si samples) or 90 keV (Phe samples) He^+ ions at a 90° scattering angle. The analysis times for each spectrum were 30 minutes and the beam current was 100 pA, without secondary electron suppression.

3. Results and discussion

a. Si samples

The MEIS spectra obtained in a channeling direction for the five Cs craters in Si (2 – 20 s) are displayed in Fig. 1. The Cs, Si and O peaks are observed resp. at 74, 59 and 48 keV. The Cs peak intensity is clearly rising for the shortest Cs sputtering times (2-10s). The MEIS spectrum obtained for 10 s Cs sputtering was simulated with a model adjusting the Si, Cs and O concentration on stacked layers. The best fit was obtained with a 2.8 nm SiO_2 layer on top of Si, with 3 at.% Cs concentration at the extreme surface (0.5 nm layer). The Cs in the model is mostly present in the SiO_2 layer and does not extent below 4 nm. For this profile, the total Cs fluence was $7.2x10^{14}$ ions.cm^{-2} and the estimated implanted Cs content is $3.0x10^{14}$ at.cm^{-2}. In Fig. 2, the total deposited Cs, calculated from the MEIS Cs peak area, is plotted as a function of the Cs^+ fluence. The solid line represents the 100% Cs retention rate. The Cs retention rate is close to 100% for the two first data points (2 and 4 s), but it saturates very rapidly to a relatively low level around $3x10^{14}$ at.cm^{-2}. The data also seem to indicate that the deposited Cs is slightly lower for the longest sputtering time (20 s), for which the native oxide layer has been sputtered away. This suggests that the Cs surface concentration is lower on Si than on SiO_2, which is not unexpected since oxygen could hold Cs more efficiently [9,10]. Wittmaack [11] has explained the very short transient by

a fast relocation of Cs atoms to the surface as adatoms. Vandervorst et al. uses the low sublimation energy of cesium to explain its preferential departure that leads to lower cesium contents and limited Cs adsorption on metals and semiconductors [10]. The inset in Fig. 2 shows the SiO_2^- and $^{29}Si^-$ ToF-SIMS signals (in dual beam with Bi_3^+ as analysis beam), with the same fluence scale. There is a good correlation between the deposited Cs amount as measured with MEIS and the SiO_2^- signal, which is not surprising as Cs is mostly responsible for the negative ionization within the transient region.

The low surface Cs content at saturation is in excellent accordance with data published by van der Heide *et al* [4], who measured the implanted Cs content onto Si *in situ*, with XPS and RBS. They found a $4x10^{14}$ at.cm^{-2} Cs content with RBS, and a 4 at.% Cs with XPS, for 1 keV Cs^+ at 60° incidence. Moreover, their data indicate an increase of the Cs surface concentration with the Cs^+ energy, so that it is not surprising to measure a slightly lower Cs content in our experiment carried out at 500 eV.

One should remember that the samples were exposed several days to the atmosphere prior analysis with ToF-MEIS. The adsorbed Cs is certainly immediately oxidized when exposed to atmospheric oxygen. Both diffusion and oxidation might modify the internal depth profile but not the Cs content. Our estimate of the retention rate should therefore be realistic.

b. Phe samples

The MEIS spectra acquired on the four Cs craters on Phe are shown in Fig. 3. A strong Cs surface peak is detected at 83 keV, with the intensity rising as a function of the Cs^+ fluence, indicating a rising surface concentration. Another important observation is the buildup of a strong subsurface contribution for higher fluences (at 60 s and 400 s). The spectra at 60 s and 400 s were simulated by a model of stacked layers with varying concentrations of H, C, O, N and Cs. The best model obtained for 400 s sputtering is shown in Fig. 4. A strong surface peak, with ~7 at.% Cs concentration is observed at the extreme surface (< 0.5 nm), followed by a long tail extending as far as 65 nm, which is well beyond the expected implantation range of 500 eV Cs^+ into Phe, estimated from SRIM simulation as 4 nm. For a total fluence of $2.81x10^{16}$ ions.cm^{-2}, the retained Cs content is estimated as $1.4x10^{15}$ at.cm^{-2} from the simulation, with ~10^{14} at.cm^{-2} in the surface peak and $1.3x10^{15}$ at.cm^{-2} in the subsurface region. The relatively large amount of subsurface Cs located far away from the implantation range, along with the roughly exponential decay of the Cs internal profile, suggest a strong diffusion of the implanted Cs into the bulk. Cesium diffusion in the bulk of an organic material (para-sexiphenyl) was already shown by Koch *et al* [12] using Ultra-violet Photoemission Spectroscopy on a synchrotron beam line.

On the simulation performed on the 60 s sputtering crater ($4.23x10^{15}$ ions.cm^{-2} fluence), a strong surface peak is again observed, with ~7 at.% Cs concentration and ~10^{14} at.cm^{-2} content. The subsurface Cs content is estimated to be $5x10^{14}$ at.cm^{-2}. Therefore, the surface Cs concentration appears to saturate around 7 at.%, as no changes occur from 60 s to 400 s, but a large amount of Cs diffuses far into the bulk even when the surface steady state is reached, increasing the retained Cs content. This is summarized in Fig. 5. showing the retained Cs content as a function of the Cs^+ fluence. No saturation is reached even when the surface concentration is saturated, due to strong Cs diffusion away from the surface.

4. Conclusions

On the SiO_2/Si samples, the Cs surface content saturates very rapidly to a low value around $3x10^{14}$ at.cm^{-2}, which is estimated as 3 at.% Cs surface concentration. The saturation occurs before 10 s of sputtering (fluence of $7x10^{14}$ ions.cm^{-2}). The Cs was found only at the extreme surface but this may result from diffusion occurring during the sample transfer. On the Phenylalanine surface, a surface Cs saturation was reached, with 7 at.% Cs surface concentration, but the total Cs content in the sample did not reach saturation even for the highest fluences. This is due to a strong Cs diffusion from the surface to the bulk, extending as far as 50-100 nm.

References

[1] K. Wittmaack, Surface Science Reports 68 (2013) 108-230
[2] L. Houssiau, B. Douhard, N. Mine, Appl. Surf. Sci. 255 (2008) 970-972
[3] N. Wehbe, L. Houssiau, Anal. Chem. 82 (2010) 10052-10059
[4] P.A.W. van der Heide, C. Lupu, A. Kutana, J.W. Rabalais, Appl. Surf. Sci. 231-232 (2004) 90-93
[5] J. Brison, R.G. Vitchev, L. Houssiau, Nucl. Instr. And Meth. B266 (2008) 5159-5165
[6] J. Brison, J. Guillot, B. Douhard, R.G. Vitchev, H.N. Migeon, L. Houssiau, Nucl. Instr. And Meth. B267 (2009)519-524
[7] R. Valizadeh, J.A. van den Berg, R. Baheka, A. Al Bayati, D.G. Armour, D. Sykes, Nucl. Instr. And Meth. B64 (1992) 609-613
[8] R.G.Vitchev, J. Brison, L. Houssiau, Appl. Surf. Sci. 255 (2009) 7586-7589
[9] R. Kroon, A. Sinke, Surf. Sci, 399 (1998) 284
[10] W. Vandervorst, T. Janssens, C. Huyghebaert, B. Berghmans, Appl. Surf. Sci. 255 (2008) 1206-1214
[11] K. Wittmaack, International Journal of Mass Spectrometry, 313 (2012) 68-72
[12] N. Koch, C. Chan, A.Kahn, Phys. Rev. B 67 (2003)195330

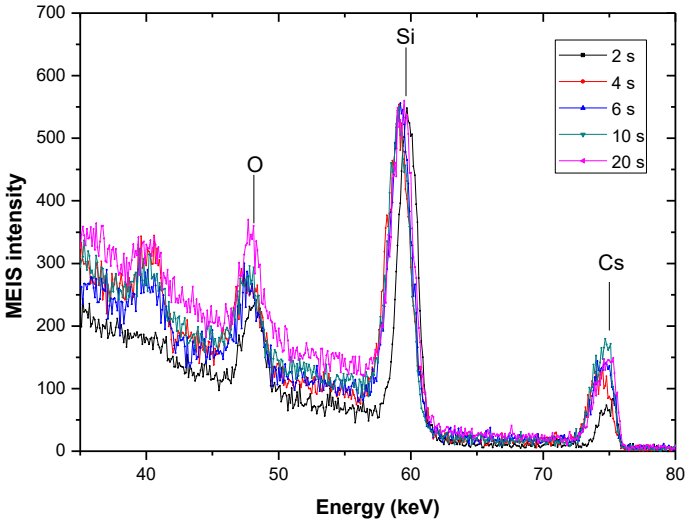

Figure 1. ToF-MEIS spectra obtained with 80 keV He^+ at a 90° scattering angle, on SiO_2/Si surfaces sputtered with 500 eV Cs^+ during 2 s, 4 s, 6 s, 10 s and 20 s.

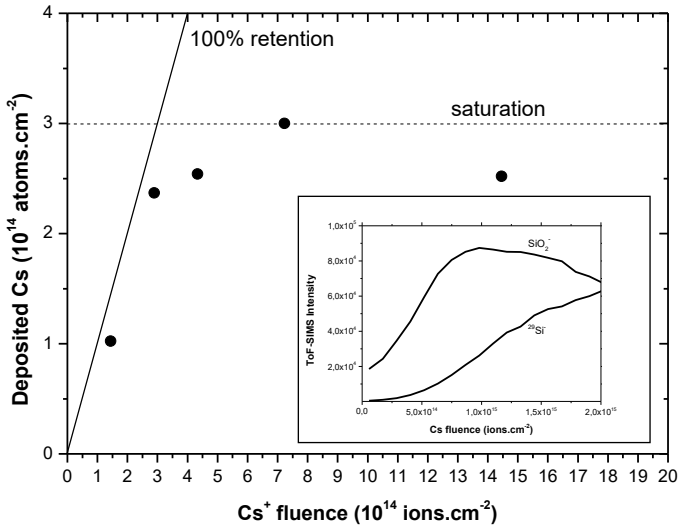

Figure 2. Cs retention as a function of the 500 eV Cs^+ fluence on SiO_2/Si surfaces, as measured by ToF-MEIS.

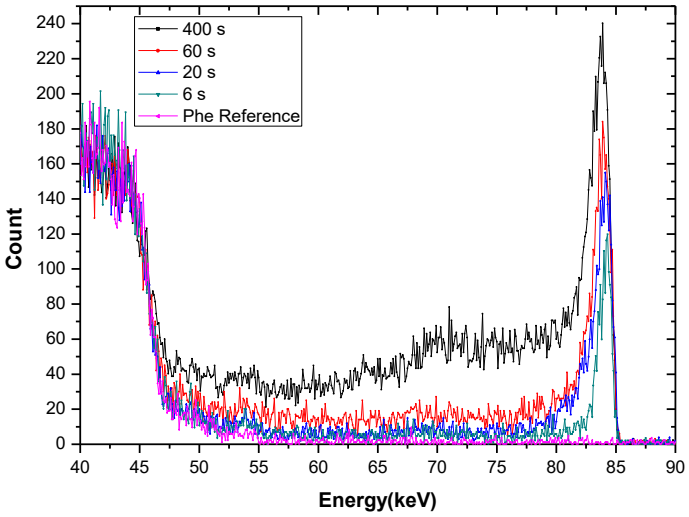

Figure 3. ToF-MEIS spectra obtained with 90 keV He^+ at a 90° scattering angle, on a Phenylalanine layer sputtered with 500 eV Cs^+ during 6 s, 20 s, 60 s and 400 s.

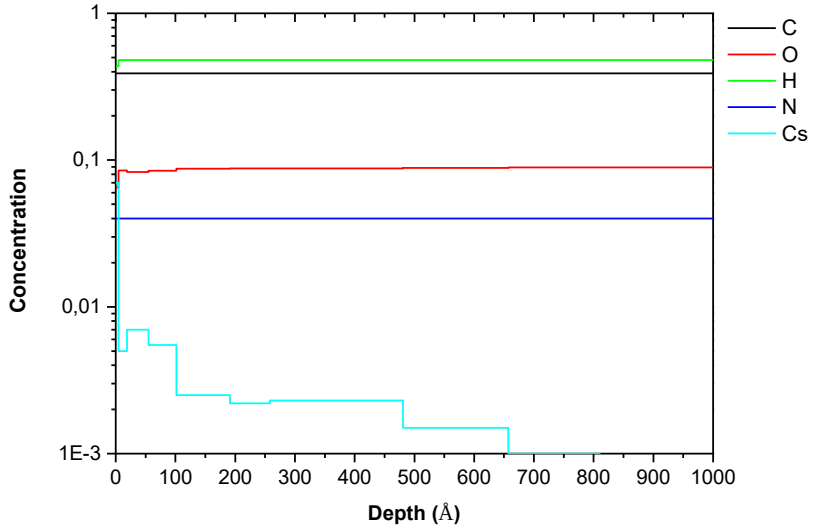

Figure 4. Simulated depth-profiles extracted from the ToF-MEIS spectrum obtained with 90 keV He^+ at a 90° scattering angle, on a Phenylalanine layer sputtered with 500 eV Cs^+ during 400 s.

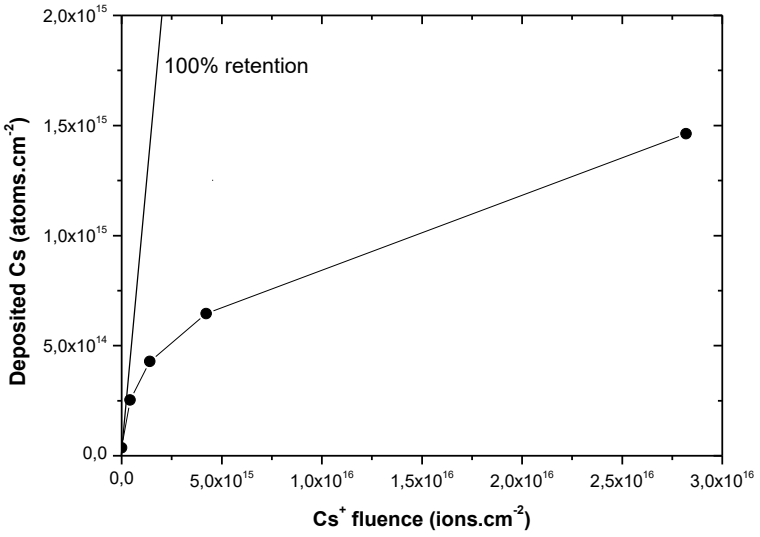

Figure 5. Cs retention as a function of the 500 eV Cs^+ fluence on a Phenylalanine layer, as measured by ToF-MEIS.

XPS Depth profiles of organo lead halide layers and full perovskite solar cells by variable-size argon clusters

Yan Busby*[a], Celine Noël[a], Sara Pescetelli[b], Antonio Agresti[b], Aldo Di Carlo[b,c], Jean-Jacques Pireaux[a] and Laurent Houssiau[a]

[a] Laboratoire Interdisciplinaire de Spectroscopie Electronique (LISE), Namur Institute of Structured Matter, University of Namur, rue de Bruxelles 61, B-5000 Namur, Belgium

[b] C.H.O.S.E. - Centre for Hybrid and Organic Solar Energy, Department of Electronic Engineering, University of Rome Tor Vergata, via del Politecnico 1, 00133 Rome, Italy

[c] L.A.S.E. - Laboratory for Advanced Solar Energy, National University of Science and Technology "MISiS", 119049 Leninskiy Prosect 6, Moscow, Russia

ABSTRACT

Organic and inorganic materials are more and more frequently combined in high-performance hybrid electronic and photonic devices. For such multilayered stacks, the identification of layers and interface defects by depth profile analysis is a challenging task, especially because of the possible ion beam induced modifications. This is particularly true for perovskite solar cells stacks that in a mesoscopic structure usually combine a metal electrode, a mesoscopic conductive oxide layer, an intrinsically hybrid light absorber, an organic hole extraction layer and a metal counter electrode. While depth profile analysis with X-ray photoelectron spectroscopy (XPS) was already applied to investigate these devices, the X-ray and ion beam induced modifications on such hybrid layers have not been previously investigated. In this work we compare the profiles obtained with monatomic Ar^+ beam at different energies, with the ones obtained with argon ion clusters (Ar_n^+) with different sizes ($150<n<1000$) and energies (up to 8 keV). A systematic study is performed on full mesoscopic perovskite ($CH_3NH_3PbI_3$) solar cells and on model hybrid samples ($(FA_xCs_{1-x}PbI_3)_{0.85}$ $(MAPbBr_3)_{0.15})/TiO_2$). The results show that for monatomic beams, the implantation of positively charged atoms induces the surface diffusion of free iodine species from the perovskite which modifies the I/Pb ratio. Moreover, lead atoms in the metallic state (Pb^0) are found to accumulate at the bottom of the perovskite layer where the Pb^0/Pb_{tot} fraction reaches 50%. With argon clusters, the ion beam induced diffusion of iodine is reduced only when the etch rate is sufficiently high to ensure a profile duration comparable with low-energy Ar^+. Convenient erosion rates are obtained only for n=300 and n=500 clusters at 8 keV, which have also the advantage of preserving the TiO_2 surface chemistry. However, with argon cluster ions, Pb^0 particles in the perovskite are less efficiently sputtered which leads to the increase of the Pb^0/Pb_{tot} fraction (up to 75%) at the perovskite/TiO_2 interface. Finally, ion beam and X-ray induced artifacts on perovskite absorbers can be reasonably neglected for fast analysis conditions in which the exposure time is limited to few hours.

Keywords: Depth profiling, XPS, Solar cells, perovskite, hybrid devices, argon clusters

Physical Chemistry of Semiconductor Materials and Interfaces XVII, edited by Hugo A. Bronstein, Felix Deschler
Proc. of SPIE Vol. 10724, 1072408 · © 2018 SPIE · CCC code: 0277-786X/18/$18 · doi: 10.1117/12.2320488

1. INTRODUCTION

Modern electronic and photonic devices are more and more based on organic/inorganic multilayers, where interface effects are well known to play a strong role by influencing the device performance and operation stability. Such complex architectures based on thin layers deposited by different techniques require an accurate characterization of the different layers and interfaces to perform device optimization steps, to derive structure-to-function properties or to study aging effects. This is particularly true for the so-called organo lead halide perovskite solar cells which typically combine metal electrodes deposited by thermal evaporation, spin coated organic semiconductors for carrier extraction, intrinsically hybrid absorbers based on organic (mainly $CH_3NH_3^+$ and $HC(NH_2)_2^+$) and/or inorganic cations[1] (such as Cs^+ and Ru^+) and mixed inorganic anions[2] (PbI_3^-, BrI_3^-, etc.). Thanks to recent advances and a more and more sophisticated chemical engineering of the light absorber, perovskite solar cells have demonstrated an extremely fast increase of the solar to power conversion efficiency, which is now above 22%.[3] Despite of the very encouraging progress of the device efficiency, the market breakthrough of the perovskite technology is still hindered by their insufficient long term stability under real operation conditions due to the instability of the absorber and the interfaces under humidity,[4] light[5] and high temperature[6] (above 80°).

One promising approach to increase the perovskite stability is to apply interface modifications through the so called interface engineering;[7,8] for example, the addition of graphene platelets into the mesoporous TiO_2 has been shown to remarkably enhance the stability of the $CH_3NH_3PbI_3$ perovskites.[9] One promising tool to investigate interface engineered solar cells, is to perform depth profile analysis combining a surface analysis, as with X-ray photoelectron spectroscopy (XPS) or time of flight secondary ion mass spectrometry (ToF-SIMS) with ion beam sputtering to reconstruct to the in-depth elemental and chemical composition or for the 3D molecular reconstruction of the full device stack. Both techniques have been recently combined to study perovskite absorbers[10] and perovskite solar cells or LEDs.[11–14] In previous works, monatomic ion beams with energy below 1 keV have been reported for profiling perovskite solar cells in order to preserve the delicate organic/inorganic interfaces. However the effect of the ion beam on the layers and on the interface degradation have not been previously investigated in details. In particular, it is well known that argon clusters ion beams (Ar_n^+) are the most appropriate sources to profile organic materials because of the much lower energy-per-atom value and the lower penetration depth, resulting in a much lower in-depth modification of soft materials with respect to monatomic beams. Despite of this advantage, large cluster ion beams are highly ineffective for eroding oxides and metal layers; the erosion rates are very low unless the cluster energy is raised above 10-20 keV. Overall, the strongly material-dependent sputtering rate of large cluster ion beams is a strong limitation for profiling of hybrid multilayer stacks.

In this work, we have investigated a different approach for profiling hybrid and multilayered stacks based on medium energy (with energy up to 8 keV) and variable-size (from few hundred to 1000 atoms) argon clusters which is regulated by a mass filter in the ion beam gun. The cluster size was varied between few hundred atoms up to 1000 atoms and the energy from 6 to 8 keV to ensure viable erosion rates on inorganic layers. The results obtained on a full perovskite solar

cell and on a triple cation perovskite deposited on TiO_2 have been compared with the ones obtained with a low-energy (below 1 keV) monatomic Ar^+ beam. This study has allowed identifying the best profile conditions ensuring that minimum artifacts are induced by the sputtering beam.

2. MATERIALS AND METHODS

2.1 Deposition of full solar cells Au/spiro-OMeTAD/$CH_3NH_3PbI_3$//TiO_2 /FTO solar cells

Patterned florine-doped tin oxide (FTO) coated glasses were firstly washed with a liquid detergent, dissolved in deionized water and then cleaned by ultrasonic bath with acetone and IPA for 10 min. The compact TiO_2 blocking layer was deposited by spray pyrolysis with a solution of acetylacetone (2 mL), titanium diisopropoxide (3 mL) and ethanol (45 mL) at 460 °C. The TiO_2/FTO substrate is coated by a thin mesoporous TiO2 porous film (~150 nm) deposited by spin coating a TiO_2 paste (Dyesol 18 NR-T paste diluted in ethanol 1:5 in wt.) at 4000 rpm for 20 s, followed by the subsequent sintering at 460 °C for 30 min in air. The $CH_3NH_3PbI_3$ layer is deposited on the mesoscopic TiO_2 by the sequential deposition of PbI_2 (500 g $\cdot L^{-1}$, in dimethylformamide) and CH_3NH_3I (10 g$\cdot L^{-1}$ in IPA) in a nitrogen filled glovebox system. The supersaturated PbI_2 solution was first deposited by spin coating at 6000 rpm for 10 s and then directly dipped into the CH_3NH_3I solution for 15 min. During the second step, the $CH_3NH_3PbI_3$ layer formation was completed by thermal annealing at 80 °C and by rinsing with anhydrous IPA. Then, the spiro-OMeTAD (73.5 g$\cdot L^{-1}$ in chlorobenzene solution doped with TBP (26.7 µL$\cdot mL^{-1}$)), LiTFSI (16.6 µL$\cdot mL^{-1}$) and a Cobalt(III) FK209 complex (7.2 µL$\cdot mL^{-1}$) were sequentially deposited by spin coating at 2000 rpm for 20 s in a glovebox. Finally, the device was completed by the high-vacuum thermal evaporation of a gold counter electrode (~100 nm) on an active area of 0.1 cm^2 defined by a shadow mask. The devices were encapsulated with a glass lid sealed on the device only on the substrate edge and sent for the analysis.

2.1 Deposition of triple-cation perovskite layers on compact TiO_2

The perovskite layer was deposited on a FTO substrate coated by compact TiO_2 blocking layer realized in the same way of the full solar cells previously described.

The $Cs_x(MA_{0.17}FA_{0.83})_{(100-x)}Pb(I_{0.83}Br_{0.17})_3$ triple cation perovskite was deposited with one-step deposition and antisolvent method in a nitrogen filled glovebox system. The organic cations were purchased from Dyesol; the lead compounds from TCI; CsI from abcr GmbH. The precursor perovskite solution was prepared by dissolving, with the molar ratio suggested in ref [1] the mixture of lead(II) iodide (PbI_2), lead(II) bromide ($PbBr_2$), methylammonium bromide (MABr), formamidinium iodide (FAI) and cesium iodide (CsI) in a solvent mixture of anhydrous N,N-dimethylformamide (DMF) and dimethylsulfoxide (DMSO) in a 3:1 ratio (v:v). The obtained mixed perovskite solution was spin coated on the substrate in a two steps program at 1000 and 5000 rpm for 10 and 30 s respectively. During the second step, 200 µL of chlorobenzene was poured on the spinning substrate 7 s prior to the end of the program. Immediately after spin coating the substrates were annealed at 100°C for 1 h in nitrogen filled glovebox.

2.3 XPS depth profile analysis

The XPS depth profile analysis was performed on a ESCALAB 250Xi spectrometer by Thermo Scientific equipped with

a Monatomic And Gas Cluster Ion Source (MAGCIS) allowing to select monoatomic Ar^+ or variable-size Ar_n^+ clusters with 75<n<2000. Typically the intensities are in the μA range with the monatomic beam and about 10 nA with the cluster source. Solar cells were stored in dark conditions under vacuum before the analysis and were analyzed by alternating ion sputtering and XPS analysis performed in the scan mode. Both survey scan and high-resolution scans were acquired at each profile step, especially to monitor Pb 4f and I 3d spectra. The spectrometer is equipped with a monochromatic Al Ka X-ray beam with a spot size set at 200 μm and a raster area set at 1 mm to ensure that the analysis is safely performed at the center of the crater. A dual beam flood gun was always used for charge compensation. The surface atomic percentages (at.%) were evaluated at each profile step by peak fitting with Shirley-type background using Avantage© software.

3. RESULTS AND DISCUSSION

3.1 Depth profile analysis on full perovskite solar cells

The perovskite solar cell with Au/spiro-OMeTAD/$CH_3NH_3PbI_3$/TiO_2/FTO structure is the most commonly studied perovskite solar cell. However, previous XPS and ToF-SIMS depth profile analyses have been reported mainly based on monatomic ion beam sputtering.[13] Different groups have reported about two important facts that occur when profiling the $CH_3NH_3PbI_3$ layer; (1) Pb atoms show two chemical components and (2) the Pb/I ratio always deviates from the theoretical value of 3;[12] this parameter was also suggested as good indicator of the average degradation of the $CH_3NH_3PbI_3$ layer.[15] In order to investigate the origin of these two effects and to assess to which extent they are affected by the sputtering beam, we have performed the depth profile of the full solar cells structure with 500 eV monatomic Ar^+ and compared the results with variable size (from 150 to 1000 atoms) and energy (up to 8 keV) argon clusters corresponding to energy per atom values from few eV to few tens eV. Since the erosion rate of the metal electrodes is small with all the explored cluster conditions, a pre-sputtering with 1 keV Ar^+ was performed until reaching the Au/spiro-OMeTAD interface, as marked by the raise of the C signal and the drop of the Au signal to less than 10 at.%; then the sputtering source was switched to the different conditions of the cluster beam. The depth profiles obtained with 500 eV Ar^+, Ar_{300}^+ and Ar_{500}^+ at 8 keV and are shown in **Figure 1** (the profile obtained at Ar_{500}^+ at 8 keV is not shown being very similar to the one of Ar_{300}^+ at 8 keV). Surprisingly, for a fixed energy (8 keV) the erosion rate did not monotonically evolve with the cluster size, for very small (below 150 atoms) or for very large clusters (above 1000 atoms) the sputtering rate was not sufficient to reach the TiO_2 interface in a reasonable amount of sputtering time (the profile was stopped after 10000 s of sputtering). The best erosion rate was obtained for 8 keV n=300 and n=500 clusters; we did not explore a wide cluster energy range because when the n=300 energy was lowered to 6 keV the sputtering time to reach the TiO_2 interface increased by 30% and less sharp interfaces were obtained. Overall, the higher erosion rate corresponds to clusters ions with n=300 and E=8 keV corresponding to an erosion rate which is close to the one of 500 eV Ar^+. One important drawback is that when the sputtering rate is low, the capability of the sputtering beam to remove the residual Au from the top electrode material drops, leading to the artificial persistence of the Au signal in the reconstructed depth profiles. This artifact is not observed for the best performing Ar_{300}^+/8 keV condition, for which the

Au signal reaches quickly values below 1 at.% as with the monatomic beam (not shown here). However, this is not the case for Ar_{300}^{+}/6keV for Ar_{500}^{+}//8 keV that result in a considerably lower erosion rate and are considerably less effective in removing the residual gold particles. A detailed analysis on the Pb/I ratio was made taking into account the fact that the Pb 4f spectrum features two chemical components (Figure 1c); the first component, at lower binding energy, is ascribed to metallic Pb atoms (Pb^0 at about 137 eV binding energy) and the other is associated with lead atoms forming lead-iodide bonds (PbI_x at about 139 eV binding energy). By evaluating the I/PbI_x ratio and the Pb fraction in the Pb^0 state (Figure 1d, 1e and 1f) we observe that while the I/PbI_x ratio at the top of the $CH_3NH_3PbI_3$ layer is about 3 when the sputtering is made with the monatomic beam, it is rather between 2.2 and 2.4 when using cluster. The I/PbI_x ratio always increases with the depth when using clusters while it decreases and then increases with the monatomic sputtering. The fraction of Pb atoms in the Pb^0 chemical state increases with the sputtering time to reach about 50% of the peak area when the profile is in the mesoscopic TiO_2 region. The I/PbIx ratios suggest that by comparison with the clusters, a stronger iodine diffusion toward the top interface (spiro-OMeTAd/$CH_3NH_3PbI_3$) occurs when profiling the $CH_3NH_3PbI_3$ layer with the monatomic beam (thus artificially enhancing the I/PbI_x value at the top of the perovskite layer). Interestingly, for each profile condition, we observe the formation of metallic lead atoms (and consequently free iodine atoms). Our results do not allow concluding whether Pb^0 is induced by the X-Rays or the ion beam exposure, however some information will be provided in the next section. Overall, the fraction of Pb atoms in the Pb^0 chemical state reaches up to 50% of the total lead atoms when the profile reaches the mesoscopic TiO_2 region.

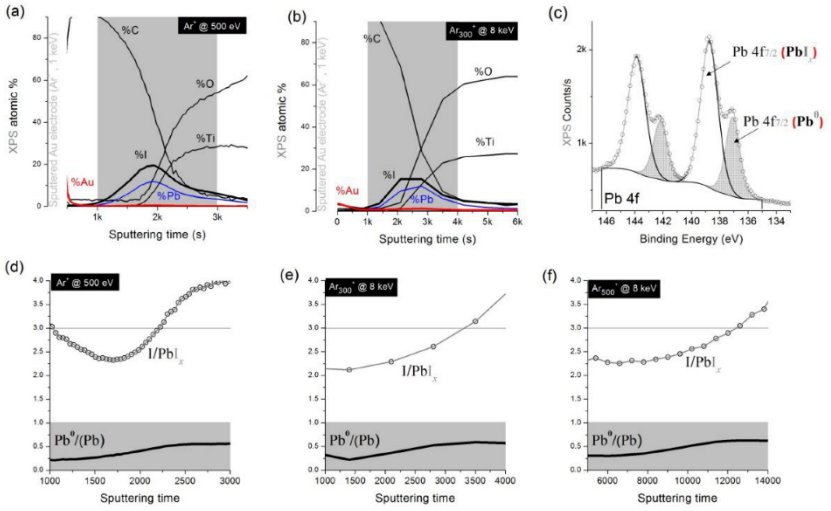

Figure 1. Comparison between the XPS depth profiles on a Au/spiro-OMeTAD/$CH_3NH_3PbI_3/TiO_2$ device obtained with 500 eV monatomic beam (a and d), with the Ar_{300}^{+} at 8 keV (b and e) and with Ar_{500}^{+} at 8 keV (f). In the d, e and f the I/PbI_x ratio (i.e. excluding Pb^0 signal) and fraction of Pb^0 in the total Pb signal are displayed for the different sputtering conditions. Note that the *x*-scale in (d), (e) and (f) is limited to the region where the Pb and I signals indicated the presence of the CH3NH3PbI3 layer. Panel (c) illustrates a typical Pb 4f spectrum showing the presence of two chemical components ascribed to Pb0 and PbIx.

To get more insights into the ion beam induced modifications of the hybrid perovskite layer, we have performed a similar comparative analysis on a model sample based on a triple-cation perovskite layer deposited on TiO_2. State-of-the-art perovskite absorbers were selected in order to safely exclude complications arising from the possible degradation of the perovskite resulting from the environment exposure: indeed, triple-cation perovskite absorbers are characterized by a much higher environmental stability with respect to $CH_3NH_3PbI_3$ thanks to the sophisticated chemical engineering of their composition.[16] The perovskite formula is based on the mixed anions and cations, precisely with the nominal stoichiometry $(FA_xCs_{1-x}PbI_3)_{0.85}$ $(MAPbBr_3)_{0.15}$ where MA stands for methylammonium ions ($CH_3NH_3^+$) and FA stands for formamidinium ions ($HC(NH_2)_2^+$). This absorber has shown outstanding light to power conversion efficiency and stability.[3,17,18]

3.1 Depth profile analysis on the intrinsically hybrid perovskite layer

We have compared the influence of the energy of the monatomic Ar^+ sputtering beam on the as-deposited $(FA_xCs_{1-x}PbI_3)_{0.85}$ $(MAPbBr_3)_{0.15}$ /TiO_2 samples. The depth profiles at 500 eV and 1 keV are shown in **Figure 2**; at 1 keV, the Pb content in the perovskite layer is constant through the entire profile (Figure 2e) while at 500 eV, the depth profile features a few at% increase of the Pb content with the increasing of the sputtering time (see Figure 2b). For these two energy conditions, the iodine is clearly found to diffuse toward the top of the perovskite layer (Figure 2b and 2e) which results in the decrease of the I/Pb ratio from 2.1 (at the top perovskite layer) to 1.5 at the TiO_2 interface (Figure 2c and 2f). This result is in contrast with what has been previously observed with the profile of full $CH_3NH_3PbI_3$ solar cells, for which the I/Pb ratio increase during the profile may rely on the higher absorption of free iodine species at the surface of the mesoporous TiO_2 (see the discussion below and in Figure 5).

Finally, the fraction of Pb in the Pb^0 state increases during profile and reaches up to 75% of the Pb 4f peak area at the perovskite/TiO_2 interface (where the total Pb content is less than 10 at.%) with 500 eV sputtering energy while it reaches only 50% of the peak area at 1 keV. The origin of such a high Pb^0 fraction needs still to be further clarified, one possibility is that it may be induced by the X-ray or the sputtering beam or, alternatively, Pb^0 particles may be formed during the layer synthesis and accumulate at the bottom of the perovskite layer during the crystallization. The dependence of the Pb^0 fraction from the sputtering conditions may result from the slower etch rate of Pb particles respect to the other elements of the perovskite; in other words, the slower erosion of Pb^0 would artificially increase its content during the profile.

In order to get more insights into this effect, we have compared the profiles obtained with Ar_{300}^+ and Ar_{500}^+ cluster beams at 8 keV (**Figure 3**). For these profiles, high-resolution scans were acquired for the different atomic species after each erosion step to perform chemical analysis. Similarly to what observed in the monatomic profiles in Figure 2c and 2f, the results in Figure 3d show that, for Ar_{500}^+ cluster beams the I/Pb ratio (excluding Pb^0) varies from 2.2 in the perovskite layer to less than 1.5 at the TiO_2 interface (Figure 3f); The lowering of the I/Pb ratio is less pronounced with Ar_{300}^+ cluster beams as it varies from from 2.2 to 1.7(Figure 3c). The trend of the I/Pb ratio (excluding Pb^0) may be explained by the surface migration of negatively charged iodine species due to the implantation of positively charged Ar ions; this

effect is expected to be reduced with clusters, however, if the perovskite layer sputtering time increases (~3500 s are needed with Ar_{500}^{+} cluster beams) then we observe a similar iodine diffusion as for the 500 eV Ar^{+} profile during which the perovskite layer was profiled in about half of the time (~1500 s).

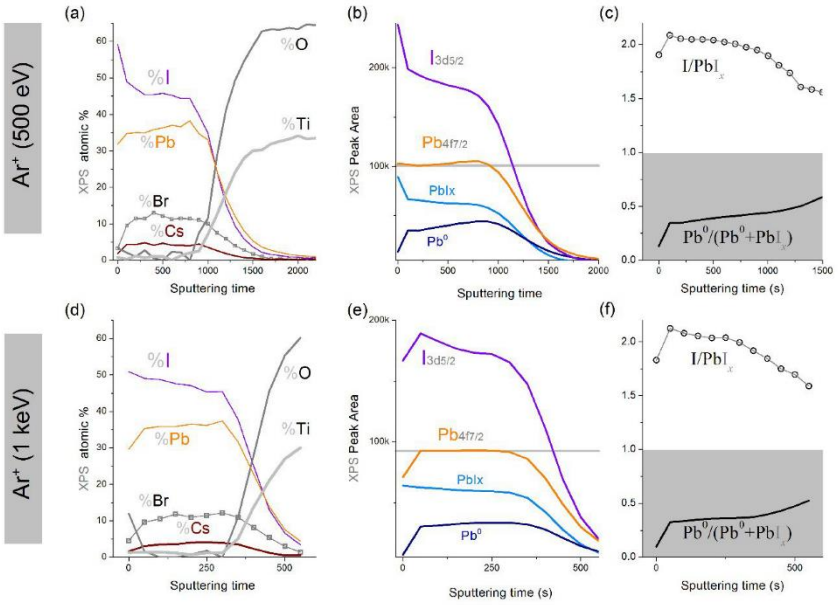

Figure 2. XPS depth profiles on $(FA_xCs_{1-x}PbI_3)_{0.85}(MAPbBr_3)_{0.15}/TiO_2$ samples obtained with a monatomic Ar^{+} beam at 500 eV (a, b and c) and 1 keV (d, e and f). The (a) and (d) panels allow comparing the elemental species profiles, the panels (b) and (e) show the evolution of the I 3d5/2 and Pb 4f7/2 peak areas and the Pb^0 and PbI_x components. The (c) and (f) panels allow comparing the evolution of the I/Pb ratio (excluding the Pb^0 contribution) and the ratio of Pb which is in the metallic state (Pb^0).

The Pb^0 fraction evolution is similar for the two cluster conditions (Figure 3c and 3d) and is clearly higher respect to the 1 keV Ar^{+} profile. This result supports the hypothesis the slower erosion of Pb^0 particles could artificially enhance the Pb^0 content and also the total Pb content as observed in Figure 3b and 3e (peak areas) into the perovskite layer.

When the cluster size is increased to n=1000 atoms (at 8 keV this corresponds to the energy-per-atom value of 8 eV), the sputtering rate of the perovskite layer drops and the TiO_2 interface could not be reached even after 16000 s of sputtering. However, since the Pb fraction in the Pb^0 state only increases from 13 to 20% of the total Pb peak area during this profile (**Figure 4**), one can conclude that the presence of Pb^0, is not principally due to the ion gun and to the X-Rays exposure (the X-ray gun was on during the entire depth profile duration). In other words, while it was not expected to find such a

high amount of Pb^0 into the perovskite layer, its presence is not an artifact due to the X-rays or ion gun exposure, however its exact quantification may be slightly altered by the depth profile analysis conditions.

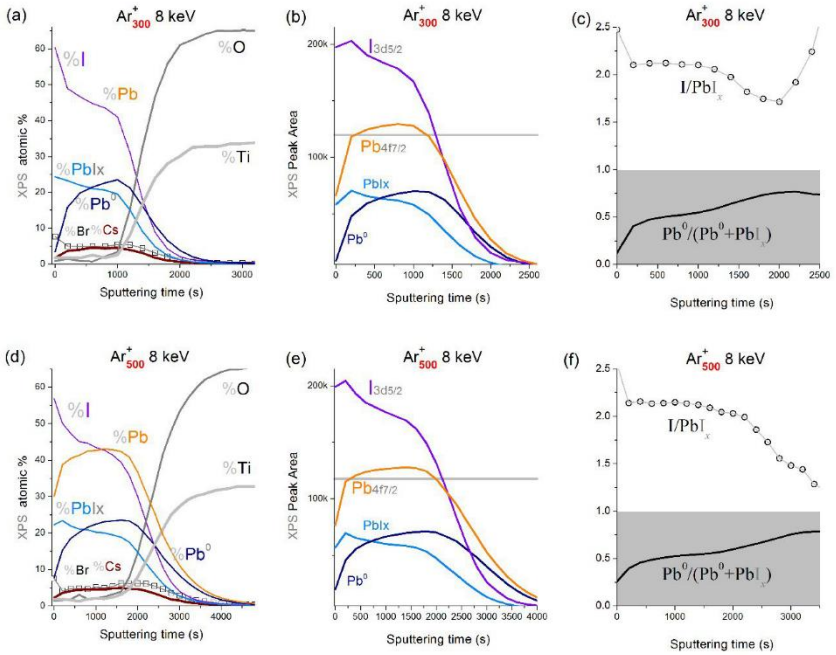

Figure 3. XPS depth profiles on $(FA_xCs_{1-x}PbI_3)_{0.85}(MAPbBr_3)_{0.15}/TiO_2$ samples obtained with Ar_{300}^+ (a, b and c) and Ar_{500}^+ (d, e and f) clusters. The panels (c) and (f) show the I/Pb ratios excluding Pb^0 and the Pb^0 fraction in the Pb signal.

Finally, by comparing on **Figure 5** the profiles obtained with the different sputtering beams, a clearly different ion beam induced modification of the TiO_2 substrate is observed: namely, monatomic beams are found to reduce the TiO_2 layer (Figure 5a), while this modification is not observed with cluster ions (Figure 5b). In particular, we could evidence the presence of a two chemical components within the Ti 2p spectrum with the one at higher binding energy (~460 eV binding energy) ascribed to $TiO_{2-x}I_x$ species and the other ascribed to Ti in the TiO_2 chemical state (at about 457.5 eV). The lowering of the $TiO_{2-x}I_x$ component with the sputtering time (see Figure 5b and 5c), suggests that free iodine atoms present in the perovskite could chemically bond to Ti atoms at the perovskite/TiO_2 interface. This result shows that

respect to monatomic ion beams, a much more precise chemical analysis on hybrid layer/oxides interfaces is possible when profiling with cluster ion beams.

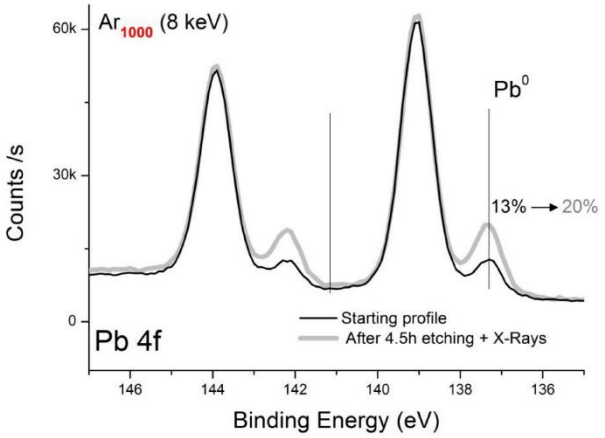

Figure 4. Comparison between Pb 4f spectra obtained at the beginning and at the end of the depth profile (corresponding to 16000s sputtering) operated with Ar_{1000}^{+} clusters at 8 keV energy showing that only a moderate increase of the Pb^0 component intensity is observed during such a long exposure to the ion beam and to X-Rays.

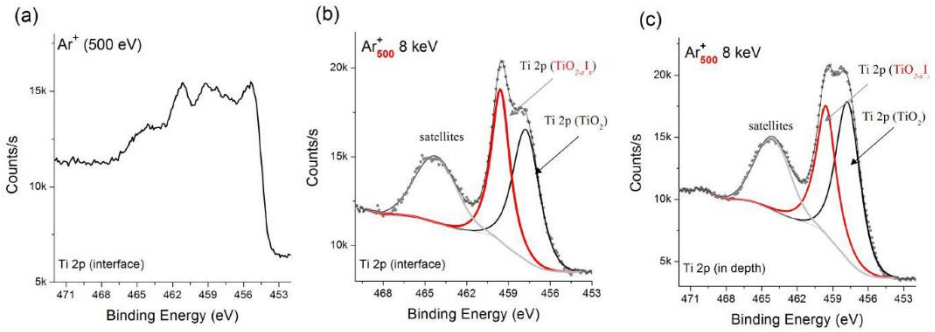

Figure 5. Comparison between the Ti 2p high resolution spectra obtained when profiling the TiO_2 substrate with the 500 eV monatomic beam (a) or with argon clusters at the perovskite/TiO_2 interface (b) and deeper into the TiO_2 layer (c). The TiO_2 is evidently reduced by monatomic beams while two chemical components are clearly distinguishable when profiling with the cluster beam (the profile corresponds to the one shown in Figure 3b).

4. CONCLUSION

Variable-size (from n=150 to n=1000) and energy (up to 8 keV) argon clusters (Ar_n^+) are investigated to profile full perovskite solar cells and intrinsically hybrid $(FA_xCs_{1-x}PbI_3)_{0.85}(MAPbBr_3)_{0.15}/TiO_2$ model samples. The results obtained with low-energy monatomic Ar^+ sputtering (at 500 eV and 1 keV) have been compared with the ones obtained with the different cluster ions. With small clusters (n=150) the sputtering rate is low which suggests that for the explored materials the energy-per-atom value is not the key parameter ruling the erosion rate. However, for too low energy/atom values (below 10 eV) the profile was also not achieved. Overall, we find that the bests erosion rate is obtained for n=300 clusters at 8 keV; in this conditions, the sputtering rate is comparable with the one obtained with the 500 eV monatomic beam.

The advantage of the clusters is mainly ascribed to the lower implantation of positive ions into the perovskite layer thus reducing the surface charging induced migration of free anions, in particular iodine species. This allows obtaining a less variable I/Pb ratio when excluding lead in the Pb^0 state (Figure 3c). Another advantage of clusters is the lower tendency to reduce oxide layers as shown for TiO_2 which allows to perform chemical analysis at the perovskite/TiO_2 interface.

One drawback of argon clusters is that metal particles are not efficiently sputtered and may artificially accumulate into the sputtered layer. This effect was observed for Au residual particles from the top electrode and for Pb^0 particles that are present in the perovskite layer. For the model $(FA_xCs_{1-x}PbI_3)_{0.85}(MAPbBr_3)_{0.15}/TiO_2$ samples, the total Pb content was constant when profiling with 1 keV Ar^+ (Figure 2e), while the total Pb content and the Pb^0 fraction increases with clusters.

While more detailed studies are in progress to determine the origin of such a high Pb^0 content in the perovskite layer and the evolution of organic fragments during the profile, which are particularly difficult to assess with the present XPS study, this work indicates the principal artifacts that may be induced in the explored sputtering conditions and identifies 8 keV Ar_{300}^+ and Ar^+ 1 keV as the best conditions for the explored size/energy range.

REFERENCES

(1) Saliba, M.; Matsui, T.; Seo, J.-Y.; Domanski, K.; Correa-Baena, J.-P.; Nazeeruddin, M. K.; Zakeeruddin, S. M.; Tress, W.; Abate, A.; Hagfeldt, A.; et al. "Cesium-Containing Triple Cation Perovskite Solar Cells: Improved Stability, Reproducibility and High Efficiency." *Energy Environ. Sci. 9* (6), 1989–1997, (2016).

(2) Assadi, M. K.; Bakhoda, S.; Saidur, R.; Hanaei, H. "Recent Progress in Perovskite Solar Cells." *Renew. Sustain. Energy Rev. 81* (1), 2812–2822, (2018).

(3) Mesquita, I.; Andrade, L.; Mendes, A. "Perovskite Solar Cells: Materials, Configurations and Stability." *Renew. Sustain. Energy Rev. 82* (July 2017), 2471–2489, (2018).

(4) Han, Y.; Meyer, S.; Dkhissi, Y.; Weber, K.; Pringle, J. M.; Bach, U.; Spiccia, L.; Cheng, Y.-B. "Degradation Observations of Encapsulated Planar CH3NH3 PbI3 Perovskite Solar Cells at High Temperatures and Humidity." *J. Mater. Chem. A 3* (15), 8139–8147, (2015).

(5) Li, Y.; Xu, X.; Wang, C.; Ecker, B.; Yang, J.; Huang, J.; Gao, Y. "Light-Induced Degradation of CH 3 NH 3 PbI 3 Hybrid Perovskite Thin Film." *J. Phys. Chem. C 121* (7), 3904–3910, (2017).

(6) Divitini, G.; Cacovich, S.; Matteocci, F.; Cinà, L.; Di Carlo, A.; Ducati, C. "In Situ Observation of Heat-Induced Degradation of Perovskite Solar Cells." *Nat. Energy 1* (2), 15012, (2016).

(7) Zhou, Z.; Pang, S.; Liu, Z.; Xu, H.; Cui, G. “Interface Engineering for High-Performance Perovskite Hybrid Solar Cells.” *J. Mater. Chem. A 3* (38), 19205–19217, (2015).
(8) Agresti, A.; Pescetelli, S.; Palma, A. L.; Del Rio Castillo, A. E.; Konios, D.; Kakavelakis, G.; Razza, S.; Cinà, L.; Kymakis, E.; Bonaccorso, F.; et al. “Graphene Interface Engineering for Perovskite Solar Modules: 12.6% Power Conversion Efficiency over 50 Cm^2 Active Area.” *ACS Energy Lett. 2* (1), 279–287, (2017).
(9) Agresti, A.; Pescetelli, S.; Taheri, B.; Del Rio Castillo, A. E.; Cinà, L.; Bonaccorso, F.; Di Carlo, A. “Graphene–Perovskite Solar Cells Exceed 18 % Efficiency: A Stability Study.” *ChemSusChem 9* (18), 2609–2619, (2016).
(10) Ralaiarisoa, M.; Busby, Y.; Frisch, J.; Salzmann, I.; Pireaux, J.-J.; Koch, N. “Correlation of Annealing Time with Crystal Structure, Composition, and Electronic Properties of $CH_3NH_3PbI_{3-X}Cl_x$ mixed-Halide Perovskite Films.” *Phys. Chem. Chem. Phys. 19* (1), (2017).
(11) Domanski, K.; Correa-Baena, J.-P.; Mine, N.; Nazeeruddin, M. K.; Abate, A.; Saliba, M.; Tress, W.; Hagfeldt, A.; Grätzel, M. “Not All That Glitters Is Gold: Metal-Migration-Induced Degradation in Perovskite Solar Cells.” *ACS Nano 10* (6), 6306–6314, (2016).
(12) Matteocci, F.; Busby, Y.; Pireaux, J.-J.; Divitini, G.; Cacovich, S.; Ducati, C.; Di Carlo, A. “Interface and Composition Analysis on Perovskite Solar Cells.” *ACS Appl. Mater. Interfaces 7*, 26176–26183, (2015).
(13) Li, J.; Dong, Q.; Li, N.; Wang, L. “Direct Evidence of Ion Diffusion for the Silver-Electrode-Induced Thermal Degradation of Inverted Perovskite Solar Cells.” *Adv. Energy Mater.* 1–8, (2017).
(14) Palma, A. L.; Cinà, L.; Busby, Y.; Marsella, A.; Agresti, A.; Pescetelli, S.; Pireaux, J.-J.; Di Carlo, A. “Mesoscopic Perovskite Light-Emitting Diodes.” *ACS Appl. Mater. Interfaces 8* (40), 26989–26997, (2016).
(15) Busby, Y.; Agresti, A.; Pescetelli, S.; Di Carlo, A.; Noel, C.; Pireaux, J. J.; Houssiau, L. “Aging Effects in Interface-Engineered Perovskite Solar Cells with 2D Nanomaterials: A Depth Profile Analysis.” *Mater. Today Energy 9*, 1–10, (2018).
(16) Saliba, M.; Matsui, T.; Seo, J.-Y.; Domanski, K.; Correa-Baena, J.-P.; Nazeeruddin, M. K.; Zakeeruddin, S. M.; Tress, W.; Abate, A.; Hagfeldt, A.; et al. “Cesium-Containing Triple Cation Perovskite Solar Cells: Improved Stability, Reproducibility and High Efficiency.” *Energy Environ. Sci. 9* (6), 1989–1997, (2016).
(17) Qin, X.; Zhao, Z.; Wang, Y.; Wu, J.; Jiang, Q.; You, J. “Recent Progress in Stability of Perovskite Solar Cells.” *J. Semicond. 38* (1), 011002, (2017).
(18) Correa-Baena, J.-P.; Abate, A.; Saliba, M.; Tress, W.; Jesper Jacobsson, T.; Gratzel, M.; Hagfeldt, A.; Vrućinić, M.; Alsari, M.; Snaith, H. J.; et al. “The Rapid Evolution of Highly Efficient Perovskite Solar Cells.” *Energy Environ. Sci. 10* (3), 710–727, (2017).

RSC Advances

PAPER

View Article Online
View Journal | View Issue

Check for updates

Cite this: *RSC Adv.*, 2019, **9**, 2292

Surface modification and direct plasma amination of L605 CoCr alloys: on the optimization of the oxide layer for application in cardiovascular implants

Sergio Diaz-Rodriguez,[a] Pascale Chevallier,[a] Carlo Paternoster,[a] Vanessa Montaño-Machado,[a] Céline Noël,[b] Laurent Houssiau[b] and Diego Mantovani *[a]

Received 15th October 2018
Accepted 8th December 2018

DOI: 10.1039/c8ra08541b

rsc.li/rsc-advances

Stents are cardiovascular devices used to treat atherosclerosis, and are deployed into narrowed arteries and implanted by expansion to reopen the biological lumen. Nevertheless, complications after implantation are still observed in 10–14% of the implantations. Therefore, functionalizing these devices with active molecules to improve the interfacial effects with the surrounding tissue strongly impacts their success. A plasma-based procedure to directly graft biomolecules to the surface of cobalt chromium alloys, without any polymeric coating, has been recently reported. Assuring the stability of the coating during plastic deformation generated during the implantation whilst avoiding the corrosion of the surface is crucial. This study explores different surface treatments to be used as a pre-treatment for this novel procedure. The effects of (i) electropolishing, (ii) thermal treatments, and (iii) the plasma immersion ion implantation of oxygen on the chemical composition, roughness, wettability and efficiency during the plasma-amination procedure whilst avoiding cracks after deformation, thus maintaining corrosion resistant behaviour, were investigated by XPS, AFM, ToF-SIMS imaging and depth profile, and WCA. Furthermore, the hemocompatibility of the surface and cell viability assays were also performed. Results showed that all of the treatments created a different surface chemical composition: EP mainly of chromium oxide, PIII with a layer of cobalt oxide and TT with a mixture of oxides, as observed by XPS and ToF-SIMS. Moreover, EP was the process that generated a surface with the highest efficiency to amination and the most corrosion resistance among the treatments, and it appeared as the most suitable pre-treatment for stent functionalization.

1 Introduction

Atherosclerosis is a cardiovascular disease characterized by the formation of a plaque that narrows the arterial walls, leading to thrombus formation and ultimately heart attacks.[1] Once it has progressed to the late stages, this disease is surgically treated by the implantation of a stent which is a metallic wire mesh. This device is introduced with a catheter to the narrowed zone and is expanded up to 25% deformation to reopen the arterial flow, deploying the device whilst avoiding the collapse of the artery.[2,3] Among the materials used for bare metal stents (BMS), there is cobalt chromium L605 alloy, which has interesting mechanical properties and is covered with a passive oxide layer that protects the surface from potential corrosion. Furthermore, this alloy allows for the fabrication of thinner devices with smaller struts that have been correlated to lower clinical post-implantation adverse effects.[4] Nevertheless, complications with BMS remain, for example in-stent restenosis, thrombus formation, and endothelium damage still occur due to the invasive procedures of stent deployment.[5] Although, drug eluting stents (DES) have been developed to counter these complications by releasing drugs from a polymeric coating (deposited on the surface). Nonetheless, cracks and delamination of this coating have been observed due to the lack of adhesion and cohesion between the surface and the coating.[6,7] This finding can be related to the complex geometry of the stents and the deposition techniques of the polymeric layer (dip coating, spray coating, layer by layer coating, *etc.*) that can not assure coating stability during the deployment of the device.[8]

Therefore, a novel procedure that allows for the direct covalent grafting of active molecules without any intermediate layer to enhance the biological performance of cardiovascular devices has been developed. Briefly, this procedure focuses on direct functionalization with primary amine groups ($-NH_2$),

[a]*Laboratory for Biomaterials and Bioengineering (CRC-I), Department of Min-Met-Mat Engineering and the CHU de Québec Research Center, Laval University, PLT-1745G, Québec, Québec G1V 0A6, Canada. E-mail: diego.mantovani@gmn.ulaval.ca; Tel: +1 (418) 656-2131 ext 6270*

[b]*Laboratoire Interdisciplinaire de Spectroscopie Electronique, Namur Institute of Structured Matter, University of Namur, 61 Rue de Bruxelles, 5000 Namur, Belgium*

known for their high reactivity,[9] on the surface of the L605 alloys that act as anchor points for the further grafting of molecules of interest with free carboxylic groups in their structure (–COOH). Assuring the stability and the properties of the surface (oxide layer) thus appears crucial for the application of this strategy for cardiovascular devices. This oxide layer must resist deformation related to the deployment of the device, and must be corrosion resistant to avoid the release of toxic ions in the blood stream, whilst being biocompatible.[6,10,11] Among the different strategies to modify the oxide layers and the finishing of metallic substrates, procedures can be divided into mechanical treatments, thermal treatments, ion implantation and chemical treatments.[12] All of these treatments can modulate properties such as chemical composition, surface roughness, corrosion and deformation resistance, wettability, blood compatibility and cytotoxicity.

Although all of these treatments can modify the surface of metallic substrates, regarding the stent applications mechanical treatments (mechanical polishing for example) are not suitable due to the complex geometry of the devices. Therefore, thermal treatments, ion implantation and chemical treatments represent suitable modification procedures. For instance, thermal treatments in a controlled atmosphere can be used to achieve homogeneous changes in the chemical and structural composition.[12,13] In regards to ion implantation processes, such as plasma immersion ion implantation (PIII), these can produce changes both on the surface and in the internal structure, producing an amorphous oxide layer, due to the acceleration of ions into the metallic substrate.[11,14–16] Finally, chemical treatments, for example electropolishing, allow for the removal of any surface contaminant and the passivation of the surface whilst obtaining a nano-smooth surface with a mirror like finish.[7,12,17]

This study focuses on the surface preparation step of L605 alloys for their direct plasma amination. Three different surface treatments on L605 CoCr alloys to modify the oxide layer are proposed: electropolishing (EP), as a base treatment, followed by either thermal treatment (TT) or the PIII of oxygen. The specimens were thoroughly characterized by X-ray Photoelectron Spectroscopy (XPS), Time of Flight-Secondary Ion Mass Spectrometry (ToF-SIMS), Atomic Force Microscopy (AFM), Scanning Electron Microscopy (SEM) and Water Contact Angle (WCA) to study their chemical composition, topography and wettability. Furthermore, the influence of these properties on the plasma amination efficiency of the surface was assessed. The deformation resistance and the corrosion behaviour were also determined along with the biological performance of the surface (hemocompatibility and short-term cellular response). These biological properties were selected to study the potential effect of the device on wound healing of the endothelium and thrombus formation.

2 Materials and methods

2.1 Materials

L605 alloy sheets (nominal composition wt%: Co 51%, Cr 20%, W 15%, Ni 10%, Fe ≤ 3%) were purchased from Rolled Alloys Inc. (QC, Canada). Acetone and methanol (ACS grade, respectively) were purchased from Fisher Scientific (NJ, USA). Phosphoric acid (85%), sulfuric acid (ACS grade), and hydrofluoric acid (48%) were purchased from Laboratoire MAT (QC, Canada). From Sigma-Aldrich, the following reagents were purchased: sodium hydroxide (≥97%, pellets), calcium chloride (99.99%) and 5-bromosalicyladehyde (98%). PBS (phosphate buffered solution, 1× powder) was purchased from Fisher Scientific.

2.2 Sample preparation

2.2.1 Sample cleaning. To remove impurities, round 12.7 mm diameter specimens cut from the L605 alloy sheets were first cleaned in three successive 10 min ultrasonic baths of acetone, nanopure water (18.2 MΩ cm at 25 °C), and methanol. Samples were air-dried after each cleaning and stored under vacuum until further use.

2.2.2 Electropolishing. All samples underwent a three-cycle electropolishing procedure; each cycle was performed for 2 minutes with a fixed current density of 2.4 A cm^{-2} in a solution containing 67 vol% phosphoric acid, 20 vol% sulfuric acid, 10 vol% nanopure water and 3 vol% hydrofluoric acid at 10 °C in an ice bath with a round L605 specimen as the cathode. After electropolishing, samples were cleaned in three ultrasonic baths for 10 min each using nanopure water, sodium hydroxide 2 N and nanopure water, respectively.

2.2.3 Surface treatments. To modify the composition of the oxide layer and to study its effect on the direct plasma amination, EP samples were further treated by two different surface modifications: thermal treatment and the PIII of oxygen. For the thermal treatments, samples were placed in an air furnace at atmospheric pressure at three different temperatures and for two different times: 400, 500 and 600 °C for one or two hours. On the other hand, samples modified by the PIII of oxygen were implanted using a Plasmionique Inc. (QC, Canada) reactor with a gas flow of 10 sccm of O_2, a pulse of 50 μs, a frequency of 100 Hz at 5 mTorr, and 300 W of power; for 60 min at −10 kV, −1 kV or −0.1 kV as bias; or for 15 min and 30 min at −10 kV bias.

2.3 Stability tests

2.3.1 Deformation test. Treated samples were deformed up to 25% using a custom-made small punch test device, mounted on a SATEC T20000 testing machine (Instron, Norwood, USA), which has already been described elsewhere.[18] Deformations were performed at room temperature with a displacement rate of 0.05 mm s^{-1} with a maximal load of 2800 N, adapted for L605, and were further characterized.

2.3.2 Corrosion test. Corrosion tests were carried out using a standard 3 electrode electrochemical set up using large carbon electrodes as the counter electrodes and a saturated calomel electrode as the reference in a 1 L corrosion cell. The selected solution was PBS at 37 ± 1 °C under mechanical stirring. Open circuit potential analyses were performed for one hour followed by potentiodynamic analyses. Corrosion rate calculations were performed following the ASTM G102-89, as previously

described.[19] Briefly the corrosion rate was calculated based on Faradays law (eqn (1)).

$$\text{Corrosion rate} = 0.003272 I_{\text{corr}} \frac{E_{\text{W}}}{d} \quad (1)$$

where 0.003272 is the conversion factor (mm per μA per year), I_{corr} is the corrosion current density, expressed in μA cm^{-2}, E_{W} is the equivalent weight of the alloy (26 g) and d is the density of the L605 alloy (9.134 g cm^{-3}). Measurements were performed with a Model K47 Corrosion Cell system and a Versa-STAT 3 Potentiostat controlled *via* Versa-Studio software (AMETEK Princeton Applied Research, TN, USA).

2.4 Plasma functionalization

2.4.1 Plasma amination. Direct plasma amination was performed in microwave plasma (Plasmionique Inc., QC, Canada) through a two-step procedure: the first step used a mixture of N_2 (grade 4.8, Linde, QC, Canada) and H_2 (grade 5.0, Linde, QC, Canada) as feeding gases at 150 W for 10 min at 100 mTorr with a 5/5 sccm flow.[9] The second step was carried out at 150 W for 30 s at 300 mTorr with a 10 sccm flow of hydrogen. This short plasma treatment using hydrogen was performed to promote the formation of amine groups and reduce the presence of other nitrogen species.[20] During both steps, the samples were placed in the after-glow (~7 cm). Amination efficiency was assessed by chemical derivatization with 5-bromosalicylaldehyde as described by Chevallier *et al.*[21] immediately after the plasma treatments. Briefly, the vapor-phase reaction took place in a sealed glass tube at 40 °C for 2 h to complete the derivatization. This molecule was selected due to its specific selectivity to primary amine groups.

2.5 Biological tests

2.5.1 Cell viability. Human umbilical vein endothelial cells (HUVEC) were isolated from an umbilical cord with the previous consent of donor mothers as previously described.[22] Cells from third to sixth passages were used to evaluate the interaction with the surfaces. 40 000 cells in M199 (Thermo Fisher, 11150-067) culture media containing serum and penicillin-streptomycin (Gibco, 15140-122) were deposited on surfaces and incubated at 37 °C. After adhesion for 24 h, cells were rinsed with PBS in order to eliminate all remaining culture medium. 300 μL of solution of resazurin in the culture medium (1 : 10) were then added to the samples and allowed to react for 4 h. 150 μL were taken from each sample and the fluorescence was measured at 570 nm using a spectrophotometer ELISA reader (BioRad mod.450, ON, Canada).

2.5.2 Haemolysis rate. In order to study the hemocompatibility of the different surfaces, a hemoglobin free methodology was assessed.[23] Briefly, 120 μL of recalcified citrated blood were immediately dropped onto the surfaces. Samples were incubated at 37 °C and after 20 min, 2 mL of distilled water were added to each surface. Red blood cells not entrapped in a thrombus were hemolyzed. Free hemoglobin molecules were measured using a spectrophotometer ELISA reader at 540 nm. The test was performed 3 independent times with 2 samples per condition each time. Blood from different donors was used for each experiment.

2.6 Surface characterization

2.6.1 X-ray photoelectron spectroscopy (XPS). The chemical composition of the different surfaces was assessed by XPS (depth analysis of ~5 nm). The analyses were carried out using an X-ray Photoelectron Spectrometer (XPS-PHI 5600-ci Spectrometer-Physical Electronics, MN, USA). Survey spectra (0–1400 eV) were acquired with a standard aluminium X-ray source (1486.6 eV) at 300 W. Charge neutralization was not applied for the analyses. The detection was performed at 45° with respect to the surface normal and the analyzed area was 0.005 cm^2.

2.6.2 Time of flight secondary ion mass spectroscopy (ToF-SIMS). All analyses were performed using a ToF-SIMS IV spectrometer (ION-TOF GmbH, Münster Germany) with, for the surface spectra and images, the following operating conditions: a pulsed 25 keV Bi_3^+ ion beam (current = 0.3–0.4 pA; pulse width = 20 ns; pulse width after bunching = 1.0 ns; repetition rate = 10 kHz) was rastered during an acquisition time of 100 s over a 250 × 250 μm^2 area. The total ion fluence was kept under 10^{12} ions per cm^2 in order to guarantee static conditions. The secondary ions were extracted at a 2 kV acceleration voltage. Positive and negative spectra were calibrated to the CH_3^+, $C_3H_3^+$ and $CrOH^+$ peaks and to the C_2^-, CrO^- and CoO_2^- peaks, respectively. ToF-SIMS spectra were acquired from 0 to 880 m/z.

During ToF-SIMS depth profiling, the analysis beam (as previously described) and the erosion beam (Cs^+ at 500 eV, current: 40–45 nA), rastered over a 500 × 500 μm^2 area to avoid border effects, were operated in non-interlaced mode with one analysis frame (1.6384 s) and 5 s erosion per cycle, both with a 45° incidence angle to the sample surface.

2.6.3 Scanning electron microscopy. The sample surfaces were imaged by SEM using a FEI Quanta 250 (FEI Company Inc. Thermo-Fisher Scientific, OR, USA), with a tungsten filament and an acceleration voltage in the range of 10–30 kV in secondary electron mode.

2.6.4 Atomic force microscopy. Surface texture investigations were performed using the tapping mode on a DimensionsTM 3100 Atomic Force Microscope (Digital Instruments/Veeco, NY, USA) with an etched silicon tip (model NCHV, tip radius = 10 nm, Bruker). Areas of 20 × 20 μm^2 were recorded and analyzed using the NanoScope Analysis software (Bruker). Surface roughness was assessed with NanoScope Analysis (Bruker Corporation, MA, USA) and reported as the root mean square roughness (Rq).

2.6.5 Water contact angle. Surface wettability was assessed by water contact angle measurements with a video contact angle system VCA-2500 XE™ (AST products Inc., MA, USA) in static mode before and after plasma functionalization. A 1 μL droplet of nanopure water was used.

2.6.6 Statistical analysis. For XPS, WCA, hemoglobin free, cell viability and corrosion tests, the data were represented as the mean ± standard deviation of 9 measurements, corresponding to 3 independent experiments with each condition in triplicate. For all tests, significant differences were determined

by running a one-way ANOVA followed by Tukeys *post-hoc* method to test all possible pairwise comparisons and to determine where the differences lied. A p-value < 0.05 was considered significant (*).

3 Results

3.1 Selection of conditions

Due to the importance of the mechanical stability of the oxide layer during the deployment of a stent, a deformation test was performed in order to evaluate the resistance of the different treatments. As observed in Fig. 1, conditions such as 600 °C for 1 h for TT and in the case of PIII, −10 kV for 1 h, presented cracks and peelings on their oxide layer. Therefore, such conditions were discarded. From the remaining conditions, only one for each treatment was selected for the complete study. The selected conditions were EP as a base treatment, TT at 400 °C for 1 h and PIII −0.1 kV for 1 h.

3.2 Surface treatments

The chemical composition of the oxide layers, assessed by XPS survey analyses, shown in Fig. 2a, showed that the first few nanometers of the oxide layer of the EP sample surface were composed mainly of chromium (%Cr = 4.8 ± 0.2); on the contrary, the PIII sample surface was composed of cobalt (%Co = 13.5 ± 0.7%); finally, the TT sample surfaces showed the presence of both cobalt and chromium oxides (%Cr = 1.5 ± 0.2, %Co = 12.1 ± 0.5) with traces of other metals such as nickel. Moreover, the distribution of CrO_2^- and CoO_2^- ions was studied for each of the metallic oxides by ToF-SIMS imaging in negative mode (Fig. 2b). This confirmed what was observed in the XPS survey results, where it was found that the composition of the outmost layers of EP, TT and PIII follows the same trend. ToF-SIMS depth profile analyses were also performed to obtain information about the depth distribution of the different elements of the oxide layers. Fig. 3 shows the obtained profiles where it was found that the EP oxide was the thinnest of them all (~50 s of sputtering) and is composed mainly of chromium oxide. PIII on the other side, has a thicker oxide layer that is composed of a topmost cobalt oxide layer on a chromium oxide sublayer (~150 s and ~350 s of sputtering, respectively). Finally, TT has a thick oxide layer composed of both cobalt and chromium oxides on the topmost layer of the surface (~600 s of sputtering). It is worth noting that SRIM simulations have been performed to estimate the sputter yields of chromium and cobalt oxides under Cs bombardment and that their similar values (2.4 and 2.6 atoms per ion, respectively) allowed us to safely compare the sputter times between the profiles and equate them with depths.

The morphology of the substrate surface was evaluated through AFM (Fig. 4). The presence of grain boundaries can be observed on the EP surface, but not as visibly as on the TT surface, whereas on PIII, grain boundaries are not clearly present. Regarding the surface roughness, Rq, it was found that the smoothest surface among the different treatments was EP and that after surface modification this value increased significantly on both TT and PIII.

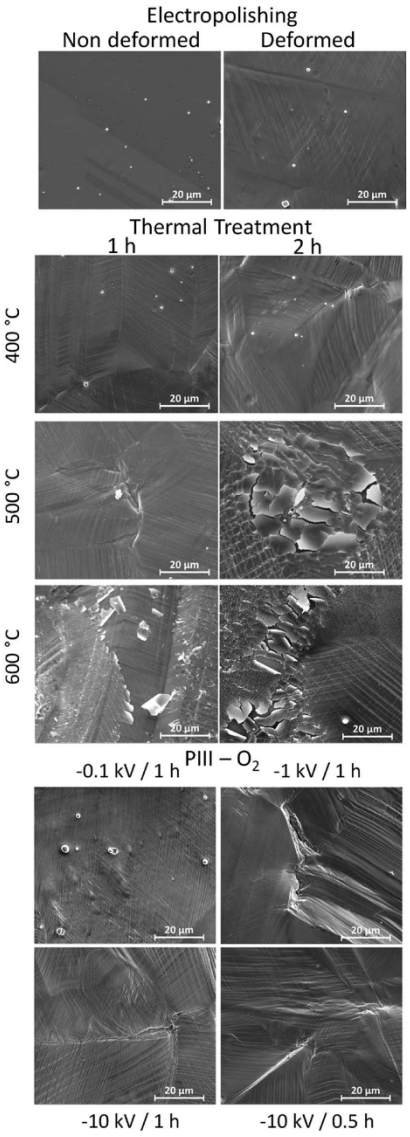

Fig. 1 SEM images of the surfaces after small punch tests to simulate deformation up to 25%. Cracks and delamination were observed under some TT and PIII conditions. Selected conditions for the further steps of the study were EP, as a base surface, 400 °C for 1 h for TT and −0.1 kV for 1 h for PIII. Magnification of 2000× was used for all of the images. TT and PIII images were all obtained after deformation.

To investigate the corrosion behaviour of the different surface treatments, OCP and potentiodynamic polarization analyses were performed. Regarding OCP (Fig. 5a) it was found

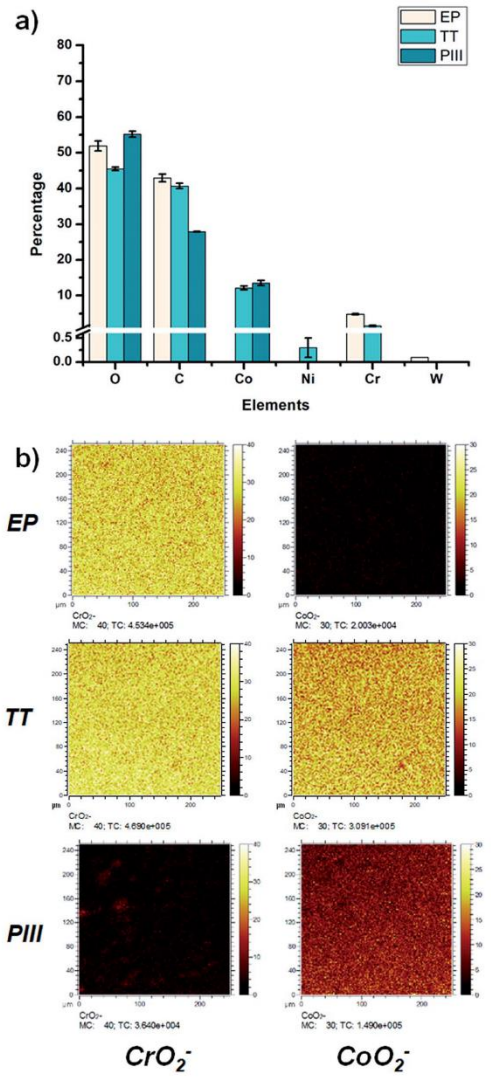

Fig. 2 Chemical composition of the studied surfaces. (a) XPS survey analyses and (b) ToF-SIMS imaging mode of the surface of the specific metallic oxide fragments for chromium CrO_2^- (84 *m*/*z*) and for cobalt CoO_2^- (91 *m*/*z*).

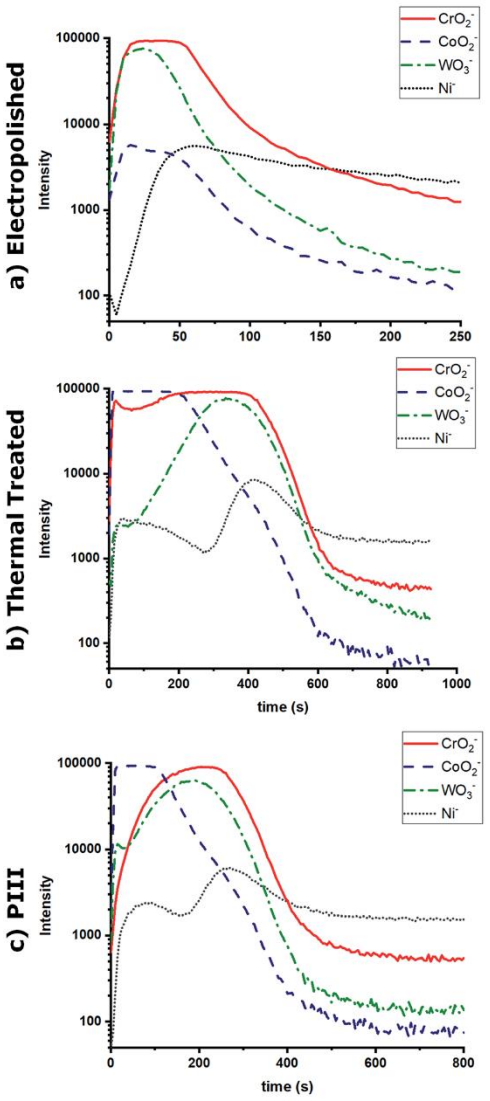

Fig. 3 ToF-SIMS depth profile of surface treatments. (a) EP, thin layer composed mainly of chromium oxides, (b) TT, thicker layer composed of both oxides on the same depth, and (c) PIII, two layers, first cobalt oxides then chromium oxide.

that TT, composed of a mixture of chromium and cobalt oxides, had the lowest open circuit potential, had the most reactive oxide layer and was the most susceptible to corrosion, compared to the other surfaces, whilst PIII was the one with the most positive potential and had the least reactive oxide layer. Potentiodynamic curves (Fig. 5b) allowed for the calculation of the corrosion rate where it was found that, as observed in the OCP curves, TT was the surface treatment with the highest corrosion rate, followed by PIII and finally EP with a ~20× decrease compared to TT. These values and a summary of the results are shown in Fig. 5c.

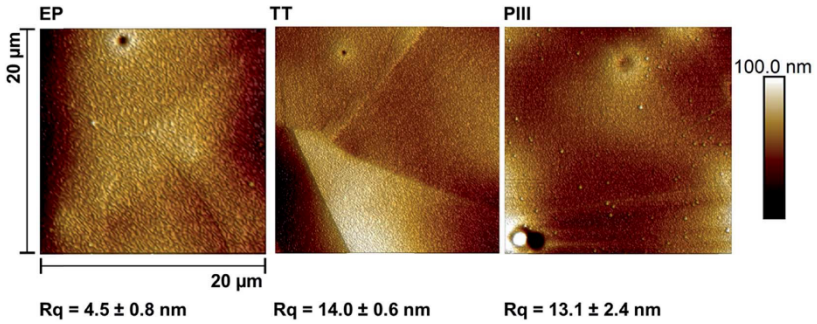

Fig. 4 AFM images (20 × 20 µm^2, height mode) of the different samples with their respective roughness values. It can be observed that EP is significantly smoother than the other two surface treatments. TT and PIII present no significant difference among them.

3.3 Plasma functionalization

After the complete characterization of the different oxide surfaces, direct plasma amination was carried out. For the characterization of the surface, chemical derivatization was performed in order to confirm the presence of the amine groups.[21] XPS survey analysis results show that on the TT and PIII surfaces there was a significantly higher percentage of nitrogen on the surface compared to EP, as shown in Fig. 6a. Moreover, there was a significant difference in the percentage of NH_2 on EP compared with the other two surface treatments, but not between TT and PIII. Finally, the efficiency of the functionalization (%NH_2/N) was assessed. This was calculated from the percentage of amine groups deduced from chemical derivatization (%NH_2) and the percentage of nitrogen on the surface after plasma treatment. It was found that EP was the one with the highest efficiency, close to 15%, compared to the other surface treatments, around 9%, as observed in Fig. 6a.

Due to the present debate for the use of chemical derivatization as a valid quantification method for primary amine groups, supplementary surface characterization was performed.[24] Complementary results obtained from ToF-SIMS static mode analyses for the NH_2^+ fragment confirmed that EP has a higher relative concentration of this fragment, followed by PIII and then TT with the lowest signal, as observed in Fig. 6b. Another characterization technique that was performed was contact angle, where it was found that the wettability of all surface treatments changed from a relatively hydrophobic behaviour to a more hydrophilic surface after plasma amination, as observed in Fig. 7.

3.4 Biological performance

Further characterization of the surfaces was performed in order to evaluate the biological performance of the different conditions. The viability of HUVEC was studied after 24 h of contact with the samples. As observed in Fig. 8a, significantly higher cell

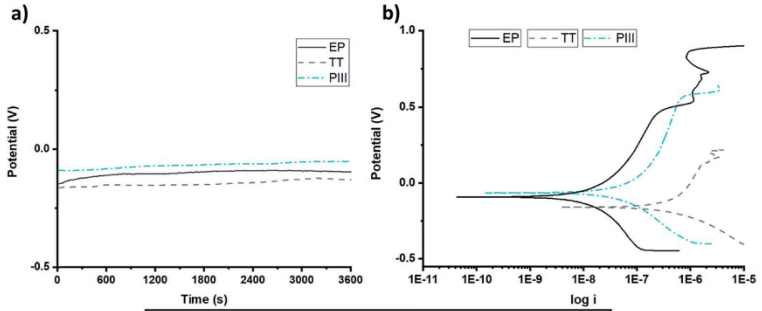

Sample	E_{oc} mV	E_{corr} mV	i corr µA/cm²	Corrosion Rate µm/year
EP	-97.1 ± 12.5	-84.3 ± 9.9	0.013 ± 0.005	0.12 ± 0.05
TT	-150.2 ± 11.5	-125.7 ± 33.5	0.27 ± 0.14	2.55 ± 1.29
PIII	-66.4 ± 11.9	-74.8 ± 16.7	0.05 ± 0.03	0.47 ± 0.29

Fig. 5 Corrosion rate of the surface treatments. It was found that EP is the most corrosion resistant, followed by PIII and finally TT, the least resistant. Potentiodynamic tests were performed in PBS at 37 °C.

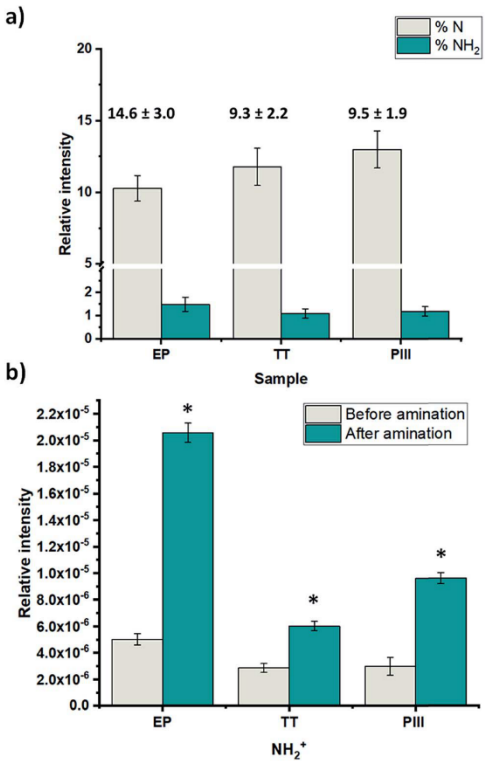

Fig. 6 Nitrogen and amine quantification after plasma treatment of the surfaces. (a) Percentage of nitrogen and percentage of amine groups after chemical derivatization, obtained by XPS survey analyses with the amination efficiency on top of each sample % (NH_2/N). (b) Comparison of the presence of the NH_2^+ fragment on the different surfaces, before and after amination, performed by ToF-SIMS where EP showed the highest presence of the fragment compared to the other surfaces, which was similar to results obtained after XPS analyses. It should be noted that the intensity of the fragments was normalized by the complete total signal in order to be able to compare the results. Significant differences were determined by running a one-way ANOVA followed by Tukeys *post-hoc* method. A p-value < 0.05 was considered significant (*).

viability was observed under the EP conditions (>80%) when compared to the PIII ones (>60%), while TT presented intermediate behaviour with no significant difference with TT nor with EP (>70%). Hence, EP exhibited the higher viability of all the samples. Regarding the evaluation of the hemocompatibility, neither of the samples presented thrombus formation after 20 min of contact with whole blood (Fig. 8b). The TT conditions seemed to present a higher amount of free hemoglobin and therefore the best hemocompatibility. However, no significant differences were found among the different conditions after statistical analysis, mainly because of the high variations observed.

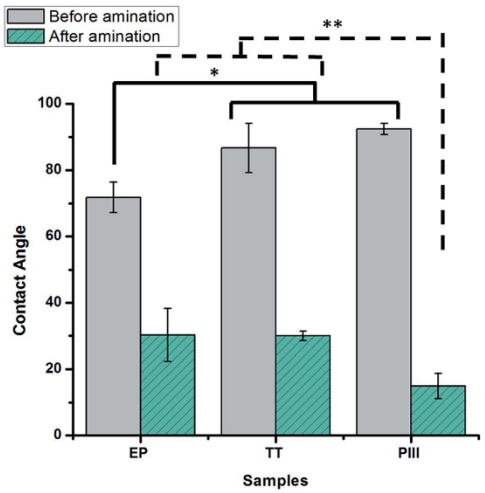

Fig. 7 Water contact angle of the surfaces before and after plasma amination. It was found that after functionalization all of the surfaces presented a hydrophilic behaviour. Significant differences were determined by running a one-way ANOVA followed by Tukeys *post-hoc* method. A p-value < 0.05 was considered significant (*).

4 Discussion

The aim of this work was to study different surface treatments on L605 CoCr alloys with potential application for cardiovascular devices. In order to find the most suitable oxide layer, properties such as deformation and corrosion resistance, efficiency towards direct functionalization (therein amination) and biological performance in terms of cytotoxicity and hemocompatibility were studied.

Therefore, one of the initial properties that was sought after for these oxide layers was the resistance to deformation, without showing either cracks or delamination. After deforming them up to 25%, similar to a stent deployment,[18] some of the initially proposed conditions exhibited cracks and delamination, as observed in Fig. 1, meaning that their oxide layers were unstable and not suitable for application. This may be explained by the formation of brittle or too thick oxide layers that were not able to sustain deformation. Regarding the thermal treated samples, the only oxide layer to not exhibit cracks and delamination was the one obtained at 400 °C for 1 h (Fig. 1), despite being approximately 10 times thicker than the oxide layer obtained after EP, as observed by the ToF-SIMS depth-profile results (sputter time 600 s *versus* 60 s, respectively – Fig. 3). The failure of thermal treatments at higher temperatures and longer times could be related to the formation of bigger oxide crystals (as seen in Fig. 1 for 500 °C – 2 h, and 600 °C – 1 h and 2 h). Similar observations have already been described by Griffage *et al.* where they found that during thermal treatments the L605s surface had a low resistance to oxidation, resulting in a thicker

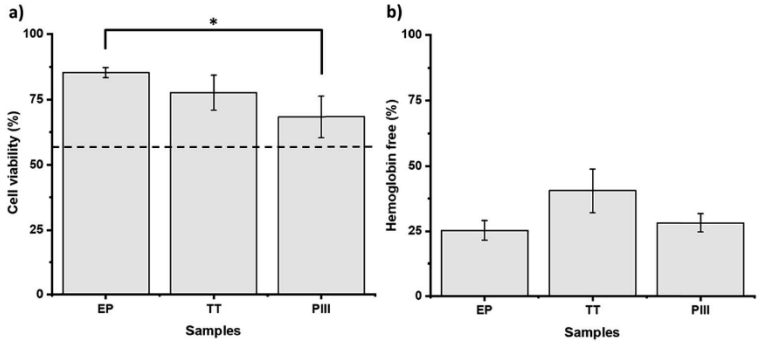

Fig. 8 Biological performance of the different treated surfaces. (a) HUVEC viability, normalized to polystyrene well. There was no significant difference among samples, except EP with PIII, but the viability higher than 60% of the cells is represented by the dashed line. (b) Hemocompatibility test, normalized to haemolysed blood, where there was no significant difference between samples after the haemoglobin free test. Significant differences were determined by running a one-way ANOVA followed by Tukeys *post-hoc* method. A p-value < 0.05 was considered significant (*).

oxide layer as a function of temperature and time.[25] Moreover, the mechanism for cracks and delamination proposed by Wang *et al.* was considered, which involves the formation of microcracks/voids and a high density of oxide particles on the grain boundaries in the near-surface area that propagate parallel to the alloy surface with deformation.[26] These features create a less ductile surface than the underlying bulk leading to peeling, cracks and delamination. This mechanism explains what was observed at the higher temperatures of the thermal treatments (Fig. 1), making these conditions not suitable for the desired application.

In the case of the PIII treatments, a higher bias voltage (−1 kV and −10 kV) appeared to induce a thicker oxide layer which was unstable to deformation, without formation of crystals compared to TT, as observed in Fig. 1, whereas the oxide surface obtained at the lowest bias, −0.1 kV, sustained the deformation. It is known that oxygen implantation doses can modulate the crystalline structure (hexagonal Co-oxygen rich phase), and the oxide layer thickness, thus leading to changes in the mechanical properties (hardness).[27,28] The ion doses are higher when the bias voltage applied on the sample is more negative, leading to the acceleration of positive ions which are thus more implanted (an increase of the oxide thickness). Thus, −1 kV and −10 kV should create a thicker oxide layer than the one obtained at −0.1 kV, which already needed a sputter time of 400 s (Fig. 3, ToF-SIMS depth profile). Moreover, as can be observed in Fig. 1, the failure of the PIIIs oxide layer is mainly due to delamination rather than to the formation of cracks, as seen in the thermal treatments. This behaviour might be related to the amorphization of the oxide layer after the implantation of the oxygen ions.[27] Hence, due to their resistance to deformation, only EP, as a base surface treatment, TT at 400 °C for 1 h and PIII with a bias of −0.1 kV for 1 h of implantation of oxygen were considered.

Another desired surface property for stent application is corrosion resistance. Due to the composition of the alloy, the concern of the release of potential cancerogenic ions, such as nickel and chromium, into the blood stream is latent. It is known that alloys such as L605 are resistant to corrosion due to its percentage of chromium oxide,[29,30] but modifying its surface composition can influence its corrosion resistance. To get a better idea of the oxide layer stability and resistance to corrosion, both Open Circuit Potential (OCP) and potentiodynamic tests were performed (Fig. 5). As shown in this figure, EP, the treatment with the thinnest oxide layer (Fig. 3) composed of chromium oxides on the surface, based on XPS and ToF-SIMS analyses (Fig. 2), was the most corrosion resistant compared to the other ones. This can be attributed to the formation of a passive layer by the Cr_2O_3 surface, similar to what Sojitra *et al.* observed on stainless steels.[17] Furthermore, the corrosion rate for PIII was not far from that of EP, which could be associated to the "bilayer" composition of the oxide layer of the PIII treatment. The topmost layer was composed mainly by cobalt oxides then followed closely by chromium oxides, as observed *via* ToF-SIMS depth analyses (Fig. 3c). This change in both composition and corrosion is similar to what was found by Lutz *et al.*:[31] a diffusion of cobalt to the topmost layer of the alloy. This increases the dissolution of this ion during the initial step of corrosion, followed by a decrease of the corrosion rate by the presence of the passive layer conferred by Cr_2O_3. Moreover, as observed in Fig. 5, PIII exhibited the highest E_{oc}, meaning that this oxide layer behaves as the noblest surface compared to the 2 other samples. However, all of the samples exhibited a stable oxide layer as no increase nor decrease was observed during the 1 h of OCP. Finally, on the TT surface, a combination of chromium and cobalt oxides are present on both the surface and in depth (Fig. 3b). In fact, this surface chemical composition could be related to the potential formation of a spinel ($CoCr_2O_4$) which has been described previously in literature.[25,32] Furthermore, after thermal treatments at higher temperatures, a dark blue colour, characteristic of this compound, was observed under polarized light (image not shown). The formation of this

spinel added to the increase in the roughness of the surface, as observed by AFM (Fig. 4), and produced the lowest values of both E_{oc} and E_{corr} (Fig. 5), leading to a surface more prone to corrode and thus an increase in the corrosion on the surface.

Regarding the direct amination of the different oxide layers by plasma functionalization, it was found that all of the surfaces changed their hydrophobic behaviour after plasma treatment to a more hydrophilic surface as shown by the contact angle (Fig. 7). This can be related to the nitrogen species formed after the plasma treatments since surfaces functionalized with amine groups can lower the contact angle of the oxide layers *via* hydrogen bond interactions.[33] Furthermore, the nitrogen content incorporated on the surfaces was assessed by XPS survey analyses (Fig. 6a). Among the proposed surface treatments, EP was the one with the smaller percentage of nitrogen on the surface with around 10%, whilst TT and PIII were both around 15%. However, the percentage of primary amine groups on the surfaces on metallic substrates is around 1.5% with no significant difference between the surfaces. When evaluating the efficiency of the direct plasma amination, $\%NH_2/N$, EP was the surface treatment with the highest efficiency, as observed in Fig. 6a. Moreover, this observation was further confirmed by ToF-SIMS analyses on the static mode of the NH_2^+ fragment related to the primary amine group (Fig. 6b). Indeed, similar to the XPS survey analyses, EP was the oxide layer that showed the highest concentration of this specific fragment on the first layer of its atomic composition, followed by PIII and finally TT, which had the lowest presence of this fragment on its surface. The main hypothesis for this preferential formation of amines on the EP surface could be explained by a substitution reaction of $-NH_2$ on the surface hydroxyl groups (–OH), which are already present in the surface of the L605 alloy and are generated during the basic bath performed just after electropolishing.[34] Nevertheless, when performing the thermal treatment and the ion implantation, these –OH groups could be lost by re-oxidizing the surface, therefore decreasing the amination efficiency.

The biological performances of the different samples were also assessed to ensure that the proposed surface treatments were suitable for stent application. Therefore, the interaction of the samples with blood and endothelial cells was evaluated. The decreasing cell viability observed in the samples as EP > TT > PIII, as observed in Fig. 8a, can be explained with the chemical composition of the surfaces. As it was previously stated, the EP sample has mainly chromium at the surface, PIII has mostly cobalt, while TT has a mixture of both elements. Hence, our results are coherent with previous works comparing the behaviour of different cell types in the presence of chromium and cobalt. Indeed, Rushton *et al.* compared these two elements when in contact with osteoblast-like cells, proving that cobalt has the most negative effect when compared to chromium and to an alloy of both elements.[35] Other groups have also evaluated the negative effect of the presence of cobalt in the proliferation and collagen production of osteoblast-like cells.[36–38] Moreover, Maffi *et al.* also proved higher endothelial cell viability when cobalt–chromium alloys were enriched with Cr at the surface.[39] However, chromium, and specifically Cr_6^+, has also been proven to reduce cell survival, which explains the limited difference among all samples, as well as the decrease of cell viability when compared to the positive control. These findings are also coherent with the intermediate behaviour of TT between EP and PIII, mainly because TT has both Cr and Co at the surface. When it comes to hemocompatibility, shown in Fig. 8b, all samples presented promising results with no thrombus formation after 20 min of contact with the samples. These results are coherent with previous clinical studies comparing several alloys used in biomaterials where cobalt–chromium presented high hemocompatibility.[37,40] The different treatments performed had no significant impact on the hemocompatibility of the samples.

5 Conclusions

In this study, different surface treatments have been explored in order to reach the most suitable surface, regarding oxide layer stability towards deformation and corrosion, and for amination efficiency. Some surface treatment conditions were discarded as after deformation their surfaces showed cracks or delamination. The other treatments led to different oxide layer compositions and thicknesses as evidenced by XPS and ToF-SIMS depth profiling analyses. Indeed, the EP surface was mainly composed of a thin layer of chromium oxide, whereas PIII surface oxides exhibited a bilayer arrangement, with essentially cobalt oxides on the outermost layer followed by chromium oxides underneath and, finally, TT displayed the thickest oxide layer of mixed chromium and cobalt oxides on the surface. Corrosion performance showed that among the three proposed surface treatments EP was the surface with the lowest corrosion rate, followed by PIII and finally TT with the highest corrosion rate, which was ~20 times more than EP. Then, regarding biological tests, the different surface compositions of the oxides exhibited no significant differences among them. In the short-term, it appeared to not induce a negative cellular response, cell viability was higher than 60%, and to not induce thrombus formation as evidenced by hemocompatibility tests. Concerning direct plasma functionalization, it was found that all the surfaces could be directly functionalized with primary amine groups regardless of initial oxide layer composition. However, regarding the amination efficiency, EP oxide composition seemed to promote amine formation as evidenced by XPS and ToF-SIMS analyses.

Therefore, among the different surface treatments, the EP oxide surface displayed the best corrosion resistance as well as the highest amination efficiency, and did not induce a negative cellular response or thrombus formation. Thus, EP treatment appeared as the most suitable metallic interface for the further grafting of biomolecules. This direct amination of metallic substrates and grafting of biomolecules, without any intermediate layer, emerges as a potential approach for a new generation of bioactive cardiovascular devices, aiming to lower post implantation complications. Future studies will investigate different grafting strategies of peptides on EP aminated samples, their stability under pseudo-physiological conditions and their biological performances.

Conflicts of interest

There are no conflicts to declare.

Acknowledgements

Sergio Diaz-Rodriguez is a recipient of a PhD scholarship from the NCPRM (www.ncprm.ulaval.ca). Our thanks to Prof. Frederic Chaubet (U. Paris XIII), and Dr Giuseppina Caligiuri (INSERM, Hopital Bichat, France) for scientific help and guidance. This work was supported by the Natural Sciences and Engineering Research Council of Canada (NSERC), the CHU de Québec Research Center, The Ministry of Economy, Science and Innovation of Quebec, and the Linkage Grants Québec/Wallonie-Brussels of the Ministery of International Relations and "La francophonie" of Quebec.

Notes and references

1 M. R. Adams, S. Kinlay, G. J. Blake, J. L. Orford, P. Ganz and P. Selwyn, *Curr. Atheroscler. Rep.*, 2000, **2**, 251–258.
2 T. Xi, R. Gao, B. Xu, L. Chen, T. Luo, J. Liu, Y. Wei and S. Zhong, *Biomaterials*, 2010, **31**, 5151–5158.
3 F. Migliavacca, L. Petrini, V. Montanari, I. Quagliana, F. Auricchio and G. Dubini, *Med. Eng. Phys.*, 2005, **27**, 13–18.
4 J. Pache, A. Kastrati, J. Mehilli, H. Schühlen, F. Dotzer, J. Hausleiter, M. Fleckenstein, F. J. Neuman, U. Sattelberger, C. Schmitt, M. Müller, J. Dirschinger and A. Schömig, *J. Am. Coll. Cardiol.*, 2003, **41**, 1283–1288.
5 R. X. Yin, D. Z. Yang and J. Z. Wu, *Theranostics*, 2014, **4**, 175–200.
6 G. Mani, M. D. Feldman, D. Patel and C. M. Agrawal, *Biomaterials*, 2007, **28**, 1689–1710.
7 H. Takahashi, D. Letourneur and D. W. Grainger, *Biomacromolecules*, 2007, **8**, 3281–3293.
8 M. Cloutier, S. Turgeon, P. Chevallier and D. Mantovani, *Adv. Mater. Res.*, 2011, **409**, 117–122.
9 S. Diaz-Rodriguez, P. Chevallier and D. Mantovani, *Plasma Processes Polym.*, 2018, e1700214.
10 T. Hryniewicz, R. Rokicki and K. Rokosz, *Mater. Lett.*, 2008, **62**, 3073–3076.
11 M. M. Dorri, S. Turgeon, M. Cloutier, P. Chevallier and D. Mantovani, *Corrosion*, 2018, 2674.
12 E. Almeida, *Ind. Eng. Chem. Res.*, 2001, **40**, 3–14.
13 A. A. John, A. P. Subramanian, M. V. Vellayappan, A. Balaji, S. K. Jaganathan, H. Mohandas, T. Paramalinggam, E. Supriyanto and M. Yusof, *RSC Adv.*, 2015, **5**, 39232–39244.
14 G. Wu, P. Li, H. Feng, X. Zhang and P. K. Chu, *J. Mater. Chem. B*, 2015, **3**, 2024–2042.
15 Y. Tian, H. Cao, Y. Qiao and X. Liu, *RSC Adv.*, 2016, **6**, 46495–46507.
16 S. Ghosh, R. Bhattacharyya, H. Saha, C. R. Chaudhuri and N. Mukherjee, *Phys. Chem. Chem. Phys.*, 2015, **17**, 27777–27788.
17 P. Sojitra, C. Engineer, D. Kothwala, A. Raval, H. Kotadia and G. Mehta, *Trends Biomater. Artif. Organs.*, 2010, **23**, 115–121.
18 F. Lewis and D. Mantovani, *Macromol. Mater. Eng.*, 2009, **294**, 11–19.
19 F. Lewis, M. Cloutier, P. Chevallier, S. Turgeon, J.-J. Pireaux, M. Tatoulian and D. Mantovani, *ACS Appl. Mater. Interfaces*, 2011, **3**, 2323–2331.
20 A. A. Meyer-Plath, K. Schröder, B. Finke and A. Ohl, *Vacuum*, 2003, **71**, 391–406.
21 P. Chevallier, M. Castonguay, S. Turgeon, N. Dubrulle, D. Mantovani, P. H. McBreen, J.-C. Wittmann and G. Laroche, *J. Phys. Chem. B*, 2001, **105**, 12490–12497.
22 C. Loy, D. Pezzoli, G. Candiani and D. Mantovani, *Biotechnol. J.*, 2018, **13**, 1700359.
23 E. C. Michel, V. Montaño-Machado, P. Chevallier, A. Labbé-Barrère, D. Letourneur and D. Mantovani, *Biomatter*, 2014, **4**, F28805.
24 C.-P. Klages and S. Kotula, *Plasma Processes Polym.*, 2016, **13**, 1213–1223.
25 S. J. Griffage and C. E. Lowell, *NASA TN D-5019*, 1968, pp. 1–37, Id. 19690007945.
26 J. Wang, X. Zhou, G. E. Thompson, J. A. Hunter and Y. Yuan, *Mater. Charact.*, 2015, **99**, 109–117.
27 M. Dorri, S. Turgeon, N. Brodusch, M. Cloutier, P. Chevallier, R. Gauvin and D. Mantovani, *Microsc. Microanal.*, 2016, **22**, 997–1006.
28 S. Mändl, C. Díaz, J. W. Gerlach and J. A. García, *Nucl. Instrum. Methods Phys. Res., Sect. B*, 2013, **307**, 305–309.
29 V. Milleret, A. Ziogas, S. Buzzi, R. Heuberger, A. Zucker and M. Ehrbar, *J. Biomed. Mater. Res., Part B*, 2015, **103**, 629–640.
30 A. W. E. Hodgson, S. Kurz, S. Virtanen, V. Fervel, C.-O. A. Olsson and S. Mischler, *Electrochim. Acta*, 2004, **49**, 2167–2178.
31 J. Lutz, C. Díaz, J. A. García, C. Blawert and S. Mändl, *Surf. Coat. Technol.*, 2011, **205**, 3043–3049.
32 D. Jasaitis, A. Beganskienė, J. Senvaitienė, A. Kareiva, R. Ramanauskas, R. Juškėnas and A. Selskis, *Chemija*, 2011, **22**, 125–130.
33 C. Holmes and M. Tabrizian, *Stem Cell Biology and Tissue Engineering in Dental Sciences*, Elsevier, 2015, pp. 187–206.
34 Y. Tanaka, H. Saito, Y. Tsutsumi, H. Doi, H. Imai and T. Hanawa, *Mater. Trans.*, 2008, **49**, 805–811.
35 M. J. Allen, B. J. Myer, P. J. Millett and N. Rushton, *J. Bone Jt. Surg., Br. Vol.*, 1997, **79B**, 475–487.
36 L. Anissian, A. Stark, H. Dahlstrand, B. Granberg, V. Good and E. Bucht, *Acta Orthop. Scand.*, 2002, **73**, 369–374.
37 M. G. Permenter, W. E. Dennis, T. E. Sutto, D. A. Jackson, J. A. Lewis and J. D. Stallings, *PLoS One*, 2013, **8**, e83751.
38 L. O. Simonsen, H. Harbak and P. Bennekou, *Sci. Total Environ.*, 2012, **432**, 210–215.
39 R. Rokicki, W. Haider and S. K. Maffi, *J. Mater. Eng. Perform.*, 2015, **24**, 345–352.
40 Y. Yang, S. F. Franzen and C. L. Olin, *J. Heart Valve Dis.*, 1996, **5**, 532–537.